



UNIVERSITÀ DI NAPOLI "FEDERICO II"

DOTTORATO DI RICERCA IN FISICA

CICLO XXXIII

COORDINATORE: PROF. SALVATORE CAPOZZIELLO

**Physics of the Josephson Effect in
Junctions with Ferromagnetic
Barriers towards Quantum Circuits
and RF Applications**

SETTORE SCIENTIFICO DISCIPLINARE: FIS/03

Dottorando:

Halima Giovanna
AHMAD

Tutor:

Prof. Francesco TAFURI

ANNI 2018/2021

Contents

Introduction	1
1 Josephson effect in ferromagnetic Josephson junctions	3
1.1 Critical current modulation in magnetic fields	4
1.2 Critical current dependence on the thickness and the temperature	10
1.3 The electrodynamics in SIS and SFS heterostructures	17
1.3.1 The $I(V)$ curves: models and study of the quasiparticles dissipation	18
1.3.2 The phase-dynamics	24
1.4 Transport properties in tunnel ferromagnetic Josephson junctions	28
2 Experimental setup	31
2.1 The Evaporation cryostat	31
2.2 Dilution fridges	32
2.3 The Triton filtering systems and electronics	35
2.3.1 DC setup	35
DC-measurements techniques	40
Discussion on the errors	42
2.3.2 RF setup	43
3 Transport properties in spin-filter Josephson junctions: a protocol to demonstrate spin-triplet correlations	60
3.1 Samples scheme	61
3.2 Spin-dependent transport properties	63
3.2.1 $R(T)$ curves	63
3.2.2 $I(V)$ curves	64
3.3 Magnetic phenomena in spin-filter JJs	68
3.4 Spin-triplet superconductivity in spin-filter JJs	70
3.4.1 Phenomenological approach	71
3.4.2 Atomistic modeling	73
4 Electrodynamics of ferro-tunnel JJs	80
4.1 Study of the electrodynamics in SI_fS JJs	81
4.1.1 $I(V)$ curves analysis	81
4.1.2 The phase-dynamics: the SCDs	86
4.2 Comparative electrodynamic study of ferro-tunnel JJs	88

5	Towards SFS active quantum devices: future perspectives	96
5.1	Ferro-transmon with a hybrid DC-SQUID	101
5.2	Transmon with a capacitively coupled tunnel-SFS JJs	106
	Conclusions and perspectives	117
A	Triton DC and RF system CADs	119
A.1	Brass-powder filters	119
A.2	DC-sample stage	119
A.3	Amplifiers	120
B	Software	124
B.1	PSCAN2 and MiTMojCo	124
B.1.1	The codes	124
B.1.2	Discussion on the $I(V)$ curves simulations parameters	127
C	The Transmon: an overview	131
C.1	Qubit Hamiltonian derivation: a protocol	131
C.2	The transmon Hamiltonian	133
C.2.1	The charge dispersion vs. the anharmonicity in a transmon	134
C.2.2	Transmon read-out and circuit QED	136
C.2.3	Flux modulation	139
C.3	Noise and decoherence in a qubit	140
C.3.1	Decoherence in a transmon qubit	141
	Bibliography	147

List of Figures

1.1	SIS JJ wavefunctions schematics	4
1.2	Andreev reflections	5
1.3	Fraunhofer pattern schematics	6
1.4	$M(H)$ and $I_c(H)$ for SFS JJs	8
1.5	Pulsed-field sequence in CMRAMs	9
1.6	CLR in SIS, SNS and SFS JJs	11
1.7	$I_c(T)$ vs. L/ξ_s	12
1.8	$0-\pi$ transitions in SFS JJs	13
1.9	Spin-mixing schematics	15
1.10	$I(V)$ curve	18
1.11	Overdamped vs. Underdamped $I(V)$ curve	19
1.12	RCSJ model circuit	19
1.13	Washboard potential vs. bias-current	20
1.14	TJM model circuit	22
1.15	TA vs. MQT schematics	24
1.16	f -dependent RCSJ model circuit	25
1.17	MQT-TA-PD transition	26
1.18	Barrier height in a spin-filter device	29
2.1	Heliox system	32
2.2	Dilution phase-diagram	33
2.3	Wet and dry dilution refrigerators thermodynamics	34
2.4	DC setup scheme of Triton system	36
2.5	EMI filters	37
2.6	RC-filters	38
2.7	RC-filters Bode diagrams	39
2.8	Powder-filters	39
2.9	Triton DC-sample stage	40
2.10	DC-circuit schematics	41
2.11	Discussion on the performances of the Triton: the $I(V)$ curves in the nA regime	43
2.12	Discussion on the performances of the Triton: the $I_c(H)$ curve in the nA regime	44
2.13	RF setup scheme of Triton system	45
2.14	Characterization of the RF-lines	46
2.15	S -parameters of the isolators at 300 K	46
2.16	S_{21} and gain of the amplifier at 300 K and 7 mK	47
2.17	Measurement pack by NPL and SeeQC-EU	48
2.18	RC-filters Bode diagram for flux-bias	48

2.19	RC-filters for flux-bias	49
2.20	ECCOSORB filter Bode-diagram	50
2.21	Keysight modular rack	51
2.22	S-parameters	52
2.23	Qubit measurement setup scheme	53
2.24	Mixer calibration	53
2.25	Up- and down-conversion	54
2.26	Down-converted output signal	54
2.27	Qubit spectroscopy	55
2.28	Rabi measurement scheme and chevron plot	56
2.29	T_1 measurement scheme	57
2.30	Ramsey measurement scheme	58
2.31	Spin-echo sequence	59
3.1	Spin-filter devices	61
3.2	$R(T)$ in spin-filter JJs	62
3.3	$R(T)$ semiconducting fit in spin-filter JJs	63
3.4	Spin-filtering efficiency	64
3.5	Comparison of the $I(V)$ curves in spin-filter JJs	65
3.6	Tunnel-dependence of R_N and I_c vs. GdN thickness in spin-filter JJs	65
3.7	MITMoJCO simulations on spin-filter JJs	66
3.8	α vs. t in spin-filter JJs	68
3.9	$I_c(H)$ in spin-filter JJs	69
3.10	ΔH and H_y in spin-filter JJs	70
3.11	$4\pi M(H)$ in a spin-filter JJ with $t = 2.0$ nm	71
3.12	Comparison of the normalized $I_c(T)$ curves in spin-filter JJs	72
3.13	Phenomenological $I_c(T)$ fit in spin-filter JJs	73
3.14	Microscopic model of a spin-filter JJ	74
3.15	Atomistic fitting of the $I_c(T)$ curve in spin-filter JJs	75
3.16	p-wave correlation functions in spin-filter JJs	76
3.17	Density-plots $I_c(T)$ vs. H in spin-filter JJs	77
3.18	Role of the impurities in spin-filter JJs and an analogy with the magnetic field	78
4.1	TJM simulations	82
4.2	PD resistance in spin-filter JJ with 4.0 nm thick barrier	83
4.3	Fit of the PD resistance $R_0(T)$ for a spin-filter JJ with a GdN thickness of 4.0 nm	84
4.4	Capacitance in spin-filter JJs	85
4.5	TJM simulations	86
4.6	Subgap comparison in spin-filter	87
4.7	SCDs for spin-filter JJs	87
4.8	SCDs parameters for spin-filter JJs	88
4.9	PD-TA-MQT phase diagram	89
4.10	Py-based SIsFS JJ samples	91
4.11	Py-based SIsFS JJs $I_c(H)$	92
4.12	Py-SIsFS JJs characterization vs. T	93

4.13	Subgap comparison for Py and PdFe	94
5.1	Charge dispersion in a transmon design and circuital schematics	97
5.2	Ferro-transmon with a hybrid DC-SQUID	99
5.3	E_J 3D-plot in a hybrid ferro-transmon	100
5.4	E_J/E_C , ω_Q and α_r for a ferro-transmon with PdFe-based hybrid transmon	101
5.5	E_J/E_C , ω_Q and α_r for a ferro-transmon with Py-based hybrid transmon	104
5.6	Ferro-transmon schematics	104
5.7	Design of the resonator in the ferro-transmon proposal	105
5.8	RF-simulation of the $\omega_Q^{\text{high (low)}}$ in a ferro-transmon	106
5.9	RF-simulation of the resonator shift in a ferro-transmon	107
5.10	Ferro-transmon with an SIS coupled capacitively to a tunnel-SFS JJ	107
5.11	Linear approximation of a ferro-transmon with an SIS coupled capacitively to a tunnel-SFS JJ	109
5.12	Resonance frequency of a ferro-transmon with an SIS coupled capacitively to a tunnel-SFS JJ schematics	109
5.13	ω_2 vs. $C_b = C_f$	110
5.14	Tuning of ω_2 with H -pulses in a ferro-transmon with an SIS capacitively coupled to a tunnel-SFS JJ schematics	112
5.15	Comparison between $E_J(\phi)$ for the SIS and the SFS JJ in a ferro-transmon with one coupling capacitance	113
5.16	Anharmonicity in a ferro-transmon with an SIS JJ capacitively coupled to a ferro-tunnel JJ	114
5.17	E_J/E_C and $ \alpha_r $ in a ferro-transmon with an SIS JJ capacitively coupled to a ferro-tunnel JJ	115
5.18	E_J/E_C , ω_Q and α_r vs. C_r in a ferro-transmon with an SIS JJ capacitively coupled to a ferro-tunnel JJ	116
A.1	Powder-filters support CAD	120
A.2	DC-holder stage	121
A.3	Coil and screens support for the DC-stage	122
A.4	HEMT amplifier U-support	123
B.1	SPICE netlist in PSCAN2	125
B.2	$I(V)$ vs. α	127
B.3	$I(V)$ vs. β	129
B.4	$I(V)$ vs. R_N/R_{sg}	129
B.5	$I(V)$ fitting on standard SIS JJ	130
C.1	Transmon circuit	132
C.2	Charge dispersion in CPBs vs. transmon design	135
C.3	Charge dispersion vs. α_r	136
C.4	Dispersive shift	138
C.5	ω_Q vs. flux-field	139
C.6	Qubit frequency vs. flux-field	140

C.7 Dispersive shift vs. flux-field	141
---	-----

List of Tables

3.1	Measured parameters in spin-filter JJs	62
3.2	Simulated α and δ parameters in spin-filter JJs	67
3.3	Fitting parameters in the phenomenological model of the $I_c(T)$ in spin-filter JJs	72
4.1	TJM model measured electrodynamic parameters	81
4.2	TJM parameters	83
4.3	Py SIsFS JJs thickness and area	90
4.4	Electrodynamic parameters in ferro-tunnel JJs	95
5.1	Hybrid SQUID-based ferrotransmon parameters @ $\Phi_{\text{ext}} = 0$.	102
5.2	Hybrid SQUID-based ferrotransmon parameters @ $\Phi_{\text{ext}} = 0.5\phi_0$	103
C.1	T_1 and T_φ in transmons	143

Introduction

Since 1962, when Brian D. Josephson predicted for the first time that a non-dissipative current can flow between two superconducting electrodes separated by non-superconducting barriers of a few nanometers[1], the scientific community has made amazing progress in the field of superconducting electronics, and several key applications directly use the Josephson effect. The improvements in both material science and nanotechnologies allowed to build novel types of hybrid and unconventional junctions, characterized by the presence of competing processes.

A traditional research path first aims at a complete understanding of the processes occurring in hybrid and unconventional [Josephson Junctions \(JJs\)](#) to be integrated in a second stage into real applications and hopefully in frontier quantum circuits [2–10]. In my work, I have addressed some key aspects of the physics of the Josephson effect in junctions with ferromagnetic barriers, which fully fall in this category of unconventional junctions, as it will be clear in the following of my thesis.

[Superconductor/Ferromagnet/Superconductor \(SFS\) JJs](#) are an ideal platforms to study the competition between superconductivity and ferromagnetism[11], and they have attracted considerable attention in the emerging fields of superconducting spintronics[12–16]. In these devices, we can observe a wide range of exciting and exotic phenomena, which can be related to both well-known spin-singlet pairing, as $0-\pi$ transitions, and the more intriguing spin-triplet superconductivity[11, 12, 15–17]. Triplet currents are of extreme interest on their own, and they are also expected to be more robust against fluctuations of the magnetic exchange field[15, 16, 18], and thus of potential impact for applications in real circuits. These fundamental issues will be presented in Chap.1.

Standard [SFS JJs](#) are commonly overdamped because ferromagnets are metallic, and thus characterized by a small capacitance and high quasiparticle dissipation[11, 19, 20]. The metallic nature of [SFS JJs](#) has hampered the use of ferromagnetic [JJs](#) in circuits in which it is important to have a rather high $I_c R_N$ product and low damping[19]. In the last few years a novel and unique class of [SFS JJs](#) have earned the attention of the scientific community: the ferro-tunnel [JJs](#). These devices mix the typical tunnel behavior of underdamped non-magnetic [JJs](#) with all the interesting phenomena characteristic of more standard metallic [SFS JJs](#), and may add new functionalities increasing the overall impact of [JJs](#) in superconducting electronics.

In this work, I discuss the possibility to identify novel self-consistent and complementary protocols for the study of the fundamental physics in ferro-tunnel [JJs](#), with a special focus on the dissipation mechanisms and

the unconventional triplet pairing in **Superconductor/Insulating Ferromagnet/Superconductor (SI_fS) JJs**, or spin-filter JJs. We have proved the occurrence of spin-triplet superconductivity providing a new hallmark, i.e. a non-monotonous dependence of the critical current I_c on the temperature T [21]. This is a unique feature, which reveals that, increasing the thickness of the I_f barrier, the role of the spin-active interface competes with the impurities distribution in the barrier, revealing a tunable spin-triplet device as a function of an external weak magnetic field[21, 22]. An accurate microscopic modeling of the junction allows to calculate the relative weight of spin-triplet and singlet currents, and an exact correspondence between the thermal behavior of the supercurrent and the emergence of spin-triplet correlations inside the junction can be solidly established. This will be discussed in Chap.3.

In Chap.4 I elaborate a complete picture of the electrodynamics in tunnel **SFS JJs**, based on the estimation of parameters fundamental for the implementation of hybrid superconducting circuits. A special focus will be given to spin-filter JJs[23]. I will demonstrate that the low-dissipative behavior in these devices is consistent with the **Macroscopic Quantum Tunneling (MQT)** phenomena[24], which also paves the way for novel ferromagnetic quantum devices. The developed methods, based on numerical codes reported in App.B, can be also extended to other types of ferromagnetic junctions, such as **Superconductor/Insulator/small superconducting buffer/ Ferromagnet/Superconductor (SIsFS) JJs**, as discussed in Chap.4. The strenght of **SIsFS JJs** resides in the possibility to freely engineer the barrier choosing different ferromagnetic and insulating materials in order to meet specific circuit requirements.

The characterization of the electrodynamics of **JJs** is a solid basis for their possible use in more complex devices. The future perspective is to embed **SFS JJs** in a quantum circuit, in order to build a novel platform for the study of the unconventional physics in **SFS JJs** down to dilution temperatures and in a **MicroWave (MW)**-environment. The main idea is to exploit the sensitivity of a qubit to study the unconventional phase-dynamics in ferro-tunnel **JJs**, which may further enlight spin-triplet superconductivity and dissipation mechanisms due to the magnetization dynamics, as discussed in Chap.5. I will also discuss the possibility to integrate **SFS JJs** in a special qubit design, the transmon (App.C), reporting a circuital analysis and a feasibility test of two specific circuits[25]. I will show that ferro-tunnel **JJs** allows to get suitable scaling energies and operational frequencies for the implementation of a measurable and reliable hybrid ferromagnetic transmon, in which the frequency can be tuned by exploiting the typical *memory*-like behavior in ferromagnetic **JJs**[25].

Josephson effect in ferromagnetic Josephson junctions

The aim of this chapter is to give a comprehensive discussion of the phenomenology in standard tunnel insulating and metallic ferromagnetic JJs typically reported in literature, providing the notions used all over this thesis and a comparison with the unique tunnel ferromagnetic JJs reported here. A brief overview of the phenomenology in ferro-tunnel JJs is reported in Sec. 1.4.

At temperatures lower than the critical temperature of the superconducting electrodes of a JJ T_c , a condensate of Cooper pairs forms [26]. The wavefunctions $\Psi_{L(R)}(\mathbf{x}) = \rho_{L(R)} e^{i\varphi_{L(R)}}$ in the left (L) and right (R) electrodes in a JJ overlap across the barrier region (Fig. 1.1), giving rise to a finite current of Cooper pairs, the supercurrent I_s . Here $\rho_{L(R)}$ and $\varphi_{L(R)}$ are the Cooper pair densities and phases, respectively. The first and second Josephson equations

$$\begin{aligned} I_s &= I_c \sin \varphi, \\ \frac{\partial \varphi}{\partial t} &= \frac{2eV(t)}{\hbar} \end{aligned} \tag{1.1}$$

regulate I_s and the voltage $V(t)$ across the JJ, and state that the phase-difference across the barrier $\varphi = \varphi_L - \varphi_R$ is a macroscopic quantum observable [26]. Here, I_c is the maximum supercurrent that the JJ can sustain.

In **Superconductor/Insulator/Superconductor (SIS) JJs** the Josephson supercurrent arises because of the Cooper pairs tunneling across the barrier, while in **Superconductor/Normal metal/Superconductor (SNS)** and **SFS JJs** it is due to proximity effect and the Andreev reflection [11, 26, 27]: an electron with an energy below the superconducting gap is reflected at the interface as a hole, and the corresponding charge $2e$ is transferred to the Cooper pair on the superconducting side of the interface (Fig. 1.2)[11, 28–31]. A closed path between electron and hole is established and a bound state is induced. Within

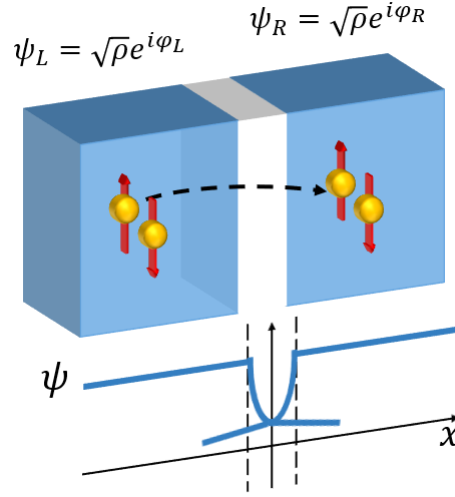


FIGURE 1.1: Scheme of a **Josephson Junction (JJ)**, and wavefunctions decay inside the barrier. ρ is the charge density in the superconductors and $\varphi_{L(R)}$ are the phases of the superconducting wavefunctions in the L (R) electrodes

this picture, $I_s(\varphi)$ can be written in terms of the occupied Andreev bound states energies ϵ_n [32]

$$I(\varphi) = -\frac{e}{\hbar} \sum_{\epsilon < 0} \frac{\partial \epsilon(\varphi)}{\partial \varphi} \tanh\left(\frac{\epsilon_n}{2k_B T}\right). \quad (1.2)$$

The Andreev levels within the energy gap region directly depend on the energy gap Δ and the transparency of the barrier τ [32]. This powerful formalism allows to describe a wide range of transport behaviors and will be also used for the phenomenological modeling of the low-temperature transport properties in spin-filter **JJs** in Chap. 3. An important role is here played by τ : for $\tau \sim 0$, the barrier is insulating, while for $\tau \sim 1$, it is metallic [32].

In the following, I will recover the most important features of the Josephson effect in **SFS JJs**: in Sec. 1.1, I discuss the modulation of the critical current I_c as a function of an external magnetic field H , while in Sec. 1.2 I report the dependence on the barrier thickness t and the temperature T of I_c , giving a panoramic on what occurs in **SIS JJs**, **SNS JJs** and **SFS JJs**. A special focus will be given to the unconventional spin-triplet conduction mechanisms in ferromagnetic devices. The models and methods used to analyze and quantify the level of dissipation in standard and unconventional **JJs** are reported in Sec. 1.3.1 and Sec. 1.3.2. Finally, once given an overlook on the theoretical tools necessary for the study of the unconventional physics in hybrid **JJs**, in Sec. 1.4 I will recover the most interesting properties of ferro-tunnel **JJs**.

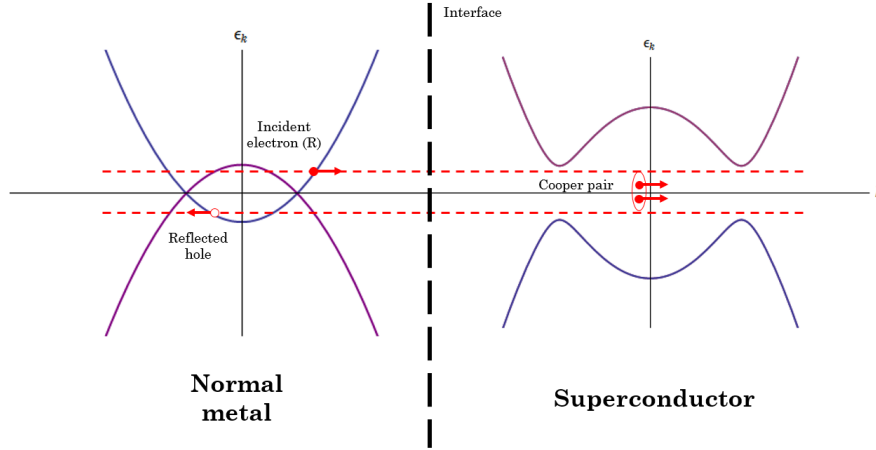


FIGURE 1.2: Andreev reflections at the interface between a superconductor and a normal metal

1.1 Critical current modulation in magnetic fields

The interference of the Cooper pairs wavefunctions in a JJ is depicted in the modulation of the critical current I_c when an external magnetic field H orthogonal to the transport direction is applied [26]. For squared JJs, this modulation takes the form of the Fraunhofer pattern (Fig. 1.3 (b))

$$I_c(H) = I_c(0) \left| \frac{\sin\left(\frac{\Phi(H)\pi}{\phi_0}\right)}{\frac{\Phi(H)\pi}{\phi_0}} \right|, \quad (1.3)$$

where $\phi_0 = h/2e$ is the magnetic flux quantum and $\Phi(H)$ is the magnetic flux

$$\Phi(\mathbf{H}) = LHd. \quad (1.4)$$

For circular JJs, instead, the modulation takes the form of an Airy pattern

$$I_c(H) = \pi R^2 I_c(0) \left| \frac{2\mathcal{J}_1\left(\frac{2\pi d}{\phi_0} RH\right)}{\frac{2\pi d}{\phi_0} RH} \right|, \quad (1.5)$$

where \mathcal{J}_1 is the Bessel function of the first kind and R is the radius of the JJ[26].

For H oriented along \hat{x} or \hat{y} (Fig. 1.3 (a)) (if \hat{z} is the transport direction) and uniform J_c , the critical current is zero when the magnetic field flux is an integer multiple of the magnetic flux quantum, $\Phi = \phi_0 n$. The periodicity of the $I_c(H)$ is defined as half the amplitude of the first lobe of the Fraunhofer pattern, and depends on the geometry of the device, i. e. it is

$$\begin{cases} \Delta H = \frac{\phi_0}{Ld} \text{ for squared JJ} \\ \Delta H = \frac{\phi_0}{Rd} \text{ for circular JJ} \end{cases} \quad (1.6)$$

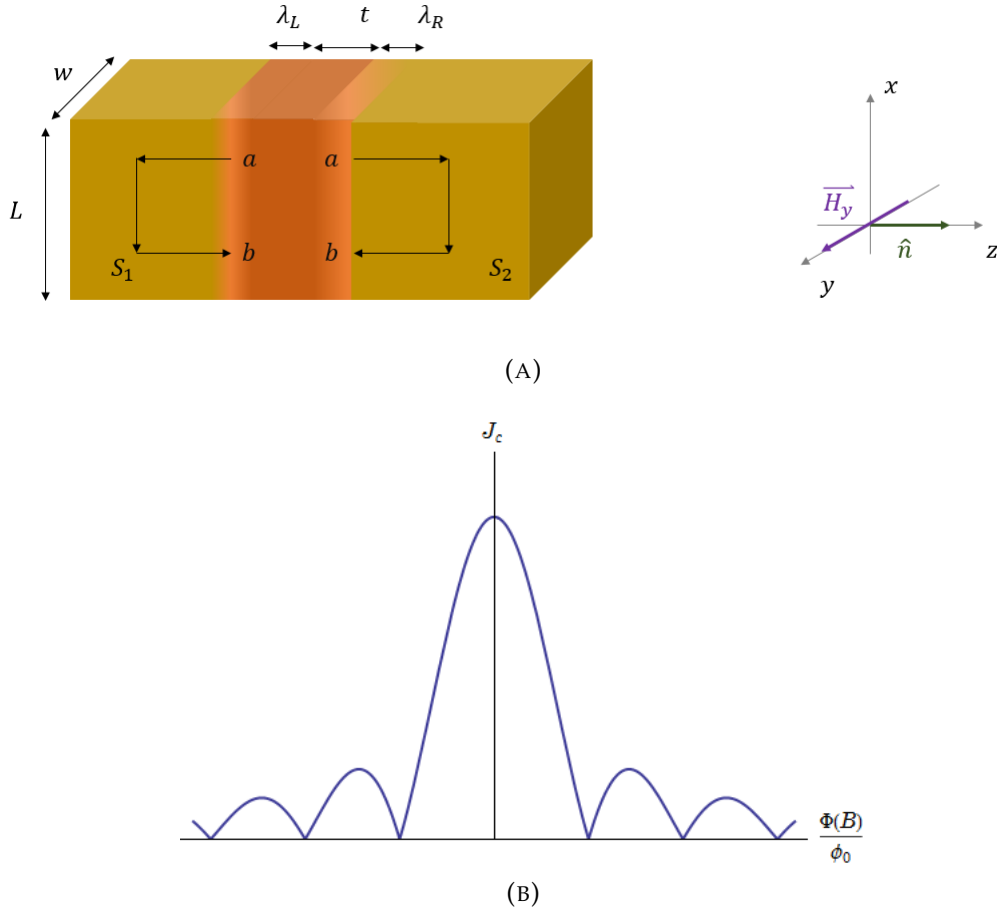


FIGURE 1.3: In (a): schematics of a JJ in a magnetic field applied orthogonally to the transport direction \hat{n} . Shaded areas refer to the London penetration depth in the L (R) electrodes, while S_1 and S_2 are the integration path used for the calculation of the variation of the phase-difference φ in a magnetic field [26]. In (b): simulated Fraunhofer pattern, in which the minima are multiple integer of ϕ_0

The quantity d in the above formula reported is the effective magnetic length, which takes into account that the magnetic field penetrates inside the superconducting electrodes for the Meissner effect in a length equal to the London penetration depth λ [33, 34],

$$d' = (\lambda_L + \lambda_R + t), \quad (1.7)$$

where t is the thickness of the barrier and $\lambda_{L(R)}$ is the London length in the left (right) superconductor. This relation is valid until the electrodes can be considered bulk, i. e. when $d_{L(R)} > \lambda_{L(R)}$, where $d_{L(R)}$ are the left (right) electrode thicknesses. For thin electrodes, a specific inductance is induced by the Meissner currents in the electrodes,

$$L_0^{-1} = \int_0^L dy (\mu_0 d')^{-1}, \quad (1.8)$$

and the effective magnetic spacing becomes [33, 34]

$$d'' = t + \lambda_L \tanh\left(\frac{d_L}{2\lambda_L}\right) + \lambda_R \tanh\left(\frac{d_R}{2\lambda_R}\right). \quad (1.9)$$

Deviations from the $I_c(H)$ expected behavior, like minima with non-zero current, suppression of the amplitude of some lobes, asymmetry of the pattern and distortions in standard JJs can be related to non-uniform current distributions, arbitrary orientation of the in-plane magnetic fields applied or structural fluctuations [26]. However, asymmetries in the first lobe of the pattern can also be due to the comparable values of the transverse dimensions of the JJ and the Josephson penetration depth λ_J ,

$$\lambda_J = \sqrt{\frac{\phi_0}{2\pi\mu_0 J_c d'}} \quad (1.10)$$

which is defined as the penetration length for the phase-difference φ . We will define small or long junction a JJ with transverse dimensions smaller or larger than λ_J . In the latter case, the self-field due to the current flowing in the electrodes can not be neglected and a distortion of the Fraunhofer pattern is experimentally measured [26].

In SFS JJs, aside from the effects observable also in non-magnetic JJs, other interesting phenomena take place. The most important is that the magnetization of the F-layer below the Curie temperature T_{Curie} (Fig. 1.4 (a)) introduces an additional flux into the junction. Considering that in a ferromagnet the magnetic induction field B in the CGS system is

$$B = H + 4\pi M(H), \quad (1.11)$$

where $M(H)$ is the hysteretic magnetization of the ferromagnet, Eq. 1.3 reads as

$$I_c(H) = I_c(0) \left| \frac{\sin\left(\pi \frac{\Phi(H) \pm \Phi_M(H)}{\phi_0}\right)}{\pi \frac{\Phi(H) \pm \Phi_M(H)}{\phi_0}} \right|. \quad (1.12)$$

Let us first consider applied magnetic fields $H > H_c$, with H_c the coercive field of the F layer (Fig. 1.4 (a)). In this case, a horizontal translation of the Fraunhofer pattern can be measured accordingly to the sign of the derivative of the magnetic field applied in time dH/dt (Fig. 1.4 (b)): ramping the field from negative to positive values ($dH/dt > 0$, red curve in Fig. 1.4 (a) and (b), from now on defined as up-curve), the rigid shift of the Fraunhofer pattern occurs for positive H , while ramping the field from positive to negative values ($dH/dt < 0$, blue curve in Fig. 1.4 (a) and (b), from now on defined as down-curve) the Fraunhofer pattern is shifted towards negative H values [35].

The hysteresis observed in the Fraunhofer pattern of SFS JJs can be exploited for the implementation of **Cryogenic Magnetic Random Access Memory (CMRAM)** in superconducting circuits [36]. The logic states '0' or '1' in Josephson **CMRAM** are the low and high $I^{\text{low (high)}}$ values, respectively,

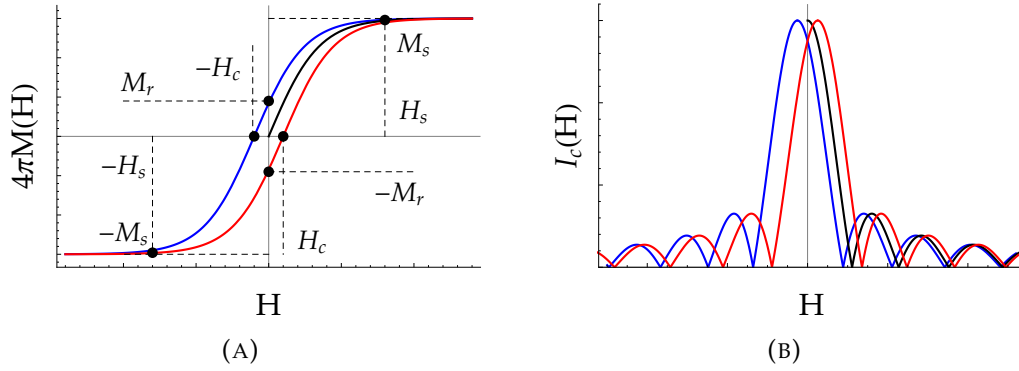


FIGURE 1.4: In (a): hysteretic magnetization curve for a ferromagnet $M(H)$; in (b): Fraunhofer pattern for SFS JJs depending on dH/dt . The black curves are related to the virgin curves, i. e. obtained ramping the field from 0 to positive values, when the sample is cooled down in absence of external magnetic fields. The blue curves are related to the ramping of the field from positive to negative values. The contrary occurs for the red curve. In (a), the magnetic parameters for the barrier are highlighted: the residual magnetization M_r , the saturation magnetization and magnetic field H_s and M_s , and the coercive field H_c

achieved applying external field pulses (WRITE and RESET operations)[37–42].

The WRITE operation consists in the preparation of the memory state in a high or low current level: as reported in Fig. 1.5, we first set a working point within a fixed magnetic field, corresponding to an initial state for the memory (let us say, for example, '1'). Then, on the rise of the magnetic field pulse with amplitude given by the saturation field $\pm H_s$ of the ferromagnetic barrier, the JJ runs on the up- $I_c(H)$ curve (if the amplitude of the pulse is positive). Finally, on the fall of the pulse, the JJ runs on the down-curve, reaching another current-level at the working point (in this case '0'). Another magnetic field pulse with amplitude given by $-H_s$ resets the memory and leads to the initial state. The READ operation, instead, uses a bias current for the JJ in between the '0' and '1' level state: if a finite voltage is detected, the memory is in the '1' level state; *viceversa*, for zero-voltage measured, the memory state is '0'.

The shift of the pattern maximum arises at fields corresponding to the saturation magnetization M_s when the coercive field H_c is of the order of the saturation magnetic field H_s (squared hysteresis loop typical for hard ferromagnets)[43]. Instead, for small coercive fields $H_c < H_s$, the maximum of the pattern corresponds to the residual magnetization M_r of the ferromagnet. This is due to the fact that the maximum of the Fraunhofer pattern always occurs when the induction magnetic field B equals zero, i. e. $H_0 = -4\pi M$, and the residual flux is

$$\Phi_M = -4\pi d_f w M_r. \quad (1.13)$$

Distortion of the Fraunhofer pattern and suppression of I_c in SFS JJs can

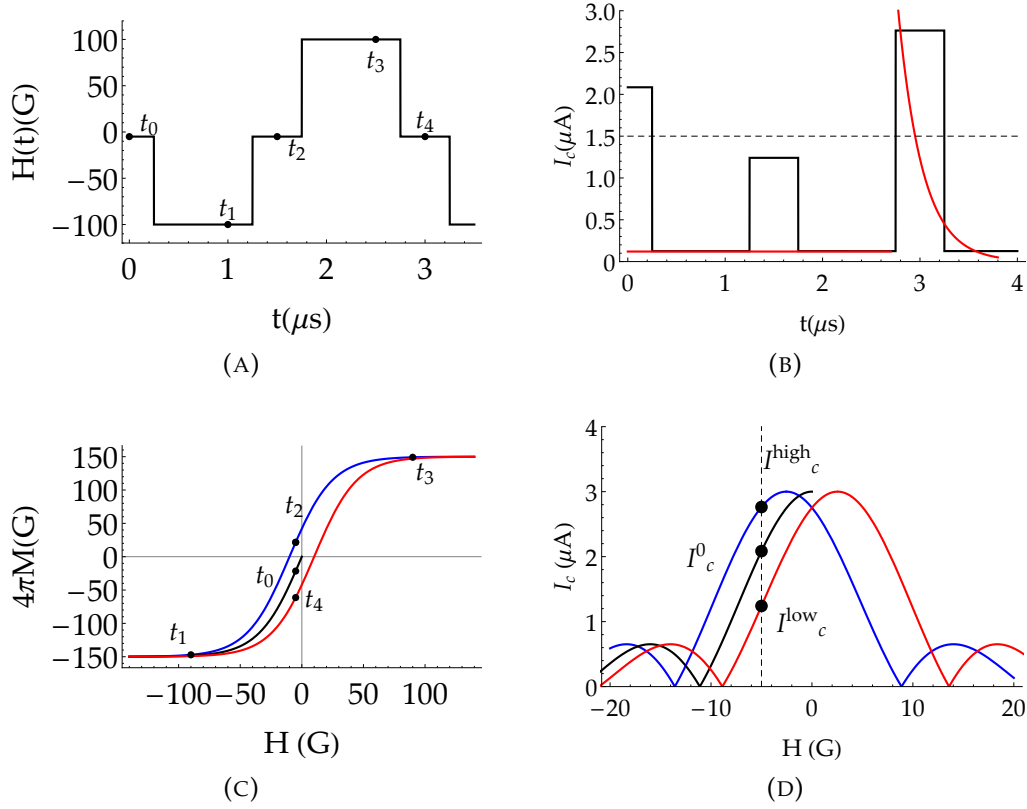


FIGURE 1.5: In (a): magnetic field pulse sequences $H(t)$ necessary to pass from low (state '0') to high (state '1') of the critical current I_c . In (b): simulated response of the I_c in SFS JJ (black line) to the pulse sequence $H(t)$ in (a). In red, voltage pulse measured at $I = I_{\text{READ}}$, represented by the dashed line. In (c), we highlight the position on the magnetization curve at different time positions. In (d), we highlight the low- and high- critical current level states $I_c^{\text{low(high)}}$

be also related to the magnetic domain configuration in the barrier. The hysteresis and the residual magnetization in a ferromagnet may arise because of the switching of the magnetic momenta (if the ferromagnet is characterized by a single magnetic-domain), or pinning of the domain walls to impurities and localized non-ferromagnetic particles (when the ferromagnet is in a multi-domain configuration)[35]. The latter is the most common situation when dealing with large ferromagnetic areas, in which the complex magnetic-domain configuration is a consequence of anisotropies and inhomogeneities [35].

The study of the Fraunhofer modulation of I_c in SFS JJs is a tool to get fundamental information on the magnetic nature of the barrier. The measurement of the Fraunhofer pattern in SFS JJs, for example, allows for an estimation of the magnetization curve $M(H)$ of the F-layer (Josephson magnetometry). The position of the maxima and the minima of the $I_c(H)$ is determined by the

relations [36, 38]

$$\Phi_{\min} = \phi_0 n \quad (1.14)$$

$$\Phi_{\max} \sim \phi_0 (n + 1/2), \quad (1.15)$$

and it allows to calculate the $M(H)$ curve, related to the total flux through the JJ Φ and the external field flux $\Phi(H) = Hwd_f$ as [38]

$$4\pi M(H) = \frac{\Phi}{\phi_0} \frac{\phi_0}{wd_f} - H \frac{d}{d_f}. \quad (1.16)$$

Here d_f is the thickness of the ferromagnetic layer, while d is the effective magnetic spacing that must be opportunely chosen among the Eqs. 1.7 and 1.9[36, 38], explicitly taking into account the permeability μ_r of the ferromagnet, i. e. using [34]

$$d'' = \mu_r t + 2\lambda \tanh\left(\frac{d}{2\lambda}\right), \quad (1.17)$$

or

$$d' = \mu_r t + 2\lambda. \quad (1.18)$$

1.2 Critical current dependence on the thickness and the temperature

Up to now arguments to demonstrate the arising of unconventional Josephson phenomena in SFS JJs have been mostly based on the dependence of the I_c on the length of the barrier t , or **Current Length relation (CLR)**, and the temperature T . Deviations from the exponential dependence expected from tunneling or proximity models may point towards unconventional conduction processes [11, 13–15, 44–47].

In SIS JJs, the exponential dependence of the tunnel probability of Cooper pairs with energy E , $T(E)$, on the energy U of barrier height and shape [26]

$$T(E) = e^{-2 \int_{x_1}^{x_2} dx \sqrt{\frac{2m}{\hbar^2} [U(x) - E]}}, \quad (1.19)$$

which reduces to

$$T(E) = e^{-2 \frac{t}{\hbar} \sqrt{2mE_0}} \quad (1.20)$$

for perfectly squared barriers with thickness t , determines the exponential dependence of the **Current Length relation (CLR)** (Fig. 1.6 (a)). In S/N heterostructures, instead, the Cooper pairs penetrate across the interface with the barrier at some distance inside the metal because of the proximity effect [11, 48].

The Ginzburg-Landau equation for the superconducting order parameter Ψ in space in non-magnetic SNS JJs is [48]

$$a(T) - |\gamma| \frac{\partial^2 \Psi}{\partial x^2} = 0, \quad (1.21)$$

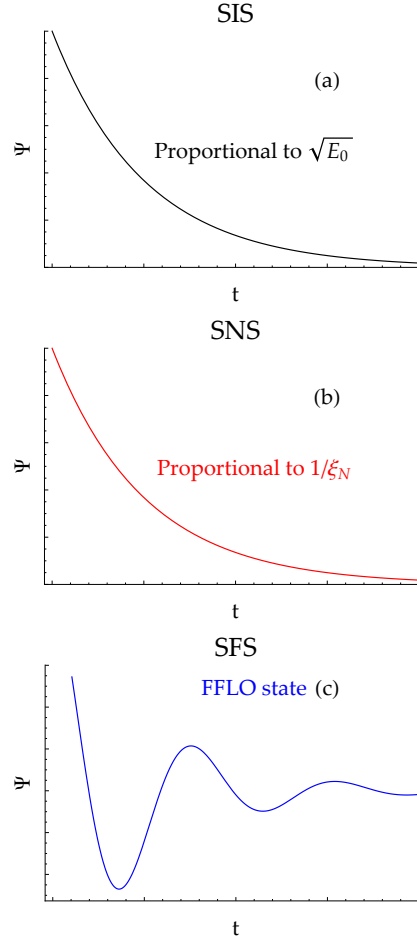


FIGURE 1.6: In (a): decay of the order parameter Ψ in the barrier of thickness t in SIS JJs due to the tunnel effect; in (b): decay of Φ in SNS JJs, due to the proximity effect; in (c): decay of Φ in SFS JJs and oscillations due to the Fulde-Ferrel-Larkin-Ovchinnikov (FFLO) state

where the solution is [11, 48]

$$\Psi = \Psi_0 e^{-\frac{t}{\xi_N(T)}}. \quad (1.22)$$

As a consequence, the CLR exponentially decays over the coherence length ξ_N [11, 48] (Fig. 1.6 (b))

$$\xi_N = \sqrt{\gamma/a(T)}. \quad (1.23)$$

The coherence length is also a function of the temperature T : as a matter of fact, the parameter a in Eq. 1.23 is proportional to the difference between T and the critical temperature of the superconducting state T_c [11]. It is straightforward that $I_c(T)$ in SNS JJs exponentially decays for $T \sim T_c$, depending on the ratio between the thickness of the barrier and the coherence length $l = t/\xi_N$.

In Fig. 1.7, we show the $I_c(T)$ curves theoretically predicted by Likharev in

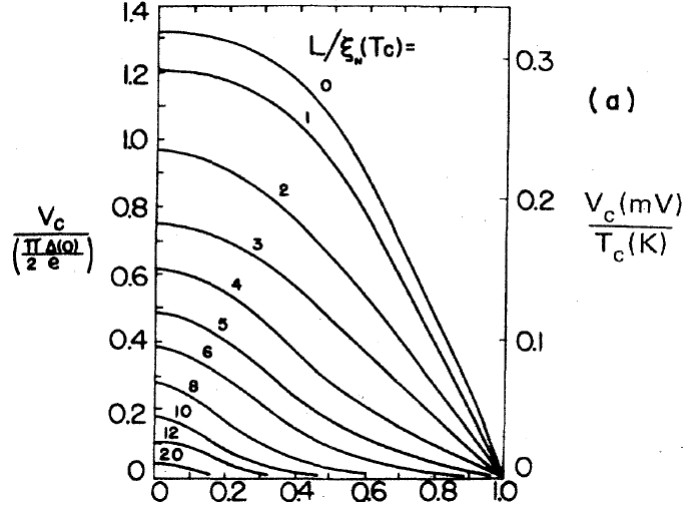


FIGURE 1.7: Temperature dependence of the normalized characteristic voltage $V_c / (\pi/2\Delta(0)/e)$ as a function of T/T_c in SNS structures, as a function of the ratio between the length of the barrier (defined as L in Ref.[48]) and the superconducting coherence length ξ_N at T_c [48]

Ref.[48] as a function of the ratio $l = L/\xi_N$, where L is the length of the barrier in Ref.[48]. The more l increases, the more the $I_c(T)$ exhibits an exponential tail near T_c [27, 48]. At low temperatures, instead, the $I_c(T)$ has in general a higher saturation value compared with the standard Ambegaokar-Baratoff (AB) trend for the $I_c(T)$ in SIS JJs, as theoretically proposed by Kulik and Omel'yanchuk (KO1 and KO2 theory)[48].

In the AB theory, the phase-transition of the superconducting order parameter in JJs is related to the Bardeen-Cooper-Schrieffer (BCS) energy gap $\Delta(T)$ of the superconducting electrodes [49],

$$I_c(T) = \frac{\pi}{2eR_N} \Delta(T) \tanh\left(\frac{\Delta(T)}{2k_B T}\right), \quad (1.24)$$

which saturates at $\frac{\pi}{2eR_N} \Delta(0)$. In the KO1 theory, instead, the saturation at low temperatures occurs at a value 32% larger than in SIS JJs, and 50% larger in the clean limit predicted by the KO2 theory [27, 48]. The $I_c(T)$ behaviour in SNS JJs is finally stressed towards a full exponential trend in the long-junction limit, i. e. for $L \gg \xi_N$.

In S/F heterostructures, the Fulde-Ferrel-Larkin-Ovchinnikov (FFLO) theory [50, 51] predicts that a Zeeman splitting of the electronic levels due to the exchange field h in the ferromagnet generates two different Fermi surfaces for spin up and down electrons. Cooper pairs will acquire a finite center-of-mass momentum $q = 2\mu_B h v_f$, where μ_B is the Bohr magneton and v_f is the Fermi velocity [11]. Thus, in metallic SFS JJs the CLR does not simply decay in the barrier, but modulates sinusoidally on a characteristic coherence length scale

$\zeta_{F1(2)}$ [11] with the wave-vector q [50, 51],

$$I_c \propto e^{-\frac{x}{\zeta_{F1}}} \cos\left(\frac{x}{\zeta_{F2}}\right). \quad (1.25)$$

The Ginzburg-Landau theory is a powerful analytic tool for the understanding of the effect of the FFLO state in S/F heterostructures, but it admits the existence of ferromagnets with unphysical weak ferromagnetism, i. e. $h \ll k_B T_c$. This assumption is unrealistic, and other more complex methods based on a microscopic approach must be used to obtain the same results. In the diffusive (dirty) limit, i. e. when $t > \zeta$, we must use the Usadel equations for the Green's functions averaged over the Fermi surfaces [52]. The coherence lengths $\zeta_{F1(2)}$ are the real and the imaginary part of the complex ferromagnetic coherence length ζ_F ,

$$\zeta_F = \sqrt{\hbar \frac{D_F}{2(\pi k_B T + ih)'}} \quad (1.26)$$

where D_F is the diffusion constant of the ferromagnet [53–55]. Instead, in the ballistic (clean) limit ($t < \zeta$) we must solve the Eilenberger equations for the Green's functions [56]. The S/F transport is governed by two coherence lengths: ζ_{F1} and ζ_{F2} . The former is equivalent to the normal metal coherence length

$$\zeta_{F1} = \frac{v_{fF}}{2\pi k_B T'} \quad (1.27)$$

where the fundamental energy scale is the Boltzmann thermal energy. ζ_{F2} , instead, depends on the exchange field in the ferromagnet h ,

$$\zeta_{F2} = \frac{v_{fF}}{2\pi h'} \quad (1.28)$$

with v_{fF} the Fermi velocity in the ferromagnet.

The damped oscillatory behavior of the superconducting order parameter inside the F-layer results in:

- a non-monotonic dependence of T_c as a function of t [57–71];
- a non-monotonic behavior of the I_c as a function of t and T [53, 54, 72–83]. The latter is due to the dependence of the critical ferromagnet thickness t_c on T [53, 54].

While the $I_c(t)$ and $I_c(T)$ oscillations have been reported in several manuscripts [53, 54, 72–83], it is not rare to find in literature reports of monotonic T_c dependence, differently from theoretical expectations [11, 17, 67, 84, 85].

The oscillations of the $I_c(t)$ and $I_c(T)$ means that a change in the sign of I_c can be obtained for certain values of the barrier thickness, i. e. an additional phase of π in Eq. 1.1 can be detected in the ground state of these devices, also known as π -JJs[11, 53, 54, 86–89], both in the ballistic [90] and diffusive regime [57]. The inversion point signals what is known as 0 - π transition (Fig. 1.8).

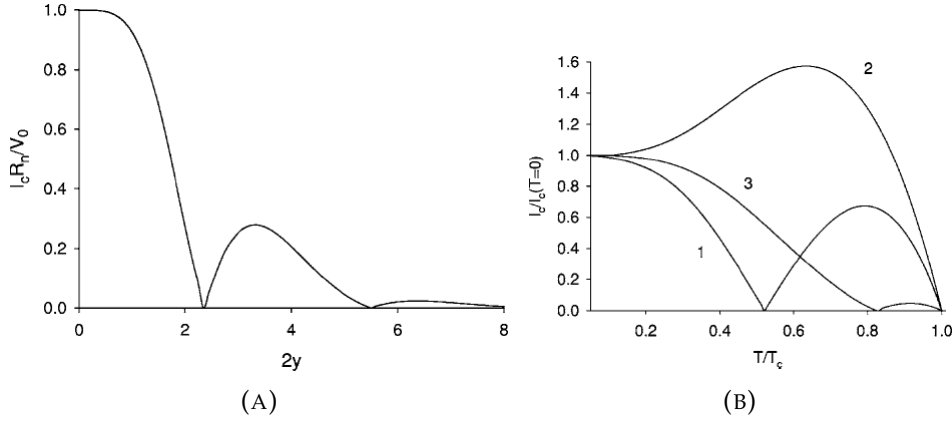


FIGURE 1.8: CLR $I_c(t)$ and $I_c(T)$ curves in SFS JJs, as reported in Ref.[11]. Here y is the normalized ferromagnet thickness t/ξ_F , R_N is the normal resistance and $V_0 = \pi\Delta^2/(2eT_c)$, while the numbers labelling curves in the $I_c(T)$ curves refer to different values of t/ξ_F and normalized field $h/(k_B T_c)$ [11]. The oscillations are related to the $0-\pi$ transitions

It was also predicted theoretically that in S/F heterostructures phases other than 0 or π can be achieved [58]. However, the appearance of what is known as φ_0 -state is difficult to get in single-layered SFS JJs, since it is confined to some percent near the critical ferromagnet layer t_c [11]. Another mechanism for the realization of the φ_0 phase due to the fluctuations of the thickness of the F layer requires to make the 0 and π phases of the JJ coexist in two different regions in the barrier [91, 92]. Experimentally, the first implementation of a φ_0 JJ was reported in Ref.[93]. Other ways to induce a $0-\varphi_0$ transition employs multilayer ferromagnetic barriers and other geometries with both Zeeman splitting and Spin Orbit Coupling (SOC)[94–100].

In the vicinity of the $0-\pi$ transition (when the first-order term in the Current Phase Relation (CPR) vanishes), higher-order harmonics in the CPR in Eq. 1.1 can not be neglected [101, 102]. Especially at low-temperatures, the presence of higher harmonics at the $0-\pi$ transition prevents a complete suppression of the critical current [90, 102, 103]. This influences also the phase-dynamics, the Shapiro steps amplitude and the Fraunhofer pattern periodicity [35, 55, 75, 81, 104, 105], since the washboard potential will change accordingly with the CPR[53, 55, 104]. Theoretical and experimental proposals that exploit the presence of 0 , φ_0 and π states in SFS JJs include: phase-batteries, phase-shifters and quiet-qubits [16, 19, 53, 106–110].

Finally, while the CLR in metallic JJs decays exponentially with ξ_N , the $I_c(t)$ curve in SFS JJs may be characterized by a much slower decay on the barrier thickness. Such experimental evidence is often related to Long-Ranged spin-Triplet Correlation (LRTC)[11, 13–15, 44–47].

Spin-triplet superconductivity allows to create pseudo-chargeless spin-1/2 excitations with extremely long spin lifetimes, which is a historical request for the spintronics, i. e. the field of engineering circuits in which logic operations controlled by spin currents can be performed faster and with higher

energy-efficiency than the charge-based equivalent in semiconductor transistor technologies [16, 111, 112]. Among these applications we can find: spin-diodes and transistors, spin-field-effect and magnetic bipolar transistors, spin-qubits in semiconductor nanostructures and spin-filter devices [111] for efficient cooling detectors, sensors and quantum devices [113].

It could seem counterintuitive that spin-correlations can arise in a superconducting system. In most superconductors, the Cooper pair wave-function is in a singlet state, and if the exchange field in the ferromagnet is sufficiently strong, it will tend to align the spins of the pairs, thus breaking the superconductivity [11, 12, 17, 114]. However, under some circumstances, superconductivity is not suppressed, because LRTC are robust against the exchange-field [115, 116] and can survive over a distance much larger than the coherence length in the ferromagnetic layer. Nevertheless, spin-triplet superconductivity can arise also on a short-range, comparable with ξ_s . Such **Short-Ranged spin-Triplet Correlation (SRTC)** typically oscillates with t [15].

Spin-triplet superconductivity is theoretically justified considering that the two-fermion correlation function f that describes Cooper pairs must satisfy the Pauli principle [16]. The f spin-part does not necessarily have to be in a spin-singlet (antisymmetric) state $1/2(|\uparrow\downarrow\rangle - |\downarrow\uparrow\rangle)$, but it can reside in a spin-triplet state

$$\begin{cases} 1/2(|\uparrow\downarrow\rangle + |\downarrow\uparrow\rangle) \\ |\uparrow\uparrow\rangle \\ |\downarrow\downarrow\rangle, \end{cases} \quad (1.29)$$

provided that f remains antisymmetric [11, 12, 15, 16, 44, 117, 118]. Spin-triplet superconductivity in SFS JJs is often related to odd in time (or odd-frequency) pairing, earning the name of *odd triplet superconductivity*.

The main ingredients necessary for the formation of spin-triplet currents are [15, 16, 44]:

- the spin-mixing;
- the spin-rotation.

The effect of the spin-mixing, due to the spin-active interface between superconductors and the ferromagnet, is to combine conventional Cooper pairs to get in return a spin-triplet wave function with total spin-momentum $S = 1$ and zeta component $s_z = 0$, i. e. the opposite-spin triplet currents (first case in Eq. 1.29).

Let us define for convenience the spin-quantization axes along the exchange field direction. In Fig. 1.9, we report a schematics of the spin-mixing mechanisms. The Bloch waves for spin up and down will be reflected at the interface with different reflection amplitude [15]

$$r_\alpha = \frac{k - i\kappa_\alpha}{k + i\kappa_\alpha}, \quad (1.30)$$

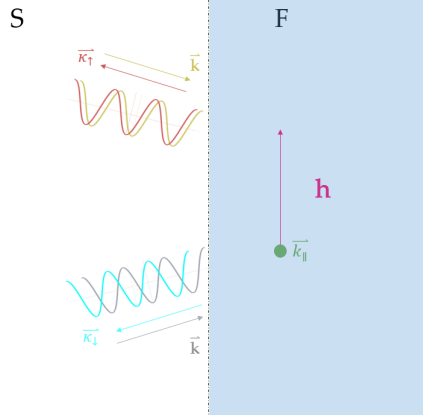


FIGURE 1.9: Schematics of the spin-mixing mechanism, as discussed in the text. Adapted by Ref.[15]

where k is the momentum and κ_α is

$$\kappa_\alpha = \sqrt{2m(V - E - \alpha h) + k_\parallel^2}. \quad (1.31)$$

In Ref.[15], the discussion was specifically addressed to a system in which the barrier was an insulating ferromagnet, because the amplitude of the reflection components in metallic SFS JJs are expected to be small, given that the transparency of the barrier is $\tau \sim 1$. Nevertheless, reflections are never completely suppressed and the spin-mixing can also arise in metallic SFS JJs.

The difference in the reflection amplitudes for spins up and down is the main cause for which the reflected waves acquire a mutual spin-dependent phase-delay [15]

$$\varphi_\alpha = \pi - 2 \arctan \left(\frac{\kappa_\alpha}{k} \right), \quad (1.32)$$

where α is the spin index. Thus, we can define the spin-mixing angle as the spin-dependent interface scattering phase-shift

$$\theta = \varphi_\uparrow - \varphi_\downarrow, \quad (1.33)$$

or equivalently the precession angle that the spins undergo when rotating around the quantization axis [15]. In Fig. 1.9, dark yellow and gray Bloch waves refers to the spin-up and down components of the incident Cooper pair. In red and cyan, the reflected wave-functions are phase-shifted compared with the incident ones.

The spin-rotation, finally, makes the spin of the carriers rotate such as to have a wave-function with $S = 1$ and zeta components $s_z = \pm 1$ (equal-spin triplet current)[11, 15, 44]. There are two ways to induce such a conversion [16]:

- the magnetization of the system must be textured and inhomogeneous;
- in the superconductor, lack of an inversion symmetry (either due to the geometry of the set-up or its crystal structure) must occur, which

generally feature antisymmetric SOC coupling, like the Rashba Spin Orbit Coupling (SOC).

In the former, the spin-rotation mechanism is the following: once the Cooper pair in a singlet or opposite-spins triplet configuration interferes with different magnetizations vectors oriented in a non-collinear fashion, an infinite set of spin-projections along the magnetization axis will be generated [12, 15]. Both the modeling and the experimental demonstration of such Long-Ranged spin-Triplet Correlation (LRTC) is based on the fabrication of complex magnetic multilayers: tuning the relative magnetization orientation between one or more ferromagnetic layers, it is possible to increase the probability to observe LRTC [13, 14, 45–47, 114, 119–124]. It was also theoretically proposed that the inhomogeneity in the magnetization could be intrinsic in the material, as it occurs in multi-domain ferromagnets, since we expect that the pair-breaking parameter is suppressed near the domain walls [11].

The latter mechanism that can generate spin-triplet superconductivity is based on the assumption that a spin-orbit interaction takes place at the interface between the superconductor and the ferromagnet, since a SOC can mix the triplet and the singlet components [125, 126]. The electron-electron interaction in such systems, in fact, is non-zero not only in the s-wave singlet channel, but also in the p-wave triplet channel [16, 125–127]. A SOC can result synthetically from magnetic textures [128–131], in which a relevant role is played by the magnetic anisotropy of the ferromagnet that alters the degree of orthogonality between the exchange field and the SOC [16, 130, 132–134].

While there is evidence of the existence of spin-triplet superconductivity in S/F heterostructures, an unambiguous evidence does not exist so far [12]: it can not be excluded that a long-range proximity may be due to other physical mechanisms [11, 12, 135, 136]. For instance, it was theoretically suggested that a slower decay of I_c in clean SFS heterostructures can be due to a phase-compensation mechanism resulting from the magnetic domain configuration [137, 138]. As a matter of fact, the spin-singlet suppression in SFS devices due to the magnetic exchange field can be seen as a sort of destructive interference for the Cooper pairs wavefunctions [137]. Under certain circumstances, the magnetic domain can induce a finite rotation of the relative phase between electron and hole-like Cooper pair wavefunctions, contributing to the transport with an additional phase that restores a conventional s-wave superconductivity [137]. More importantly, it is hard to quantify the amount of spin-polarized current [16, 17].

In this work, I will discuss the thermal behavior of the I_c in Superconductor/Insulating Ferromagnet/Superconductor (SI_fS) JJs, which is a benchmark for spin-triplet superconductivity. A microscopic fitting of the $I_c(T)$ curves allows for a direct calculation of the spin-triplet and spin-singlet correlation functions (Chap. 3).

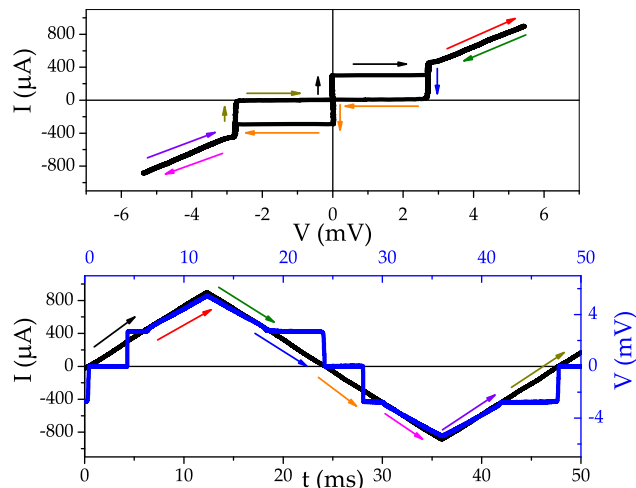


FIGURE 1.10: Measured $I(V)$ curve for a SIS Nb-AlO_x-Nb JJ at 2 K, and corresponding current-bias ramp in time $I(t)$ (black line) and measured voltage $V(t)$ (blue curve). The arrows refer to the regions highlighted in the $I(V)$ curve, and discussed in the text

1.3 The electrodynamics in SIS and SFS heterostructures

Possible applications for SFS JJs require a deep understanding of their electro-dynamics, in order to quantify the level of dissipation for their implementation also in phase-coherent devices (Chap. 4 and 5).

The first step in the study of the dissipation in JJs is the analysis of the $I(V)$ curve, and in Sec. 1.3.1 a special care will be given to the description of the models currently used to describe the $I(V)$ curves. Among these models, the Tunnel Junction Microscopic (TJM) model is the most powerful tool to get an estimation of fundamental electro-dynamics parameters, not only in standard SIS JJs, but also in the more unconventional ferromagnetic tunnel JJs. An overlook of fast calculations of the $I(V)$ curve in tunnel JJs employing the TJM model will be given in App. B.

The $I(V)$ curve behavior is strictly linked to the phase-dynamics, which is in general frequency-dependent. We will distinguish between the high- and low-frequency electro-dynamics, discussing what are the main dissipation sources in the two regimes, and how their study allows for a complete characterization of JJs.

1.3.1 The $I(V)$ curves: models and study of the quasiparticles dissipation

In my work, the $I(V)$ curve is generally measured current-biasing the JJ. As it is shown in Fig. 1.10, the bias-current is a triangular waveform with a certain frequency. The supercurrent in a JJ is a non-dissipative current, i. e. there is no finite voltage across the junction in the superconducting state. On the rise

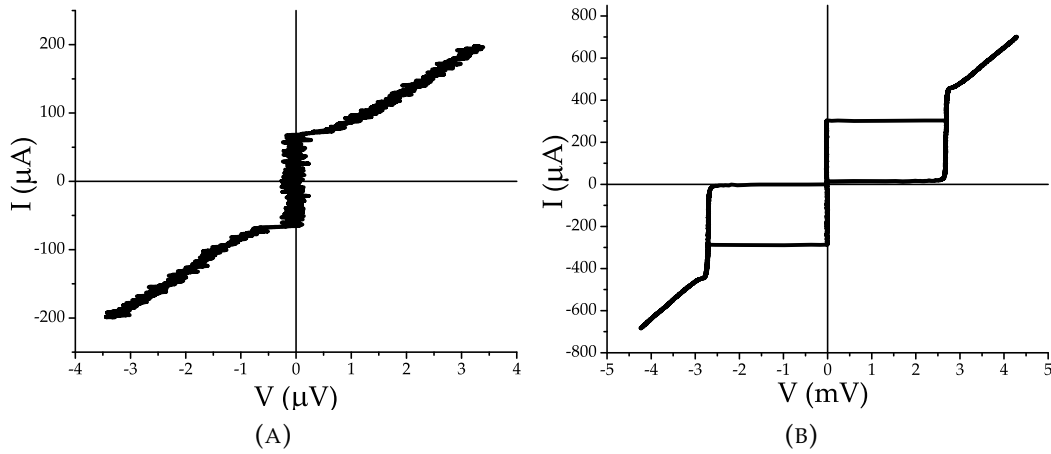


FIGURE 1.11: Comparison of the $I(V)$ curves in the overdamped (a) and underdamped (b) regimes. In (a), metallic SFS JJ with a Co barrier between two Nb electrodes. In (b), tunnel SIS JJ with Nb electrodes and AlO_x barrier

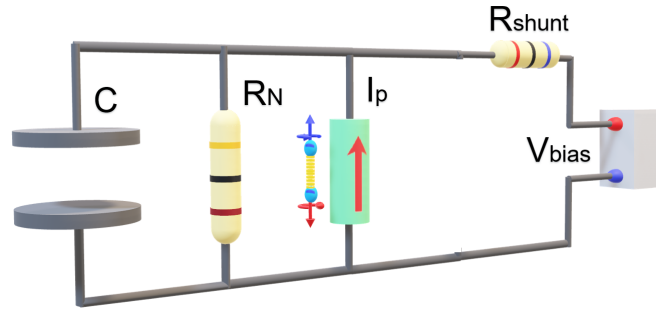


FIGURE 1.12: RCSJ model circuit schematics: C is the capacitance, R_N is the normal resistance and I_p is the Cooper pairs current, i. e. the supercurrent. The bias current is generally given using a voltage generator in series with a shunt resistance R_{shunt}

of the ramp, in fact, the voltage is zero until I_c is reached. Above this value, the voltage increases up to the gap voltage $V_g = (\Delta_L + \Delta_R)/e$, with $\Delta_{L(R)}$ superconducting gap of the left and right electrodes, respectively. Increasing the current, the $I(V)$ curve follows the typical ohmic behavior of a resistor with resistance R_N . When the bias current is decreased, we can face two situations:

- the JJ returns in the zero-voltage state at exactly the same value as in the rise of the ramp, i.e. at $I_b = I_c$;
- the JJ returns in the zero-voltage state at a value of the bias current much smaller than I_c (retrapping current I_r), i. e. the $I(V)$ curve is hysteretic.

The simplest approach typically used to model the shape of the $I(V)$ curve is the Resistively and Capacitively Shunted Junction (RCSJ) model, in which a JJ is schematized as an RLC damped oscillator. Combining the formula in

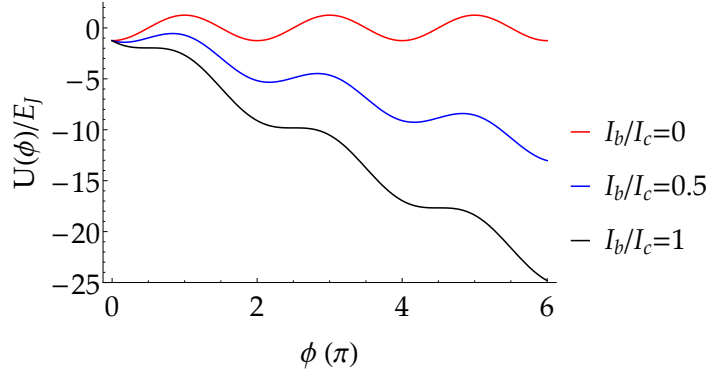


FIGURE 1.13: Normalized washboard potential $U(\varphi)/E_J$ as a function of the normalized bias current I_b/I_c

Eq. 1.1, the voltage across the JJ is [26]

$$V(t) = \frac{\hbar}{2e} \frac{1}{I_c \cos \varphi} \frac{dI}{dt'} \quad (1.34)$$

i. e. a JJ is a non-linear inductor with

$$L_J = \frac{\hbar}{2e} \frac{1}{I_c \cos \varphi}. \quad (1.35)$$

The capacitance C arises because of the charge accumulation at the interfaces between the superconducting electrodes and the barrier, and it generates a displacement current [26],

$$I_d = C \frac{dV}{dt}. \quad (1.36)$$

The ohmic element in the circuit, finally, is due to the generation of a dissipative current of quasiparticles,

$$V_N = I_N R_N, \quad (1.37)$$

i. e. a finite voltage across the junction can be detected [26].

Solving the second Kirchhoff law for the **Resistively and Capacitively Shunted Junction (RCSJ)** circuit for a given bias current I_b ,

$$I_b = I_s + I_N + I_d, \quad (1.38)$$

which can also be written in terms of the phase-difference as

$$I_b = I_c \sin \varphi + \frac{2e}{\hbar R_N} \frac{\partial \varphi}{\partial t} + \frac{2eC}{\hbar} \frac{\partial^2 \varphi}{\partial t^2}, \quad (1.39)$$

we can calculate the voltage across the JJ as a function of the bias current.

Let us first consider an unbiased JJ, in which the Kirchhoff law in Eq. 1.39 in terms of the phase is

$$0 = I_c \sin \varphi(t) + C \frac{2e}{\hbar} \frac{\partial^2 \varphi}{\partial t^2}. \quad (1.40)$$

In this regime, the JJ is schematized as an anharmonic LC oscillator, with resonant frequency (plasma frequency)

$$\omega_P = \frac{1}{\sqrt{L_J C}} = \sqrt{\frac{2eI_c}{\hbar C}}, \quad (1.41)$$

i. e. the phase-difference across the junction φ can be treated as an oscillating particle that lays in one of the minima of the potential energy $U(\varphi)$ (washboard potential),

$$U(\varphi) = E_J (\cos \varphi(t_f) - \cos \varphi(t_i)), \quad (1.42)$$

with E_J the Josephson energy

$$E_J = \frac{\hbar I_c}{2e}. \quad (1.43)$$

Increasing the bias-current I_b , the washboard potential is tilted: the phase-particle remains in the minimum until $I_b = I_c$ is reached, while for $I_b > I_c$ it rolls along the washboard (Fig. 1.13).

The motion of the phase-particle is strongly related to the ohmic and dissipative resistive element in the RCSJ model by means of the Stewart-McCumber parameter β , defined as

$$\beta = Q^2, \quad (1.44)$$

where Q is the quality factor associated with the RLC-circuit that schematizes the JJ in presence of dissipation,

$$Q = \omega_P C R_N. \quad (1.45)$$

When the retrapping current corresponds to I_c , β and Q are small ($\beta \sim 1 \times 10^{-3} - 1 \times 10^{-1}$) [139] (Fig. 1.11 (a)) and we are in the overdamped regime, while when β assumes higher values, the phase-particle is retrapped at $I_b = I_r < I_c$ (Fig. 1.11 (b)): the smaller is I_r , the higher is Q , and the lower is the dissipation (underdamped regime).

From the relation between β , Q and the capacitance of the barrier C in Eqs. 1.44 and 1.45, it is straightforward that when the barrier is an insulator, Q is higher than in JJs with metallic barriers: in fact, the capacitance in metals can be considered as a first approximation equal to zero, and in general much smaller than the capacitance found in typical insulating materials [26, 27]. As a consequence, we can qualitatively confirm that an overdamped $I(V)$ is the typical curve measured in metallic JJs, and the hysteresis is instead a feature

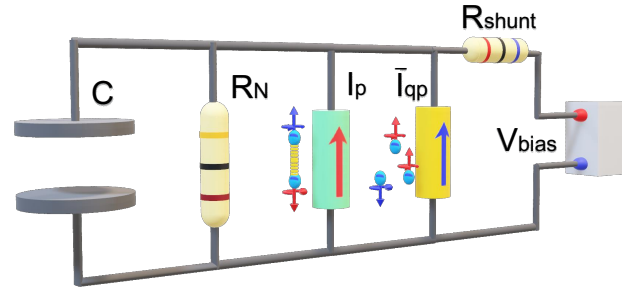


FIGURE 1.14: Tunnel Junction Microscopic (TJM) model circuit schematics: compared with the RCSJ circuit schematics in Fig. 1.12, the quasiparticles current is added in parallel to the supercurrent

of SIS JJs.

The phase-dynamics (electrodynamics) in a JJ is governed by the following parameters:

- the critical current I_c , necessary to estimate the Josephson inductance L_J , the Josephson energy E_J and the plasma frequency ω_P ;
- the normal state resistance R_N ;
- the superconducting gap Δ of the electrodes;
- the quality factor Q , which quantifies the dissipation in a JJ;
- the capacitance, necessary to estimate another fundamental energy scale for a JJ, the Coulomb (or charging) energy

$$E_c = e^2 / (2C). \quad (1.46)$$

All these parameters are crucial for the implementation of superconducting circuits, and in particular in qubits, as discussed in more detail in Chap. 4 and Chap. 5. While the first three parameters are easily extracted from the experimental curves, Q and C might be tricky to estimate. The $I(V)$ curve shape strongly depends on the coupling with the environment, as it will be clarified in the next section. Moreover, the study of the electrodynamics becomes even more important when dealing with unconventional JJs, in which novel combinations of materials may introduce novel physical problems. The question is: can we extract these parameters by fitting the $I(V)$ curves?

The RCSJ model is appropriate when the JJs fall in the overdamped regime (Fig. 1.11 (a)). When the resistance below the gap depends on the voltage, as it occurs in hysteretic $I(V)$ curves (Fig. 1.11 (b)), the RCSJ model can not describe the physical processes occurring in the device. An analytic correction to the RCSJ model is depicted by the Non-Linear RCSJ (NLRCSJ) model, in which a non-linear dependence on the voltage (typically a power-law V^n , with integer n) is introduced in the dissipative element $R_N(V)$ for voltages

below the gap, i. e. the subgap region [26, 27]. This model does not give any further information on the dissipation mechanisms inside a JJ.

An almost exact description of hysteretic JJs with insulating barriers can be instead given by a purely microscopic approach, the TJM model, developed by Werthamer, Larkin and Ovchinnikov in 1966 [140, 141].

In the TJM model, the total tunnel current is the sum of the supercurrent I_s and an additional quasiparticles current I_q (Fig. 1.14), written as a function of time as [26, 27]

$$I_s(t) = \text{Im} \int_{-\infty}^{\infty} d\omega_1 \int_{-\infty}^{\infty} d\omega_2 W(\omega_1) W(\omega_2) I_p(\omega_2 + 2eV_{\text{DC}}) e^{i(\omega_1 + \omega_2 + eV_{\text{DC}})t}, \quad (1.47)$$

and

$$I_q(t) = \text{Im} \int_{-\infty}^{\infty} d\omega_1 \int_{-\infty}^{\infty} d\omega_2 W(\omega_1) W^*(\omega_2) I_{\text{qp}}(\omega_2 + eV_{\text{DC}}) e^{i(\omega_1 - \omega_2)t}, \quad (1.48)$$

where V_{DC} is the DC component of the voltage across the JJ [142]. The function $W(\omega)$ is obtained by the Fourier transform [142]

$$e^{i\phi(t)/2 - ieV_{\text{DC}}t} = e^{i\phi/2} \int_{-\infty}^{\infty} d\omega W(\omega) e^{i\omega t}, \quad (1.49)$$

with

$$\frac{d\phi}{dt} = \frac{2e}{\hbar} \bar{V}, \quad (1.50)$$

and it is related to the temporal mean value of the voltage across the barrier \bar{V} [142].

All the information on the physics of the device and the microscopic tunneling of Cooper pairs and quasiparticles is directly depicted by the kernels $I_p(\xi)$ and $I_{\text{qp}}(\xi)$ in Eq. 1.47 and 1.48, defined by the Green's functions of the left ($F_L(\omega)$ and $G_L(\omega)$) and right ($F_R(\omega)$ and $G_R(\omega)$) superconducting electrodes in Fig. 1.1, respectively [26, 49],

$$I_p(\omega) = \frac{1}{2\pi^3 e R_N} \int_{-\infty}^{\infty} d\omega_1 \int_{-\infty}^{\infty} d\omega_2 \left(\tanh \frac{\hbar\omega_1}{2k_B T} + \tanh \frac{\hbar\omega_2}{2k_B T} \right) \frac{\text{Im}F_L(\omega_1) \text{Im}F_R(\omega_2)}{\omega_1 + \omega_2 - \omega + i0}, \quad (1.51)$$

and

$$I_{\text{qp}}(\omega) = \frac{1}{2\pi^3 e R_N} \int_{-\infty}^{\infty} d\omega_1 \int_{-\infty}^{\infty} d\omega_2 \left(\tanh \frac{\hbar\omega_1}{2k_B T} + \tanh \frac{\hbar\omega_2}{2k_B T} \right) \frac{\text{Im}G_L(\omega_1)\text{Im}G_R(\omega_2)}{\omega_1 + \omega_2 - \omega + i0} + \text{const.} \quad (1.52)$$

What makes the TJM model so powerful is that the phase-dependent quasiparticle term in Eq. 1.52 is not simply related to the ohmic resistance above the gap voltage, but to the shape of the subgap branch ($V < V_g$) in the $I(V)$ characteristic, and the slope of the $I(V)$ curve near the superconducting branch, the subgap resistance R_{sg} . R_{sg} is related to the quasiparticles tunneling current and their dissipation [26, 143, 144]. It is therefore crucial for the engineering of superconducting circuits [19, 145–148]. As an example, in transmon qubits (App. C), the quasiparticles dissipation might affect both the relaxation and the coherence times [145, 148, 149].

In addition to this, the direct dependence of the total tunnel current on the Green's function for Cooper pairs and quasiparticles, hence on the tunneling Hamiltonian, allows to take into account also unconventional transport mechanisms not included in the Ambegaokar-Baratoff (AB) theory [26, 49], such as: eventual suppression of the pair current due to inelastic relaxation processes in the superconducting electrodes and in the tunneling mechanisms (spin-flipping processes at the interface between the superconductors and the insulator, for example), as discussed by Kulik and Zorin [150, 151], and large-scale inhomogeneities of the electrode materials [151]. A special mention must be given to the presence of singularities in the tunnel current at the gap frequency of the superconductor predicted by the standard Bardeen-Cooper-Schrieffer (BCS) theory, also known as Riedel peaks [140, 152]. In real systems, such singularities are in general smeared because of the aforementioned processes. The microscopic approach allows to explicitly consider this effect by introducing a smearing factor δ for the Riedel peaks [153]

In conclusion, in literature it is plenty of powerful models perfectly suited for the description of the electrodynamics in standard non-magnetic JJs, such as in Al/Nb technology. These tools can be successfully used also on less traditional JJs, as discussed in Chap. 4, on which this approach is a novelty.

1.3.2 The phase-dynamics

The understanding of the phase dynamics of a JJ allows to distinguish the contributions to dissipation coming from the JJ itself and the environment.

The effect of the environment is explicitly taken into account in the frequency-dependent RCSJ model [154–156]. Within the approach proposed by Kautz and Martinis in Refs.[155, 156], the equivalent circuit of the JJ in Fig. 1.12 is replaced by the circuit in Fig. 1.16[154–156], in which three additional elements can be found:

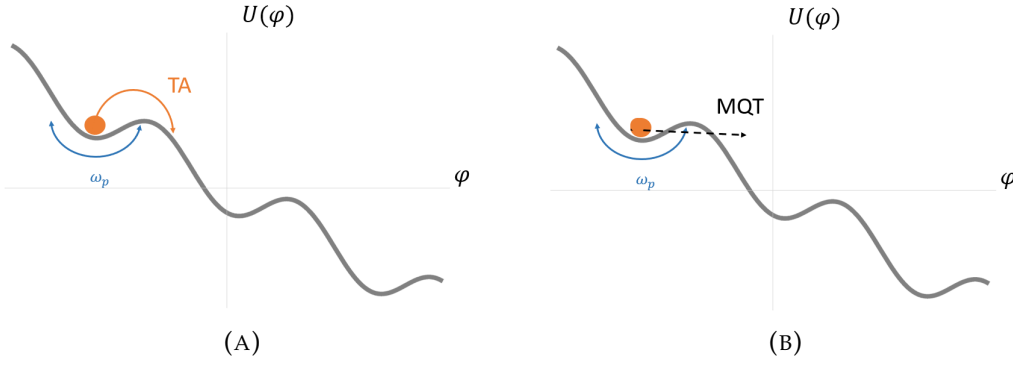


FIGURE 1.15:]

In (a): escape of the phase dynamics for thermal activation (TA); in (b): escape of the phase dynamics for macroscopic quantum tunneling phenomena (MQT)

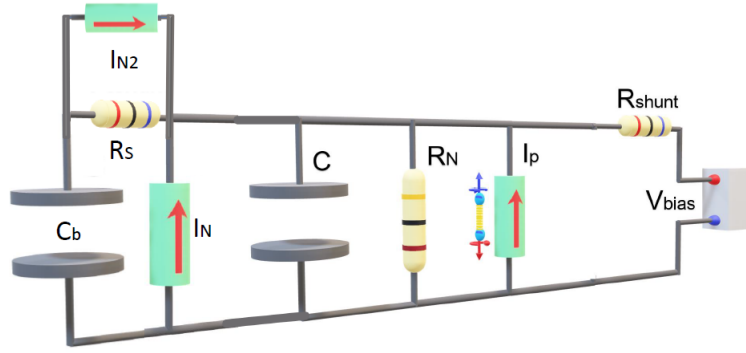


FIGURE 1.16: Frequency-dependent RCSJ model circuit schematics: with respect to the RCSJ circuit schematics in Fig. 1.12, an additional branch, which schematizes the environment in which the junction is embedded, has been added. This is composed of two noise current sources $I_{N(2)}$, with a resistive and capacitive shunt R_s and C_b

- a parasitic capacitance C_b ;
- a shunt resistance R_s ;
- a Johnson noise current contribution I_{N2} , i. e. a Gaussian signal with zero time-averaged mean $\langle I(t) \rangle$ and random autocorrelation $\langle I(t + t')I(t') \rangle = 2k_B T / R \delta(t')$ (white noise power spectrum).

The circuit quality factor $Q = \sqrt{2eI_c C / (\hbar G^2(\omega))}$ becomes frequency-dependent by means of the impedance $G(\omega)$ [156]

$$G(\omega) = \frac{1 + R_J / R_{\parallel} R_s^2 C_b^2 \omega^2}{R_J (1 + R_s^2 C_b^2 \omega^2)}, \quad (1.53)$$

where R_J is the intrinsic resistance of the JJ and $R_{\parallel} = R_J \parallel R_s$. The dissipation at low frequencies is mostly due to the resistance of the JJ, i. e. R_{sg} below

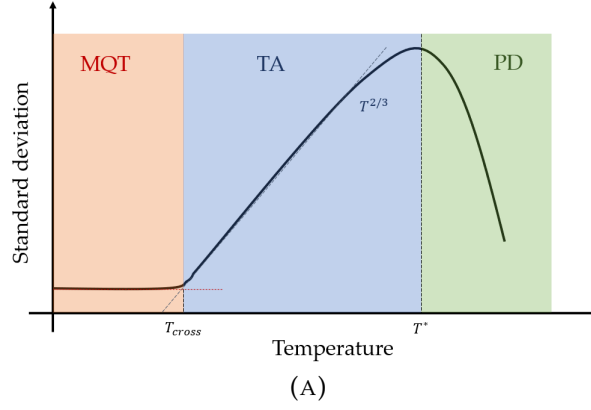


FIGURE 1.17: Transition from the MQT to TA to the PD regime in standard deviation as a function of the temperature. The curve is a pictorial representation of the three transitions, here given as a guide for the eye

the gap and R_N above the gap. In the subgap branch of the $I(V)$ curve, in particular, the quasiparticles tunneling is the strongest source of dissipation, and the quality factor becomes

$$Q(\omega \sim 0) = Q_0 = \omega_P C R_{sg}. \quad (1.54)$$

In the vicinity of I_c , the phase-particle may randomly escape from the minimum of the washboard potential with an escape rate $\Gamma(I)$ exponentially dependent on the height of the energy barrier $\Delta U(I)$

$$\Delta U = \frac{4}{3} \sqrt{2} E_J \left(1 - \frac{I}{I_{c0}}\right)^{3/2}, \quad (1.55)$$

with I_{c0} the critical current in absence of fluctuations. This escape dynamics occurs because of two main processes: **Thermal Activation (TA)** (Fig. 1.15 (a)) and **Macroscopic Quantum Tunneling (MQT)** (Fig. 1.15 (b)). In the **Thermal Activation (TA)** regime, the escape rate

$$\Gamma_{TA} = a_{TA} \frac{\omega_P(I)}{2\pi} e^{-\Delta U(I)/k_B T} \quad (1.56)$$

strongly depends on the temperature [157]¹. This phase-dynamics occurs in a frequency range of the order of the plasma frequency ω_P , which typically lays in the gigahertz range. In this high-frequency regime, the quality factor reduces to

$$Q(\omega \sim \omega_P) = Q_1 = \omega_P C R_{\parallel}, \quad (1.57)$$

i. e. the dissipative components mostly come from the environment in which the JJ is embedded, here schematized with the resistor R_{\parallel} . The pre-factor a_{TA}

¹Here the plasma frequency have been corrected to the value at non-zero bias current $\omega_P(I) = \omega_P \left(1 - (I/I_{c0})^2\right)^{1/4}$ [26, 158]

in Eq. 1.56 is an amplitude term related to Q_1 and the temperature T [26, 158]

$$a_{\text{TA}} = \left(\frac{2}{\sqrt{1 + \frac{Q_1 k_B T}{1.8 \Delta U}} + 1} \right)^2. \quad (1.58)$$

At very low-temperatures and for high-quality **JJs**, the temperature is no more the cause of the critical current fluctuations [159–161]. The escape is, instead, given by a pure quantum tunnel effect and the relevant energy that competes with the ΔU is the quantum energy $\hbar\omega_P$ [160, 161]. Here the escape rate becomes

$$\Gamma_{\text{MQT}} = a_{\text{MQT}} \frac{\omega_P(I)}{2\pi} e^{-7.2 \frac{\Delta U(I)}{\hbar\omega_P} (1+0.87/Q_1)}, \quad (1.59)$$

with a_{MQT}

$$a_{\text{MQT}} = \sqrt{\frac{864\pi\Delta U}{\hbar\omega_P}}. \quad (1.60)$$

Given the stochastic nature of the escape processes, the distribution of the switching events, or **Switching Current Distribution (SCD)**, is characterized by a standard deviation σ dependent on the temperature as $\sigma \propto T^{2/3}$ [162–167], and a negative skewness (measure of the asymmetry in a distribution) of the order of -1 , i. e. it is generally observed a tail for switching currents $I_{\text{sw}} < I_{\text{mean}}$, where I_{mean} is **SCD** mean value. A saturation in the σ below a cross-over temperature T_{cross} signals the transition between the **TA** and the **MQT** regimes [162–167] (red and blue boxes in Fig. 1.17),

$$T_{\text{cross}} = \frac{\hbar\omega_P}{2\pi k_B} \left(\sqrt{1 + \frac{1}{4Q_1^2}} - \frac{1}{2Q_1} \right). \quad (1.61)$$

For perfect **JJs** with $Q_1 \rightarrow \infty$, T_{cross} equals the ratio $\hbar\omega_P/(2\pi k_B)$, while for overdamped **JJs** T_{cross} tends to zero, i. e. **MQT** arises only for low-dissipative **JJs** in the underdamped regime.

The distinction of the dissipation in the high- and low-frequency regimes is especially relevant when the **JJ** falls in the moderately damped regime ($1 < Q_1 < 5$). In this last case, multiple phase-particle escapes and retrapping events in the washboard potential compete, generating what is known as **Phase Diffusion (PD)**. **PD** processes are in general accounted for thermal and electrical noise [156], schematized in the equivalent circuit of the **JJ** in Fig. 1.16 with the white noise term, typically simulated using Monte Carlo procedures [164–168].

The retrapping rate Γ_R analytically introduced by Ben-Jacob in Ref. [169], which accounts for the probability for the phase-particle to be retrapped several times along the washboard, is

$$\Gamma_R = \frac{I - I_{R0}}{I_{c0}} e^{-E_J Q_1^2 \frac{(I - I_{R0})^2}{2k_B T I_{c0}}}. \quad (1.62)$$

where I_{r0} is the retrapping current in absence of thermal fluctuations.

Below a certain temperature T^* , $\Gamma_R \ll \Gamma_{TA}$, and switching phenomena are solely due to TA processes. When increasing the temperature above T^* , retrapping processes counterbalance the escape processes, leading to a reduction of the width and a symmetrization of the SCD (blue and green boxes in Fig. 1.17), i. e. the skewness γ progressively increases from -1 to 0 . The transition between TA and PD regimes is governed by the quality factor Q_1 : the lower is Q_1 , the lower is the transition temperature T^* , and the higher is the probability to face PD phenomena.

The effect of Phase Diffusion (PD) processes can be observed also in the $I(V)$ curves. Thermal fluctuations in moderately damped JJs induce simultaneous presence of hysteresis and a finite resistance in the superconducting branch, which can be fitted only by using the frequency-dependent Kautz-Martinis RCSJ model [154–156, 164–168, 170].

1.4 Transport properties in tunnel ferromagnetic Josephson junctions

In the last twenty years, the scientific community has shown a great interest in hybrid ferromagnetic JJs with tunnel barriers, such as Superconductor/Insulator/Ferromagnet/Superconductor (SIFS) JJs, Superconductor/Insulator/small superconducting buffer/Ferromagnet/Superconductor (SIsFS) JJs and SI_fS JJs.

The former ones were first used to study the $0-\pi$ transition [34, 78, 171–177]. Compared with standard metallic SFS JJs, in which the presence of spontaneous fractional fluxes due to the $0-\pi$ transition was quite difficult to detect, Superconductor/Insulator/Ferromagnet/Superconductor (SIFS) JJs were characterized by $I_c R_N$ products two orders of magnitude higher [171, 177]. The advances in fabrication technology were fundamental to build structures with step- or wedge-like ferromagnetic barriers, making possible to induce a coexistence between 0 and a π states [78, 171–176]. Fraunhofer and Shapiro steps analysis, as a function of the ferromagnet thickness d_f and the temperature T , were the main tools for the measurement of 0 , π and $0-\pi$ states in these systems [34, 78, 171–177], fundamental for the proposal of novel flux-qubits based on semifluxons dynamics [177, 178].

The request for high $I_c R_N$ products has led to tunnel-SFS JJ of the SIsFS type [37–40]. The insertion of a superconducting interlayer between the insulating barrier and the ferromagnet in SIsFS JJs enhances the critical current up to values of an SIS JJ [38] and decreases the impact of quasiparticles losses in the systems, depending on the relative thickness between the intermediate superconducting layer and the ferromagnet [179]. Even if increasing the s thickness the onset for the 0 to π transition becomes harder to detect [179, 180], the highest $I_c R_N$ values make this configuration more suitable for practical implementations inside superconducting circuits, such as Cryogenic Magnetic Random Access Memory (CMRAM) based on the residual magnetization of the barrier [38–40]. The CMRAM addressing in Sec. 1.1, in fact, has been

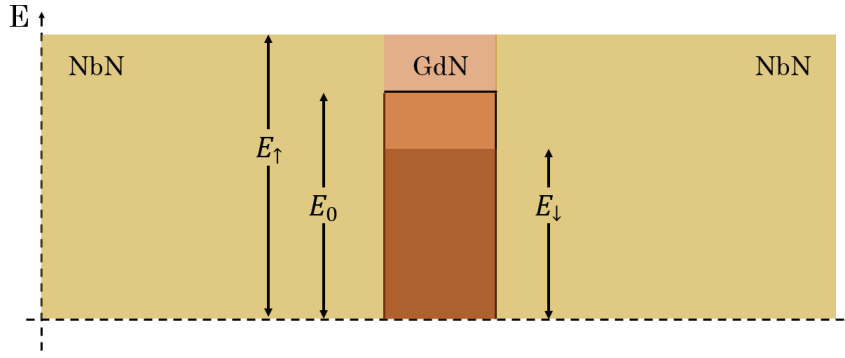


FIGURE 1.18: Scheme of the energy barrier that the carriers need to overcome in a spin-filter device, such as NbN-GdN-NbN JJs: E_0 is the energy barrier for $h = 0$, i. e. for $T > T_{\text{Curie}}$, while $E_{\uparrow(\downarrow)}$ are the energy barriers for $T < T_{\text{Curie}}$ in Eq. 1.63

first proposed on metallic SFS JJs with PdFe barrier [36], but the operational speed was too slow compared with standard values required in high-efficiency superconducting digital technology, such as the Single Flux Quantum (SFQ)-based circuitry.

Finally, since the first theoretical predictions of the macroscopic quantum dynamics in JJs with ferromagnetic insulating barriers and the emergence of a π -state exploitable in hybrid ferromagnetic quantum active devices such as quiet-qubits [109, 181, 182], the first experimental evidence of a Josephson effect in real SI_fS JJs was accomplished on GdN-based JJs[183], and to our knowledge there are no equals in literature. Detailed investigation and application of the transport properties in a few known I_f materials, such as EuO and EuS, has been limited by difficulties associated with growth and stoichiometry [184, 185].

The simultaneous presence of tunnel transport mechanisms (Eqs. 1.19 and Eq. 1.20 in Sec. 1.2) and a ferromagnetic ordering in the GdN barrier give rise to a spin-filtering effect, which gives to these devices the name *spin-filter*[183]. For temperatures above T_{Curie} , carriers with up and down spin equally contribute to the current, but when the material goes through its ferromagnetic transition ($T < T_{\text{Curie}}$) the presence of exchange interactions in the barrier leads to a spin asymmetry for the two spin channels: electrons of different spins will experience different barrier heights

$$\begin{cases} E_{\uparrow} = E_0 - \frac{h}{2} & \text{for spin } \uparrow \\ E_{\downarrow} = E_0 + \frac{h}{2} & \text{for spin } \downarrow, \end{cases} \quad (1.63)$$

where h is the ferromagnet exchange field. This causes the formation of a net spin-polarized current in the device (Fig. 1.18), which can be exploited in spintronics devices [183, 185–187].

The spin-filtering efficiency P is defined in terms of the tunneling probabilities across the energy barriers for spin up (down) $T_{\uparrow(\downarrow)}^2$ as [183, 185, 187]

$$P = \frac{T_{\uparrow}^2 - T_{\downarrow}^2}{T_{\uparrow}^2 + T_{\downarrow}^2}, \quad (1.64)$$

where $T_{\uparrow(\downarrow)}$ is related to the energy barriers $E_{\uparrow(\downarrow)}$ in Eq. 1.63 through Eqs. 1.19 and 1.20.

The generation of spin-polarized currents can be intuitively related to the arising of spin-triplet supercurrent, as predicted by F.S.Bergeret et al.[188]. It was theoretically demonstrated that if the exchange field $h = 0$, i. e. in the case of a non-magnetic tunnel JJ, the temperature-dependence of the characteristic voltage $I_c R_N(T)$ follows the standard AB-relation, but when the exchange field starts to become important the $I_c R_N(T)$ curve behaves in a very different manner from that observed in conventional junctions. For certain values of the exchange field and the degree of inhomogeneity at the interface with the electrodes, the $I_c R_N(T)$ curves can assume a non-monotonic behavior. In particular, in case of a non-collinear magnetic field and fully-polarized barriers the Josephson current is mainly due to a spin-triplet component and such behavior becomes a fingerprint for unconventional pairing mechanisms [188].

Experimental evidence of spin-triplet superconductivity in spin-filter JJs were first inferred in Refs.[185, 189, 190] to explain the unconventional conductance spectra measured in both NbN-GdN-NbN JJs and GdN-NbN-GdN heterostructures, but as will be discussed in Chap. 3 the $I_c(T)$ curves in spin-filter JJs are a solid benchmark for the study of spin-triplet superconductivity.

Moreover, spin-filter JJs are the first ferromagnetic JJs in which a clear transition between TA and MQT was experimentally captured: the study of the phase-dynamics in these devices gave a clear demonstration of their quantum nature, which opens the door to the predicted implementation inside quantum circuits that require high quantum coherence. Therefore, the estimation of the electrodynamic parameters of spin-filter as a function of the thickness and the temperature reported in Sec. 4.1 is a strong requirement for practical engineering implementations.

Experimental setup

In my three-years-long Ph.D. experience I had the chance to employ different cryogenic systems, equipped with low- and [Room-Temperature \(RT\)](#) electronics that allow to perform low-noise and accurate transport measurements of superconducting systems in DC- and RF-environment. A special focus will be given to the dry dilution cryostat: the *Triton*, which I contributed to mount and setup. An important part of my Ph.D., in fact, was focused on engineering, mounting and testing DC- and RF-lines necessary for low-temperature measurements of superconducting systems and qubits. Other cryogenic systems used to perform low-temperature measurements reported in this thesis are the *Heliox*, and a wet dilution refrigerator, the *Kelvinox*, both from *Oxford Instruments*. The former is suitable for cool-downs in a wide range of temperature (from 300 mK up to 80 K), while the dilution refrigerators are in general preferred for measurements in the quantum regime, i. e. in a range of temperatures from ~ 10 mK to hundreds of millikelvins.

I will also give an overview on the techniques used to perform DC-measurements for [JJs](#) and, in general, on superconducting systems, and the protocol for the characterization of qubits, using conventional heterodyne detection and RF-pulses.

2.1 The Evaporation cryostat

The DC-measurements in a temperature range from 300 mK to about 80 K were performed by using an evaporation cryostat *Oxford Instruments HelioxVL*, immersed into a ^4He bath (Fig. 2.1).

The cryostat is enclosed in an [Inner Vacuum Chamber \(IVC\)](#) (Fig. 2.1), sealed with vacuum grease, in which we put a small amount of helium exchange gas to favor the thermalization with the main bath. It is composed of:

- a capillary;

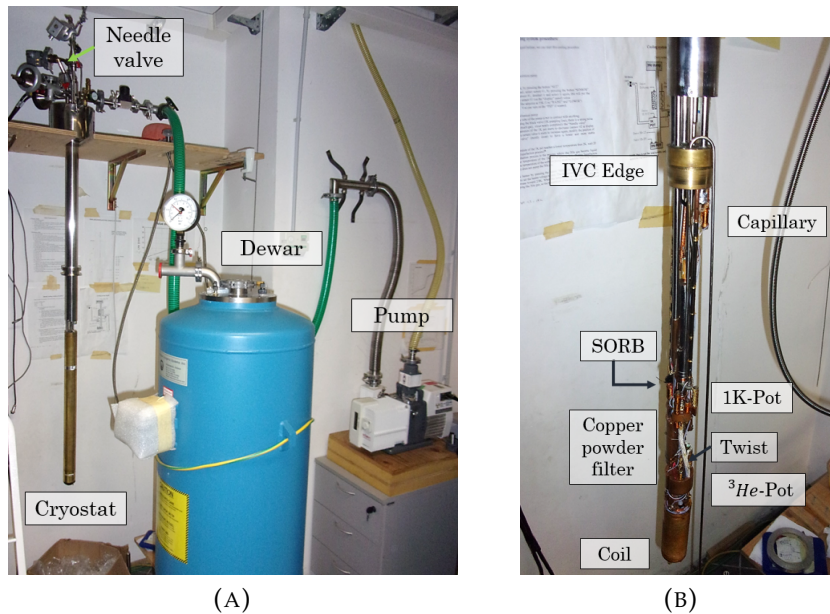


FIGURE 2.1: In (a): view on the Heliox evaporation cryostat. In (b): inner view of the Heliox system

- a pot at 1 K, the *1K-Pot*;
- a pot at 300 mK, the *³He-Pot*.

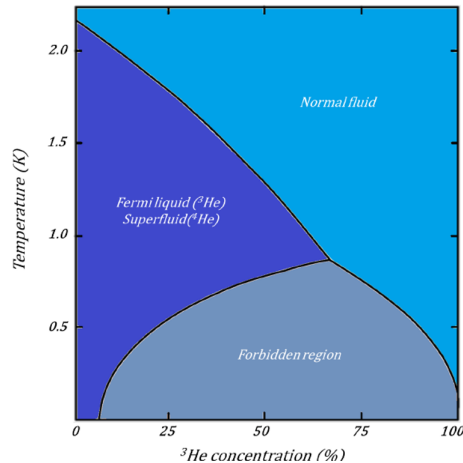
In this system, we have a closed ³He cycle: the main ⁴He bath allows to reach 4.2 K, while in the 1K-Pot, in which we store the liquid ⁴He sucked by the capillary from the main bath, we can reach $\sim 1.8 - 2.2$ K, by regulating the pressure on the 1K-Pot with an external rotary pump and a needle valve. The ³He condenses in the ³He-pot, which is the coldest stage of the cryostat. Finally, pumping on the surface of the liquid ³He with an adsorption pump made of a zeolitic material, the *SORB* (active below 30 K), we reach the base temperature (300 mK).

2.2 Dilution fridges

To perform transport measurements at very low temperatures, of the order of 10 mK, two dilution fridges have been used. The *Kelvinox* is a wet dilution refrigerator, i. e. it is assisted by an external liquid ⁴He bath. Instead, the *Triton* is a cryofree refrigerator [191], and as a consequence it is a dry system. The dilution procedure is the same in the two cryostats [192], therefore we will here highlight the main differences between the two systems.

The *Triton* is composed of six copper gold- and silver-covered plates, thermally decoupled one from each other by means of *Stainless-Steel* (SS) supports. Starting from the top of the cryostat, we have:

- the RT-Plate, at RT;
- the PT1, at ~ 70 K;

FIGURE 2.2: Phase diagram of the ^3He - ^4He mixture

- the PT2, at ~ 4.2 K;
- the still-plate, at ~ 700 mK;
- the IAP-plate, or cold-plate, at ~ 100 mK;
- the MC-plate, at ~ 10 mK.

The temperature of the last three plates is determined by the dilution process proposed by Heinz London in the early 1950s [193], characterized by three main stages: the condensation, the mixing/dilution and the evaporation (Fig. 2.2).

Condensation The first phase in the dilution process is the condensation. An ^3He - ^4He mixture gas preserved in a tank is first cooled and purified in liquid nitrogen. In the Kelvinox, it is first cooled down to 4.2 K by using the external ^4He bath. Then, the mixture passes through the *condensing line* thermalized by the 1K-pot stage at about 1.7 – 1.8 K.

In the Triton, the ^4He bath is replaced by a **Pulse Tube Refrigerator (PTR)**, which precools the system down to about 10 K. The PTR vibrations, which can induce noise during the measurements, are significantly lowered by copper braids at the 4K-plate, which decouples the PTR heads from the other plates.

In the **Pre-Cooling (PC)** phase the mixture is first cooled down to 10 K using a series of heat-exchangers located at PT1, PT2, the still, the cold-plate and the **Mixing Chamber (MC)**, the coldest stage of the cryostat. A counter-flow heat exchanger located at the top plate improves the cooling of the gas before it reaches PT1.

When the system reaches ~ 10 K, the pre-cool loop (highlighted in red in Fig. 2.3 (B)) is evacuated using a turbo pump, and the mixture is compressed using a high-pressure (~ 2.5 bar) pump, the *KNF* ^3He compressor. By using a series of heat exchangers and pressure impedance in the condenser line, we reach temperatures below ~ 2 K by means of

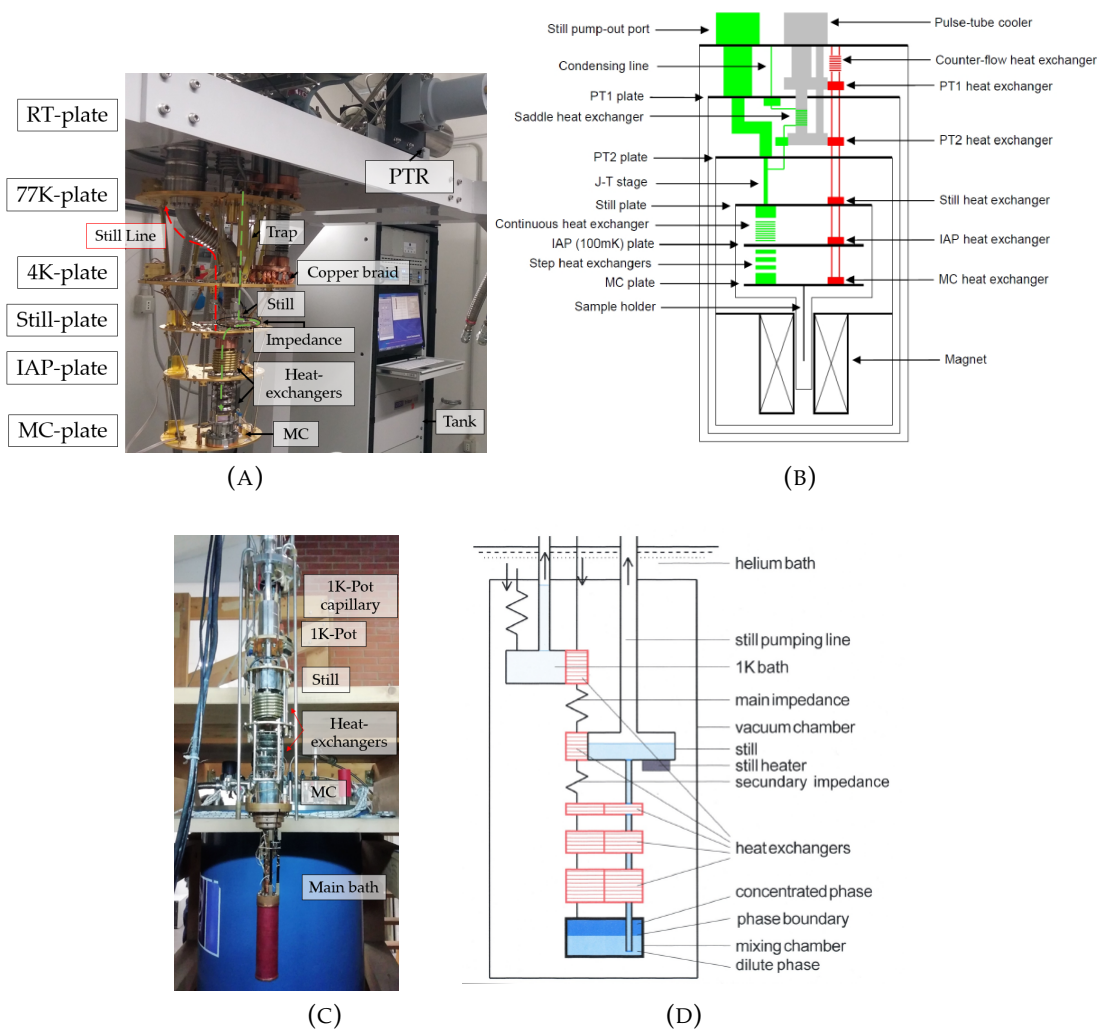


FIGURE 2.3: In (a) and (b): view on the Triton system and a scheme of the Dilution Unit (DU) (green path in (a) and (b)) and Pre-Cooling (PC) units (red path in (a) and (b)) [191]. In (c) and (d) view on the Kelvinox system and the scheme of its thermodynamics

a Joule-Thomson (JT) effect. This occurs in the Dilution Unit (DU), in green in Fig. 2.3 (B).

At this point, the ^3He in the mixture is still gaseous and the next step is to reach its condensing temperature (1.7 K). In the Triton, this is achieved combining the effect of an extra heat-exchanger in the still and an impedance in the JT stage.

Mixing and dilution The circulation of the mixture through the condensing and still lines by using the external pump rack allows to reach a temperature of about 800 mK, below which a phase boundary between the concentrated and the dilute phases of ^3He in the ^3He - ^4He mixture occurs (Fig. 2.2). The remotion of the ^3He out of the MC is an endothermic

process that lowers the temperature down to 10 mK. This is known as dilution phase.

Evaporation and circulation Finally, the ^3He molecules in the MC are pumped out through the *still-line* and then recondensed again (circulation). In the still chamber, which has optimal temperature between 700 mK and 800 mK (corresponding to an ^3He concentration $x_3 = 1.0\%$ to 1.2% in the dilute phase, see Fig. 2.2), we can increase the evaporation of the mixture using a heater. In this way, we can optimize the circulation process.

The control of the pumps, pressures, temperatures and valves in both the cryostats is achieved with the use of an **Intelligent Gas Handling system (IGH)**, driven by an *Oxford Instruments LabVIEW* software.

The Kelvinox in Fig. 2.3 (C) is enclosed in an **IVC** screen sealed with an indium ring¹. In the Triton, instead, since there is no liquid helium and no need to add exchange gas to favor the cooling in the system, the cryostat does not require an **IVC**. Thus, an **Outer Vacuum Chamber (OVC)** is just needed to guarantee the vacuum.

Finally, it is important to avoid any kind of thermal coupling with the environment by means of radiations. In the Kelvinox, an RF-field copper screen is anchored to the still-plate, while in the Triton we have two additional aluminum screens at the 4K- and 70K-plates, respectively.

2.3 The Triton filtering systems and electronics

Compared with the Kelvinox, the strengths of the Triton system are:

- its cryogen-free nature, which makes it suitable for long-term and less-expensive cool-downs;
- its larger dimensions which allow to implement multiple sample stages, and the presence of free **Lines of Sight (LOS)** ports assigned to RF-equipment.

Here, I widely discuss the engineering, mounting, testing and characterization of the DC- and RF-filtered electronics.

2.3.1 DC setup

An accurate measurement of the transport properties of **JJs** and superconducting nanostructures requires special care to filter electrical and thermal noise. The scheme of the DC-lines in the Triton is inspired to the Heliox and the Kelvinox configurations, but, while in the formers we can measure just two samples at a time in a four-contact configuration, the Triton is equipped with 48 DC-lines, 24 lines to current-bias the devices (current-carrying lines) and

¹As in the Heliox, a small amount of exchange gas in the **IVC** is added to favor the thermalization with the main bath.

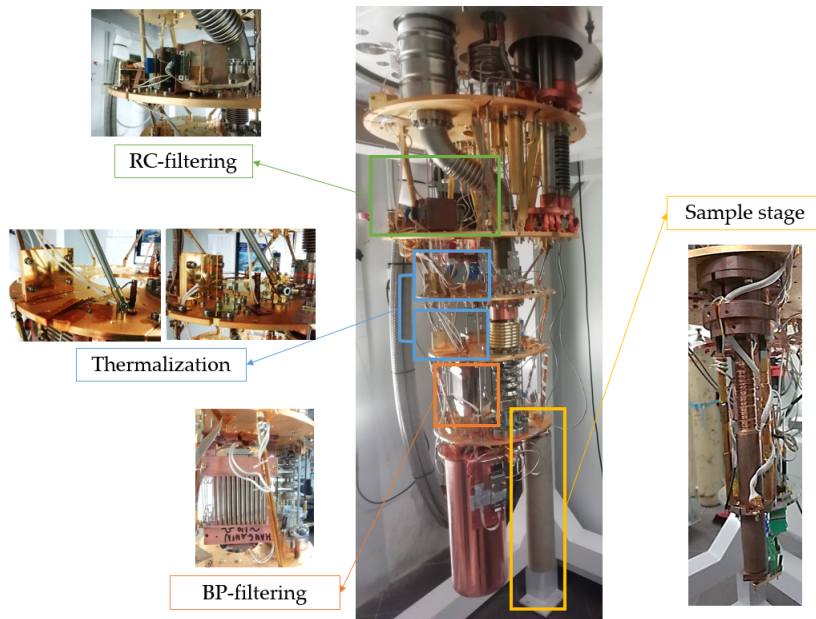


FIGURE 2.4: Scheme of the DC-filtering systems in the Triton system, thermalization stages and DC-sample stage

24 lines to measure the voltage drop across the devices (voltage lines). Half of these lines (12 current lines and 12 voltage lines) are designed to be filtered, i. e. we can measure up to 6 samples at a time. The other lines, instead, can be used for other DC sample-stages which do not require a strong filtering, or for the monitoring of additional RuO thermometers.

From the RT-plate to the 4K-Plate, I -lines and V -lines are twisted pairs in a copper and constantan DC-loom from *Oxford instruments*, respectively. From the 4K-Plate to the MC-plate, instead, I -lines are in a NbTi DC-loom from *Oxford Instruments*, while the V -lines are homemade manganin twisted cables.

The constantan and the manganin are characterized by a low thermal conductivity, and therefore suitable for voltage measurements. The manganin has best performances at low temperatures compared with the constantan [194]. Copper lines are, instead, characterized by a lower resistance compared with the voltage-lines, thus reducing heating when current-biasing the devices. Finally, the NbTi is superconducting below 10 K, i. e. it ensures no heat dissipation at the coldest stages of the cryostat.

The home-made wiring is electrically isolated from the environment with fiberglass gloves. Some sections of the wires are left uncovered for the thermalization: the lines are spiraled around copper pillars thermally anchored at the 4K-, the still- and the IAP-plates. Varnish glue ensures electrical insulation and favors the thermalization (blue boxes in Fig. 2.4).

In Fig. 2.4, we report the different filtering stages of the DC setup in the Triton.

RT to 4K The first filtering stage is at RT via two *EMI filters* connected to the I and V input on the top of the cryostat. Such filters are composed of ferrite beads followed by 24-channel filter boxes with paththrou RC- π

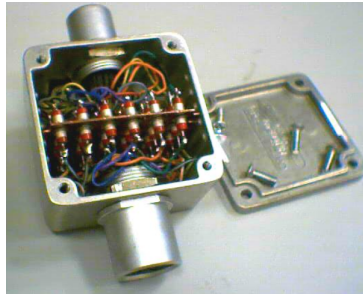


FIGURE 2.5: EMI filters in the Kelvinox and the Triton setup at RT

filters (Fig. 2.5). This stage helps cut-off high frequency peaks due, for example, to mobile phones.

The I - and V -lines, then, passes through two [Electrolitic Tough Pitch \(ETP\)](#) copper boxes anchored at the 4K-plate (Fig. 2.6 (A)). In each copper box, there are two electrically isolated chips with six RC-filters each (Fig. 2.6 (C)), with a common ground at the copper-box. The schematics of the filters is reported in Fig. 2.6 (D). 12 twisted I and V pairs pass through the box and are directly connected to the output Cinch of the box (unfiltered lines), while the other lines are connected to the filters. The motivation for which we use second-order RC-filters rather than standard RC-stages is related to the need to get different degrees of attenuation for the input signal at different frequency-bands. This occurs also in the Kelvinox and in the Heliox by means of RLC- π filters thermally and mechanically anchored at the 1K-Pot stage [164, 165].

The RC-filters Bode diagrams at RT and at 77 K are reported in Fig. 2.7. We used a lock-in amplifier for the characterization in the frequency-range between 10 Hz to 100 kHz, and a [Vector Network Analyzer \(VNA\)](#) up to 1 GHz. The first cut-off frequency at RT is at 3 kHz, while at 77 K it increases to 900 kHz.

IAP to MC At low temperatures and above 10 MHz, the RC-filters present losses in attenuation. Thus, we need another filtering stage able to cut-off signals at higher frequencies. As occurs in the Heliox and the Kelvinox, we installed at the IAP-Plate in the Triton two *brass-powder filters* stages. Here, both RC-filtered and unfiltered I and V -lines pass through this stage (red box in Fig. 2.4).

Metal powder filters were first proposed by Martinis et al. [161], and subsequently developed and discussed in more details by other groups [195–197]. A low-pass metal powder filter is an insulated wire surrounded by fine metal grains. The attenuation of high-frequency signals occurs due to the dissipation of current induced in the grains. As a consequence, it depends on the powder material, the size of the grains, the diameter and the length of the wire.

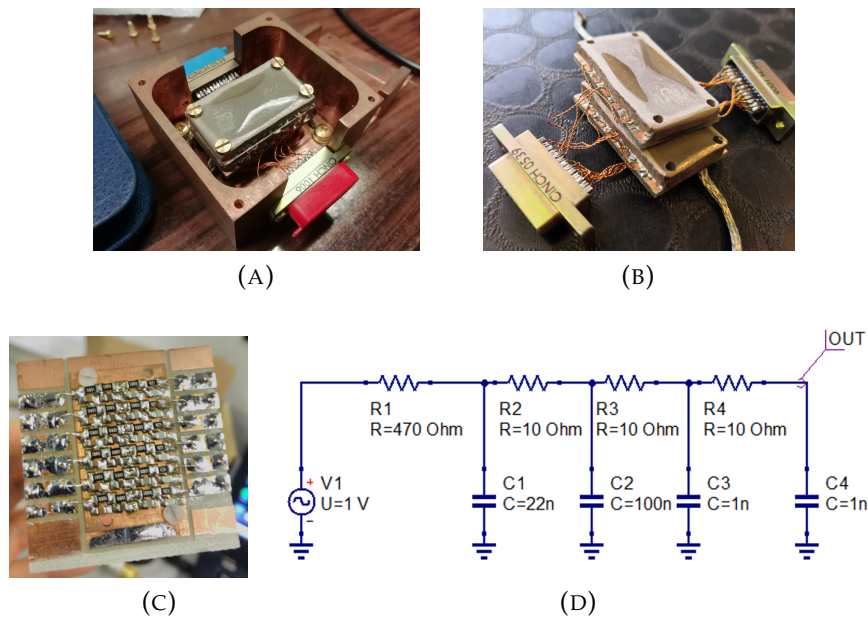


FIGURE 2.6: In (a): RC-copper box for the DC-filtering stage; in (b) RC-filters for DC-voltage lines, on which a sandwich of stycast and copper powder was added to improve the performances of the filters; in (c) a single RC-chip before the mounting; in (d) RC-filters schematics

In the Triton, we have two rows of 12 insulated manganin (for the voltage lines) and copper wires (for the current lines) with a 0.1 mm-diameter, encapsulated in a cylindric paste made of resin, hardener and brass powder. Generally, mixing the powder with epoxies allows to obtain a better thermalization of the central wire compared with pure powder-made filters (Fig. 2.8 (B)) [161, 195–197]. Both manganin and copper wires are shaped into a spiral, with a distance between the loops of 0.1 mm-diameter. The total length of the wires is of the order of 2.5 m.

The 24 filtered I and V lines terminate with a Cinch connector, which is plugged in the sample holder stage, thermally and mechanically anchored to the bottom of the MC plate (yellow box in Fig. 2.4). In the sample holder, there is a Cinch-to-Fischer home-made cable of NbTi (for the current lines) and manganin (for the voltage lines), thermalized on the sample holder. Details on the sample stages are reported in Fig. 2.9 (A).

Josephson devices must be shielded from external magnetic fields. While in the Heliox this is guaranteed by the screened dewar of the main bath, which is composed of a first screen of *cryoperm* and by a second one in lead, in the Kelvinox and the Triton the magnetic field screening is installed directly on the sample stage. The Triton and the Kelvinox sample holders, in fact, are designed to allocate lead and cryoperm magnetic field screens (Fig. 2.4) around the samples.

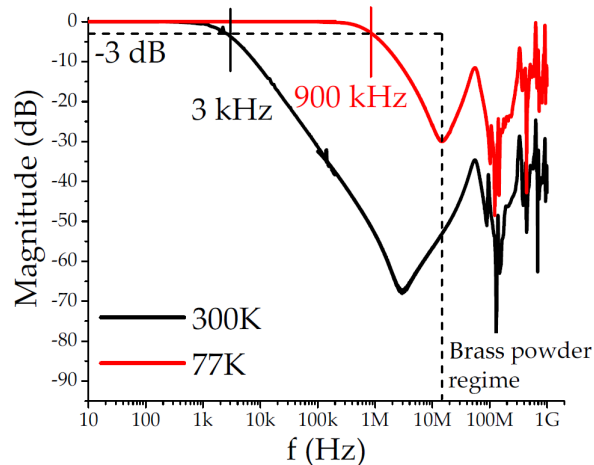


FIGURE 2.7: Bode diagrams of the RC-filters in the Triton measured at RT and at 77 K, and cut-off frequency. The dashed line signals the loss of attenuation of the RC-filters, which will be compensated by the BP-filtering stage

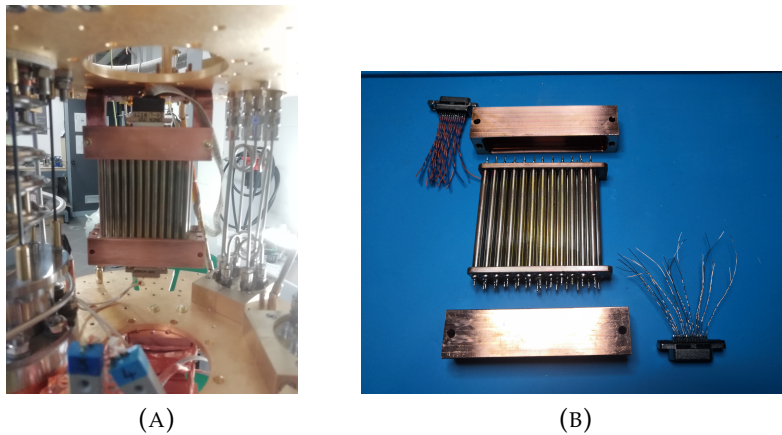


FIGURE 2.8: In (a): powder-filters for the DC-filtering in the Triton, thermalized on the cold-plate; in (b): view on the un-mounted powder filters

Finally, the characterization of JJs, and in particular of SFS JJs, requires the use of superconducting coils (in Fig. 2.9 (B) the coil of the Triton). In the Heliox, the sample holder is designed to allocate a niobium-titanium coil with a conversion factor 0.3 T/A, mechanically anchored to the ^3He -pot. In the Kelvinox and the Triton, instead, the coil is mechanically anchored to a copper ring centered on the sample stage by means of non-conducting stands (Fig. 2.9 (A)). In the Kelvinox, the stands are in graphite, while in the Triton we used SS and polyamide nylon. The conversion factor of the coil in the Triton and the Kelvinox is 0.1 T/A. Other details on the sample stage and mechanical anchoring of the coil are reported in App. A.

The coil-lines are in copper from the RT-plate to the 4K-plate, and superconducting (NbTi) from the 4K-plate down to the MC. They are thermalized at the 70K-plate, the 4K-plate and at the cold-plate (IAP), and otherwise covered by a fiberglass glove.

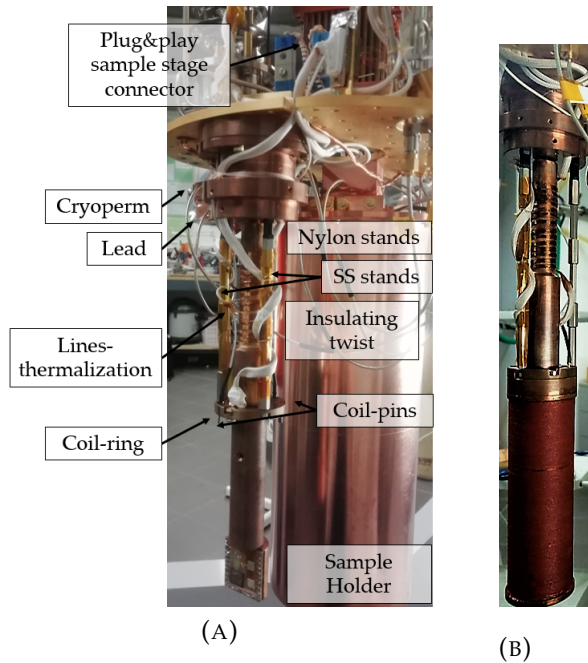


FIGURE 2.9: In (a): DC-sample stage in the Triton; in (b): superconducting coil

Finally, the coil must be thermally decoupled from the sample stage. In the Heliox and the Kelvinox this is achieved using a thermal insulating twist anchored at the 1K-Pot, so that it remains always at about 2 K during the measurements and additional Joule dissipation due to the current flow in the coil does not heat the sample stage. The presence of the main bath ensures a stable and reliable temperature for the coil stage. In the Triton, the best thermal anchoring point is the cold-plate stage, which has a higher cooling-power compared to the other low-temperature plates.

Other details on the DC setup, including the CADs of the parts and supports for the thermalization and a detailed discussion on the materials employed are depicted in App. A.

DC-measurements techniques

In this section, we will deal with the measurement techniques used for most of the characterization in a DC-environment of superconducting systems, including ferro-tunnel JJs reported in this thesis. As in most of the measurements on superconducting devices, the samples are current-biased. In Fig. 2.10, we show the schematics of the DC-measurement setup in the Triton, but we have almost the same scheme for the Kelvinox and the Heliox systems.

$I(V)$ measurements A voltage generator gives a triangular waveform with a peak-to-peak V_{pp} amplitude that falls on a variable shunt resistance R_{shunt} , so that the current flowing in the device is

$$I_{bias} = \frac{V_{pp}}{R_{shunt}}. \quad (2.1)$$

obtained using the following statistical laws:

$$\mu = \sum_i \frac{N(I_i)}{N_{\text{tot}}} I_i \quad (2.2)$$

$$\sigma^2 = \sum_i \frac{N(I_i)}{N_{\text{tot}}} (I_i - \mu)^2 \quad (2.3)$$

$$m_3 = \sum_i \frac{N(I_i)}{N_{\text{tot}}} (I_i - \mu)^3, \quad (2.4)$$

where N_{tot} is the total number of counts and I_i are the switching current values. The standard deviation σ and the skewness γ are calculated as:

$$\sigma = \sqrt{\sigma^2} \quad (2.5)$$

$$\gamma = \frac{m_3}{\sigma^3}. \quad (2.6)$$

The error on μ is the standard deviation σ , while the error on σ is obtained considering the propagation of the error

$$\Delta\sigma = \frac{1}{2\sigma} \sqrt{\sum_i \left((I_i - \mu)^2 \Delta N_i \right)^2}, \quad (2.7)$$

where ΔN_i is the Poisson error on the counts $\Delta N_i = \frac{\sqrt{N_i}}{N_{\text{tot}}}$.

Discussion on the errors

The complexity of the cryogenic systems, the presence of the filtering and amplification stages, electrical and thermal noise effects and the huge number of degrees of freedom in a DC-experiment on superconducting systems will unavoidably induce a maximum error on the measured quantities. The investigation of novel regimes often goes hand in hand with the need to measure currents (voltages) in the nanoampere (nanovolt) range, and in this case the noise may strongly affect the reliability of the experimental results.

It is therefore important to understand the capabilities of the experimental setup used for the measurements. Within this picture, we take here as a reference the $I(V)$ curve measured on a spin-filter JJ with a 4.0 nm thick GdN barrier (see Chap. 3 for further information on these structures). In presence of an external magnetic field, the critical current of the device is of the order of 1 nA. Also in the nanoampere regime, the Triton allows to measure both a clear switching current and a finite hysteresis in the $I(V)$ (Fig. 2.11). The SCD measured at base temperature for the same JJ is characterized by a standard deviation of the order of $5\% I_{\text{sw}}$, in line with other σ/I_c ratios measured on well-tested cryogenics setup [20, 24, 164, 165, 167, 199].

Also the modulation of the critical current in a magnetic field is clearly distinguished, despite the low-current regime: as an example, we show in Fig. 2.12 the Fraunhofer pattern modulation for a SIsFS JJ with a Py barrier

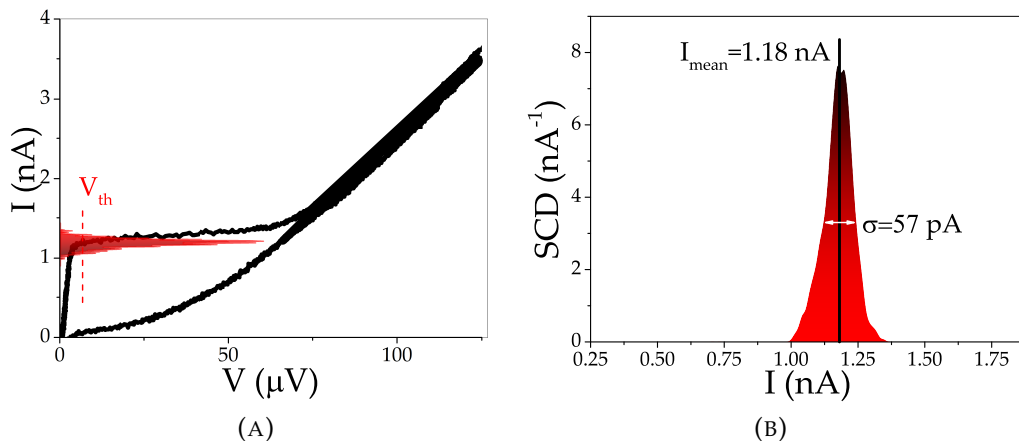


FIGURE 2.11: In (a): $I(V)$ characteristic of a spin-filter JJ with a 4.0 nm thick GdN barrier, reported here to discuss the performances of the Triton DC setup developed during this Ph.D. project, and SCD measured at the threshold V_{th} . In (b): focus on the SCD, mean switching current I_{mean} and standard deviation σ

measured at 7.5 K, at which the JJ has a $I_c \sim 50$ nA at zero field and secondary maxima of the order of some nanoamperes.

2.3.2 RF setup

The Triton is equipped with a pair of 6 input RF-lines (A and B), and 2 output lines (O) from *IntelliConnect* (Fig. 2.13). On the output lines there are no attenuation stages, while on the input lines we have three attenuators with the following nominal attenuations:

- at the 4K-Plate, 20 dB;
- at the IAP-plate, 10 dB;
- at the MC-plate, 20 dB.

Output lines are of Silver-plated Copper Nickel (SCN) and Copper Nickel (CN) from the RT-plate to the 4K-Plate, and of NbTi from the 4K-Plate to the MC-Plate. The input lines are in SS. Thermalization of the lines is guaranteed by brass bracelets on the top of each anchoring plate.

IntelliConnect RF-lines have been characterized by using a VNA from 10 MHz to 12 GHz at RT and at base-temperature. All the input lines have shown the same transmission parameter $S_{21} = S_{12}$ as reported for the line 1 of the group A in Fig. 2.14 (a) at RT, with an input signal power of 0 dB. Here we compare the S_{21} parameter at 300 K with the S_{21} parameter measured at 7 mK, at which the input line is closed on an empty output line with nominal 0 dB attenuation. At base temperature, the total attenuation of an input line closed on an empty output line ranges from ~ 60 dB – 72 dB in the frequency range 4 GHz – 9 GHz.

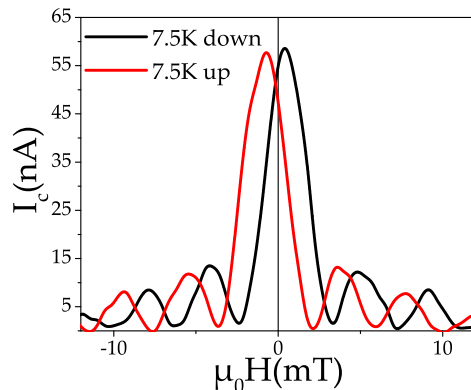


FIGURE 2.12: $I_c(H)$ pattern for a SISFS JJ with a Py barrier, reported here to discuss the performances of the Triton DC setup developed during this Ph.D. project. Red and black curves refer to the curves acquired ramping the field. The inverted magnetic hysteresis will be discussed in Sec. 4

One of the output lines is equipped with a series of two isolators from *Low Noise Factory*, thermally and mechanically anchored on the bottom of the MC, and encapsulated in a copper-tape to protect them from external spurious ElectroMagnetic (EM) signals (see the zoom of the yellow box in Fig. 2.13), and a High-Electron Mobility Transistor (HEMT) amplifier from *Low Noise Factory*, thermally and mechanically anchored on the 4K-Plate (green window in Fig. 2.13). The other output line is instead provided of a series of two circulators from *Low Noise Factory* and another HEMT amplifier. Finally, at RT we have additional amplifiers from *Mini-Circuits* with a nominal gain of 20 dB in the frequency-range ~ 0.500 GHz – 8 GHz.

MW isolators are electrical devices that are characterized by a uni-directional transfer function of the signal by means of a permanent magnetic field[200]. Their S -parameters at 300 K are reported in Fig. 2.15. As one can observe, the isolators suppress the S_{11} , S_{22} and S_{12} components of the RF-signal of ~ 20 dB, while S_{21} is attenuated by less than 5 dB. The nominal suppression of the circulators is the same as in the isolators.

HEMT amplifiers are typically used in MW experiments because of their large gain at high frequencies, and are based on field-effect transistors made with semiconductors [201]. *Low Noise Factory* amplifiers show optimal working from 4 GHz to 8 GHz at 4 K. The DC-bias of the amplifier is provided by a dedicated power supply *LNF-PS3b*, powered by a Low-Noise Power Block (LNPB), both from *Low Noise Factory*. The LNPB gives a constant DC-voltage of 12 V to the *LNF-PS3b*, while with the latter we can set the drain voltage V_d and the drain current I_d . The *LNF-PS3b* will concordly adjust the gate voltage V_g to reach the optimal working point. In Fig. 2.16 (a) and (c) we show the magnitude of the S_{21} parameter in the working-frequency range of the amplifier with the DC-bias turned off and on (black and blue curve, respectively) at 300 K, and at base-temperature. The measurements were performed using a VNA with an input signal of -10 dB, passing through one of the input and the output line of the setup. On the output lines, there are

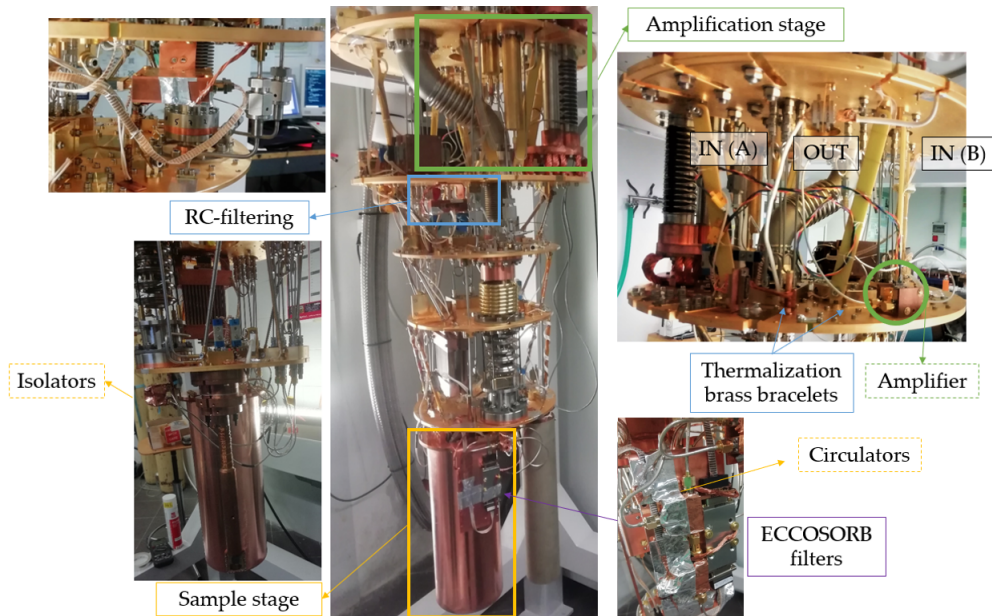


FIGURE 2.13: Scheme of the RF-lines systems in the Triton cryostat: flux-bias lines filtering, amplification stage and qubit measurement pack

also the two isolators in series. In Fig. 2.16 (b) and (d), instead, we report the gain curve of the amplifier, obtained subtracting the DC-off curve from the S_{21} parameter magnitude measured at room- and base-temperature, respectively. The measured amplification of 40 dB from ~ 4 GHz – 9 GHz is consistent with that reported in the data-sheets².

At the MC-plate, the input and output lines pass through a set of electromagnetic absorbers (*ECCOSORB*), which are specifically designed by National Physics Laboratory (NPL) in London, in collaboration with SeeQC-EU³ (Fig. 2.17 (B)). Such devices inhibit the reflection or transmission of electromagnetic radiation using dielectrics combined with metal plates spaced at prescribed intervals or wavelengths. In particular, they cut-off all the radiation with frequency far from the typical operation frequencies of superconducting qubits (~ 2 GHz – 7 GHz). In addition, the lines pass through band-pass RF-filters (working frequency band from ~ 0.250 GHz – 6 GHz), other attenuation stages if required, and enters in the measurement pack, designed and fabricated by NPL⁴ in collaboration with SeeQC-EU.

The chip holder is a mountable aluminum-based cavity with integrated RF Ardnnet connections and DC-ribbon cables, externally linked to flexible non-magnetic Teflon RF-coaxial cables and a NbTi DC-looms by *Oxford Instruments* for flux-bias lines (see the following for further information on DC-bias), respectively. It is enclosed in a tin screen with the internal walls covered with *ECCOSORB*, mechanically mounted on the MC by means of a copper support. The thermalization of the measurement pack is helped by means of a copper

²<https://www.lownoisefactory.com/>

³<https://seeqc.com/>

⁴<https://www.npl.co.uk/>

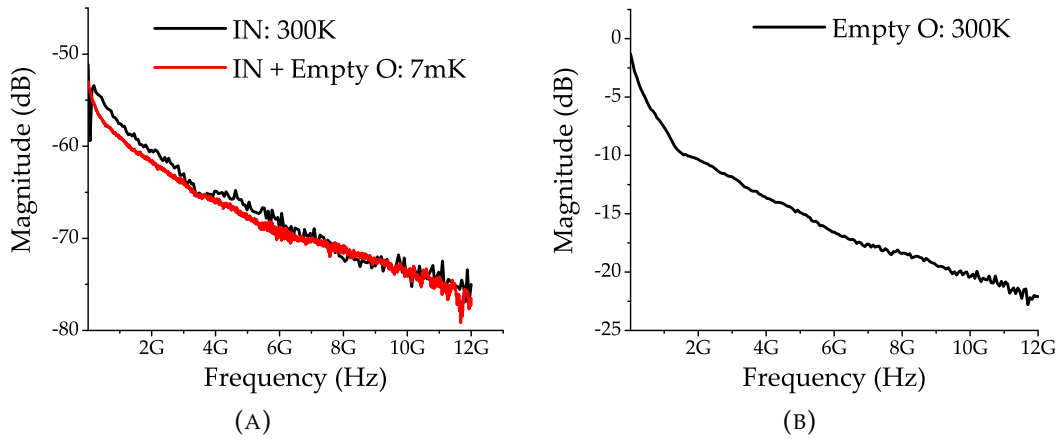


FIGURE 2.14: In (a): measured transmission S_{21} parameter at RT and base-temperature measured on an input line closed on an empty output line; in (b): measured transmission S_{21} parameter at RT of an empty output line

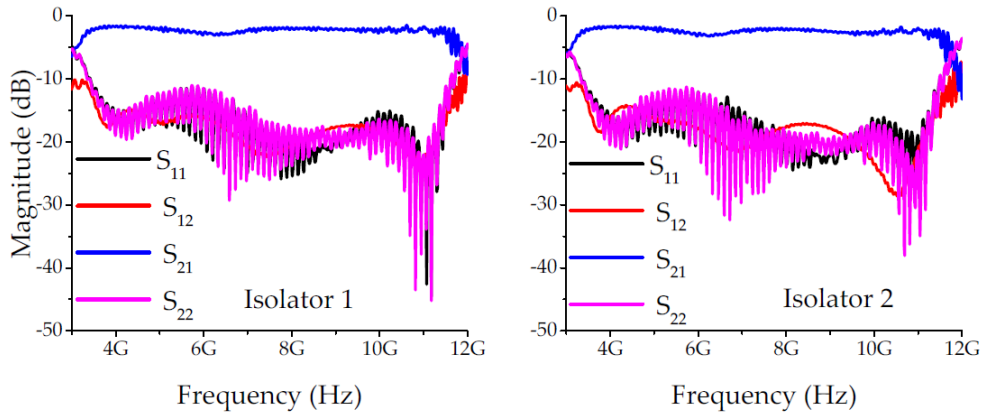


FIGURE 2.15: Measured S-parameters at 300 K of the isolators: transmission (S_{12} and S_{21}) and reflection (S_{11} and S_{22})

braid wrapped all around the support, and thermally anchored to the MC-plate. The measurement pack is finally enclosed in a cryoperm screen covered by copper to favor the thermalization and protect from external magnetic fields (see Fig. 2.17 (A) for the unshielded system).

The first set of DC-lines for what concerns the RF measurements is dedicated to the DC-bias (the ground, the drain current and the gate voltage connections) of the cryogenic amplifiers in the cryostat. These are home-made copper looms, thermally anchored at the 70K-plate and at the 4K-plate, with a vacuum-proof Fischer flange input at the top of the cryostat. An additional set of DC-lines is used for the flux-bias of qubit circuits, in the following configuration:

- from RT-plate to the 4K-Plate, 12 twisted flux-bias pairs are made of a copper-berillium loom with a Fischer to Cinch termination. Lines are thermalized at 77K-plate and on the 4K-plate.

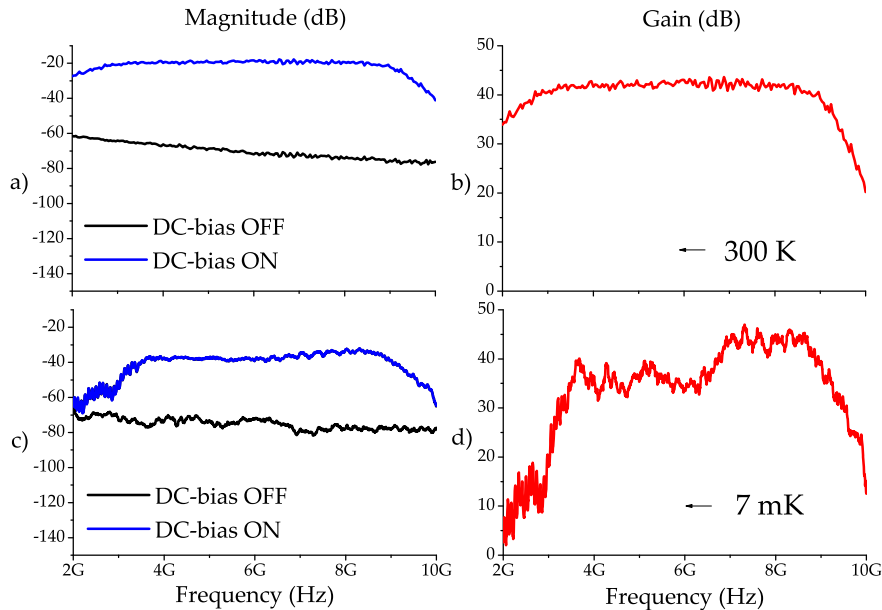


FIGURE 2.16: Measured transmission S_{21} -parameter at room- and base-temperature of the amplifier in the Triton: in a) and b) magnitude and gain of the signal at RT, respectively; in c) and d) magnitude and gain of the signal at base-temperature, respectively

- At the 4K-plate, flux-bias lines enter the first filtering stage, made of second-order RC-filters with a cut-off frequency of ~ 100 MHz at RT. In output, the lines are a NbTi DC-loom from *Oxford Instruments*.
- The flux-bias lines are thermalized on the still-plate, the IAP-plate, and they finally enter in the last filtering stage, mechanically and thermally anchored to the MC measurement pack. This stage is an ECCOSORB filter with a cut-off frequency of ~ 800 MHz.

The resistance of the flux-bias lines is of the order of $\sim 200 \Omega$ at RT and decreases to $\sim 20 \Omega$ at the base temperature.

The schematics of the RC-filters for flux-bias lines is reported in Fig. 2.19 (A), with the corresponding simulated Bode diagram with *QuCS Studio*⁵ (B). The measured Bode diagram is reported in Fig. 2.18, in which a cut-off frequency of 26 MHz is measured. Compared with the 100 MHz simulated, the resulting cut-off is far lower. However, this can be explained in the following way: the VNA used for the measurements has an impedance of 50Ω , which influences the cut-off frequency, and it was not considered in our AC simulations. As a proof of this statement, we show in Fig. 2.19 (D) the simulation obtained considering a MW source (circuit schematics in Fig. 2.19 (E)). The ECCOSORB filters Bode diagram, instead, is shown in Fig. 2.20: the cut-off frequency at -30 dB is 740 MHz.

RF-lines were tested from their mounting, and several measurements have been performed on conventional Al transmon circuits, both in the planar

⁵<http://dd6um.darc.de/QucsStudio/qucsstudio.html>

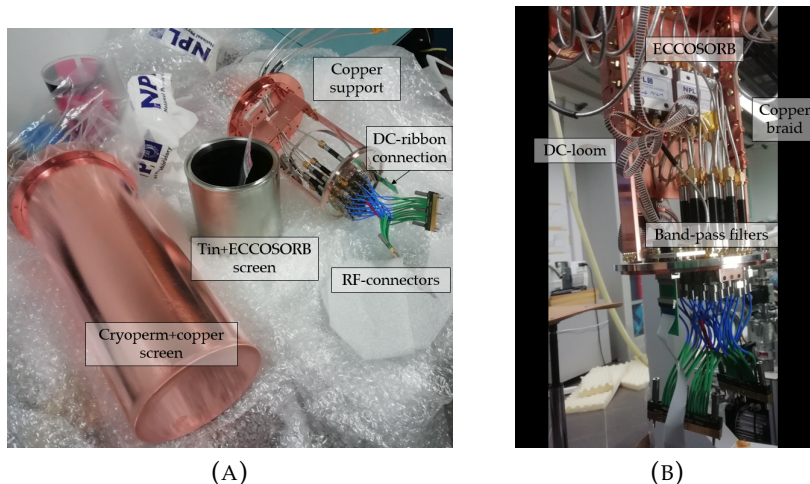


FIGURE 2.17: In (a): view of the unmounted qubit measurement pack by NPL and SeeQC-EU; in (b), inner view of the qubit measurement pack, thermalized at the MC

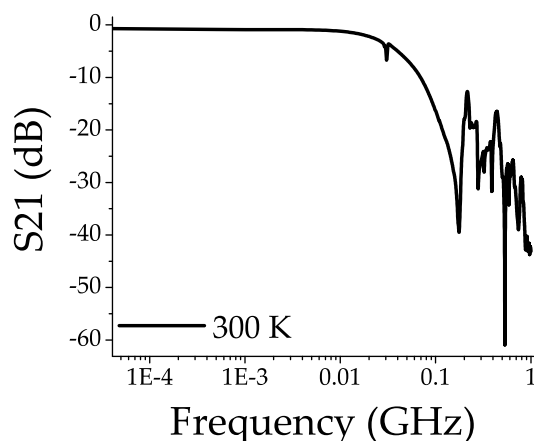


FIGURE 2.18: Measured Bode diagram with the VNA for the RC-filtering stage in the flux-bias lines

and **Multi-Chip Module (MCM)** configuration, in collaboration with SeeQC-EU [202, 203]. We here report the techniques for the characterization of qubits, used also to test the performances of our setup.

Resonator spectroscopy In a transmon, the qubit is embedded in a superconducting transmission line that opens up the possibility of **Quantum Non-Demolition (QND)** read-out of the qubit state by means of a MW spectroscopy of the resonator [147, 204], as discussed in App. C. The frequency spectrum of a resonator can be quickly and reliably inferred by using a VNA. This two-ports instrument allows to measure the scattering parameters, or S-parameters, of an electrical network, i. e. the reflection ($S_{11} - S_{22}$) and the transmission ($S_{12} - S_{21}$) of an electrical signal in the RF/MW regime, defined

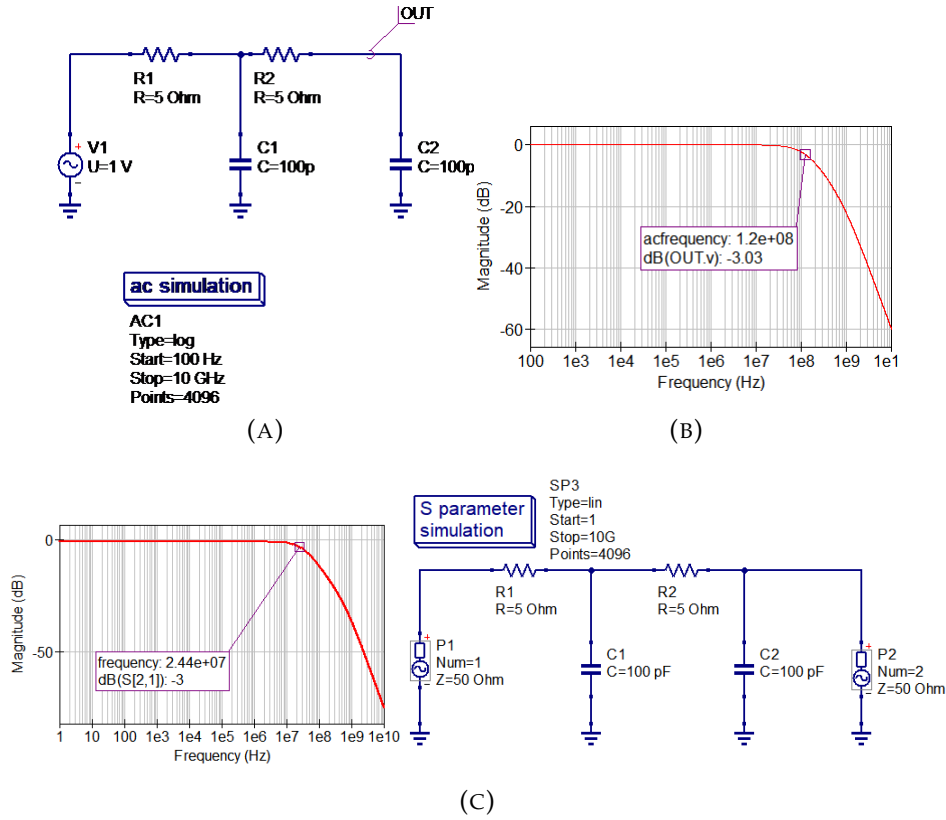


FIGURE 2.19: In (a): schematics of the RC-filters for the flux-bias lines; in (b) simulated Bode diagram with 120 MHz in AC; in (c) simulated Bode diagram considering explicitly the VNA and relative schematics

as

$$\begin{cases} S_{11} = \frac{V_1^-}{V_1^+} \\ S_{12} = \frac{V_2^-}{V_1^+} \\ S_{21} = \frac{V_1^-}{V_2^+} \\ S_{22} = \frac{V_2^-}{V_2^+} \end{cases} \quad (2.8)$$

Here, the pedix + (−) defines the incident (reflected) electromagnetic waves, respectively from port 1 or 2 (Fig. 2.22). Our setup allows for transmission experiments, but it can be extended to reflection measurements with opportune variations on the output line scheme. The EM signal recorded is complex, and the VNA can measure both the real and the imaginary parts in the form of a magnitude (in dB) and a phase. In general, it is necessary to set the frequency windows, by choosing or the center frequency and the span window, or the start and stop frequency. This kind of measurement is known as continuous wave, since the input signal is a continuous excitation of the resonator [204, 205]. However, in order to perform a time-domain characterization of the devices, the ability to generate pulsed tones is necessary (pulsed wave measurements) [204]. Limiting the excitation of the resonator in time allows for a

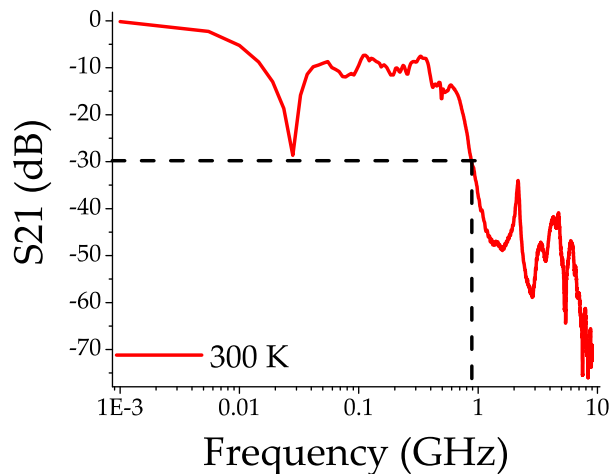


FIGURE 2.20: Measured Bode-diagram for the ECCOSORB filter on the flux-bias DC lines. The dashed lines highlights the frequency corresponding to an attenuation of -30 dB, required to suppress the loss in attenuation of the RC filtering stage

less noisy measurement [204, 206].

In Fig. 2.23, a schematic of the experimental setup employed for this type of measurement is shown. The input signal is a combination of a **Qubit Drive (QD)** and the **Read-Out (RO)** excitations. In the resonator spectroscopy, the **QD** is turned off, so that the input signal is given by the **RO** excitation only, eventually attenuated by means of fixed or variable attenuators.

The RF input signal is obtained by mixing a **Local Oscillator (LO)** (cards number 13 and 14 in Fig.2.21) and the in- (I) and quadrature- (Q) components of an **Arbitrary Waveform Generator (AWG)** (cards number 2 and 6 in Fig.2.21). The mixing stage is a module card designed and mounted by the SeeQC-EU (cards number 3 – 4 and 7 – 8 in Fig.2.21 and Fig. 2.24 (a)), which can be properly calibrated in order to minimize unwanted leakage signals, and allows for an optimal signal *up-conversion* (Fig. 2.25). In this process, the **AWG** signal oscillates with a frequency known as **IF**, order of magnitudes smaller than the typical frequencies of the **LO** and the resonator. The mixing between the **AWG** and the **LO** gives two separate RF frequencies, $\omega_{RF1} = \omega_{LO} - \omega_{IF} < \omega_{LO}$ and $\omega_{RF2} = \omega_{LO} + \omega_{IF} > \omega_{LO}$, as can be captured in Fig. 2.24 (b). IQ mixers, however, allows for single side-band modulation, i. e. one of the two sidebands can be suppressed with an opportune calibration. In Fig. 2.24 (b), we show the comparison between the **LO** signal and the output signal from the mixer before and after the calibration. The optimal power for the **RO** single side-band modulation was found to be 3 dB. For positive (negative) sideband modulation, we fix the **LO** frequency so that the total input signal frequency is given by $\omega_{RO} = \omega_{IF-RO} \pm \omega_{LO-RO}$.

The I and Q signals amplitude can be set by a Labber⁶ soft-panel between some millivolts and 1.5 V. The input power can be then changed both by making a sweep on the **AWG** channels amplitude, or by using the variable

⁶<https://www.keysight.com/it/en/products/software/application-sw/labber-software.html>

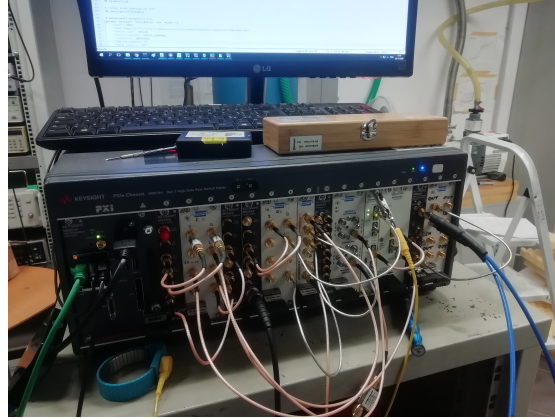


FIGURE 2.21: Keysight modular rack. From left to right, we have: an **Arbitrary Waveform Generator (AWG)** module with 4 channels, a home-made card for the up- and down-conversion of the **Read-Out (RO)** probe signal and reading, another 4-channel **AWG** module, a 4-channel digitizer, a home-made card for the **Qubit Drive (QD)**, a home-made card for adjustable attenuation, a **PXI CLK10** card module, a set of electrical switching, two **Local Oscillator (LO)** modules, a **VNA** and a home-made card with adjustable amplifiers

attenuators, governed by a Labber soft-panel between 0 dB – –31.75 dB (card number 9 in Fig.2.21). The **RO** pulse duration in this measurement is of the order of $20\ \mu\text{s}$ – $30\ \mu\text{s}$ so that the output signal can be acquired several times and averaged to obtain a low-noise measurement.

The output RF-signal, amplified at 4 K by the **HEMT** and at **RT**, is *down-converted* using the same **LO** of the input signal (Fig. 2.26). The output of the down-conversion in the **RO** mixing-stage is obtained using a 3-port mixer that takes the **LO** signal and the output complex RF-signal from the **Device Under Test (DUT)**, and converts it into the **IF** frequency signal. This down-converted signal is then acquired by the digitizer (card number 5 in Fig.2.21) for a time $t_{\text{acq}} = \frac{\#}{\nu_s}$, with # number of measurements and ν_s sampling rate of the digitizer, which is 500 MSample/s. The acquisition time length must be a compromise between a sufficient number of samples during the **RO** pulse and the need to remain inside the **RO** pulse signal. The aim is to avoid bad triggering and asynchronous acquisitions, while acquiring enough data points.

The demodulator in the digitizer finally performs a **Fast Fourier Transform (FFT)** of the time-signal acquired, giving as output a complex voltage signal. The magnitude and the phase (or the real and imaginary part of the signal) is calculated by a Labber soft-panel called *Multi-qubit pulse generator*, with which we can perform most of the spectroscopy and time-measurements in qubits.

Qubit spectroscopy The qubit spectroscopy aims at finding the spectrum location of the qubit transition frequency, corresponding to the transferring from state $|0\rangle$ to $|1\rangle$, or viceversa [204–206]. In presence of a MW drive, the

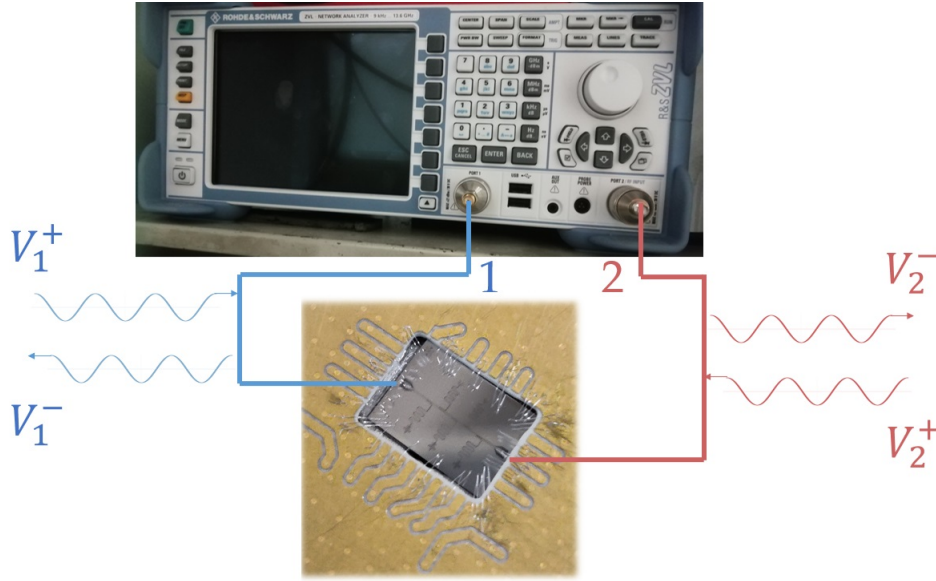


FIGURE 2.22: Scheme for the S-parameters definition. In the photo, a planar Al transmon circuit, courtesy of Dr. Marco Arzoo and SeeQC-EU

1/2-mapping of the qubit Hamiltonian reads as

$$\mathcal{H}_Q = -\hbar \frac{\omega_Q}{2} \sigma_z + \frac{C_d}{C_\Sigma^D} \sqrt{\frac{\hbar}{2Z}} V_D(t) \sigma_y, \quad (2.9)$$

where C_d is the capacitance that couples the qubit to the RT electronics, Z is the impedance of the circuit to the ground and C_Σ^D is the sum of the capacitance C_Σ of the qubit and C_d [204].

The standard procedure to study the role of the drive is to move into a frame rotating with the qubit frequency (**Rotating Wave Approximation (RWA)**), in which the drive Hamiltonian takes the form [204]

$$\mathcal{H}_d = \frac{C_d}{C_\Sigma^D} \sqrt{\frac{\hbar}{2Z}} V_D(t) (\cos(\omega_Q t) \sigma_y - \sin(\omega_Q t) \sigma_x), \quad (2.10)$$

with $V_D(t)$ the drive voltage,

$$V_D(t) = V_0 s(t) (\sin(\omega_d t) I - \sin(\omega_d t) Q). \quad (2.11)$$

The drive voltage is written in terms of a dimensionless envelope function $s(t)$, multiplied by the sum of an I- and a Q-component, oscillating with the drive-frequency ω_d . This picture is as close as possible to the experimental setup typically used in qubit measurements [204]. Performing the multiplication in \mathcal{H}_d , and using the **RWA**, the final drive Hamiltonian reads as

$$\mathcal{H}_d = \frac{C_d}{C_\Sigma^D} \sqrt{\frac{\hbar}{2Z}} \frac{V_0 s(t)}{2} (\sigma_x (Q \sin \delta \omega t - I \cos \delta \omega t) + \sigma_y (I \sin \delta \omega t - Q \cos \delta \omega t)), \quad (2.12)$$

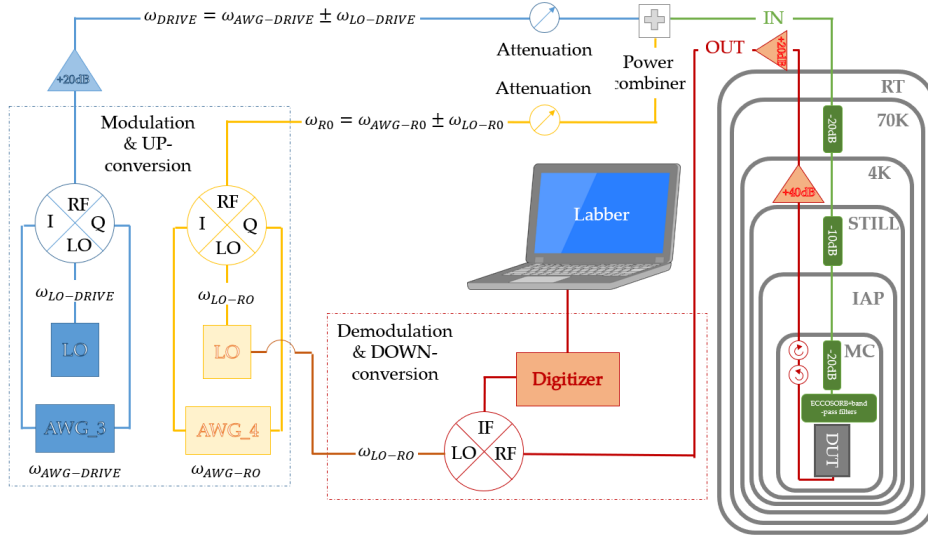


FIGURE 2.23: Setup scheme for pulsed RF-measurements

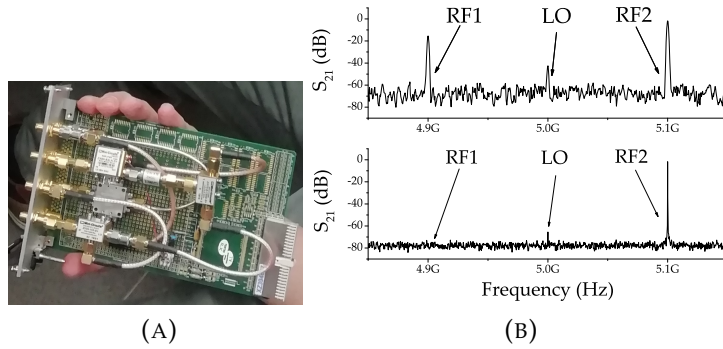


FIGURE 2.24: Mixer card for the RO (A) and example of a mixer calibration for the positive sideband modulation (LO frequency of 5 GHz and requested Intermediate-Frequency (IF) frequency of 100 MHz) (B)

with $\delta\omega = \omega_Q - \omega_d$. Applying a MW pulse at a frequency $\omega_d = \omega_Q$, i.e. $\delta\omega = 0$, the I-component induce rotations around the x -axis of the Bloch sphere; the Q-component, instead, corresponds to rotation around the y -axis [204]. The envelope function $s(t)$ for the QD pulse is a gaussian in our measurements.

In practical terms, we turn on the QD signal, fixing the resonator frequency near the dressed state (App. C.2.2) [204, 206]. As the drive tone is swept in frequency, we monitor the resonator RO signal [204, 206]. A peak (dip) in the transmitted signal states that the QD is matching the qubit frequency $f_{01,(10)} = f_d$. When the drive tone is off-resonance, the output signal is instead shunted to the ground [204, 206] (Fig.2.27).

This kind of measurement allows also for higher-order qubit transitions measurements [204]. The discrimination of spurious signals and higher-order transition is given by a QD power-sweep. Increasing the power of the QD, the peak associated with first-order transition will smear, and other

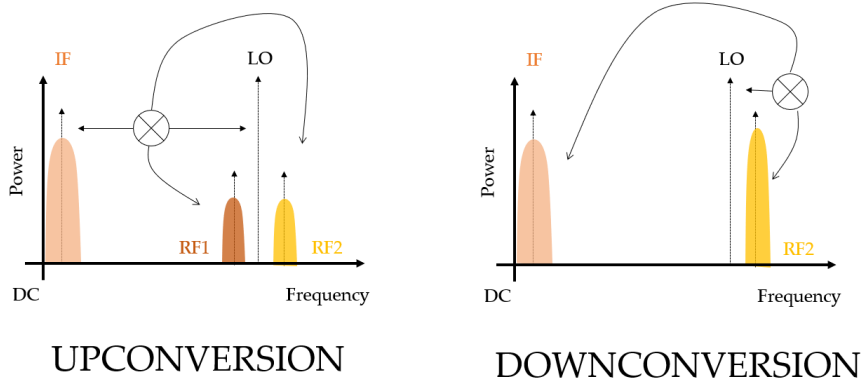


FIGURE 2.25: Schematics of the up- and down-conversion mechanisms

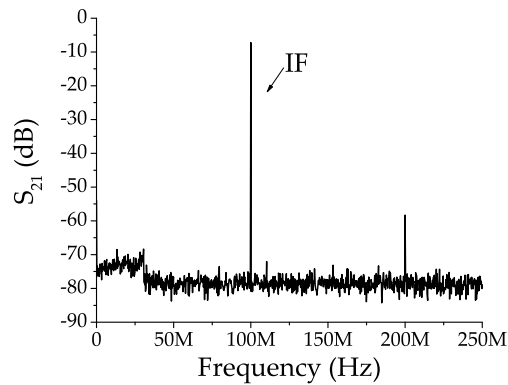


FIGURE 2.26: Down-converted output signal at the intermediate frequency related to input signal in Fig. 2.24 (B)

peaks at frequencies lower than f_{01} will appear [204] (Fig.2.27). Due to the negative anharmonicity of a transmon (App. C.2.1), in fact, the separation between the ground state and the first excited state is typically larger than the separation between the two first excited states [145, 204]. As occurs for the resonator spectroscopy, the qubit characterization in the frequency-domain can be performed not only in continuous- and pulsed-wave, but also in a hybrid wave [204]. In the continuous wave spectroscopy, we combine the **Continuous Wave (CW)** source of the **QD LO** with the input of the VNA, which will act as **RO** excitation. The VNA is not able to send a signal at a fixed frequency: we then set a frequency window around the fixed resonator frequency of some kilohertz, and we acquire only three points of the output signal in the same window. These values are then averaged with a PYTHON script, and plotted as a function of the **QD CW** source. In the pulsed wave spectroscopy, instead, both the **RO** and the **QD** are pulsed signals, and the following chains of pulses must be used:

- **QD** pulse;
- **RO** pulse, separated by the **QD** pulse by a certain delay, together with the digitalization of the output signal.

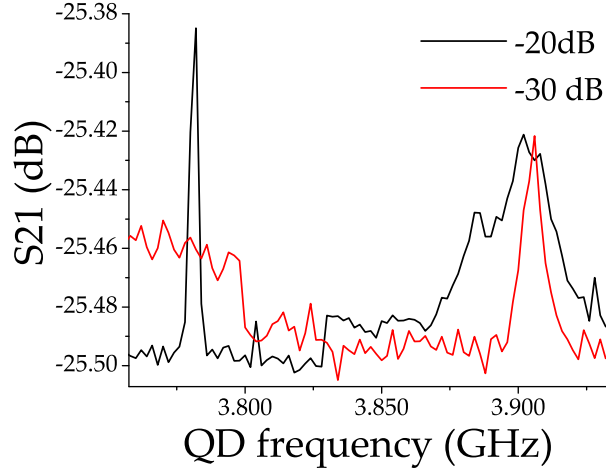


FIGURE 2.27: Qubit spectroscopy of an Al planar transmon qubit. In red, the spectroscopy at low power. In black, we increase the power of the QD signal, so that the peak corresponding to the transition between the first two-level states is smeared, and higher order transitions appear. This measurement has been done in a continuous wave configuration. S_{21} refers to the magnitude of the transmission signal

All the instruments modules in our setup are referenced via a 10 MHz signal, and synchronized by means of a specific clock card. Thus, a Labber software allows to both manually design the pulses sequence, or to use a software automated trigger. The principle is the following:

- the trigger gives the start of the sequence;
- the QD pulse will start at a delayed time t_d^{QD} with respect to the trigger;
- the RO pulse must start after the QD pulse, i. e. the delay with respect to the trigger is

$$t_d^{\text{RO}} = t_d^{\text{QD}} + \Delta t^{\text{QD}} + t_d, \quad (2.13)$$

where Δt^{QD} is the duration (plateau) of the QD pulse and t_d is an additional delay between the RO and the QD pulse;

- the digitizer must start with the RO, and it will acquire in a time window which must be inside the RO pulse time window.

The plateau of the RO pulse is in this measurement decreased to optimize the measurement time ($\sim 5 \mu\text{s}$), while the QD drive is typically one order of magnitude longer.

The hybrid wave spectroscopy, finally, uses pulsed RO signals and continuous QD drive, or viceversa. This measurement is typically noisier compared with the pulsed sequence, but gives a better Signal to Noise Ratio (SNR) with respect to the continuous wave spectroscopy. The advantage to use the continuous or the hybrid wave spectroscopy is in the fact that, due to the amount of radiation impinging the device, we can easily observe higher order transitions.

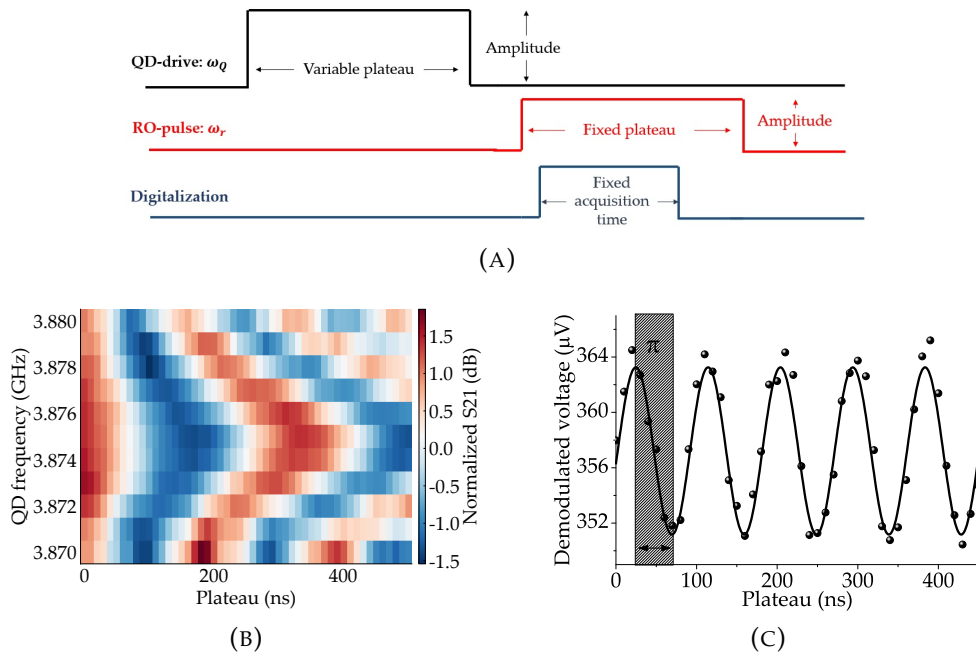


FIGURE 2.28: In (A): sequence for the Rabi oscillation measurement in the time-domain; in (B): example of a chevron plot on a reference Al transmon sample. In (c): Rabi oscillations and definition of the π -pulse

Time-domain measurements Characterizing quantum states in a time-resolved manner is an important prerequisite for the study of fundamental quantum mechanics [205, 207–209].

The first experiment in the time-domain is the measurement of the Rabi oscillations [204–206, 210, 211], thanks to which we are able to determine the π -pulse, i. e. the duration of the QD pulse necessary to take the qubit from its fundamental state to the excited state. We first fix the frequency of the qubit to the peak in the spectroscopy measurement [204, 206, 210, 211]; then we send a QD pulse with variable duration. After each QD pulse, the RO sequence starts. In this step, we may perform a sweep changing the QD frequency. The result is the chevron plot in Fig. 2.28, which allows to determine the shortest, hence the optimal, π -pulse for the preparation of the qubit [205, 206, 210, 211]. This step is fundamental for the measurement of the relaxation and coherence times. In order to increase the SNR, another refinement can be obtained changing the RO frequency and power.

In order to measure the relaxation time of a qubit (Chap. 4), we use the sequence in Fig. 2.29 (A): we first prepare the qubit in its excited state, sending the π -pulse calibrated with the Rabi oscillations measurement [205, 206]. The RO resonator response is first read immediately as the qubit has rotated in the excited state, and then the measurement is repeated changing the delay between the preparation of the qubit in the excited state and the acquisition (sequence duration). The longer is the sequence duration, the higher is the probability to decay to the fundamental state. As a consequence, an exponential decay is observed in the demodulated voltage measured as a function of the delay or the sequence duration (Fig. 2.29 (B)).

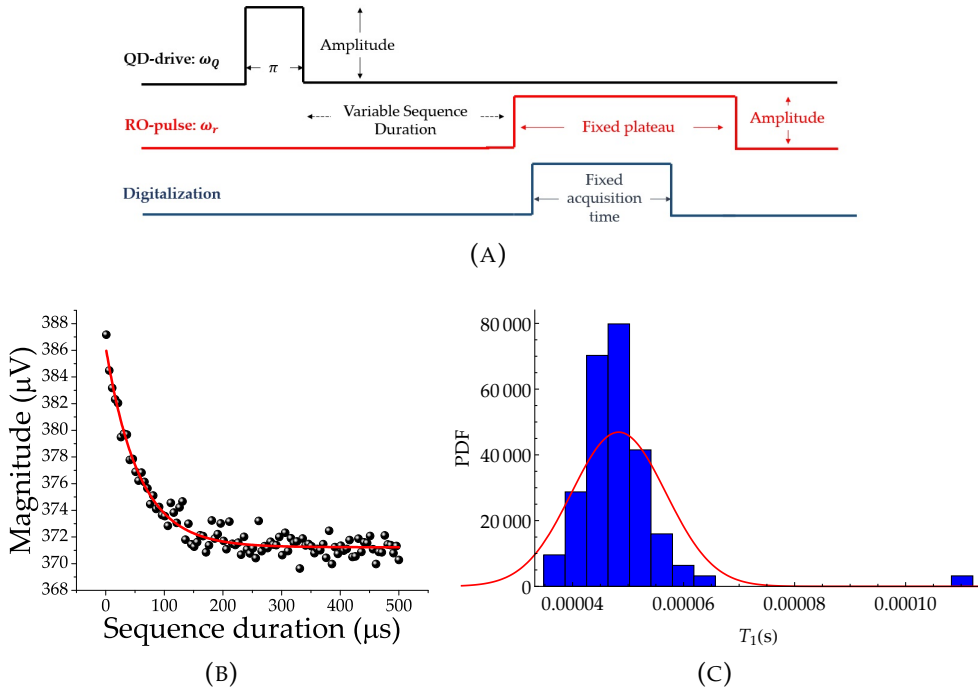


FIGURE 2.29: In (A): T_1 measurement scheme; in (B) measured exponential decay fit of the demodulated signal magnitude; in (C): T_1 statistics over 100 counts and gaussian fit with skewness $\gamma = 0$. The relaxation time measured for our reference planar transmon circuit is $48 \pm 8 \mu\text{s}$

The relaxation time measurement is a first indication of the performances of both the qubit and the experimental setup. A statistics on T_1 on a Al-based transmon circuit in a planar configuration gave a mean relaxation time $T_1 = 48 \pm 9 \mu\text{s}$, which is consistent with other transmon circuits relaxation times typically reported in literature [147, 204, 212] (Fig. 2.29 (C)).

Another fundamental time-domain measurement is the dephasing T_2^* measurement, exploited using the Ramsey sequence in Fig. 2.30. In this case, we first prepare the qubit in the equatorial plane sending a $\pi/2$ -pulse. Then, we wait a certain amount of time before another $\pi/2$ -pulse is used to bring the qubit in the ground state. The RO is performed soon after the last $\pi/2$ -pulse [206] (Fig. 2.30 (A)) [205]. This sequence is also generally referred to as Carr-Purcell (CP)/Carr-Purcell-Melbourn-Gill (CPMG) sequence [213], which is characterized by a chain of $\pi/2$ -pulses separated by a certain delay (sequence duration) [213]. Changing the delay between the two $\pi/2$ -pulses, we observe oscillations in the demodulated voltage that decay in time with a characteristic time T_2^* (Fig. 2.30 (B)). These oscillations reduce to a pure exponential decay if the QD frequency is in resonance with the qubit frequency. For this sample, T_2^* is $41 \pm 19 \mu\text{s}$.

The CP/CPMG sequence is finally interrupted by one or more π -pulses in spin-echo sequence [206, 213–215]. Here, the qubit is first projected on the equatorial plane, then rotates with an angle π , and it is finally excited (Fig. 2.31 (A)). This approach allows for controlling the motion on the equatorial plane linked to dephasing due to noise at high frequencies, and allows for a direct

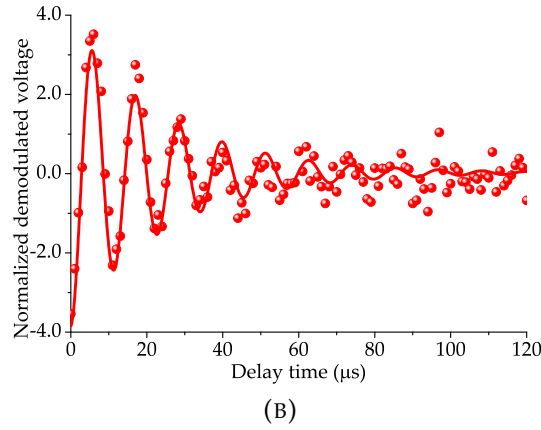
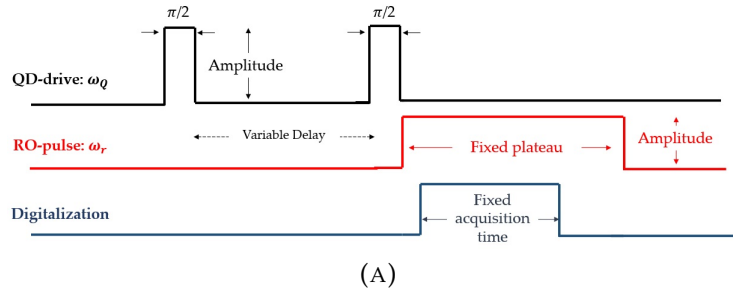


FIGURE 2.30: In (A): Ramsey measurement scheme; in (B) measured exponential cosinusoidal convolution of the demodulated signal magnitude

measurement of the decay rate due to decoherence T_2 [215]. In Fig. 2.31 (B), we show the characteristic exponential decay obtained using a spin-Echo sequence on the Al-based transmon qubit in a planar configuration taken here as a reference. The time T_2 estimated from the fit is $81 \mu\text{s}$, which is approximately $2T_1$. The coherence time T_2 tends to $2T_1$ for $T_\varphi \rightarrow \infty$. Here, we can say with good approximation that the dephasing time is much longer than T_1 . This is an additional demonstration of the good performances of our setup, since dephasing source may be related to thermal and electric noise in the experimental setup.

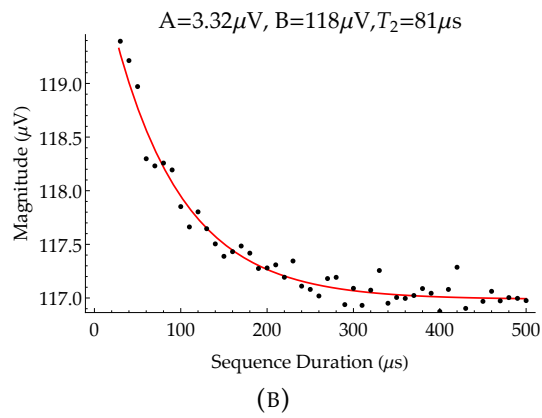
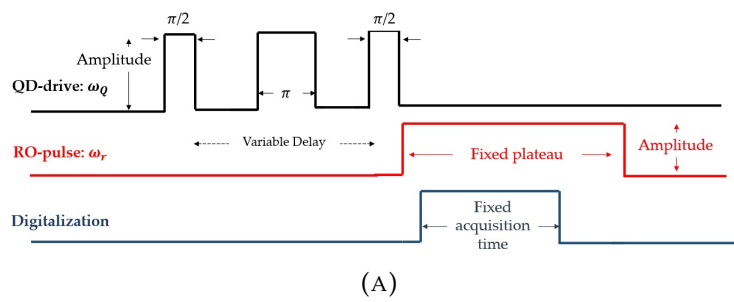


FIGURE 2.31: In (A): spin-echo measurement scheme; in (B) example of a T_2 measurements with a spin-echo sequence and relative decay fit $V(t) = Ae^{-t/T_2} + B$

Transport properties in spin-filter Josephson junctions: a protocol to demonstrate spin-triplet correlations

Gadolinium nitride (GdN) barriers sandwiched between two niobium nitride (NbN) electrodes are one of the very few examples available in literature of a junction with an insulating ferromagnetic I_f barrier. This means that the barrier is at the same time insulating, thus supporting tunneling transport, and ferromagnetic.

Some of NbN-GdN-NbN JJs properties have already been studied at the Materials Science and Metallurgy Department of the University of Cambridge, in Refs.[21, 24, 183, 185, 189], as reported in Sec. 1.3.1. The Cambridge group has given remarkable contributions in the field of SFS JJs[13, 190, 216–218], and has realized, and still realizes, different types of ferromagnetic barriers. Among these, GdN barriers have attracted our attention since the beginning, because of their undamped nature, and the possibility to study their phase dynamics at the lowest temperatures.

It was also theoretically and experimentally demonstrated that such devices are an ideal platform for the study of spin-triplet superconductivity [11, 12, 15, 16]. I will present a comparative characterization of spin-polarization and magnetic phenomena in SI_fS JJs, as a function of both the barrier thickness and the temperature. The investigation at the lowest temperatures gives evidence of unconventional behaviors of the Josephson properties, which progressively change as a function of the barrier thickness. The complex nature of the junctions requires a more elaborate microscopic modeling taking into account various features and interplaying physical effects. Fitting of $I_c(T)$ as a function of the barrier thickness through this model allows to quantify

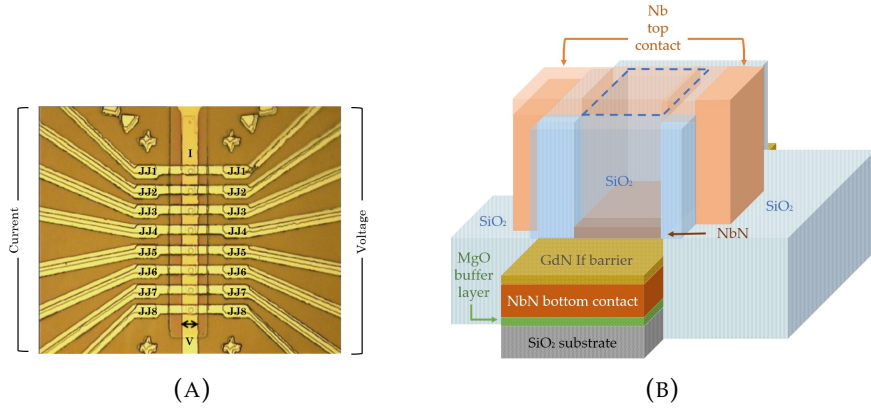


FIGURE 3.1: In (a): front view of the samples chip with fixed GdN thickness; in (b): transverse sketch of a single JJ[23]

the spin-triplet component *a posteriori*, more relevant for thicker barriers, providing a robust self-consistent criterion to evaluate spin-triplet correlations, reinforcing previous achievements.

3.1 Samples scheme

The ordered magnetism of GdN strictly depends on its stoichiometry, impurities and lattice defects [219]. As a consequence, fundamental magnetic parameters of the barrier, such as the saturation magnetization M_s and the coercive field H_c , can be changed proportionally to the content of nitrogen N[220]. At the same time, internal strain and pressure can cause an increase of the lattice parameter of the GdN layer [219], with the remarkable consequence of a reduction of the Curie temperature $T_{\text{Curie}} \sim 70$ K in a bulk [221] to nearly 30 K in a GdN film [219]. This is one of the motivations for which this material is suitable for practical implementations of a JJ inside a superconducting circuit: for certain operations, it might be required to demagnetized the ferromagnet increasing T above T_{Curie} . Hence, low and accessible T_{Curie} values are of great practical importance.

According to the strong dependence on fundamental fabrication parameters and conditions, Senapati et al. proposed that different nitrogen concentration might affect not only the magnetic properties of the barrier, but also the transport properties of the GdN[183]. The **Density Functional Theory (DFT)** predicts that in a GdN barrier a transition from a semiconductor or an insulator in the paramagnetic phase to a semimetal or a half-metal in the ferromagnetic phase might occur [222]. Experimentally, it is not easy to distinguish between all these phases, but the overall behavior of the Josephson transport in NbN-GdN-NbN JJs points towards a pure tunnel barrier [21, 23, 24, 183, 185, 189, 223].

The junctions were fabricated at the Materials Science and Metallurgy Department of the University of Cambridge (UK) by optical lithography from trilayer of NbN-GdN-NbN films prepared by DC reactive magnetron

TABLE 3.1: Measured parameters of spin-filter JJs with GdN thickness t : maximum resistance measured from the $R(T)$ curve and critical current I_c at 300 mK and at 4.2 K. The error on the resistance is of the order 4%, while on I_c is 1%

t (nm)	R_{\max} (Ω)	I_c (300 mK) (μA)	I_c (4.2 K) (μA)
1.5	5.77	704	—
1.8	8.55	203	194
2.0	7.54	258	208
2.5	13.5	40.1	—
3.0	52	4.73	2.73
3.5	261	$618 \cdot 10^{-3}$	$315 \cdot 10^{-3}$
4.0	2000	$25.8 \cdot 10^{-3}$	$15.1 \cdot 10^{-3}$

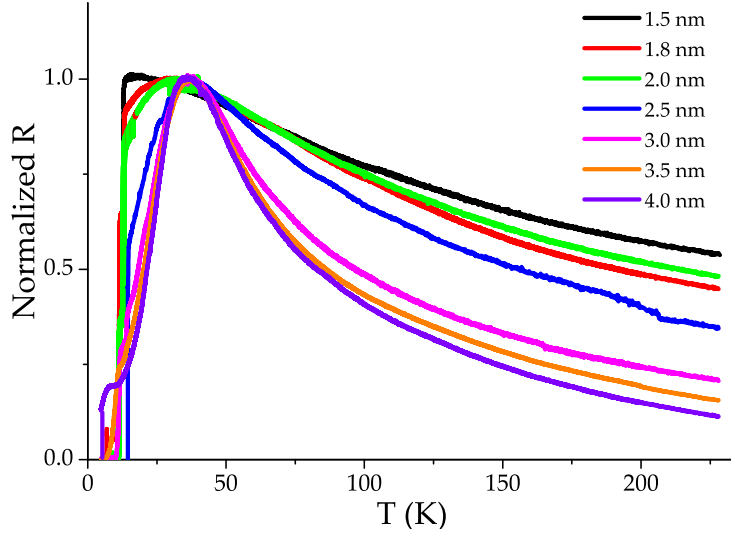


FIGURE 3.2: Normalized resistance R/R_{\max} as a function of the temperature T for different GdN thickness barriers. R_{\max} is reported in Tab. 3.1

sputtering at RT according to methods reported in Refs.[24, 184, 185, 189]. We have investigated six samples with different GdN barrier thicknesses, reported in Tab. 3.1. The junction area, in a square geometry, was defined by selective reactive etching of the top 100 nm NbN layer in CF_4 plasma. A layer of sputtered SiO_x was patterned using lift-off method to provide an electrically isolated contact window on top of $7 \times 7 \mu\text{m}^2$ junctions. In Fig. 3.1, we show the microscope picture of the chip with its bonding scheme and a sketch of the JJ.

On the same NbN-GdN-NbN sandwich there are eight junctions nominally equivalent, providing the possibility to perform a statistical study on the same fabrication run. The transport properties of the devices reported in this work are quite reproducible, thus implying that the unconventional behavior observed in these devices is strictly correlated to their specific properties.

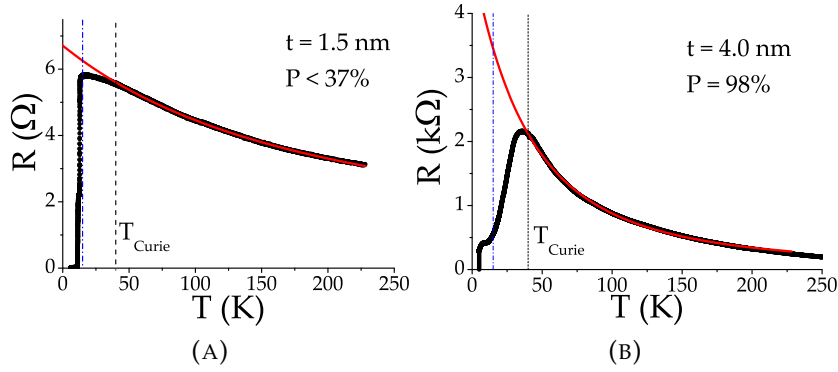


FIGURE 3.3: $R(T)$ semiconducting fit (Eq. 3.3) on spin-filter JJs in the extreme cases of thin and thick GdN barriers. The dashed line indicates the Curie temperature T_{Curie} , while the blue dotted-dashed line is the temperature at which we estimated the spin-filtering efficiency P [23]

3.2 Spin-dependent transport properties

NbN-GdN-NbN JJs are generally referred as spin-filter JJs, because of spin-polarization phenomena, as already discussed in Sec. 1.3.1. Experimentally, spin-dependent tunneling mechanisms affect both the resistance R for $T > T_c$ [183] and the critical current I_c [183, 223]. Indicative information on the spin-filtering effect can be obtained by analyzing the temperature dependence of the tunnel resistance $R(T)$ across the spin-filter JJ, using the method first formulated by Senapati et al.[183], or by characterizing the critical current I_c suppression in the $I(V)$ curves [223]. The two methods give consistent results, and allow for a complete study in temperature of the spin-filtering effect.

3.2.1 $R(T)$ curves

In Fig. 3.2, we report the measured $R(T)$ curves for all the junctions by using the Heliox system (Sec. 2.1), according to the procedures reported in Sec. 2.3.1. The curves have been normalized to the maximum measured resistance value in Tab. 3.1, in order to make a comparison between samples with resistances falling in quite different ranges. For all samples, the $R(T)$ curves exhibit a typical semiconducting behavior up to $T_{\text{Curie}} = 40$ K. The superconducting transition temperature is of about $T_c = 12$ K. We also observed that for $T_c < T < T_{\text{Curie}}$ the resistance decreases, and that this decrease is steeper the thicker the interlayer is (Fig. 3.2). This is directly related to the fact that, once the GdN becomes ferromagnetic, one of the two spin channels must overcome a smaller energy barrier height compared with the one seen at temperatures higher than T_{Curie} and the one seen by the other spin channel, thus it is favored in the conduction (Fig. 1.18)[183].

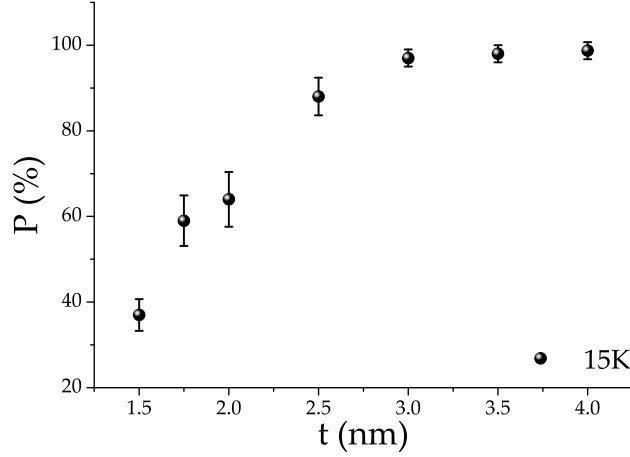


FIGURE 3.4: Spin-filtering efficiency P vs. barrier thickness t estimated from the $R(T)$ curves at 15 K. The error bars are related to the measurement technique

A first estimation of the spin-filtering efficiency P can be expressed in terms of the up (down) spin conductances $\sigma_{\uparrow(\downarrow)}$ [183]

$$P = \left| \frac{\sigma_{\uparrow} - \sigma_{\downarrow}}{\sigma_{\uparrow} + \sigma_{\downarrow}} \right|. \quad (3.1)$$

Using formulas in Eqs. 1.19 and 1.20 in Chap. 1 and an expansion in Taylor series for $h \ll E_0$ in Eq. 3.1, P can be written as

$$P \sim \tanh \left(\cosh^{-1} \left(\frac{R^*}{R} \right) \right), \quad (3.2)$$

where R^* is the resistance that the junction would have in absence of spin-polarization and R is the measured resistance. R^* has been estimated by fitting the experimental $R(T)$ curves above T_{Curie} with the function [195]

$$R(T) = A e^{\frac{B}{T+T_0}}. \quad (3.3)$$

Here, A is associated with the resistance at high temperatures and B is linked to the GdN energy gap E_0 in its paramagnetic phase. In Fig. 3.3 we show as an example the experimental fit for the JJs in the extreme cases of GdN thickness 1.5 nm and 4.0 nm, which gives an energy barrier $E_0 \sim 0.2$ meV. The spin-filtering efficiency has been calculated at an intermediate temperature between T_{Curie} and T_c , i. e. 15 K, with the formula in Eq. 3.2 for all the junctions (Fig. 3.4).

3.2.2 $I(V)$ curves

Spin-polarization phenomena in spin-filter JJs are also responsible for the suppression of the critical current I_c observed in the experimental $I(V)$ curves. In

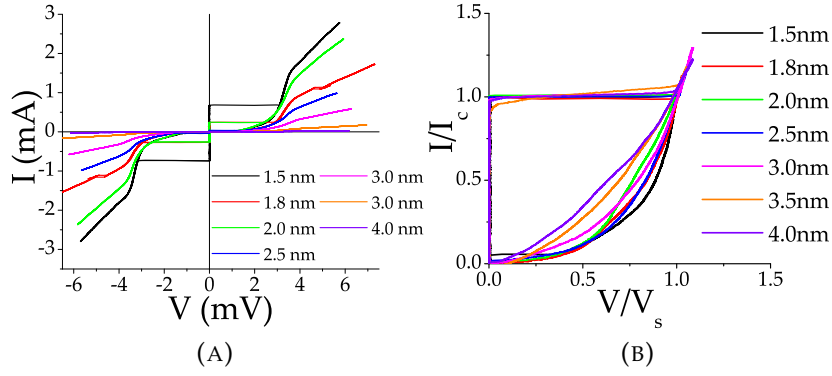


FIGURE 3.5: In (a): $I(V)$ curves up to the gap voltage V_g in spin-filter JJs with different GdN thicknesses at 300 mK. In (b): normalized $I(V)$ curves in the subgap branch in spin-filter JJs with different GdN thicknesses at 300 mK. I is normalized to I_c at 300 mK in Tab. 3.1, while the voltage is normalized to the switching voltage V_s [21]

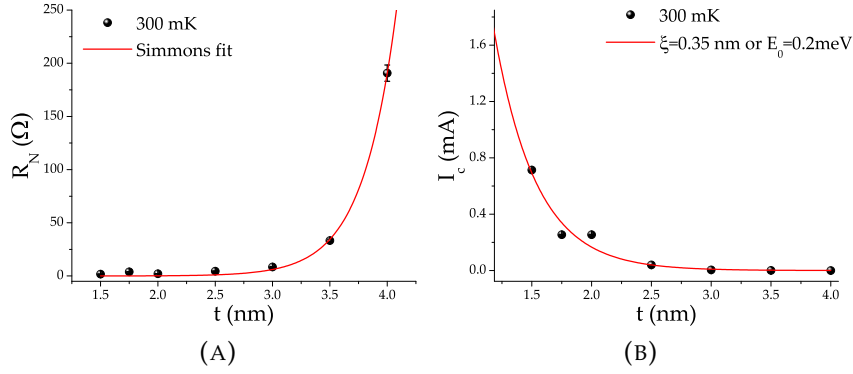


FIGURE 3.6: In (a): normal resistance R_N as a function of the thickness t , and Simmons model fitting (red straight line). In (b): $I_c(t)$ and exponential fit. The error on I_c is 1% and on R_N is 3%

Ref.[223], we have established a direct correlation between such suppression and the spin-filtering effect.

Suppression of the supercurrent in a non-magnetic JJ has been firstly addressed by Kulik [150]. As anticipated in Sec. 1.3.1, the Cooper pair tunneling current can be suppressed because of the presence of paramagnetic impurities in the insulating barrier, Spin Orbit Coupling (SOC) phenomena, or because of the formation of thin normal layers at the surface of the superconducting electrodes [150, 151]. In the tunneling Hamiltonian proposed by Kulik [150] describing tunneling processes in which the spin directions of the electrons are both preserved or flipped, the I_c can be suppressed by a factor α

$$\alpha = \frac{|T_s^2 - T_n^2|}{T_s^2 + T_n^2}. \quad (3.4)$$

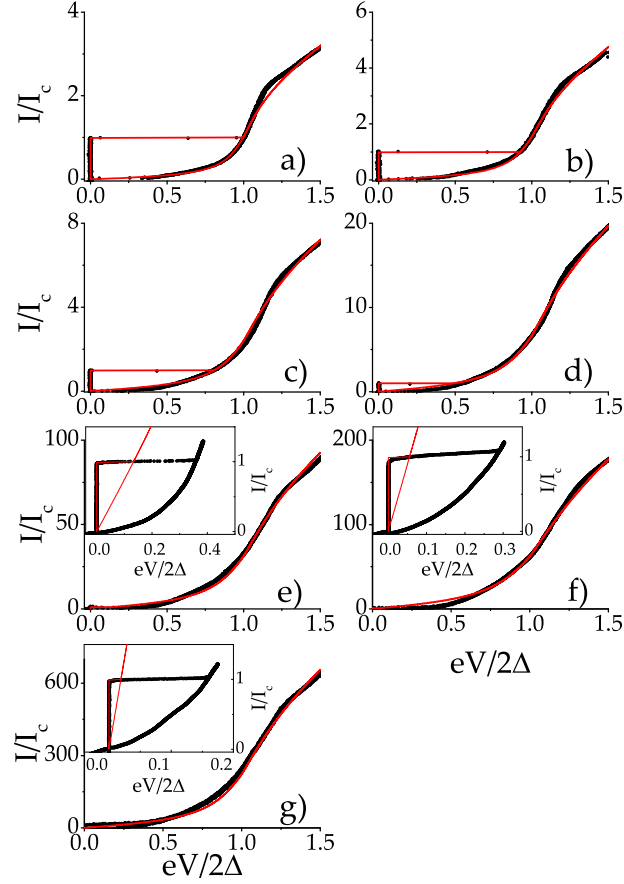


FIGURE 3.7: Comparison between the experimental $I(V)$ curves at 300 mK (black points) and the TJM simulations for GdN thicknesses: (a) 1.5 nm, (b) 1.8 nm, (c) 2.0 nm, (d) 2.5 nm, (e) 3.0 nm, (f) 3.5 nm, (g) 4.0 nm[223]. In the insets, focus on the subgap branch of the $I(V)$ curves

Here, T_s^2 and T_n^2 are the tunneling probabilities for the electrons with spin direction preserved and flipped, respectively. In spin-filter JJs, the spin-filtering efficiency P and the exchange field h are explicitly taken into account in the tunneling Hamiltonian proposed by Bergeret et al. in Ref.[188], by means of a spin-dependent \mathcal{U} and spin-independent \mathcal{T} tunneling matrices elements [188]. The tunneling amplitudes are then given by $T_{\uparrow(\downarrow)} = \mathcal{T} \pm \mathcal{U}$, and the I_c suppression parameter r is defined as

$$r = \frac{T_{\uparrow} - T_{\downarrow}}{T_{\uparrow} + T_{\downarrow}}, \quad (3.5)$$

i. e. considering Eq. 3.1,

$$r = \sqrt{1 - P^2}. \quad (3.6)$$

In Ref.[223], we demonstrate that a modeling of the JJs in terms on Tunnel Junction Microscopic (TJM) model [26, 48, 140, 224] allows to reproduce the scaling of the I_c suppression parameter α as a function of the barrier thickness.

TABLE 3.2: Simulation parameters used to fit the experimental $I(V)$ curves at 0.3 K and at 4.2 K for spin-filter JJs with GdN thickness t : the suppression parameter α and the smearing factor δ [23]

t (nm)	α (0.3 K)	α (4.2 K)	δ (0.3 K)	δ (4.2 K)
1.5	0.51	-	0.12	-
1.8	0.34	0.34	0.14	0.16
2.0	0.22	0.19	0.18	0.18
2.5	0.080	-	0.20	-
3.0	0.017	0.011	0.20	0.20
3.5	0.0087	0.0048	0.25	0.28
4.0	0.0024	0.0015	0.26	0.20

The obtained values of α are consistent with the r -factor predicted by Bergeret et al.[188].

A comparison of the $I(V)$ curves at 300 mK measured in the Heliox system for different barrier thickness is reported in Fig. 3.5. The tunnel transport in spin-filter JJs can be depicted by both the shape of the subgap branch in the $I(V)$ curves, the exponential dependence on the barrier thickness of the normal state resistance R_N and the critical current I_c in Fig. 3.6. R_N is calculated with a linear fit above the gap voltage V_g , while I_c is extracted from the $I(V)$ curves at a voltage value far from the noise detected in the supercurrent branch. According to J.G. Simmons [225], the exponential dependence of R_N is related to the current flow through the barrier by means of tunnel effect,

$$R_N(t) = \frac{2t}{3\sqrt{2m^*\bar{E}}} \left(\frac{\hbar}{e}\right)^2 e^{\frac{2t}{\hbar}\sqrt{2m^*\bar{E}}}, \quad (3.7)$$

where m^* is the effective mass of the carriers and \bar{E} is the mean energy barrier height. Using the **Wentzel-Kramers-Brillouin (WKB)** approximation for the tunneling current in a JJ, we successfully find the energy barrier \bar{E} to be consistent with the results obtained from the $R(T)$ semiconducting fitting, the $I_c(t)$ and the $R_N(t)$ tunnel fit.

In Fig. 3.7, we report the experimental $I(V)$ curves at 300 mK in normalized units (the current is normalized to I_c in Tab. 3.1 and the voltage to V_g) and the TJM simulations obtained using a MITMOJCO C-Code following the procedures in App. B. The V_g is the same for all the JJs and it is related to the BCS energy gap of NbN electrodes of the order of 1.75 meV.

TJM simulations reproduce quite well the behavior of the $I(V)$ curves. Deviations can be seen close to the retrapping branch in the highly spin-polarized regime ($t > 3.0$ nm), as shown in insets of Fig. 3.7 (e), (f) and (g). In this regime of large I_c suppression, the switching voltage V_s strongly depends on the subgap branch shape, which shows a smoother dependence on V compared with standard SIS JJs[21, 183].

The same analysis has been repeated at 4.2 K, as reported in Tab. 3.2. The fitted α at 0.3 K and 4.2 K fall within the error bars (Fig. 3.8). The suppression

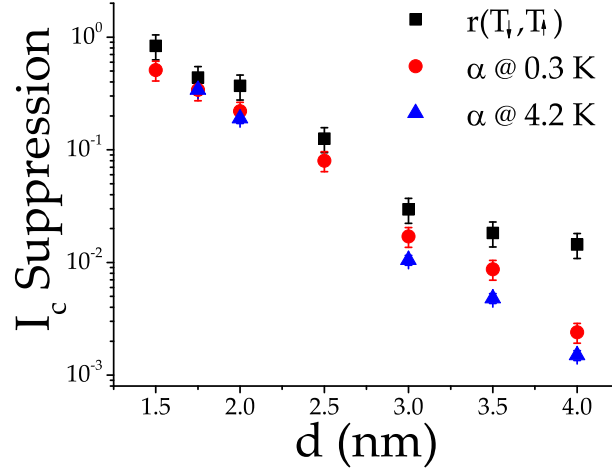


FIGURE 3.8: Comparison between the spin-polarization factor r calculated using transparencies in Ref.[21] and the suppression parameter α estimated by fitting the $I(V)$ curves at 300 mK and 4.2 K of spin-filter JJs within the TJM model, as a function of the GdN barrier thickness. The errors on r are of the order of 30%, while the errors on α are of the order of 20% [223]

parameter α decreases with increasing the thickness t of the GdN barrier, so as the spin-polarization factor r (Fig. 3.8). r is calculated using the values of transparencies $t_{\uparrow(\downarrow)} \propto T_{\uparrow(\downarrow)}$ reported in Ref.[21] for the same sample batch, and in Tab. 3.3. Details on the estimation of $t_{\uparrow(\downarrow)}$ by the phenomenological fit of the $I_c(T)$ curves in spin-filter JJs are also discussed in Sec. 3.4.1. The good quantitative agreement between α and r ensures that the I_c suppression is consistent with selective spin-polarization phenomena. This is also confirmed by the role of the magnetic nature of the barrier when increasing t , which results in an overall increase of the parameter δ [21, 183, 223, 226]. As it occurs in the Supplementary of Ref.[189], the spin-filtering efficiency P at low temperatures, calculated using both approaches, slightly increases when compared with P estimated from the $R(T)$ curves for $T_c < T < T_{\text{Curie}}$.

Small deviations observed for the thickest JJs can be explained by the fact that $t_{\uparrow(\downarrow)}$ values estimated in the highly spin-polarized regime [21], and used to calculate r , were obtained within a model that is able to describe only qualitatively the temperature behavior of JJs with thicker GdN barriers [21]. Another possible explanation lies in the insensitiveness of the TJM model to the magnetic nature of the barrier, which is more relevant for thicker junctions. The next step will be to explicitly include in the TJM model used here the magnetic nature of the barrier.

3.3 Magnetic phenomena in spin-filter JJs

The $I_c(H)$ curves reported in Fig. 3.9 are measured at 300 mK in the Heliox system (Sec. 2.1). The field was first ramped from negative to positive fields, and the other way around. The critical current was calculated as the average

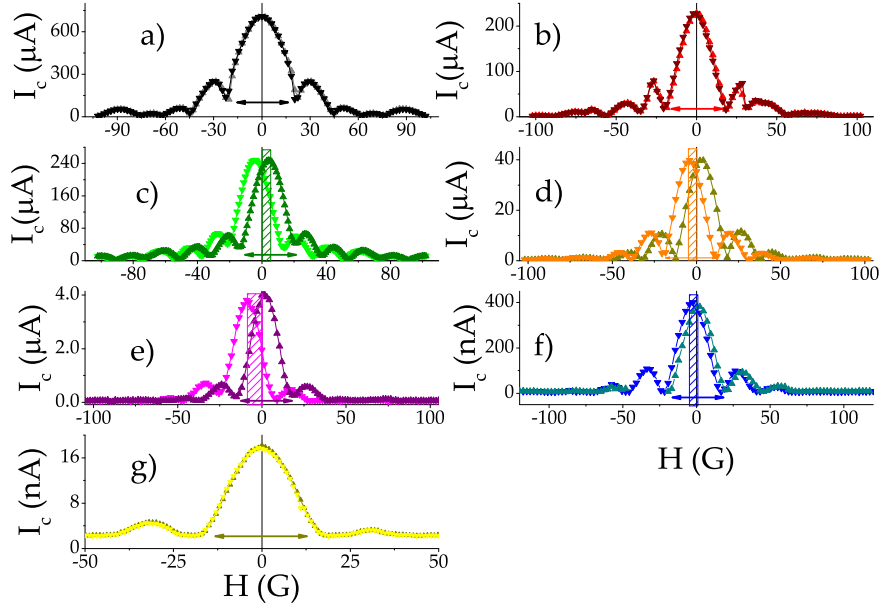


FIGURE 3.9: $I_c(H)$ curves: (a) 1.5 nm, (b) 1.8 nm, (c) 2.0 nm, (d) 2.5 nm, (e) 3.0 nm, (f) 3.5 nm, (g) 4.0 nm. The up (down)-triangle symbol is used for the up (down) curve. Straight arrows refer to the amplitude of the first lobe, while the patterned boxes highlight the shift of the Fraunhofer pattern

between the positive I_c^+ and negative I_c^- critical currents as $I_c = (I_c^+ - I_c^-)/2$.

The periodicity $\Delta(H)$ is measured considering half of the amplitude of the first lobe of the pattern (straight arrows in Fig. 3.9), while the hysteresis H_y is here defined as the shift of the Fraunhofer pattern maximum (boxes in Fig. 3.9). H_y in the $I_c(H)$ curve corresponds to the residual magnetization of the barrier if the ferromagnet has reached the saturation field H_s . In this case, the up-curve and down-curve above H_s overlap. This occurs for JJs with $t < 2.5$ nm.

In Fig. 3.10 we show ΔH and H_y as a function of t . H_y increases from 0 to 4 G for JJs with $t < 2.5$ nm. The effective magnetic area of the JJs depends on the GdN permeability μ_r as in Eq. 1.17, which has been estimated from a linear fit of the magnetization curve $M(H)$ for $H \sim 0$ [189]. In Fig. 3.11 we report the $4\pi M(H)$ curve estimated with Josephson magnetometry on a JJ with GdN barrier thickness $t = 2.0$ nm, which is consistent with typical curves measured in soft ferromagnets [43].

For $t > 2.0$ nm, ΔH increases. We can reasonably rule out that the increase is due to arbitrary orientations of the field applied, since the patterns for thicker JJs have been acquired in different cool-downs, i. e. it would have been impossible to systematically introduce the same finite angle between the sample and the field generated by the coil. To our knowledge, none of the effects reported in literature on conventional tunnel JJs causes an increase in the periodicity. Qualitatively, this phenomenon can be due to an overall decrease of μ_r increasing the thickness of the barrier. For JJs with a multi-domain barriers as in our case, the domain configuration becomes so complex

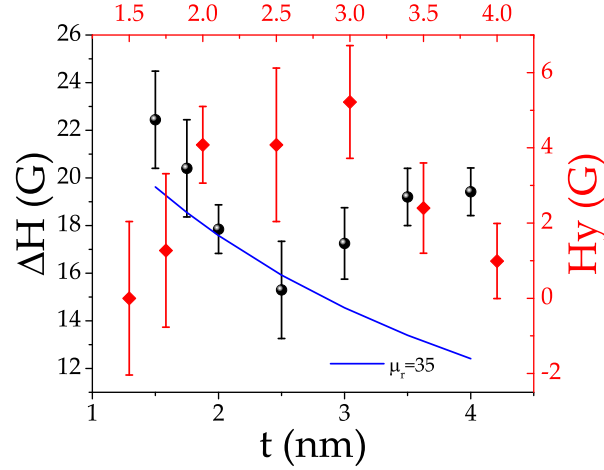


FIGURE 3.10: Periodicity ΔH (black points) and hysteresis H_y (red diamonds) as a function of the GdN barrier thickness t in spin-filter JJs. The blue straight line identifies the expected ΔH considering that the electrodes thickness $d < \lambda_L \sim 200$ nm, with λ_L London length and the relative permeability for the ferromagnet μ_r , calculated as reported in the main text

that affects the magnetization [35]. However, we are not able to prove this statement from the magnetization curves, since Josephson magnetometry fails when the junctions are not fully magnetized. Further studies are needed to understand this effect.

3.4 Spin-triplet superconductivity in spin-filter JJs

The thickness-dependent spin-polarization and the non-trivial magnetic structure of the GdN barrier in spin-filter JJs determine peculiar transport properties. In this section, I will especially focus on the supercurrent dependence on the temperature down to ~ 20 mK on JJs with different GdN barrier thickness [21, 22]. As one can observe in Fig. 3.12, a net deviation from the expected Ambegaokar-Baratoff (AB) behavior for tunnel JJs is more and more relevant when increasing the barrier thickness, which is dramatic in the highly spin-polarized regime. In fact, for $t < 2.5$ nm, the $I_c(T)$ curve shows a monotonic dependence on the temperature, while for $t > 2.5$ nm the $I_c(T)$ curves show a plateau that extends from $0.3T_c$ to $0.8T_c$, with a non-monotonic behavior that evolves into a peak at about $0.7T_c$ for the thickest JJ. This unique behavior has never been observed in any SFS JJ, or any other type of JJ. Such an unusual behavior is indicative of the emergence of an incomplete $0-\pi$ transition, only partially predicted by Kawabata et al. in Ref.[109].

The complete $0-\pi$ transition in SFS JJs is attributed to the oscillation of the superconducting order parameter in the barrier induced by the proximity effect [11, 12, 15], but in SI_fS JJs the transport is purely tunnel.

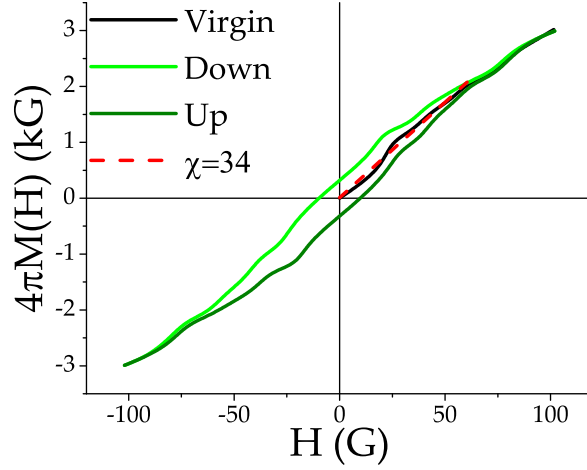


FIGURE 3.11: Magnetization curve $4\pi M(H)$ estimated by Josephson magnetometry for a spin-filter JJ with $t = 2.0$ nm. The red dashed line is the linear fit performed to estimate the permeability of the barrier $\mu_r = \chi + 1$, where χ is the magnetic susceptibility

3.4.1 Phenomenological approach

We have first developed a phenomenological model [21]. It has been used to correlate the behavior of the $I_c(T)$ to both the presence of spin-filtering and spin-mixing (Sec. 1.2), by using a ballistic transport theory and a scattering-matrix approach [21, 30, 32, 227, 228].

We used Eq. 1.2 in Chap. 1 to model the tunnel-like **Current Phase Relation (CPR)**, considering that the occupied Andreev energy levels can be expressed as

$$\epsilon_{\pm} = |\Delta| \operatorname{sgn} \left(\sin \frac{\Phi_{\pm}(\varphi)}{2} \right) \cos \frac{\Phi_{\pm}(\varphi)}{2}. \quad (3.8)$$

Here the phase-difference $\Phi_{\pm}(\varphi)$

$$\Phi_{\pm}(\varphi) = \Theta \pm \arccos \left[\sqrt{(1 - \tau_{\uparrow})(1 - \tau_{\downarrow})} - \sqrt{\tau_{\downarrow}\tau_{\uparrow}} \cos \varphi \right] \quad (3.9)$$

contains the two fundamental ingredients for the formation of spin-triplet supercurrents, as discussed in Sec. 1.2: the spin-mixing angle Θ in Eq. 1.33 and the spin-dependent transparency $\tau_{\uparrow(\downarrow)}$,

$$\begin{cases} \tau_{\uparrow} &= \tau \sin \gamma \\ \tau_{\downarrow} &= \tau \cos \gamma, \end{cases} \quad (3.10)$$

where τ is the barrier transparency and γ is an angle varying from 0 to $\pi/4$ that measures the spin-filtering efficiency P . For $\gamma = 0$, one of the two spin-channels is completely suppressed, while for $\gamma = \pi/4$ they equally contribute to the conduction.

In Fig. 3.13 we show the experimental data and an **AB** fit (blue dashed line) for all the JJs. Red straight lines are the phenomenological fit obtained using

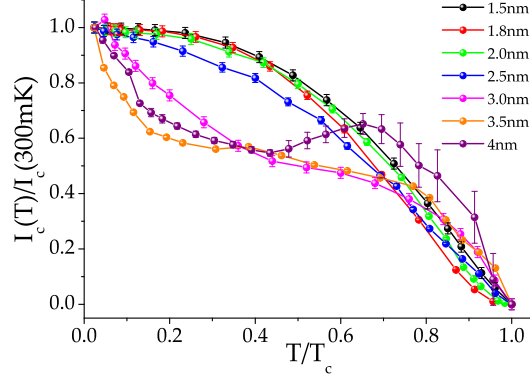


FIGURE 3.12: Normalized critical current $I_c/I_c(300\text{ mK})$, with $I_c(300\text{ mK})$ reported in Tab. 3.1 as a function of the normalized temperature T/T_c for spin-filter JJs with different GdN thicknesses

TABLE 3.3: Fitting parameters of the phenomenological model for the $I_c(T)$ curve as a function of the GdN barrier thickness t : the spin-dependent transparency $\tau_{\uparrow(\downarrow)}$, the spin-mixing angle from one (Θ_1) or two channels (Θ_1 and Θ_2) and weight parameter g [21]

t (nm)	τ_{\uparrow}	τ_{\downarrow}	Θ_1	Θ_2	g
1.5	0.107	0.198	0	-	-
1.8	$4.95 \cdot 10^{-2}$	0.215	0.470	-	-
2.0	$3.94 \cdot 10^{-2}$	0.206	0.400	-	-
2.5	$8.32 \cdot 10^{-3}$	0.132	0.935	-	-
3.0	$2.33 \cdot 10^{-3}$	0.157	1.992	3.10	0.400
3.5	$5.40 \cdot 10^{-4}$	$5.90 \cdot 10^{-2}$	2.256	3.14	0.292
4.0	$2.82 \cdot 10^{-4}$	$3.90 \cdot 10^{-2}$	2.085	2.95	0.400

parameters in Tab. 3.3. While for lower values of the barrier thickness ($t < 3.0\text{ nm}$) the model works fine with an increasing spin-mixing angle Θ that is consistent with an increasing magnetic activity in the barrier, for junctions with thicker barriers the model predicts the appearance of a complete $0-\pi$ transition (green dotted line). The smoothing of the $0-\pi$ transition can be captured, at least for the JJs with $t = 3.0\text{ nm}$ Fig. 3.13 (e) and 3.5 nm (f), considering two transport channels weighted by a parameter g and characterized by the same spin-filtering efficiency, but different spin-mixing angles Θ_1 and Θ_2 . Each of the channels can in principle undergo a $0-\pi$ transition separately, but when combined give the plateau feature. This solution can be physically related to the presence of a non-trivial magnetic texture of the barrier: in each channel, singlet Cooper pairs combine with a different degree of spin-mixing, so to affect the overall behavior of the $I_c(T)$.

This picture is not enough to describe the thickest JJ and the peculiar non-monotonic behavior of the $I_c(T)$ curve. In principle, we can increase

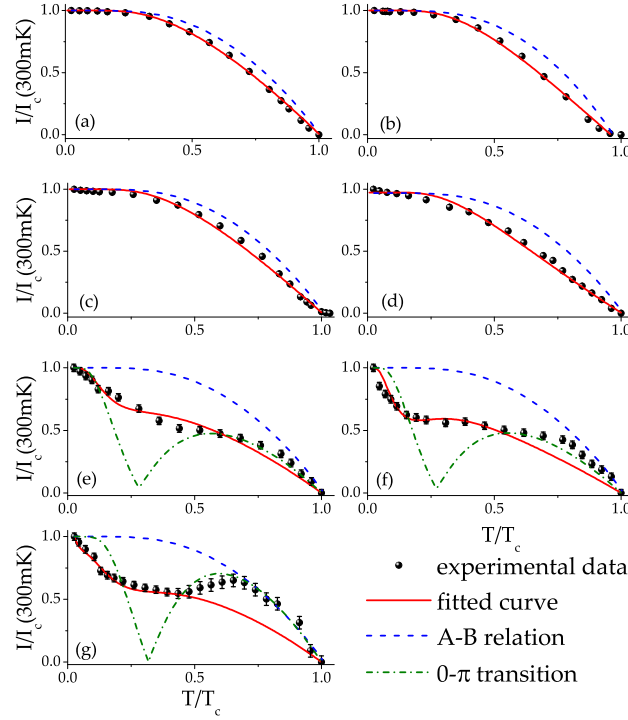


FIGURE 3.13: Normalized $I_c(T)$ curves in spin-filter JJs and AB fit (blue dotted curve), phenomenological fit with one spin-channel (red straight line) and $0-\pi$ transition (green dashed line) for highly spin-polarized devices [21]. From (a) to (g) the GdN thickness increases as in Tab. 3.3

the number of channels, but for computational reasons this is hard to accomplish. The complex magnetic structure of the barrier, combined with the presence of the exchange field, points towards an explanation of the unconventional thermal behavior of the I_c in terms of the emergence of spin-triplet superconductivity.

3.4.2 Atomistic modeling

A full microscopic and atomistic modelization of the spin-filter JJ allows to quantify and directly calculate spin-singlet and spin-triplet correlation functions. The strength of this approach lays in the ability to extrapolate *a posteriori* fundamental information on the superconducting pairing, by explicitly taking into account the physical properties of the system under analysis.

We model the experimental $I_c(T)$ curves in spin-filter JJs by using a tight-binding Bogoliubov-de Gennes Hamiltonian on a two-dimensional lattice (Fig. 3.13). Along the \hat{x} -direction, the barrier is simulated as composed of N discrete sites, so that $Na = t$, with t thickness of the ferromagnetic insulating barrier I_f and a the characteristic cell length. Along the \hat{y} -direction, the total number of sites corresponds to $Ma = L$, with L width of the junction. The two superconductors are characterized by standard s-wave uniform order parameter Δ , and are treated as border conditions [22, 94]. The physics of the

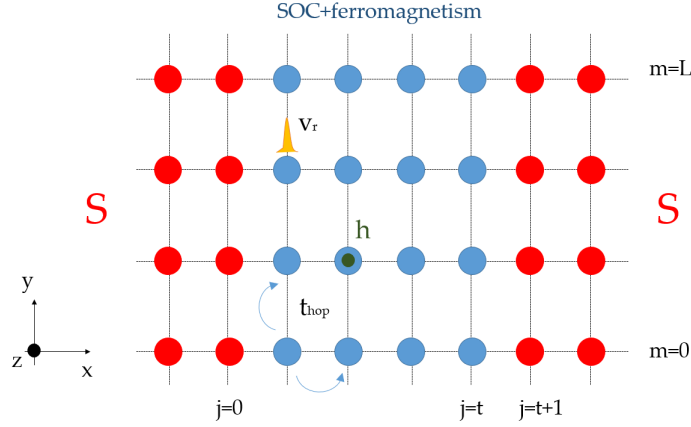


FIGURE 3.14: Scheme of the microscopic modelization of a spin-filter JJ in a 2D-lattice. Red sites represent the superconducting electrodes, the blue sites refer to the I_f barrier, in which the hopping occurs between nearest-neighbours, and an exchange field perpendicular to plane coexists with Spin Orbit Coupling (SOC) and on-site impurities, here represented as the yellow peak on a random site

system is all concentrated in the I_f barrier Hamiltonian,

$$H_{I_f} = H_k + H_{\text{SOC}} + H_h + H_i, \quad (3.11)$$

which consists of four terms:

- a tight-binding kinetic part H_k , with parameters t_{hop} (hopping parameter) and the Fermi energy level ϵ_f ;
- an exchange field Hamiltonian H_h , which captures the ferromagnetic nature of the barrier, with the exchange field h perpendicular to the lattice plane;
- a Rashba SOC, which breaks the inversion symmetry at the interface, with consequent generation of spin-triplet supercurrents. This efficiently mimics the presence of magnetic inhomogeneities, which are more likely to occur in our devices, without adding further complexity to the already hard computational approach;
- an on-site impurity potential H_i , which is randomly distributed in the barrier.

The supercurrent I_c is calculated maximizing the CPR obtained solving the Matsubara Green's functions with methods reported in Ref.[94] at different temperatures. This technique allows for a direct calculation of the anomalous Green's functions for the spin-singlet component f_0 , the opposite spin-triplet component f_3 and the equal spin-triplet components $f_{\text{up(down)}}$ by fitting the $I_c(T)$ curves.

Our approach allows to distinguish between the s- and p-wave symmetry correlation functions. While for the s-wave symmetry, spin-triplet components are odd in frequency functions, and are related to the well-known

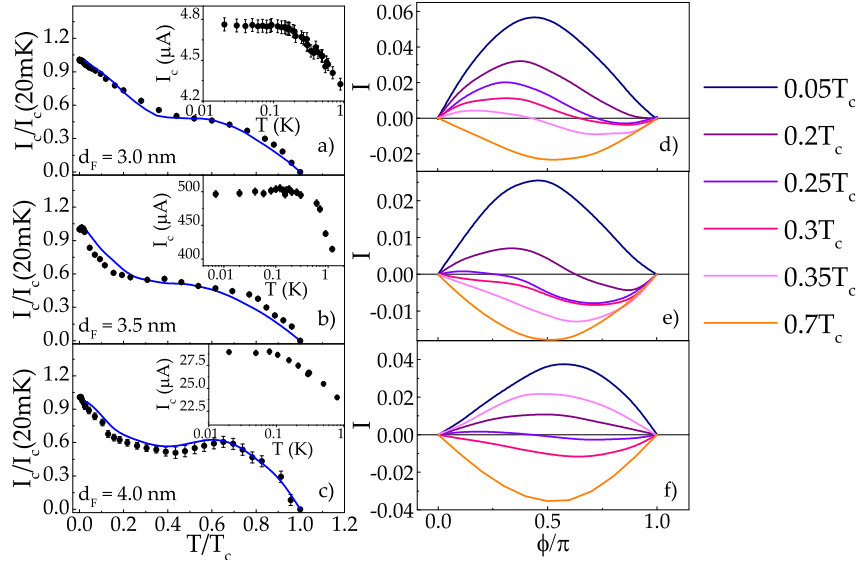


FIGURE 3.15: Normalized $I_c(T)$ curves for junctions with barrier thickness $t = 3.0$ nm (a), $t = 3.5$ nm (b) and $t = 4.0$ nm (c) (black points) and atomistic simulations (blue lines). In the insets, measured saturation of the I_c down to 20 mK for the three junctions. In (d), (e) and (f) the calculated **Current Phase Relation (CPR)** at selected temperatures for the three junctions in (a), (b) and (c), respectively.

odd-frequency superconductivity, for the p-wave symmetry, spin-triplet components are even-frequency functions [44, 229]. The main source of the triplet Josephson current in diffusive ferromagnets is the odd-frequency s-wave pairing amplitudes [44, 94, 230], but in the limit of clean systems (for instance, in half-metallic barrier), p-wave triplet pairing amplitudes also becomes significant [44, 231]. Therefore, it is important to have a method that allows to distinguish between the two components.

One of the limitations of the atomistic approach is given by the small sample size computationally manageable, but even with this limitation we successfully relate the shape of the $I_c(T)$ curves to the arising of spin-triplet superconductivity. The best simulation curves obtained within our model (Fig. 3.15 (a), (b) and (c)) gives a quantitative agreement with the experimental data for JJs with barriers 3.0 nm, 3.5 nm and 4.0 nm, for which the phenomenological model has shown strong limitations (Fig. 3.13 (e), (f) and (g) respectively). We set as external parameters: the number of sites N along the transport direction, the lateral dimension of the bidimensional lattice, the spin-orbit coupling α , the magnetic exchange field h , the chemical potential of the superconducting electrodes μ_s , the Fermi energy level ϵ_f and the superconducting gap Δ .

Compared with more standard works on spin-triplet superconductivity in SFS JJs, in which spin-triplet correlations are often posed *a priori*, we here calculated the s- and p-wave spin-triplet correlations *a posteriori* (Fig. 3.16) for the JJs with $t = 3.0$ nm, $t = 3.5$ nm and $t = 4.0$ nm, respectively. The s-wave

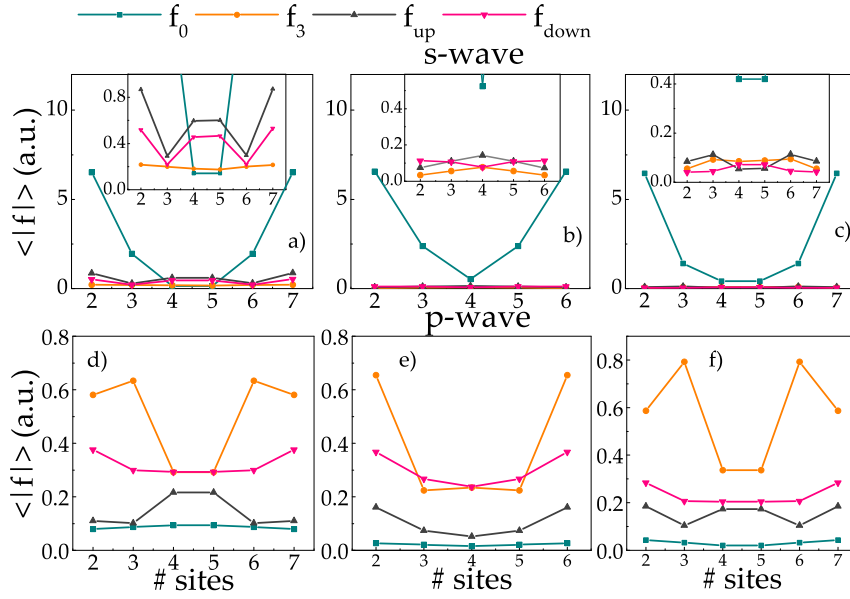


FIGURE 3.16: In (a), (b) and (c) s-wave correlation functions for the JJs with $t = 3.0$ nm, $t = 3.5$ nm and $t = 4.0$ nm, respectively. In (c), (d) and (e) p-wave correlation functions for the JJs with $t = 3.0$ nm, $t = 3.5$ nm and $t = 4.0$ nm, respectively. Here, f_0 (spin-singlet), f_3 (opposite spin-triplet) and $f_{\text{up}(\text{down})}$ (up or down spin-triplet)

pair correlation functions reported in Fig. 3.16 (a), (b) and (c) and the p-wave correlation functions in (d), (e) and (f) are calculated at 300 mK.

At the borders, the proximity with the s-wave superconducting electrodes results in a pronounced s-wave spin-singlet component, while in the middle of the barrier there is a competition between spin-singlet and spin-triplet components. As one can observe for the JJ with $t = 3.0$ nm, for which the plateau extends on a wide range of temperatures and indicates a broadened $0-\pi$ transition in temperature, the major contribution to the conduction in the middle of the barrier is given by the equal s-wave spin-triplet correlation f_{up} . In the other JJs, for which the plateau gradually becomes narrower, and a dip arises, there is a competition between the equal s-wave spin-triplet correlations and the opposite s-wave spin-triplet correlations, together with a substantial increase of the spin-singlet component. In these cases, the p-wave spin-triplet correlation amplitudes give a major contribution compared with the s-wave component. This result shows that the occurrence of an incomplete $0-\pi$ transition, confirmed also by the CPR in (d), (e) and (f), plays here a fundamental role. The more the $I_c(T)$ points towards a complete $0-\pi$ transition, the more equal s-wave spin-triplet correlations are suppressed. On the other hand, the more the plateau extends in temperature, the more equal s-wave spin-triplet contributions become important.

An important experimental key finding in this discussion is the dependence of the $I_c(T)$ curve on a weak magnetic field, which induces a dip in the plateau proportionally to its intensity. The measurement of the $I_c(T)$ in a magnetic field must take into account the I_c modulation in a magnetic field,

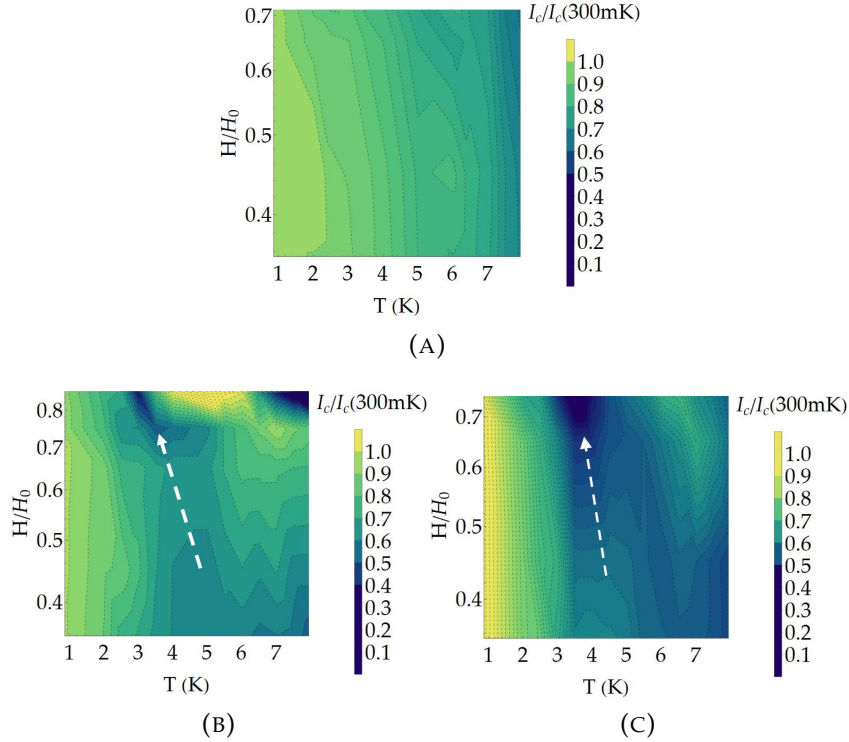


FIGURE 3.17: Normalized $I_c(T)/I_c(300 \text{ mK})$ density-plots as a function of the percentage of periodicity H/H_0 for the JJs with: (a) $t = 1.5 \text{ nm}$, (b) $t = 3.0 \text{ nm}$ and (c) $t = 3.5 \text{ nm}$

which may be affected by the ferromagnetic nature of the barrier. We solve this issue by measuring the $I_c(H)$ curve at a fixed temperature T . We then measured the magnetic area H_0 per each temperature, and the I_c was finally estimated at different percentage of magnetic area $H_0(T)$, rather than at a fixed external magnetic field value.

The step in field must be sufficiently small to avoid the interpolation of the I_c from the Fraunhofer pattern curve: in this way, the I_c can be directly measured from the $I(V)$ curve at the magnetic field corresponding to the desired magnetic field percentage area H/H_0 . Moreover, to distinguish a peak structure in temperature, the temperature step ΔT was fixed at 0.5 K. The range of explored temperatures was the plateau region (from 2 K to 8 K), while measurements at 300 mK were taken as a comparison with the normalized $I_c(T)$ curves at zero-field.

The result is reported in Fig. 3.17 in two density-plots (b) and (c) for the junctions with $t = 3.0 \text{ nm}$ and $t = 3.5 \text{ nm}$, respectively. They are also compared with the density-plot measured for a non-spin-filter JJ in (a). Increasing the field H/H_0 , the non-spin-filter JJ shows a uniform density plot, corresponding to $I_c(T)$ curves with the same trend. Instead, in JJs with thicker barriers, the plateau at zero-field evolves into a minimum (dark region around $70 - 80\%H_0$ and between 2 and 4 K) and a maximum (bright region around $70 - 80\%H_0$ and between 4 and 6 K). To our knowledge, this phenomenon was never reported for any JJ.

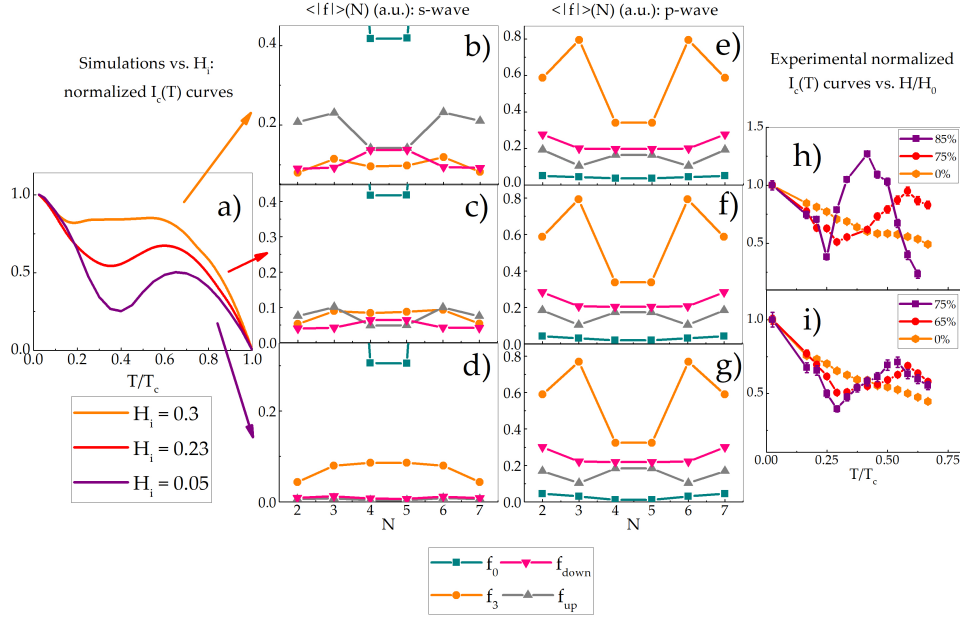


FIGURE 3.18: Normalized $I_c(T)/I_c(300 \text{ mK})$ cross-sections at fixed H/H_0 for JJs with $t = 3.0 \text{ nm}$ (h) and $t = 3.5 \text{ nm}$ (i) and analogy with the $I_c(T)$ simulations at different impurities potential strength H_i in (a). In (b), (c) and (d) the s-wave correlation functions in the barrier for the three values of H_i reported in (a), respectively. In (e), (f) and (g) the p-wave correlation functions are shown

In our microscopic approach, we explicitly consider on-site magnetic fluctuations δ_h ($|\delta_h| = h/10$) and lattice impurities. The latter plays a fundamental role in describing the experimental findings. The dip in the $I_c(T)$ curve in our simulations reduces when decreasing the impurity potential strength (Fig. 3.18 (a)), as it occurs when increasing the magnitude of the external magnetic field. Given the correlation between the arising of the complete $0-\pi$ transition and the suppression of spin-triplet components previously discussed, by decreasing the impurity potential, also the s-wave spin-triplet correlations are suppressed (Fig. 3.18 (b), (c) and (d)). In Fig. 3.18, we qualitatively compare simulated $I_c(T)$ curves for different H_i values with some line-cuts in Fig. 3.17 (b) and (c) (Fig. 3.18 (h) and (i), respectively). Finally, the p-wave components appear to be approximately unaffected by the disorder (Fig. 3.18 (e), (f) and (g)). Their insensitivity to the impurity potential may suggest that the s-wave channel is dominant on the transport properties.

If on one hand the arising of the plateau for strong impurity potentials always occurs in our model, in absence of SOC, the dip in the $I_c(T)$ always occurs at the same temperature when decreasing the impurity potential. Instead, the combined presence of the on-site impurities, magnetic fluctuations and SOC induces a shift of the minimum position in temperature, which also occurs for the experimental $I_c(T)$ curves in presence of a weak external magnetic field. The minimum temperature shift is highlighted in Fig. 3.17 (b)

and (c) by the white dashed arrow, which is here only a guide for the eye.

A possible qualitative explanation of this analogy is the following. In ferromagnetic systems with randomly placed impurities, at $T < T_{\text{Curie}}$ the impurities tend to pin the domain walls in certain energetically favorable locations [43, 232, 233]. Increasing the external magnetic field, the volume of pinned domain walls may be reduced, which gives as a result the same effect that occurs in our simulations when decreasing the strength of the impurity potential. One may argue that the intensity of our fields is less than a flux-quantum, too weak to induce the domain to re-adapt with an external magnetic field. Nevertheless, the domain-walls are much more sensitive to external fields compared with bulk-domains, and also weak magnetic fields of the order of 0.1 mT can interfere with their configuration [233].

This experimental result demonstrates that the application of weak external magnetic field can be seen as a knob for the tuning of the $0-\pi$ transition. Given the gradual appearance of spin-triplet contributions increasing the impurity potential in Fig. 3.18 (b), (c) and (d), i. e. by tuning the $I_c(T)$ trend from a $0-\pi$ transition towards a plateau structure, the application of a weak magnetic field in spin-filter JJ is also an innovative tool for the tuning and the control of spin-triplet supercurrents in spin-filter JJs.

Electrodynamics of ferro-tunnel JJs

If one wants to place a JJ in a circuit, or to couple it to a cavity [147, 204], it is important to characterize the electrodynamic of the junction. This is of particular interest in tunnel JJs, and it has never been performed on a tunnel junction with a ferromagnetic barrier. Knowledge of the electrodynamic parameters in tunnel SFS JJs, such as E_J , E_C and the quasiparticles dissipation, and how they scale with the barrier thickness and the JJ geometry is a fundamental key step to understand the potential of this type of JJs inside a more complex circuit.

In this chapter, I focus on the dissipation analysis of spin-filter JJs [23]. The characteristic spin-polarized nature of NbN-GdN-NbN JJs, the demonstration of spin-triplet superconducting transport and the dependence on the residual magnetization of the barrier suggest possible implementation in spintronics devices [12–16, 113] and in classical superconducting circuits, such as Cryogenic Magnetic Random Access Memory (CMRAM) [38, 53, 234, 235]. The anomalous $0-\pi$ transitions, tunable by means of an external magnetic field, implies that spin-filter JJs can also be implemented in the $0-\pi$ technology field [109, 182, 236], in classical devices for digital electronics [237] and efficient electron refrigeration [113]. Finally, the first evidence of Macroscopic Quantum Tunneling (MQT) in ferromagnetic JJs, which is intrinsically due to the low-dissipative nature of ferro-tunnel JJs, is an indication that spin-filter JJs can also be used as quantum devices [24], as confirmed by the results reported in this chapter.

The methodology I will describe in the following sections can be obviously extended to other types of ferro-tunnel JJs, such as SIsFS JJs, which are much more flexible for applications in superconducting devices. In this chapter, I will provide a comparison between devices with different ferromagnetic barriers, as PdFe and Py interlayers.

TABLE 4.1: $I_c R_N$ product and Josephson energy E_J of spin-filter JJs with GdN thickness t at 20 mK, 300 mK and 4.2 K

t (nm)	$I_c R_N$ (mV)			E_J (Hz)		
	20 mK	300 mK	4.2 K	20 mK	300 mK	4.2 K
1.5	-	1.24	1.13	-	$3.52 \cdot 10^{14}$	$3.22 \cdot 10^{14}$
1.8	-	0.98	0.78	-	$1.26 \cdot 10^{14}$	$9.97 \cdot 10^{13}$
2.0	-	0.55	0.50	-	$1.26 \cdot 10^{14}$	$1.14 \cdot 10^{14}$
2.5	-	0.18	0.16	-	$1.96 \cdot 10^{13}$	$1.71 \cdot 10^{13}$
3.0	0.044	0.038	0.023	$2.35 \cdot 10^{12}$	$2.22 \cdot 10^{12}$	$1.34 \cdot 10^{12}$
3.5	0.016	0.019	0.010	$2.42 \cdot 10^{11}$	$2.82 \cdot 10^{11}$	$1.53 \cdot 10^{11}$
4.0	0.0061	0.0031	0.0028	$1.43 \cdot 10^{10}$	$8.10 \cdot 10^9$	$7.36 \cdot 10^9$

4.1 Study of the electrodynamics in SI_fS JJs

We here focus on the estimation of the electrodynamics parameters in JJs in the highly spin-polarized regime ($t \geq 3.0$ nm), and we explore typical temperatures for both CMRAM and spintronics proposals (4.2 K) and for other superconducting implementations, such as active and passive elements in qubit circuits (< 300 mK) [11, 107, 109, 110, 182]. As discussed in Chap. 1.3.1 and 1.3.2, the dissipation in a JJ, measurable by means of the quality factor Q , is frequency-dependent [26, 27, 155, 156] (Sec. 1.3). We discuss the low-frequency dissipation regime by analyzing the $I(V)$ curves, and the high-frequency regime studying the Switching Current Distribution (SCD).

4.1.1 $I(V)$ curves analysis

While I_c in spin-filter JJs shows an unconventional behavior in temperature (Chap. 3), the R_N is mostly temperature independent. We report in Tab. 4.1 a summary of the $I_c R_N$ products and the Josephson energies E_J values at 20 mK, 300 mK and 4.2 K. The former is of fundamental importance in CMRAM devices, which require high commutation speeds; the latter defines the possible qubit operation mode along with the charging energy E_c [145, 204]. In standard metallic SFS JJs, the $I_c R_N$ product is of the order of a few microvolts or less [11, 13, 14], while the tunnel-like nature of spin-filter JJs leads to values of $I_c R_N$ at least two orders of magnitude higher than in metallic SFS JJs and comparable with those measured in non-magnetic SIS JJs [11, 12, 14, 38, 78, 174]. For instance, in spin-filter JJs with barrier thicknesses lower than 2.5 nm, the characteristic voltage is of the order of the millivolt [21, 24, 183]. E_J , instead, is comparable to Josephson energies in quantum circuits reported in literature, such as flux/phase-qubits or Cooper pair box (CPB) [204, 238].

The analysis of the $I(V)$ curves allows also to determine of the low-frequency quality factor Q_0 and the resistance associated with the quasi-particle dissipation R_{sg} . In highly spin-polarized JJs with low J_c we have used the Tunnel Junction Microscopic (TJM) model to obtain a self-consistent estimation of Q_0 , R_{sg} and the capacitance of the JJ C . As already anticipated in

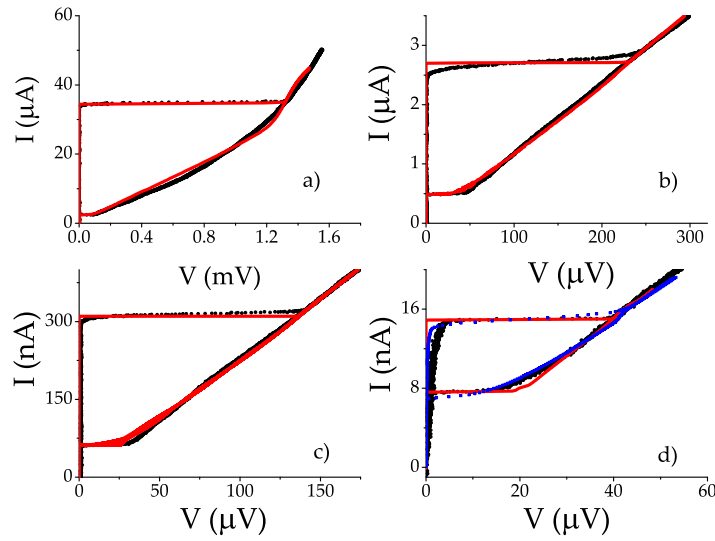


FIGURE 4.1: Measured $I(V)$ curves at 4.2 K (black points) and TJM model simulation by using PSCAN2 software (red curve) for high spin-filter JJs with thicknesses t : a) 2.5 nm, b) 3.0 nm, c) 3.5 nm, d) 4.0 nm [23]. Quality factor Q_0 and subgap resistance R_{sg} estimated from the simulations are collected in Tab. 4.2. The blue squares in d) represent the frequency-dependent RCSJ model fit curve, obtained for $Q_0 = 2.8$ and $Q_1 = 0.13$ [23].

Sec. 1.3, the TJM model can provide a complete microscopic description of the quasiparticles transport in any tunnel JJ, without taking into account the exact expression for the Current Phase Relation (CPR) [22, 23, 189]. It can be argued that the quasiparticle current in a spin-polarized system depends on the magnetic nature of the barrier. We here show that the TJM model captures the shape of the subgap branch in the $I(V)$ curves also in these unconventional devices, and allows to obtain a reliable estimation of the electrodynamics parameters [23, 128].

In Fig. 4.1 we compare the experimental $I(V)$ curves at 4.2 K with TJM simulations, calculated by using PSCAN2¹ (App. B). In our simulations, we reproduce the current biasing of a JJ with a current generator in series with the filtered lines of our evaporation cryostat (Sec. 2.1). In this analysis, the fitting parameters Q_0 and the subgap resistances R_{sg} (Tab. 4.2), are such that deviations from the experimental curves are minimal. Further details on the software parameters that govern the shape of the $I(V)$ curves can be found in App. B.

The thicker the barrier is, the higher is the subgap resistance [143, 144, 239] and the lower is the low-frequency quality factor Q_0 , which is consistent with the exponential decrease of I_c and the linear decrease of the barrier capacitance C by increasing t [26]. The decrease in Q_0 for increasing t indicates a smooth transition from an underdamped regime ($Q_0 \sim 10$) to a moderately damped regime with Phase Diffusion (PD) ($Q_0 \sim 1$) (Sec. 1.3.2) [156, 165, 170], which is confirmed by the presence of a finite slope in the supercurrent branch for

¹<http://stacks.iop.org/0953-2048/4/i=11/a=031>

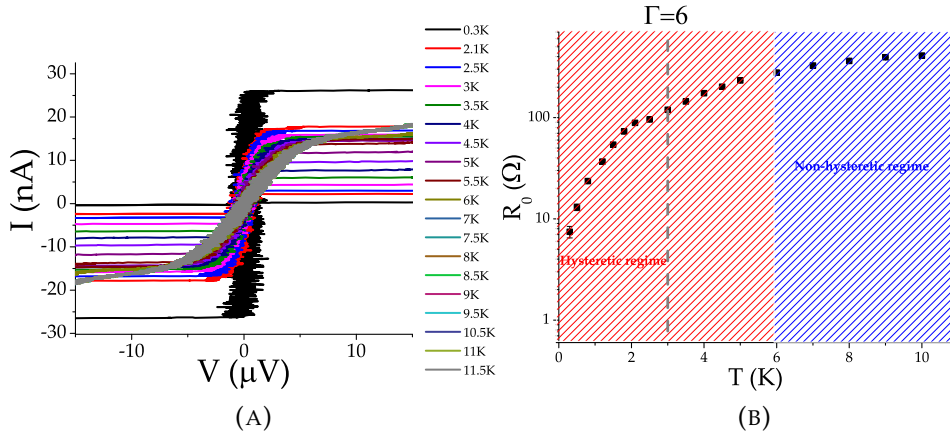


FIGURE 4.2: In (a): $I(V)$ curves as a function of T for the spin-filter JJ with $t = 4.0$ nm; in (b) slope in the superconducting branch R_0 as a function of the temperature. Here, we highlight the temperatures for which a finite voltage in the superconducting branch coexists with a hysteretic $I(V)$ curve (red shaded area), and the region in which the hysteresis disappears (blue shaded area). We also highlight the temperature T corresponding to the ratio $\Gamma = E_J/k_B T = 6$ (gray dashed line). Below this temperature value, the semiclassical model fails to work, as discussed in the main text [156]

the junction with a 4.0 nm-thick barrier [156, 164, 167, 240–245] (Sec. 1.3.2). PSCAN2 simulations cannot reproduce this effect, since they do not take into account thermal activated escape and retrapping of the phase-particle. The $I(V)$ curve in Fig. 4.1 (d) (blue square points) was simulated explicitly taking into account PD processes with a Monte Carlo simulation in the frame of the frequency-dependent Resistively and Capacitively Shunted Junction (RCSJ) model [156], discussed in Sec. 1.3.2. Details on the simulation software are widely covered in Refs. [164–168, 170, 199, 224]. The fitting parameters in Monte Carlo simulations are the low- and the high-frequency quality factors, which resulted to be $Q_0 = 2.8$ (consistent with TJM predictions) and $Q_1 = 0.13$.

TABLE 4.2: Measured electrodynamics parameters Q_0 and R_{sg} of spin-filter JJs at 20 mK, 300 mK and 4.2 K calculated with the TJM model [23]. The errors on Q_0 and R_{sg} are of 6% and 10%, respectively, which represent the range of values that provides a significant overlap between the experimental $I(V)$ characteristics and the simulated curves [23]

t (nm)	$R_{sg}@4.2$ K (Ω)	$R_{sg}@300$ mK (Ω)	$Q_0@4.2$ K	$Q_0@300$ mK
2.5	59	93	16	48
3.0	82	350	7.3	35
3.5	440	1700	6.6	32
4.0	3000	13000	2.6	26

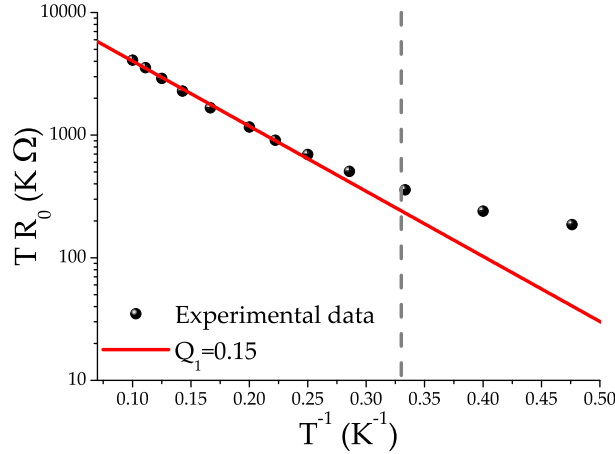


FIGURE 4.3: PD fit (red straight line) of $TR_0(T^{-1})$ (black points) with Eq. 3.7. The gray dashed line is referred to the ratio $\Gamma = E_J/k_B T = 6$ (gray dashed line). Above this T^{-1} value, the semiclassical model fails to work, as discussed in the main text [156]

The environment plays an important role in determining the value of Q_1 . The ratio between the low- and high-frequency quality factors Q_1/Q_0 equals the ratio between the resistance of the environment R_{env} and the subgap resistance, $R_{\text{env}}/R_{\text{sg}}$, as discussed in Sec. 1.3.1 and Sec. 1.3.2 [155, 156, 161]. The resistance R_{env} achieved in this case is approximately 150Ω [23].

As a further consistency of the achieved results, we performed an analysis of the finite resistance in the superconducting branch R_0 (PD resistance) as a function of the temperature T for the thicker JJ (Fig. 4.2 (a)) [154, 156, 246]. It is possible to notice that the slope in the supercurrent branch emerges also in the hysteretic regime of the $I(V)$ curves, which can be reproduced only by the frequency-dependent RCSJ model (Fig. 4.2 (b)) [154, 156, 246]. As suggested in Refs. [154, 156, 246], we plot the product TR_0 as a function of $1/T$ in Fig. 4.3. The experimental data were fitted using the expression for the PD resistance in Ref. [156]

$$TR_0(1/T) = \frac{2\pi R_P}{Q_1 k_B} E_J e^{-2\frac{E_J}{k_B T}}. \quad (4.1)$$

This expression holds under the hypothesis of semiclassical escapes and retrapping processes at the plasma frequency ω_p and for neglectable capacitance in the set-up compared with that of the JJ. This model works well for temperatures above 3 K, while it fails at lower temperatures, for which the thermal energy is not sufficiently high compared with the Josephson coupling ($\Gamma = k_B T/E_J < 6$) [246]. The high-frequency quality factor $Q_1 = 0.15 \pm 0.01$ is consistent with Monte Carlo simulations at 4.2 K.

TJM fitting of the $I(V)$ curves also allows to obtain an estimation of the capacitance of the barrier C , using Eq. 1.54 [23], and hence the charging energy E_c . In conventional JJs in the underdamped regime and with large critical current densities J_c , measurements of Fiske steps have been successfully

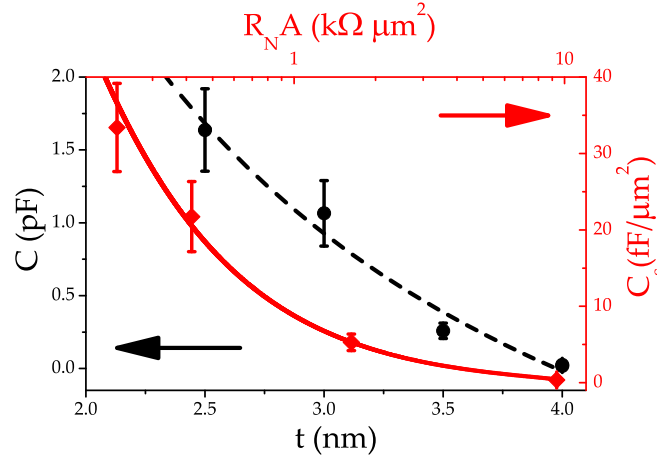


FIGURE 4.4: In black: capacitance C as a function of the GdN barrier thickness t (black circles), along with parallel-plate capacitance $C(t)$ fit (dashed curve) [23]. In red: specific capacitance C_s of the analyzed junctions as a function of $R_N A$ (red diamonds) along with a tunnel barrier model fit (straight line, see Eq. 4.2). The error bars on C and C_s are calculated using the propagation of the errors on R_{sg} , Q_0 and I_c [23].

used to derive the capacitance C [26, 27]. However, when the junctions are characterized by low values of J_c , as in the case of highly spin-polarized JJs, the Fiske resonance amplitude is vanishingly small [164, 167]. Therefore, other methods for the estimation of the JJ capacitance are highly welcomed.

In Fig. 4.4, we plot the junction capacitance C , obtained using Eq. 1.54, as a function of the GdN barrier thickness t (black circle points) and the fitting function for the capacitance in a parallel-plate capacitor $C = \epsilon_0 \epsilon_r A / t$ (black dashed line), where $\epsilon_0 = 8.85 \text{ pF/m}$ is the vacuum dielectric permittivity and ϵ_r is the GdN relative permittivity, which acts as a fitting parameter. The value of C for the GdN barrier with $t = 2.5 \text{ nm}$ is consistent with a previous estimation based on SCD measurements in Ref. [24]. The estimated $\epsilon_r = (20 \pm 8)$ is consistent with the GdN permittivity $\epsilon_r = 26.5$ obtained with spectroscopic measurements on isolated GdN thin films [247], providing an additional validation of the TJM fitting procedure. Moreover, the $R_N A$ product as a function of the specific capacitance $C_s = C / A$ (red diamonds in Fig. 4.4), follows the expected behavior for tunnel JJs [248]. The red line in Fig. 4.4 is the function

$$R_N A(C_s) = \frac{2A\epsilon_0\epsilon_r}{3C_s\sqrt{4m_e\bar{E}}} (h/e)^2 e^{\frac{2\epsilon_0\epsilon_r}{\hbar C_s} \sqrt{4m_e\bar{E}}}, \quad (4.2)$$

which is obtained by replacing t in the Simmons formula in Eq. 3.7 with its dependence on the specific capacitance C_s , $t = \epsilon_0 \epsilon_r / C_s$.

We extended the analysis at 300 mK (the results are reported in Fig. 4.5) [23]. The relative Q_0 and R_{sg} for all the devices are collected in Tab. 4.2. The best-fit curves at 300 mK are characterized by a smaller R_{sg} compared with the experimental ones. We can attribute this deviation to the unconventional

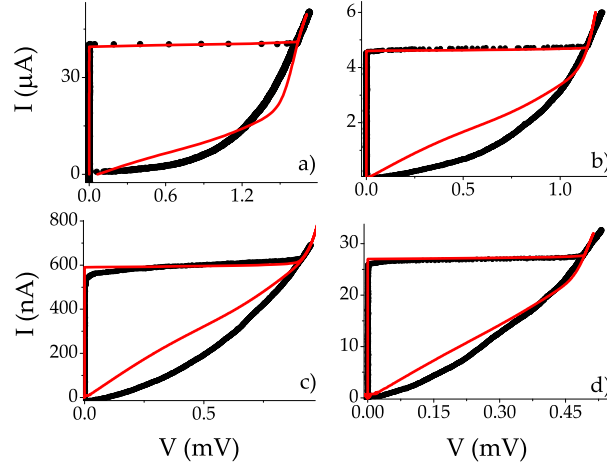


FIGURE 4.5: Measured $I(V)$ curves at 300 mK (black points) and TJM model simulation by using PSCAN2 software (red curve) for spin-filter JJs with thicknesses t : a) 2.5 nm, b) 3.0 nm, c) 3.5 nm, d) 4.0 nm [23]. Quality factor Q_0 and subgap resistance R_{sg} estimated from the simulations are collected in Tab. 4.2 [23]

magnetic activity discussed in Ref. [21] and in Chap. 3, which is at a maximum in the case of highly spin-polarized JJs, where the magnetic nature of the barriers manifests in a steep increase of $I_c(T)$ below 2 K [21]. The conventional TJM model is here pushed to its limit and gives a systematic underestimation of R_{sg} , as shown in Fig. 4.5(a). As a consequence, in Fig. 4.6 we compare the normalized $I(V)$ curves for the junctions with $t = 3.0$ nm, $t = 3.5$ nm and $t = 4.0$ nm at 4.2 K, 300 mK and 20 mK to compare the subgap branches of the $I(V)$ curves. Measurements at 20 mK have been performed by using the Kelvinox and the Triton refrigerators in Sec. 2.2. The current is normalized to the values reported in Tab. 3.1 and 4.4, while the voltage is normalized to the switching value V_s . The amplitude of the hysteresis in the $I(V)$ curves increases when going towards 20 mK, pointing to an increase of Q_0 and as a consequence of R_{sg} .

4.1.2 The phase-dynamics: the SCDs

The SCD experiment reported for the first time in Ref. [24] on a spin-filter JJ with $t = 2.5$ nm demonstrated that spin-filter JJs can show MQT phenomena at low-temperatures. Increasing the thickness of the barrier, and reducing the critical current, the phase-dynamics shows also PD processes, consistently with simulations in Sec. 4.1.1 [156, 164–168, 170, 199, 240–245].

SCD measurements in the high-temperature regime have been performed on the JJs with GdN thickness of 3.0 nm and 3.5 nm using the Heliox system (Sec. 2.1), following the procedures described in Sec. 2.3.1. The mean switching current I_{mean} , the standard deviation σ and the skewness γ , defined in Sec. 1.3.2, as a function of T are reported in Fig. 4.8.

Following the methods used and discussed in Ref. [199], the counterintuitive decrease of σ increasing T can be fitted using a single Q -model based on

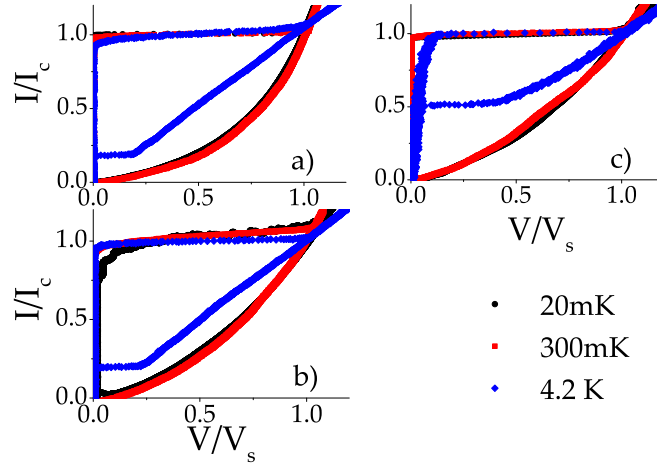


FIGURE 4.6: Comparison between the normalized $I(V)$ curves at 4.2 K, 300 mK and 20 mK for the JJs with GdN barriers: a) 3.0 nm, b) 3.5 nm, c) 4.0 nm [23]

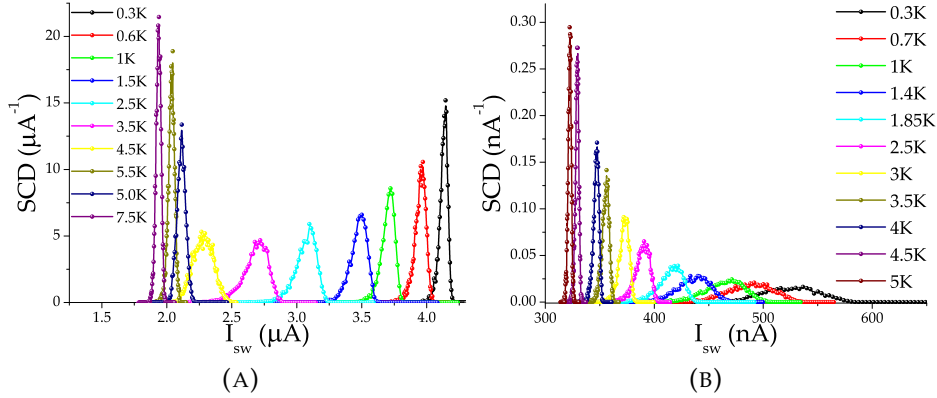


FIGURE 4.7: Switching current distributions SCD measured at high temperatures for the JJs with 3.0 nm and 3.5 nm thick barriers

Monte Carlo simulations (black straight line in Fig. 4.8 (a)) [158, 164–168, 170, 199, 249], which gives a quality factor $Q_1 = 2.9 \pm 0.4$.

While for the JJ with 3.0 nm barrier thickness a transition temperature $T^* \sim 4$ K between TA and PD regimes was observed, in the JJ with a thicker barrier T^* was not observed in the range of analyzed temperatures. Nevertheless, we can get a rough estimation of Q_1 considering the ratio $k_B T / E_J$ and its relation with Q_1 in Fig. 4.9, in which we report typical values found in literature [158, 164–166, 199]. Since the expected $T^* < 0.3$ K, the quality factor Q_1 is < 1.25 , giving an environment resistance of the order of 60Ω .

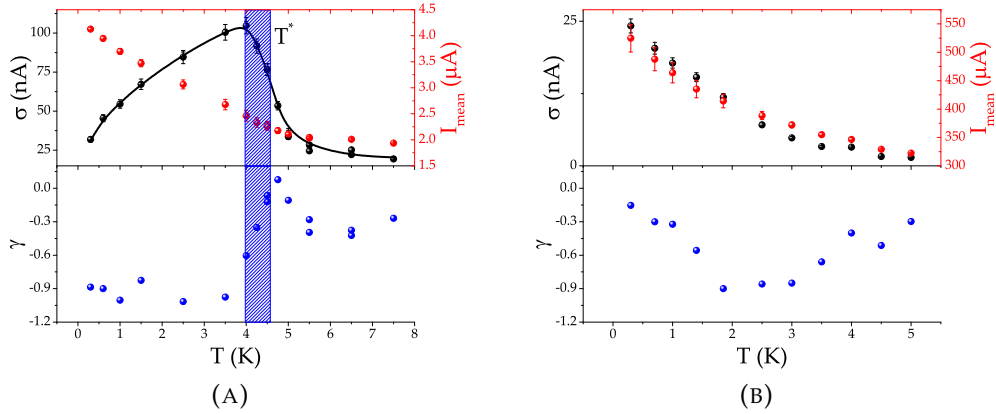


FIGURE 4.8: Mean switching current I_{mean} (red spheres), the standard deviation σ (black spheres) and the skewness γ (blue spheres) as a function of T for spin-filter JJs with $t = 3.0$ nm (first panel) and $t = 3.5$ nm (second panel). The errors have been calculated by using the procedures reported in Sec. 2.3.1. The black line in the first panel is the Monte Carlo simulation for $\sigma(T)$ [249]. The transition temperature T^* lays in the middle of the blue box in the first panel for the JJ with $t = 3.0$ nm, which also takes into account the T^* error

4.2 Comparative electrodynamics study of ferro-tunnel JJs

The estimation of the electrodynamic parameters of ferro-tunnel JJs is a fundamental step in order to study their feasibility inside superconducting quantum circuits, and this will be widely discussed in Chap. 5. In this section we finally show a comparison of the results obtained on different ferro-tunnel JJs, following the main approach discussed in the previous sections on spin-filter JJs. We here focus on Q_0 , the subgap resistance R_{sg} and the ratio between the Josephson and the charging energy E_J/E_C .

The estimated Q_0 values with the TJM model in spin-filter JJs are up to two orders of magnitude higher compared to those of standard SFS heterostructures that typically operate in the overdamped regime like SNS JJs (Q_0 ranging from 10^{-2} to 10^{-1}) [26, 27, 86], and of the same order of magnitude of those in conventional SIS junctions commonly used for the drive and for the Read-Out (RO) of components in quantum and classical circuits [251, 252]. Moreover, the Q_0 values increase of a factor 3 to 10 for the 4.0 nm thick barrier when lowering T to 300 mK. This sets a lower limit that can only increase at lower temperatures (see Fig. 4.6), and suggests possible implementation of spin-filter JJs in low-dissipative π -qubits [109, 182].

The R_{sg} values obtained ranges from tens of ohms to some kilo-ohms at 4.2 K, but when decreasing T , R_{sg} increases from a factor 2 to 5 increasing t at 300 mK. The values obtained in this work can be promising, for instance, for the engineering of complementary π -junctions for phase-bias of conventional flux-qubit (passive elements) and in transmon circuits [23]. The dephasing

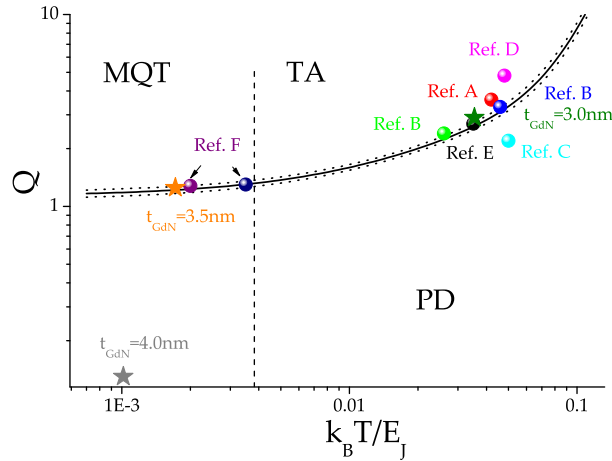


FIGURE 4.9: Phase-diagram $Q(k_B T/E_J)$ of a JJ. The stars are related to the measured/expected transition temperatures T^* of spin-filter JJs with $t = 3.0$ nm, 3.5 nm and $t = 4.0$ nm. The other symbols refer to values reported in A [240], B [241], C [242], D [243], E [244] and F [245, 250]

time in a phase-qubit biased by a π -junction is proportional to $E_J^2 R_{sg}$ of the [19]. An ideal passive phase-shifter that uses a spin-filter JJ with a $t = 3.0$ nm thick barrier, for example, has a dephasing time comparable with that of circuits with SIFS π -junctions [78], and can increase by at least a factor 100 compared to that found in circuits with standard metallic π shifters [110, 252]. In standard metallic SFS JJs, in fact, typical resistances are at most $\sim 1 \Omega$, while R_{sg} for the junction with a 3.0 nm thick barrier at dilution temperature is at least 350Ω .

Spin-filter JJs, while giving a wide range of peculiar phenomena and showing suitable electro-dynamics parameters for novel hybrid superconducting implementations in quantum devices, have two fundamental issues. First, the area of these devices is larger than that of more standard non-magnetic JJs typically employed in superconducting quantum circuits. In qubits, for example, typical junctions areas are of the order of μm^2 or less. Therefore, in order to integrate such devices inside more complex circuits, it is extremely important to scale the dimensions of the devices. In addition to this, there are few I_f barriers in nature, and at the moment only GdN-devices have shown Josephson effect, strongly reducing the alternatives in the choice of the barrier materials. SIsFS JJs, instead, are much more flexible for practical implementation in superconducting electronics. In these devices, we can play with several parameters to meet specific circuit requirements: the thickness and the materials of the superconducting electrodes, the insulator, the superconducting interlayer thickness, the ferromagnet and its geometrical parameters. Moreover, as anticipated in Sec. 1.1, SIsFS JJs combine the presence of a residual magnetization in the barrier with the high $I_c R_N$ products of a tunnel JJ, which is a fundamental request for certain applications, such as CMRAM devices compatible with a Single Flux Quantum (SFQ) logic. Such low-dissipative behavior may be useful also in view of the integration of ferromagnetic JJs in qubits.

TABLE 4.3: Py SIsFS JJs thickness t_{Py} and diameter D of the analyzed devices

t_{Py} (nm)	D (μm)
3	1
3	2
3	3
10	5
15	5
15	10
15	20

In this section, we hence report a comparative analysis of ferro-tunnel JJs, extending our approach and the methods employed for the estimation of the electrodynamics parameters (Q , R_{sg} , C) in spin-filter JJs to SIsFS JJs with different ferromagnetic materials, thicknesses of the electrodes and the barrier, and areas.

As it occurs in NbN-GdN-NbN JJs, SIsFS JJs reported in literature have often large areas (of the order of hundreds of μm^2). The scaling of tunnel SFS JJs in superconducting circuits can be achieved by both:

- providing a different type of I_c digital tuning that reduces the occupied area by the READ, WRITE and CONTROL circuits (Sec. 1.1) [37–42];
- reducing the area of the SIsFS JJ itself [42].

For what concerns the former point, in Ref. [40], it was experimentally demonstrated that the current-level separation between two digital states obtained with magnetic field pulses in PdFe-based JJs is enhanced when assisting the magnetization of the ferromagnetic interlayer using RF radiation. The percentage difference between the high- and low-level critical currents, $\Delta I = (I_{\text{high}} - I_{\text{low}})/I_{\text{high}}$, increases up to a factor 2 compared with the case in absence of RF radiation. The motivation for which it happens has been related to the instability in the magnetic structure of the PdFe in presence of MW fields [40, 253, 254]. This suggested that the CMRAM switching could occur, in principle, completely replacing the magnetic-field pulsed addressing with RF signals [21]. This opens the doors to a full RF and local manipulation of the memory state for the CMRAM integrated in SFQ logic [40, 42].

In Ref. [40], the JJs were fabricated in collaboration with Hypres, inc. and the ISSP in Moscow. First, a Nb- AlO_x -Nb trilayer with thicknesses of the electrodes of $d_b = 120$ nm and $d_s = 15$ nm, and an AlO_x thickness $t_l \sim 1$ nm was prepared in Hypres, inc.. Then, the counterelectrode was etched at the ISSP down to ~ 10 nm, and a PdFe alloy ($t = 14 - 18$ nm) was deposited, covered by a Nb top electrode with $d_t = 150$ nm [40]. The area of the JJ is $100 \mu\text{m}^2$. Nevertheless, PdFe is not suitable for the realization of reduced devices because of its percolative nature [255], thus limiting the scalability. The search for other ferromagnetic materials, which do not show significant

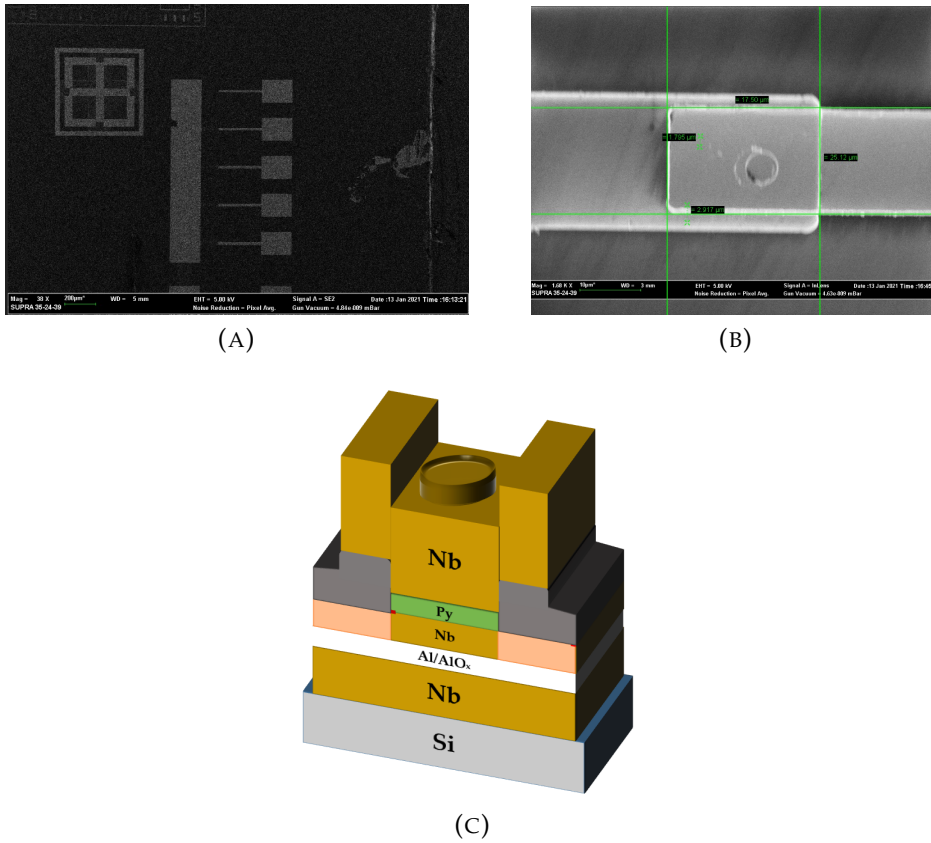


FIGURE 4.10: In (a) and (b): SEM pictures of Py-based SIsFS JJs fabricated in Naples with areas $\sim 7 \mu\text{m}^2$. In (c): scheme of the SIsFS JJs with Py barrier: in grey, the Si substrate, in dark gray the SiO insulating window and in brown residual anodized Nb. Thicknesses and dimensions are reported in the text

changes in their magnetic properties when reduced, leads us to the permalloy Py, i. e. an alloy made of iron and nickel [256].

The Py is a strong ferromagnet characterized by higher coercive H_c and saturation fields H_s compared to the soft PdFe (Tab. 4.4). Nevertheless, these parameters both depend non-monotonically on the volume: first, decreasing the F thickness, H_c increases until we reach the single-domain regime (critical volume V^*); below this value H_s and H_c decrease with V [233], giving the possibility to achieve more suitable values for Josephson CMRAM, while reducing the area.

In Ref. [42], we report the results obtained on a sample batch of circular SIsFS JJs with Py ferromagnetic barrier fabricated in Naples, scaled down to $7 \mu\text{m}^2$. To our knowledge, they are the smallest SIsFS JJs reported in literature. The fabrication procedure employed is essentially the same as in Ref. [40] and details are reported in Ref. [42]. A sketch of the device is reported in Fig. 4.10, with dimensions: $d_t = 400 \text{ nm}$, $d_b = 200 \text{ nm}$ and $t_1 = 1 - 2 \text{ nm}$. The intermediate s layer has thickness $d_s = 30 \text{ nm}$, while the Py thicknesses analyzed are collected in Tab. 4.3.

In Fig. 4.11, we report the $I_c(H)$ curves measured at 4.2 K using the Heliox

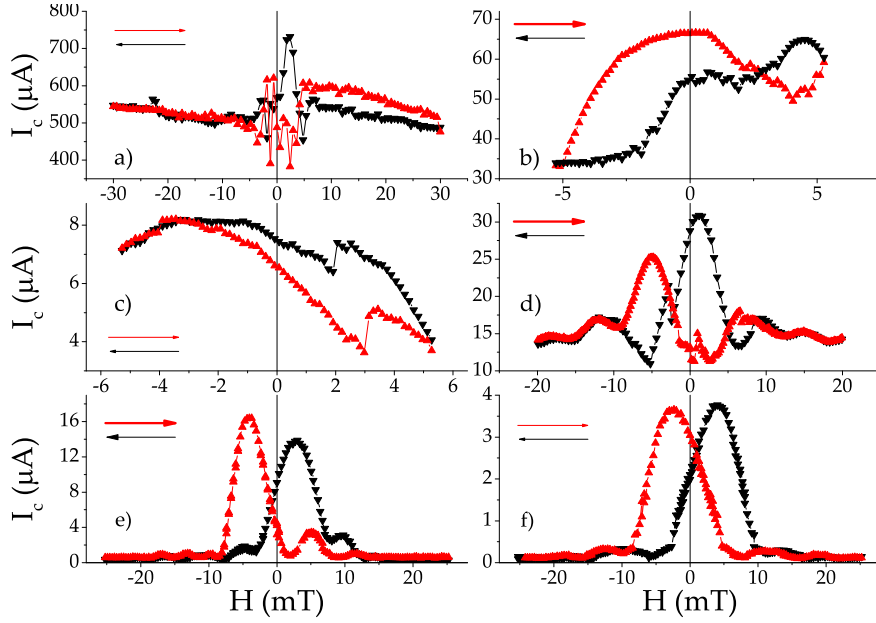


FIGURE 4.11: $I_c(H)$ curves for different SIsFS samples with Py barriers: (a) $t = 15$ nm and $D = 20$ μm , (b) $t = 15$ nm and $D = 15$ μm , (c) $t = 15$ nm and $D = 5$ μm , (d) $t = 10$ nm and $D = 5$ μm , (e) $t = 3$ nm and $D = 5$ μm , (f) $t = 3$ nm and $D = 3$ μm .

set-up in Sec. 2.1 for SIsFS with variable thickness t and area $A = \pi(D/2)^2$ (the $I_c(H)$ in (e) refers to a square JJ with $A = 25$ μm^2).

The Py has a coherence length of few nanometers, i. e. for large Py thicknesses the system is particularly sensitive to the magnetic phenomena occurring in the F layer. Even if $d_s < \lambda$, the SIsFS JJ for $t \geq 10$ nm behaves as a tunnel SIs JJ in series with a FS bilayer, and the $I_c(H)$ modulation is far from a typical Airy pattern, as it occurs for JJs in Fig. 4.11 (a)-(d). Here, ramping the field from positive to negative values, and *viceversa*, the $I_c(H)$ curves do not coincide, and a set of chaotic peaks, related to changes in the magnetic structure in the FS bilayer, prevents the use of the JJs as switching element. Nevertheless, reducing the thickness of the F layer to 3 nm, we gradually recover an Airy $I_c(H)$ (or Fraunhofer for (e)) curve (Fig. 4.11 (e) and (f)), suggesting that the JJ behaves as a single JJ.

The $I_c(H)$ curves in Fig. 4.11 are characterized by a shift in field in the opposite direction to the one commonly observed in SFS JJs. This is possibly due to inverse proximity effect phenomena [257–259]. From the practical point of view, this does not affect the CMRAM WRITE operation, since with the same sequence in Fig. 1.5, the high- and low-level current states are simply inverted. The memory effect for the smallest Py-based JJs, in fact, has been demonstrated in Ref. [42] at a working point $H_{\text{wp}} = 0$. The maximum separation between the high- and low-logic state ($\Delta I_{\text{max}} \sim 40\%$) was obtained with a magnetic pulse amplitude of 50 mT, here set up to $\sim H_s$ [258]. Compared with PdFe-based SIsFS JJs in Ref. [38–40], in which the working point was 0.12 mT, the maximum ΔI is a factor two higher. Nevertheless, also the amplitude of the field pulses was one order of magnitude higher compared with that used

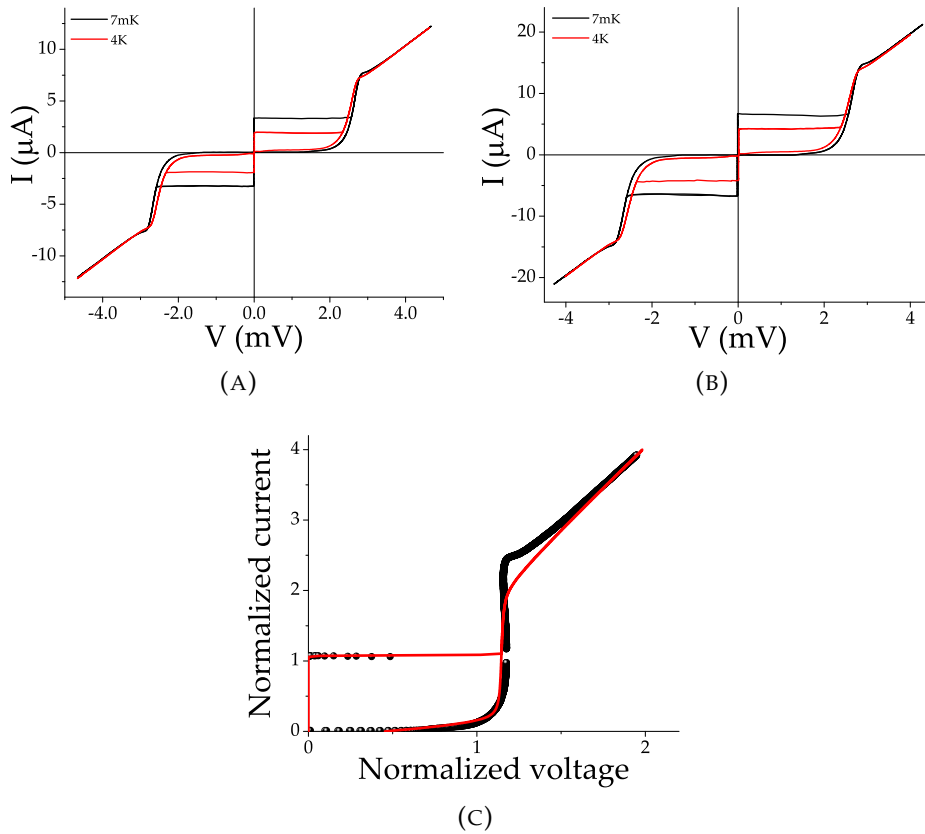


FIGURE 4.12: In (a) and (b): $I(V)$ curves at 7 mK and 4.2 mK in **SI/FS JJs** with **Py** of 3 nm with areas $3 \mu\text{m}^2$ and $7 \mu\text{m}^2$, respectively; in (c), example of a **TJM** model fit of the $I(V)$ curves at 7 mK for the smallest **JJ** [260]. Here the current is normalized to I_c and the voltage to V_s

to tune **PdFe**-based **SI/FS JJs**.

Standard optical lithography techniques were pushed to their limit with the aim to reach areas of $3 \mu\text{m}^2$, in order to achieve more suitable H_c and H_s values, but further reduction of the area must be achieved to meet specific circuit requirements for superconducting electronics, possibly using **Electron-Beam-Litography (EBL)** or **Focused Ion Beam (FIB)** techniques. We here show the first electrodynamics characterization at $\sim 10 \text{ mK}$ and at $\sim 4.2 \text{ K}$ of **SI/FS JJs** with **Py** thickness $t = 3 \text{ nm}$, and the smallest areas achieved ($3 \mu\text{m}^2$). A comparison with devices with area of $7 \mu\text{m}^2$ [42] is also reported.

R_N in **Py**-based **SI/FS JJs** is temperature-independent, and it is of the order of 362Ω for the **JJ** with area $3 \mu\text{m}^2$ and 193Ω for the **JJ** with area $7 \mu\text{m}^2$ [259, 260]. $I_c R_N$ products at 4.2 K are of the order of $700 \mu\text{V}$ for the **JJ** with area $3 \mu\text{m}^2$ and increases to $800 \mu\text{V}$ in the **JJ** with area $7 \mu\text{m}^2$ [259, 260]. These values are comparable with those reported in Ref. [38, 39, 226] on **SI/FS JJs** with **PdFe** barriers, and suitable for **CMRAM** devices working at 4 K .

In Fig. 4.12, we report the $I(V)$ curves measured with the Triton (Sec. 2.2) of **JJs** with area $3 \mu\text{m}^2$ (a) and $7 \mu\text{m}^2$ (b), which show a clear underdamped regime due to the presence of the tunnel **I** barrier. The amplitude of the hysteresis,

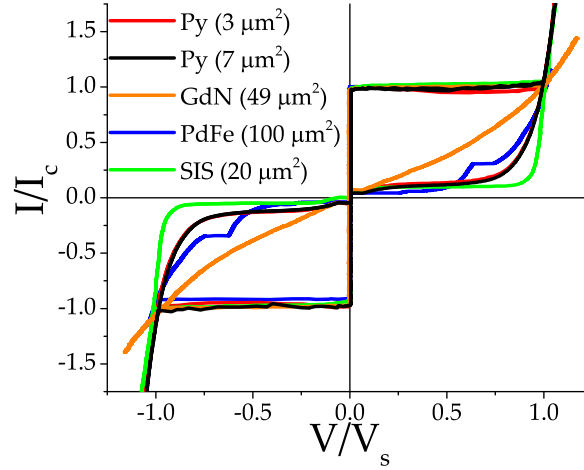


FIGURE 4.13: Comparison between the normalized $I(V)$ curves at 4.2 K of Py-based **SIsFS JJs** with areas $3 \mu\text{m}^2$ and $7 \mu\text{m}^2$, PdFe-based **SIsFS JJ**, a spin-filter **JJ** with $t = 2.5 \text{ nm}$ and a non-magnetic tunnel **SIS JJ**, taken here as a reference

defined as $(I_c - I_r)/I_c$, is of the order of $95 - 97\%I_c$ at low temperatures (respectively for **JJs** with $7 \mu\text{m}^2$ and $3 \mu\text{m}^2$). These values are comparable with those found on non-magnetic **SIS JJs** [248]. In Fig. 4.12 (c), we show an example of **TJM** fit of the $I(V)$ curve measured at 7 mK on the smallest **JJ**, which is in good agreement with the experimental data [260]. At 7 mK, the **JJ** with area $3 \mu\text{m}^2$ has a $R_{\text{sg}} = 4 \text{ k}\Omega$, while the device with $7 \mu\text{m}^2$ has a $R_{\text{sg}} = 2 \text{ k}\Omega$, in agreement with the relation $R_{\text{sg}}A = \text{const}$ [248]. The quality factor Q_0 estimated is $\gg 10$, consistently with the nearly squared shape of the $I(V)$ curve.

In Fig. 4.13 a comparison of the $I(V)$ curve subgap branch at 4.2 K in spin-filter devices, PdFe- and Py-based **SIsFS JJs** is reported. As an additional term of comparison, we add the $I(V)$ curve of **SIS JJ** made of Nb- AlO_x -Nb fabricated with the same procedure of the **SIsFS JJs** in Ref. [42]. As one can observe, the subgap branch in **SIsFS JJs** with Py barriers shows slightly larger subgap conductance compared with the **SIS JJ**, and much smaller than the one in PdFe and the spin-filter **JJ**. This behavior is consistent with the estimated R_{sg} and Q_0 by using the **TJM** model on the measured $I(V)$ curves, and suggests that Py-based **SIsFS JJs** may be successfully integrated into hybrid quantum devices.

Finally, in Tab. 4.4, we collect the I_c at 20 mK, the capacitance of the barrier C estimated with the **TJM** model, the ratio E_J/E_c , and the magnetic parameters for the pulsed I_c tuning on spin-filter **JJs** and the Py-based **SIsFS JJs**, compared with those in PdFe devices: the amplitude of the magnetic pulse H_s and the coercive field H_c . The Josephson energy E_J for spin-filter **JJs** are reported in Tab. 4.1, while E_J estimated from the I_c in Tab. 4.4 for Py-based **SIsFS JJs** is 1.7 THz for the smallest **JJ** and 3.3 THz for the largest one. These values are two order of magnitudes larger than those in standard superconducting qubits [204, 238].

The order of magnitude of the ratio E_J/E_c for the investigated spin-filter

TABLE 4.4: Estimated E_J/E_c ratios in ferro-tunnel JJs at dilution temperatures 20 mK and magnetic parameters for the pulsed I_c tuning: saturation field H_s and coercitive field H_c . It is here reported also the values of the capacitance C , the charging energy E_c , and the critical current I_c measured at low-temperatures, while E_J for spin-filter JJs can be found in Tab. 4.1 and that of Py-based devices in the text

	I_c (μA)	C (pF)	E_c (Hz)
PdFe [41] ($A = 100 \mu\text{m}^2, t = 14 - 18 \text{ nm}$)	-	~ 6	$3 \cdot 10^6$
GdN ($A = 49 \mu\text{m}^2, t = 3.0 \text{ nm}$)	4.75	1.1	$1.75 \cdot 10^7$
GdN ($A = 49 \mu\text{m}^2, t = 3.5 \text{ nm}$)	0.489	0.26	$7.43 \cdot 10^7$
GdN ($A = 49 \mu\text{m}^2, t = 4.0 \text{ nm}$)	0.0290	0.018	$1.07 \cdot 10^9$
Py ($A = 3 \mu\text{m}^2, t = 3 \text{ nm}$) [259, 260]	3.28	0.10	$190 \cdot 10^6$
Py ($A = 7 \mu\text{m}^2, t = 3 \text{ nm}$) [259, 260]	6.69	0.25	$76 \cdot 10^6$
	E_J/E_c	H_s (mT)	H_c (mT)
PdFe [41] ($A = 100 \mu\text{m}^2, t = 14 - 18 \text{ nm}$)	-	~ 2	~ 0.5
GdN ($A = 49 \mu\text{m}^2, t = 3.0 \text{ nm}$)	10^5	> 5	0.9
($A = 49 \mu\text{m}^2, t = 3.5 \text{ nm}$)	$3 \cdot 10^3$	> 5	0.2
($A = 49 \mu\text{m}^2, t = 4.0 \text{ nm}$)	13	-	-
Py ($A = 3 \mu\text{m}^2, t = 3.0 \text{ nm}$) [259, 260]	8900	-	-
Py ($A = 7 \mu\text{m}^2, t = 3.0 \text{ nm}$) [259, 260]	$4 \cdot 10^4$	> 50	23

junctions scales with the thickness from 10^5 to 10, suitably for applications ranging from flux-qubits [147, 204] to CPB and transmon circuits [23] (Tab. 4.4). Nevertheless, adapting the area of the devices to $\sim 1 \mu\text{m}^2$, lower values of E_J/E_c can be achieved [145, 147, 204]. Moreover, reducing the junction area by a factor ~ 50 , R_{sg} should increase up to values of the order of 50 – 100 k Ω , thus further reducing quasiparticle noise [23]. The same arguments are valid for the junction with $t = 4.0 \text{ nm}$ GdN barrier, which is characterized by a subgap resistance ~ 10 times higher [23], and Py-based devices, in which $E_J/E_c \sim 10^4$.

Towards SFS active quantum devices: future perspectives

The discussion of the outcomes of my work on SFS JJs has been an occasion to review also the progress made in these last twenty years on the understanding of the physics for these devices. While a full exploit of triplet superconductivity for applications needs time to get mature ideas, a better understanding of the electrodynamics, as discussed in Chap. 4, has an immediate impact on several applications. I will mostly focus on the possibility of embedding ferrotunnel JJs as switching elements in a real quantum circuit, and specifically inside a transmon [25].

The Josephson technology took a great leap forward in the field of quantum computation. Superconducting qubits exploit the intrinsic anharmonic potential energy of a JJ to isolate a two-level system [147, 204, 261]. They earned the attention of lead industries such as Intel [262], IBM [263], Google [264] and Rigetti [265], since they are easy to fabricate on a chip and in principle scalable. They can also be easily manipulated, controlled and read by commercial electronics [147, 204, 261]. Thus, the scientific community and the industries have made a strong effort to find novel qubit designs and combinations of materials to reduce the unavoidable decoherence due to the coupling of the qubit with the environment [266–271].

One of the most famous and promising circuit design is the transmon qubit [145]. A transmon qubit is a charge-insensitive Cooper pair box (CPB), in which three major modifications are implemented [145] (see Fig. 5.1 for the circuit schematics):

- the ratio E_J/E_C increases to values of the order of ~ 100 because another capacitance is added in parallel to the Josephson element, giving as a result that the energy levels are almost insensitive to charge fluctuations (Fig. 5.1 (b)), and characterized by a weak loss of the anharmonicity [145], as discussed in App. C.2.1;

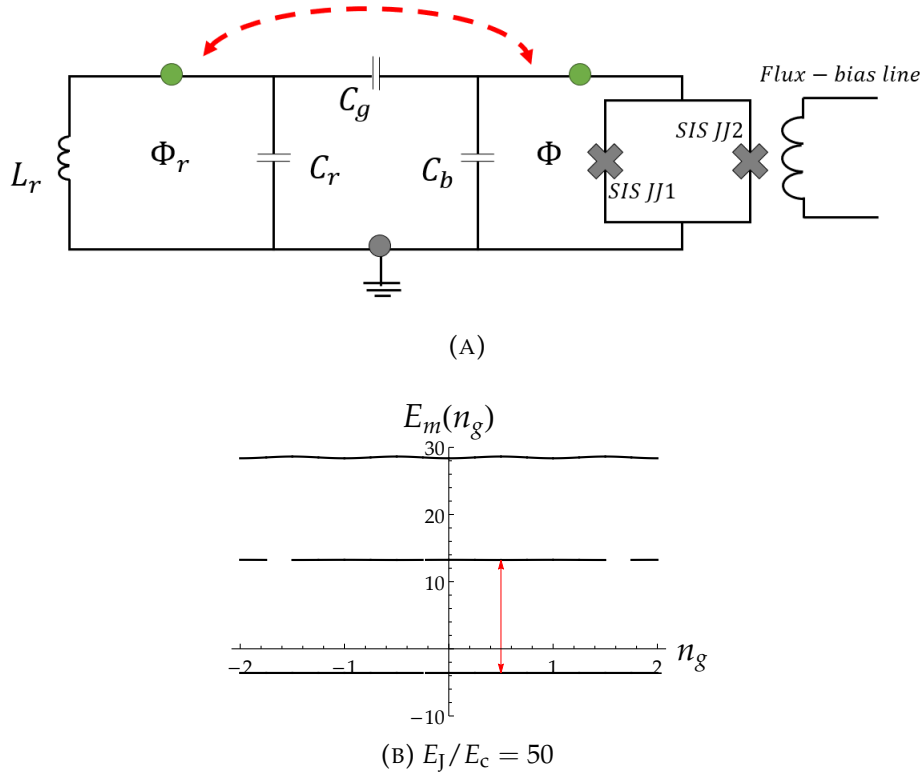


FIGURE 5.1: In (a): circuitual schematics of a transmon. In green, the active nodes are highlighted, while the grey circle refers to the ground node. The coupling between the two flux nets is depicted through the coupling gate capacitance C_g . The flux bias line is inductively coupled. In (b): first three eigenenergies in a transmon circuit with ratio $E_J/E_c = 50$. The flatness of the energy levels is the first footprint for the reduction of the charge dispersion in this device (App. C.2.1)

- the qubit in this configuration is capacitively coupled to a superconducting transmission line used to read the state of the qubit (schematized as an $L_r C_r$ oscillator in Fig. 5.1 (a)), without interrogate the qubit itself, i. e. allowing for a **Quantum Non-Demolition (QND)** measurement of the qubit state, as discussed in App. C.2.2. The name *transmon*, in fact, is an abbreviation of *transmission-line shunted plasma oscillation qubit* [145];
- the single JJ of the standard CPB is replaced by a DC-SQUID, i.e. a superconducting loop interrupted by two JJs, maximizing the tunability of E_J by means of an external magnetic flux, as discussed in App. C.2.3.

Compared with a **Cooper pair box (CPB)**, in which the bias capacitance C_b is of the order of hundreds of attofarads [272, 273], the transmon total capacitance C_Σ is

$$C_\Sigma = \frac{(C_b + C_g)C_r + C_b C_g}{C_r + C_g}, \quad (5.1)$$

and depends on the resonator capacitance C_r , which can be of the order of hundreds of femtofarads [274, 275]. Thus, the charging energy E_c in this

system is strongly reduced compared to a CPB design, protecting the system from charge noise [145].

Fully digital tuning of the qubit frequency is desirable to scale quantum processors to a higher number of qubits [25, 276]. For instance, the qubit frequency in transmons is typically changed by flux-bias signals, which are continuously applied during any logic-gate operations, affecting the coherence and the fidelity of the gates [145, 204]. Different control protocols that go in the direction of hybrid scalable systems are highly welcomed [8, 25, 276, 277].

We here propose to integrate tunnel SFS JJs in a transmon circuit to address an alternative tuning of the qubit frequency, referring to this novel element as *ferro-transmon* [25]. As discussed in Sec. 1.1, external field pulses on SFS JJs allow for the transition from one current level to another (from a high-value (low-value) I_c^{high} (I_c^{low})), and as a consequence from one E_J level to the other. This is similar to what proposed in Sec. 1.1 for Cryogenic Magnetic Random Access Memory (CMRAM) WRITE operation, but we stress that in our proposal the pulse sequence can be opportunely modified to achieve the desired separation between the two current levels [25]. Such a digital solution may help in reducing the flux-noise in transmons, since the application of the field is limited to the pulse sequence operation [25].

The ferromagnet embedded in a JJ paves the way to the investigation of new problems. A transmon turns as a powerful sensor for the physics of the junction itself [278], and may help in answering questions like: does the spin-triplet superconductivity contribute to the high-frequency dynamics? How much the magnetization dynamics affect the transport? What is the nature of noise sources in SFS JJs?

Studying noise sources affecting quantum mechanical systems is of great importance to quantum information, quantum sensing and the fundamental understanding of microscopic noise mechanisms [204, 279–281], and it was already implemented across many qubits platforms, including Nitrogen-Vacancy Centers (NVC) [282, 283], nuclear spins [284, 285] and cold atoms [286], while it is still an unexplored field for ferromagnetic devices. In a recent work by Sung et al., for instance, the multi-level energy structure of a transmon can be exploited to implement a Quantum Noise Spectroscopy (QNS) protocol [278]. One of the ideas proposed in this work is to exploit the sensitivity of a transmon qubit to noise to actively detect both the high- and low-frequency noise in ferro-tunnel JJs [25, 284, 287–290].

The fundamental requirements for our ferro-transmon proposal are to design a circuit for which:

- the ratio E_J/E_c remains of the order of $\sim 50 - 100$ in the two frequency levels;
- the anharmonicity $\alpha = -E_{c\Sigma}$ allows to define a two-level system;
- the operational frequency of the qubit must be easily accessed employing conventional experimental set-up and measurement protocol ($\omega_Q \in [4 - 8]$ GHz, limitation given by the High-Electron Mobility Transistor (HEMT) amplifiers typically used for the qubit Read-Out (RO), as discussed in Chap. 2);

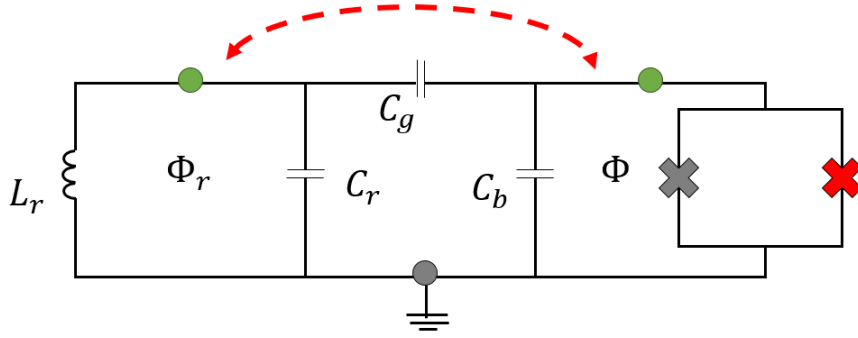


FIGURE 5.2: Ferro-transmon with a hybrid DC-SQUID circuit schematics: in red, the tunnel SFS JJ

- the two-levels separation must be of the same order of magnitude of typical tuning ranges in conventional flux-tuned transmon;
- the coupling between the resonator and the qubit must be sufficient to observe a dispersive shift in the resonator frequency of the order of tens or hundreds of megahertz.

As a first step, in the following sections, we will propose a ferro-transmon device with a tunnel SFS JJ that replaces one of the SIS JJs in the DC-SQUID (hybrid asymmetric DC-SQUID) [25]. We have also explored other configurations, such as a transmon with a single non-tunable SIS JJ capacitively coupled to a tunnel SFS JJ [25]. The analysis of the two circuits allows to get some prior estimation of the ferro-tunnel JJ parameters needed to build the ferro-transmon. As a term of comparison, we will consider the circuitual parameters and energies of a standard Al-based qubit, characterized within a collaboration with SeeQC-EU (App. C).

The pulsed critical current tuning has been simulated building a magnetic field sequence considering the $M(H)$ curve in the F barrier, which can be roughly described by a $\tanh H$ function, in which the magnetic and geometrical parameters of the SFS JJ enter into play: the coercive field H_c , the saturation field H_s and the residual magnetization M_r [43], which all affect the shape of the $I_c(H)$, as discussed in Sec. 1.1. Ferromagnetic materials show a large variety of magnetization curves, depending on their domain structure, and such analytical representation of the $M(H)$ can be reductive. In the future, more precise results will be achieved by explicitly considering the measured experimental $M(H)$ curve of the tunnel-SFS JJ under analysis, or by using the analytical formula

$$M(H) = \frac{2M_s}{1 + e^{-b(H \pm H_c)} - 2M_s'} \quad (5.2)$$

with b phenomenological parameter that weights the squareness of the $M(H)$ loop [189].

In the former ferro-transmon proposal (Sec. 5.1), the integration of the ferro-tunnel JJ in the DC-SQUID allows to get suitable frequencies with standard capacitance values [25]. For this system, we will show a comparison between

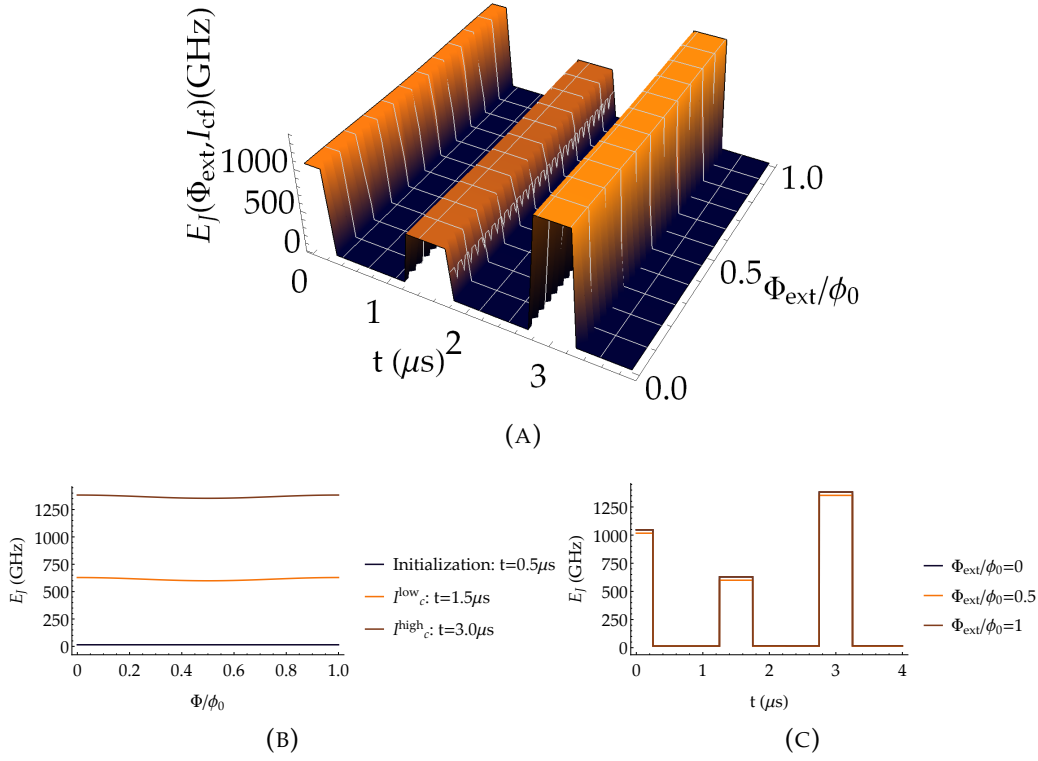


FIGURE 5.3: In (a): 3D-Plot of the total Josephson energy $E_{J\Sigma}$ in a ferro-transmon with a PdFe-based **SI_sFS JJ** in the SQUID. In (b): 2D-plot of $E_{J\Sigma}$ at a fixed the current level state (initialization, low- and high-current level states). In (c): 2D-plot of $E_{J\Sigma}$ at a fixed flux-field Φ_{ext}/ϕ_0

the results achieved considering PdFe- and Py-based **SI_sFS JJs**, analyzed in Sec. 4.2. We will demonstrate that suitable frequencies can be obtained by reducing the critical current of the tunnel **SFS JJ** of one order of magnitude [25]. This can be easily achieved by scaling the dimensions of the junctions to typical areas in transmon devices. As discussed in Sec. 4.2, Py-based **SI_sFS JJs** are promising for this application [259]. Therefore, we will report preliminary RF-simulations on the hybrid DC-SQUID ferro-transmon proposal using Py-based **SI_sFS JJs** [25].

We also investigate in Sec. 5.2 another circuitual proposal, in which the ferro-tunnel **JJ** capacitively couples to both the **SIS JJ** in the circuit and the resonator [25]. On one hand, this successfully allows to tune the frequency of the device by means of a pulsed magnetic field sequence. On the other hand, the coupling between the ferro-tunnel **JJ** and the resonator unavoidably affects the **RO**. The need to reduce this coupling and, at the same time, to obtain frequency values of the order of some GHz, imposes strong requirements on the resonator and the bias capacitances, C_r and C_b . Compared with standard Al-transmon devices, C_r must be increased by at least one order of magnitude, while C_b must be 30 times higher, affecting the scalability of the system.

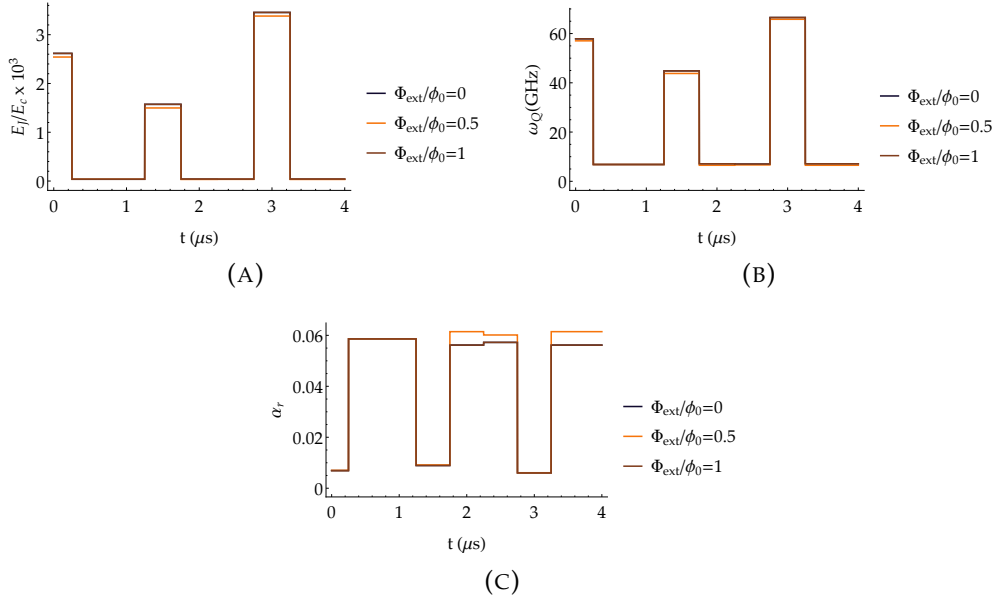


FIGURE 5.4: Ratio E_J/E_C , qubit frequency ω_Q and absolute value of the relative anharmonicity α_r for a ferro-transmon with a PdFe based SFS JJ as a function of the pulse sequence $H(t)$ used to pass from the low- to the high-current level state, at fixed external SQUID flux: $\Phi_{\text{ext}} = 0$ (blue curve), $\Phi_{\text{ext}} = 0.5\phi_0$ (orange curve) and $\Phi_{\text{ext}} = \phi_0$ (brown curve)

5.1 Ferro-transmon with a hybrid DC-SQUID

The hybrid ferro-transmon design is shown in Fig. 5.2: a tunnel-ferromagnetic JJ replaces one of the SIS JJs in the DC-SQUID.

The Hamiltonian of such circuit is equal to that of the conventional transmon in App. C.2, (Eq. C.17) with only one fundamental difference in the magnetic energy $E_m(\Phi_r, \Phi, \Phi_f)$, in which the flux due to the SFS plays a fundamental role. While fields orthogonal to the plane of the DC-SQUID give the flux-quantization law in Eq. C.11, magnetic fields directed in the plane of the SFS JJ induce a hysteretic Fraunhofer modulation for I_{cf} , due to the residual magnetization M_r , as discussed in Sec. 1.1. The magnetic energy for this circuit is

$$E_m(\Phi_r, \Phi) = \frac{\Phi_r^2}{2L_r} - E_{J\Sigma}(I_c, I_{cf}) \cos\left(\frac{\pi\Phi_{\text{ext}}}{\phi_0}\right) \quad (5.3)$$

$$\sqrt{1 + d^2(I_c, I_{cf}) \tan^2\left(\frac{\pi\Phi_{\text{ext}}}{\phi_0}\right)} \cos\left(\frac{2\pi\Phi}{\phi_0} - \varphi_0(\Phi_{\text{ext}}, I_c, I_{cf})\right), \quad (5.4)$$

where $\Phi = \Phi_I + \Phi_F^0$, and Φ_I (Φ_F) are the fluxes of the SIS (tunnel-SFS) JJ, $d(I_c, I_{cf})$ is the SQUID asymmetry and φ_0 is the phase shift. Therefore, using the same addressing depicted for CMRAM in Sec. 1.1, we can tune the total E_J of the circuit by means of external flux-field pulses, and as a consequence the

TABLE 5.1: Parameters of a ferrotransmon with a hybrid ferromagnetic SQUID for $\Phi_{\text{ext}} = 0$: E_J/E_c ratio, qubit frequency ω_Q and relative anharmonicity α_r in the high- ('1') and low-current level ('0') states

	PdFe		Py	
E_c (MHz)	400	200	400	200
E_J/E_c ('1')	$3.5 \cdot 10^3$	$6.9 \cdot 10^3$	150	297
E_J/E_c ('0')	$1.6 \cdot 10^3$	$3.2 \cdot 10^3$	55	112
ω_Q (GHz) ('1')	67	47	14	10
ω_Q (GHz) ('0')	45	2	8.7	6.2
α_r ('1')	0.005	0.004	0.04	0.03
α_r ('0')	0.008	0.006	0.09	0.07

ratio E_J/E_c , the qubit frequency ω_Q and the anharmonicity α_r . The charging energy E_c does not differ in the functional form from that of a conventional transmon circuit. In order to estimate E_J/E_c , ω_Q and α_r (App. C), we will use in the following the typical E_c in standard circuits, which is of the order of $E_c \sim 400$ MHz [238].

Given the flexibility of **SISFS JJs** for implementations in superconducting electronics, we here show a comparison between the results obtained considering devices with PdFe and Py barriers. In Tab. 5.1, we report a summary of the results obtained.

PdFe-based JJs The simulated 3D-Plot for the total Josephson energy $E_{J\Sigma}$ as a function of the pulse sequence and the SQUID flux-field is shown in Fig. 5.3 (A). $E_{J\Sigma}$ is calculated using common values of the Josephson energy for the **SIS JJ**, i. e. $E_J \sim 14$ GHz (Al-based **JJs** with lateral dimensions of ~ 250 nm, AlO_x thickness ~ 100 nm and $I_c \sim 30$ nA [238]). By fixing the critical current to its low- (high-) level, and by varying Φ_{ext} , we obtain the curves in Fig. 5.3 (B), while by fixing Φ_{ext} , we obtain the switching of the Josephson energy between the two-levels in Fig. 5.3 (C). As one can observe, the tunability due to external flux is strongly reduced compared with standard transmons, since $d \sim 1$ in both the high- and low-Josephson energy levels.

The ratio E_J/E_c passes from $\sim 1.5 \cdot 10^3$ in the low-level state and duplicates in the high-level state. It is slightly smaller when an external SQUID flux $\Phi_{\text{ext}} = 0.5\phi_0$ is applied. These values are expected to strongly decrease the charge dispersion compared with standard transmon circuits, since the ratio E_J/E_c is three orders of magnitudes higher. As a drawback, the absolute value of the relative anharmonicity is smaller than those of standard transmon circuits ($|\alpha_r| \sim 0.06$ [145, 238, 275]). The most important result is that the qubit frequency ranges from ~ 45 GHz to ~ 70 GHz, hard testing the typical equipment used in the laboratories for the transmon measurements.

TABLE 5.2: Parameters of a ferrotransmon with a hybrid ferromagnetic SQUID for $\Phi_{\text{ext}} = 0.5\phi_0$: E_J/E_c ratio, qubit frequency ω_Q and relative anharmonicity α_r in the high- ('1') and low-current level ('0') states

	PdFe		Py	
E_c (MHz)	400	200	400	200
E_J/E_c ('1')	$3 \cdot 10^3$	$6.7 \cdot 10^3$	75	150
E_J/E_c ('0')	$1.4 \cdot 10^3$	$2.9 \cdot 10^3$	18.5	10
ω_Q (GHz) ('1')	65	46	6.3	7
ω_Q (GHz) ('0')	43	30	4.3	3
α_r ('1')	0.005	0.004	0.04	0.02
α_r ('0')	0.008	0.006	0.03	0.03

More suitable frequencies can be achieved by decreasing the critical current of the tunnel-SFS JJs. We expect that a decrease of I_{cF} down to hundreds or tens of nanoamperes can give more favorable results.

The I_c^{F} reduction can be achieved by decreasing the lateral dimensions of the SFS JJ down to some μm . As discussed in Chap. 4, while PdFe-based JJs can not be successfully reduced, Py-based JJs preserve all their magnetic properties reducing the dimensions in the submicron regime [291–293]. For $d_{\text{F}} \sim 3 \text{ nm}$ and $A \sim 3 \mu\text{m}^2$, we measured a $I_{\text{cF}} \sim 3 \mu\text{A}$. Within these values of J_c , the diameter of the circular JJ must be reduced down to 400 nm to get suitable qubit frequencies. The same may be achieved reducing $J_c^{\text{req}} \sim J_c/100$ adapting the SIS trilayer fabrication process, or by changing the electrodes materials. The future perspective is to explore all these possibilities.

Py-based JJs The magnetic parameters for Py-based SIsFS JJs reported in Tab. 4.4 are too high for applications within the Josephson technology, in particular if field pulses are used. Nevertheless, the reduction of the area of these devices may also lead to more suitable magnetic parameters in the near future.

In the following simulations, we have inverted the pulse sequence to take into account the inversion in the Fraunhofer pattern observed in these devices [42] [258] (Sec. 4.2). With the parameters in Tab. 4.4 and reduced area for the ferro-tunnel JJ, the qubit frequency is expected to decrease towards 8.7 to 14 GHz at zero external flux and towards 4.3 to 6.3 GHz at $\Phi_{\text{ext}} = 0.5\phi_0$ compared to the PdFe case. The ratio E_J/E_c decreases towards values of ~ 55 to ~ 150 for zero external flux, and towards ~ 75 to ~ 18.5 at half-flux quantum applied, in the low- (high-) level state, respectively (Tab. 5.1 and 5.2). The decrease in the E_J/E_c allows also to have anharmonicity comparable with those in conventional transmon circuits, while maintaining suitable E_J/E_c ratios (Fig. 5.5).

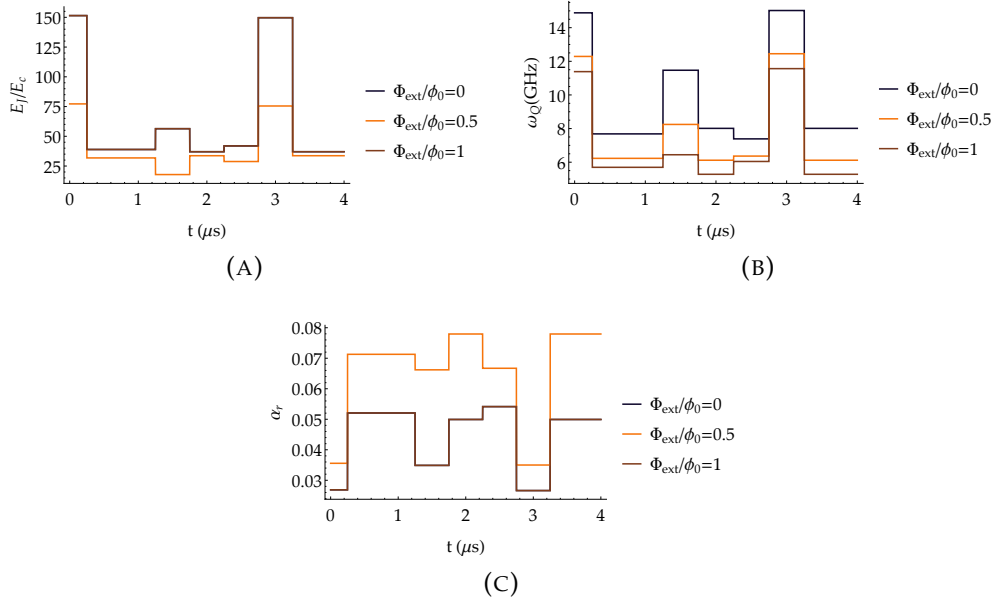


FIGURE 5.5: Ratio E_J/E_c , qubit frequency ω_Q and absolute value of the relative anharmonicity α_r for a ferro-transmon with Py based SFS JJs as a function of the pulse sequence $H(t)$ used to pass from the high- to the low-current level state

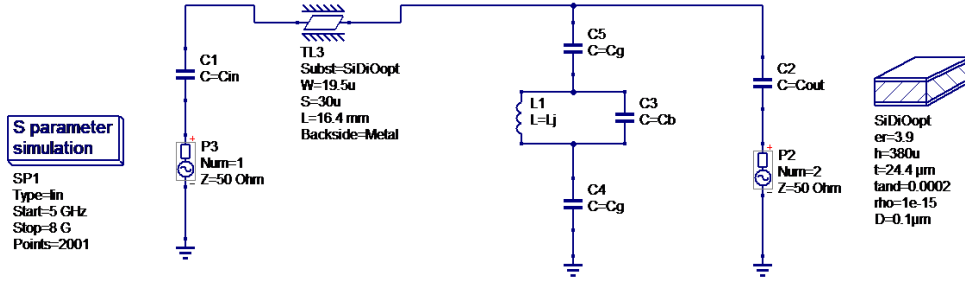


FIGURE 5.6: Ferro-transmon circuit schematics in the approximation of lumped elements, used for the RF-simulations with *QuCS Studio*

All these parameters can be further optimized decreasing the charging energy E_c of the circuit from 400 MHz to values of the order of few hundreds of megahertz. This is easily achievable, since to get $E_c \sim 200$ MHz, it is sufficient to increase the total capacitance C_Σ from ~ 50 fF to approximately ~ 100 fF.

RF-Simulations in the lumped circuit approximation Given the promising results obtained on this hybrid circuit design, we have finally performed some prior RF simulations in the lumped circuit approximation considering the parameters of the Py-based device. The final aim is to get a first estimation of the resonator response to the tuning of the ferromagnetic qubit.

While E_J is an energy scale that depends on the I_c of the SIS and the SFS JJs, E_c depends on the circuit design and how the JJs are capacitively

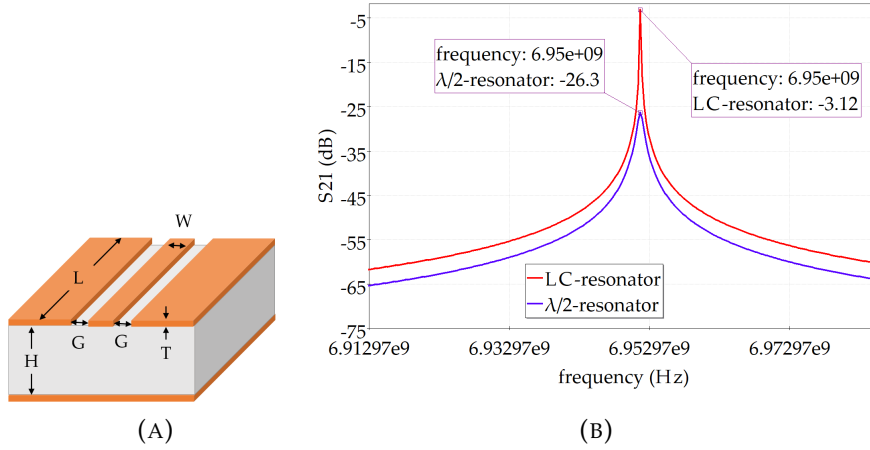


FIGURE 5.7: In (a): coplanar waveguide sketch with relative dimensions: the thickness of the insulating substrate (H) the length of the transmission line (L), the width of the coplanar waveguide (W), the gap between the ground and the transmission line (G), and the thickness of the conducting material of the resonator (T). In (b), comparison between the resonance of the $\lambda/2$ transmission line in (a) and the associated lumped LC circuit. S_{21} parameters have been calculated by sending a signal at port 2 and 3 of schematics 5.6, with power -20 dB

coupled to the resonator and the RO set-up. In the limit of a lumped circuit approximation, the qubit is represented as an inductance L_J in parallel to a capacitance C_b (Fig. 5.6), which is capacitively coupled by means of C_g to a transmission line with intrinsic capacitance C_r . In our simulations, the resonator is designed using a grounded coplanar waveguide with width W and length L . G is the gap between the line edges and the superconducting top ground plane. T is the thickness of the transmission line conducting material, while H is the thickness of the insulating substrate (Fig. 5.7 (A)).

As a first example, we considered a SiO substrate, with $\epsilon_r = 3.9$, magnetic permeability $\mu_r = 1$ and dielectric loss tangent $2 \cdot 10^{-4}$. The resistivity of the conducting material is here set of the order of ~ 0 to simulate a superconductor. We designed a $\lambda/2$ resonator, with $C_r = 470$ fF and the inductance $L_r = 1.11$ nH. The comparison between the simulated S_{21} parameter for the $\lambda/2$ coplanar waveguide and the associated lumped LC circuit is shown in Fig. 5.7 (B).

We capacitively coupled the resonator to a virtual VNA by means of C_{in} and C_{out} , connected to the ports $P3$ and $P2$ in the schematics in Fig. 5.6. The circuitual parameters that mostly affect E_c and the coupling between the resonator and the LC circuit β are C_g and C_b .

The best parameters that guarantee suitable E_J/E_c values, anharmonicities and frequencies are: $C_b = 90$ fF, $C_{in(out)} = 1$ fF, $C_g = 100$ fF,

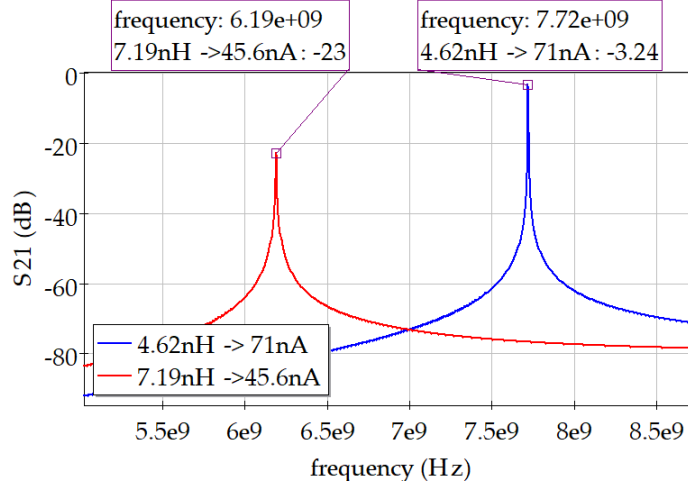


FIGURE 5.8: RF-simulations of the lumped element schematization of a qubit in a ferro-transmon with $C_b = 90$ fF, $C_{in(out)} = 1$ fF, $I_c^{high} = 71$ nA and $I_c^{low} = 45.6$ nA. The red (blue) line refers to the transmission signal S_{21} of the qubit in the low- (high-) current level state

$I_c^{high} = 71$ nA and $I_c^{low} = 45.6$ nA. Within these values, the qubit frequency can be tuned by $\Delta\omega_Q = 1.53$ GHz, passing from 7.72 GHz to 6.19 GHz in the high- (low-) level states. These values fall in an operational range suitable for the RO of the qubit state within a standard RF-equipment (Fig. 5.8). The resonator frequency ω_r in presence of the qubit is shifted of +150 MHz in the high-level state and of -60 MHz in the low-level state (Fig. 5.9). In this way, also the shift of the resonator due to the coupling with the qubit is easily detectable with standard heterodyne spectroscopy measurements (Chap. 2).

5.2 Transmon with a capacitively coupled tunnel-SFS JJs

Another ferro-transmon design is reported in Fig. 5.10: the DC-SQUID in the schematics of the conventional transmon circuit in Fig. 5.1 is replaced by a single SIS JJ capacitively coupled to a tunnel-SFS JJ. The protocol for the feasibility study for this circuit is the following:

- we first study the Hamiltonian of the circuit, in order to understand the role of the coupling between the different components;
- we find the resonance frequency of the circuit by approximating the JJs as harmonic oscillators. The inductance of the ferro-tunnel JJ is here tunable by means of an external magnetic field pulsed sequence;
- we re-introduce the anharmonicity in the potential energy of the JJs.

Circuit Hamiltonian We derived the circuit Hamiltonian using the protocol discussed in App. C.1, i. e. defying the flux-nodes per each net of the

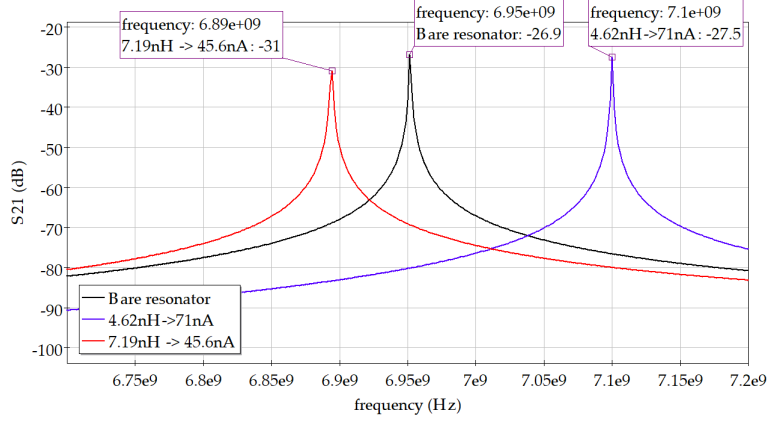


FIGURE 5.9: RF-simulations of the lumped element schematization of a ferro-transmon with $C_b = 90$ fF, $C_{\text{in(out)}} = 1$ fF, $C_g = 100$ fF, $I_c^{\text{high}} = 71$ nA and $I_c^{\text{low}} = 45.6$ nA and shift of the resonator in the two-level states. The red (blue) line refers to the transmission signal S_{21} of the transmission line resonator response to the qubit in the low- (high-) current level state. The black line is the resonator frequency in absence of the qubit (bare resonator)

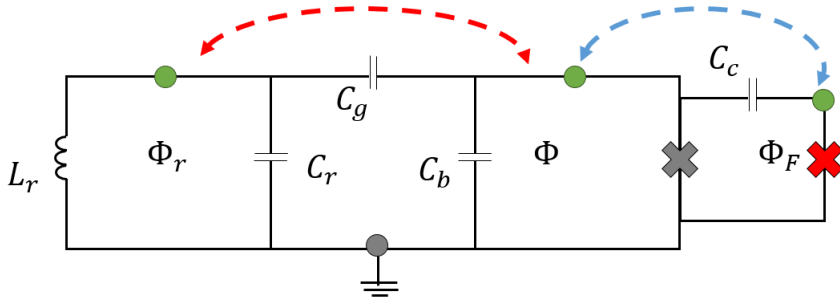


FIGURE 5.10: Ferro-transmon with an SIS coupled capacitively to a tunnel-SFS JJ: in red, the tunnel SFS JJ

circuit, with flux coordinates Φ_r , Φ and Φ_F . In this circuit design, an additional flux node in the SFS JJ net adds to the ones of the conventional transmon design discussed in App. C.2. The matrix \mathcal{M}^{-1} ,

$$\mathcal{M}^{-1} = \begin{pmatrix} C_g + C_r & -C_g & 0 \\ -C_g & C_b + C_g + C_c & -C_c \\ 0 & -C_c & C_c + C_F \end{pmatrix}, \quad (5.5)$$

that links the charge variables Q_r , Q and Q_F to generalized coordinates Φ_r , Φ and Φ_F , depends on the capacitances of the circuits. Here, the intrinsic capacitance of the SIS JJ is included in the bias capacitance C_b , and the capacitance of the SFS JJ is denoted as C_F .

The kinetic Hamiltonian \mathcal{H}_k of the circuit is given by the sum of the kinetic Hamiltonian of the resonator \mathcal{H}_{kr} ,

$$\mathcal{H}_{kr} = \frac{Q_r^2}{2C_{\Sigma r}}, \quad (5.6)$$

the qubit \mathcal{H}_{kQ} ,

$$\mathcal{H}_{kQ} = \frac{Q^2}{2C_{\Sigma Q}}, \quad (5.7)$$

and the SFS JJ \mathcal{H}_{kF} ,

$$\mathcal{H}_{kF} = \frac{Q_F^2}{C_{\Sigma F}}. \quad (5.8)$$

Here, the capacitance of the resonator $C_{\Sigma r}$ reads as

$$C_{\Sigma r} = \frac{C_g C_F (C_c + C_r) + C_c C_r (C_F + C_g) + C_b (C_c + C_F) (C_g + C_r)}{(C_b + C_g) (C_c + C_F) + C_c C_F}, \quad (5.9)$$

which reduces to C_r as occurs in a conventional transmon circuit (App. C.2) for $C_r \gg C_b, C_g, C_c, C_F$. The capacitance associated with the SIS JJ, instead, is

$$C_{\Sigma Q} = \frac{C_g C_F (C_c + C_r) + C_c C_r (C_F + C_g) + C_b (C_c + C_F) (C_g + C_r)}{(C_r + C_g) (C_c + C_F)}. \quad (5.10)$$

The capacitance $C_{\Sigma F}$ finally reads as

$$C_{\Sigma F} = \frac{C_g C_F (C_c + C_r) + C_c C_r (C_F + C_g) + C_b (C_c + C_F) (C_g + C_r)}{(C_c + C_g + C_b) C_r + C_g (C_b + C_c)}. \quad (5.11)$$

The hamiltonian of this proposal also includes three coupling terms:

- the first between the qubit and the resonator \mathcal{H}_{r-Q} ,

$$\mathcal{H}_{r-Q} = \frac{Q_r Q}{C_{\Sigma r-Q}}; \quad (5.12)$$

- the second between the qubit and the SFS JJ \mathcal{H}_{Q-F} ,

$$\mathcal{H}_{Q-F} = \frac{Q_F Q}{C_{\Sigma F-Q}}. \quad (5.13)$$

- the third between the resonator and the SFS JJ \mathcal{H}_{r-F} ,

$$\mathcal{H}_{r-F} = \frac{Q_r Q_F}{2C_{\Sigma r-F}}. \quad (5.14)$$

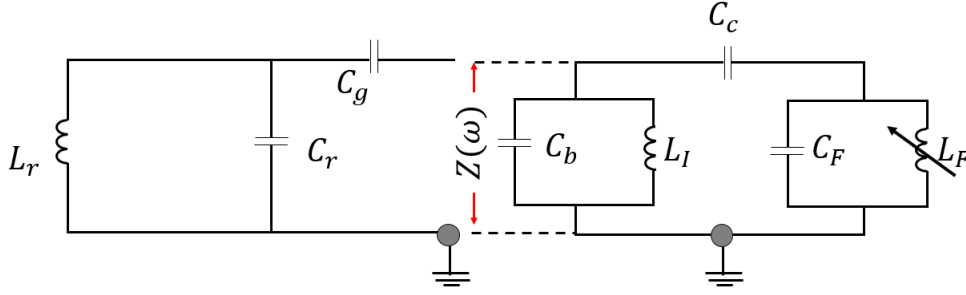


FIGURE 5.11: Linear approximation of a ferro-transmon with an SIS JJ and the SFS JJ are approximated by an harmonic oscillator. For the SFS JJ, the inductance can be tuned with external field pulses. $Z(\omega)$ is the impedance of the JJs net

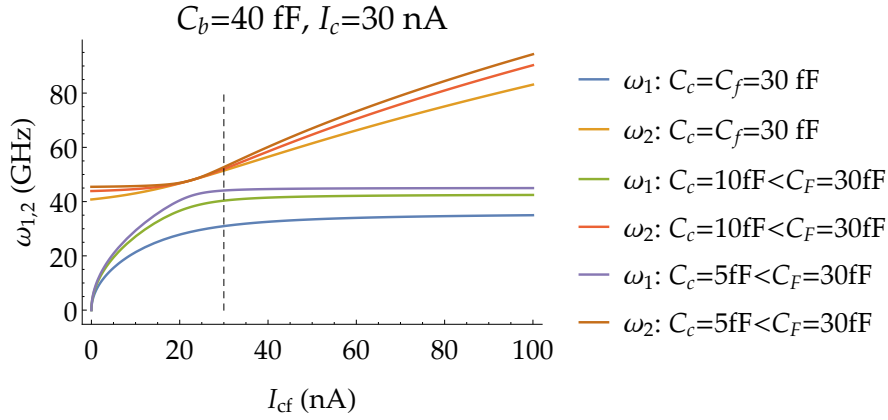


FIGURE 5.12: Resonance frequency $\omega_{1(2)}$ of a ferro-transmon with an SIS JJ coupled capacitively to a tunnel-SFS JJ as a function of the critical current of the SFS JJ I_{cf} for different values of the coupling capacitance C_c and the SFS JJ capacitance C_f . The dashed line represents the critical current of the SIS JJ

The coupling capacitance between the resonator circuit and the qubit one,

$$C_{\Sigma R-Q} = \frac{C_g C_F (C_c + C_r) + C_c C_r (C_F + C_g) + C_b (C_c + C_F) (C_g + C_r)}{(C_c + C_F) C_g}, \quad (5.15)$$

reduces to the one of a conventional transmon circuit if C_r is still larger than all the other capacitances of the circuit. Thus, provided that this condition is satisfied, the coupling between the qubit and the resonator can be adjusted to be similar to that in a conventional transmon circuit.

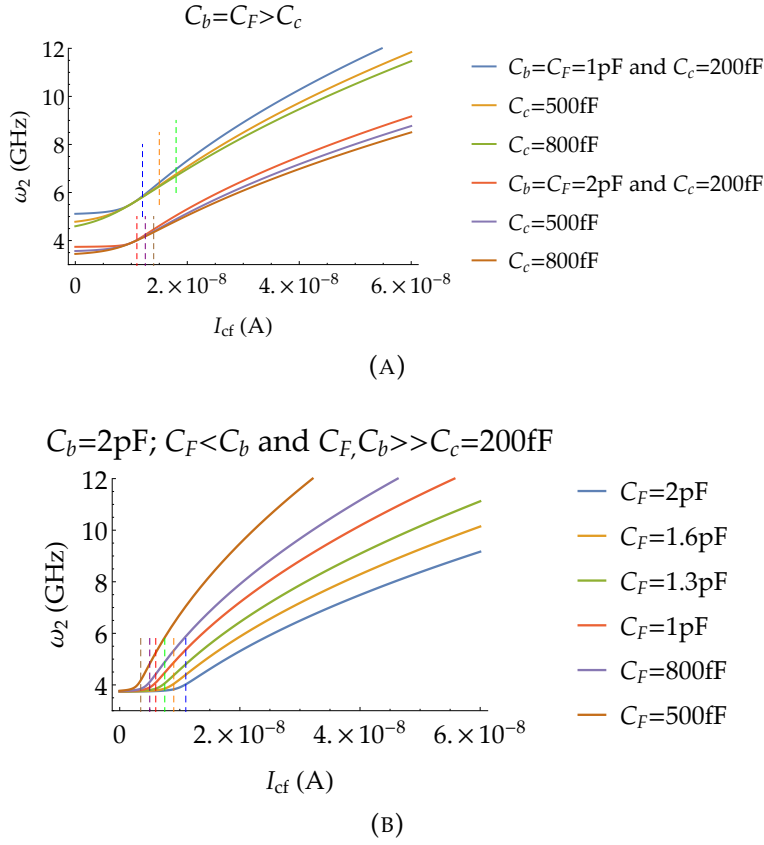


FIGURE 5.13: ω_2 of the linearized ferro-transmon circuit with an SIS capacitively coupled with an SFS JJ as a function of I_{cf} for different $C_b = C_F$ and C_c values. In (a), ω_2 vs. I_{cf} for different $C_b = C_F$ and C_c ; in (b) ω_2 vs. I_{cf} for C_c and C_b fixed and different $C_F < C_b$. Dashed lines represent the lower limit for I_{cf} , which satisfies the condition in Eq. 5.29

The coupling between the qubit and the SFS JJ depicted in Eq. 5.13, with $C_{\Sigma F-Q}$

$$C_{\Sigma F-Q} = \frac{C_g C_F (C_c + C_r) + C_c C_r (C_F + C_g) + C_b (C_c + C_F) (C_g + C_r)}{C_c (C_r + C_g)}, \quad (5.16)$$

is analytically equivalent to the coupling Hamiltonian between the resonator and the qubit (Eq. C.26). The SFS JJ, in fact, is nothing else than an oscillator. We can then define the normalized charge $n_F = Q_F / (2e)$ and flux $\phi_F = 2\pi\Phi_F / \phi_0$, so that \mathcal{H}_{Q-F} reads as

$$\mathcal{H}_{Q-F} = (2e)^2 \hat{n} \sqrt{\frac{\hbar\omega_F}{8E_{c\Sigma F}} \frac{f + f^\dagger}{\sqrt{2}C_{\Sigma Q-F}}}, \quad (5.17)$$

where f and f^\dagger annihilates and creates Cooper pairs in the SFS JJ net of the schematics in Fig. 5.10. We then expect that the presence of an SFS JJ will induce a shift in the qubit frequency depending on the coupling

$\hbar g_F = V_{0F}^{\text{rms}} \beta_F$, with $V_{0F}^{\text{rms}} = 2e \sqrt{\frac{\hbar \omega_F}{2C_{\Sigma F}}}$ and $\beta_F = C_c / (C_g + C_b + C_c)$. We here require that the **SIS** qubit and the **SFS JJ** circuits are not strongly coupled, i. e. we impose the condition

$$\frac{g_F}{|\omega_F - \omega_Q|} \ll 1, \quad (5.18)$$

which is nominally the dispersive regime (App. C.2.2).

The major drawback of this circuit design is that some coupling between the **SFS JJ** and the resonator, depicted by the coupling term in Eq. 5.14, arises. Here $C_{\Sigma r-F}$ is

$$C_{\Sigma r-F} = \frac{C_g C_F (C_c + C_r) + C_c C_r (C_F + C_g) + C_b (C_c + C_F) (C_g + C_r)}{C_c C_g}. \quad (5.19)$$

Also in this case, we can write the coupling Hamiltonian \mathcal{H}_{r-F} as

$$\mathcal{H}_{r-F} = 2e \hat{n}_f V_{0rf}^{\text{rms}} \beta_{r-f} (a + a^\dagger), \quad (5.20)$$

with $V_{0rf}^{\text{rms}} = 2e(\hbar \omega_r / (2C_r))^{1/2}$ and β_{r-f} is a coupling factor

$$\beta_{r-f} = \frac{C_g C_c}{(C_F + C_c)(C_b + C_g)}. \quad (5.21)$$

Since the **SFS JJ** must not perturb the resonator, and must only provide an alternative tuning of the frequency of the **SIS JJ**-qubit, we will require in the following that the coupling between the resonator and the **SFS** circuit must be neglectable, i. e. $\beta_{r-f} \ll \beta = C_g / (C_b + C_g)$. In other words we require that

$$\frac{C_g C_c}{(C_F + C_c)(C_b + C_g)} \ll \frac{C_g}{C_b + C_g} \implies \frac{C_c}{C_c + C_F} \ll 1. \quad (5.22)$$

Circuital harmonic approximation A rough estimation of the frequency of the qubit capacitively coupled to a **SFS JJ** can be obtained neglecting the anharmonic nature of its potential energy. Within this approximation, the total magnetic energy of the circuit is

$$E_m(\Phi_r, \Phi, \Phi_F) = \frac{\Phi_r^2}{2L_r} + \frac{\Phi^2}{2L_I} + \frac{\Phi_F^2}{2L_F(I_{cF})}, \quad (5.23)$$

where we identify the inductance of the **SFS JJ** as a variable inductance $L_F(I_{cF})$ dependent on the **SFS JJ** critical current I_{cF} . The schematics of the approximated circuit is reported in Fig. 5.11. The total impedance

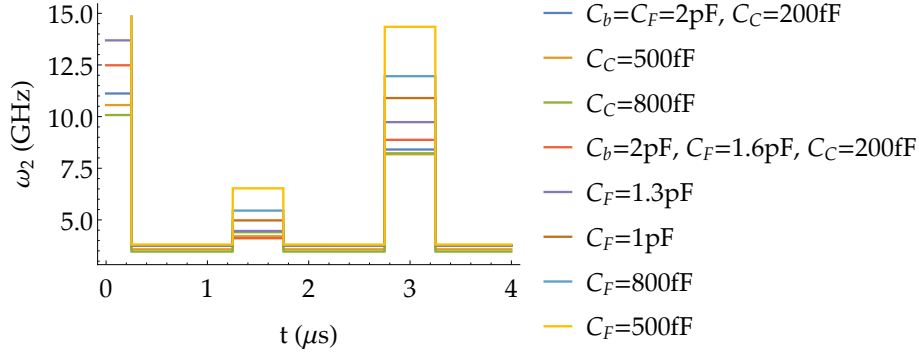


FIGURE 5.14: Tuning of ω_2 with H -pulses in a ferro-transmon with an SIS capacitively coupled to a tunnel-SFS JJ for the capacitances values in Fig. 5.13

$Z(\omega)$ at the input of the SIS + SFS net

$$Z(\omega) = \frac{i\omega L_I \left(1 - \left(\frac{\omega}{\omega_f^*}\right)^2\right)}{\left(1 - \left(\frac{\omega}{\omega_f^*}\right)^2\right) \left(1 - \left(\frac{\omega}{\omega_0}\right)^2\right) - \left(1 - \left(\frac{\omega}{\omega_f}\right)^2\right) \left(\frac{\omega}{\omega_0^*}\right)^2} \quad (5.24)$$

allows to find the resonance condition of the circuit. Here $\omega_0^{-2} = C_b L_I$ is the resonance frequency of the SIS oscillator, $\omega_f^{-2} = C_F L_F$ is the variable resonance frequency of the SFS oscillator, and $\omega_0^{*-2} = C_c L_I$ and $\omega_f^{*-2} = (C_c + C_f) L_I$ are the resonance frequencies of the coupled SIS and SFS circuits. The resonant condition is

$$\left(1 - \left(\frac{\omega}{\omega_f^*}\right)^2\right) \left(1 - \left(\frac{\omega}{\omega_0}\right)^2\right) - \left(1 - \left(\frac{\omega}{\omega_f}\right)^2\right) \left(\frac{\omega}{\omega_0^*}\right)^2 = 0, \quad (5.25)$$

with the two following positive solutions

$$\omega_{1,2} = \sqrt{\frac{2}{\omega_0^{*-2} + \omega_f^{*-2} + \omega_0^{-2}}} \sqrt{\frac{1}{1 \pm \sqrt{1 - 4 \frac{(\omega_0 \omega_f^*)^{-2} + (\omega_f \omega_0^*)^{-2}}{(\omega_0^{*-2} + \omega_f^{*-2} + \omega_0^{-2})^2}}}}, \quad (5.26)$$

both real for

$$\frac{(\omega_0 \omega_f^*)^{-2} + (\omega_f \omega_0^*)^{-2}}{(\omega_0^{*-2} + \omega_f^{*-2} + \omega_0^{-2})^2} \leq \frac{1}{4}. \quad (5.27)$$

Let us now pose some conditions on the parameters of the circuit. First of all, since the capacitances assume positive values, it is straightforward that the condition $\omega_f^* < \omega_f$ holds, i. e.

$$\frac{C_F}{C_F + C_c} < 1. \quad (5.28)$$

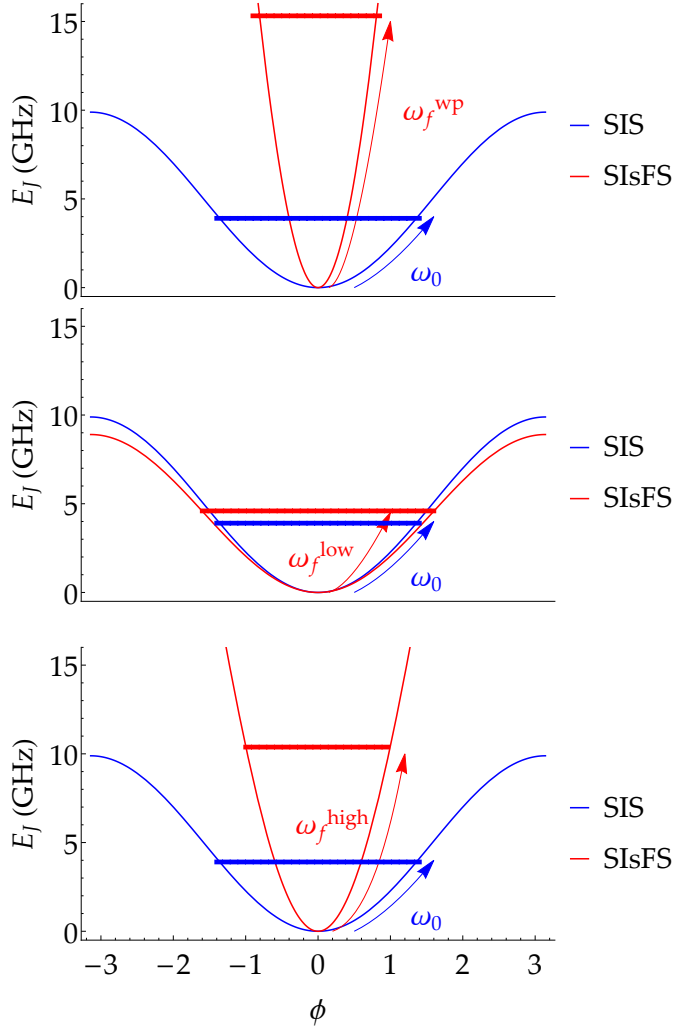


FIGURE 5.15: Comparison between the energy potential landscape of the SIS JJ and the SFS JJ in the initialization (wp), low- and high-level states

Moreover, we limit our study to tunnel SFS JJs, for which low-dissipation has been demonstrated and discussed all over this work. SIsFS JJs like the ones analyzed in this thesis, for instance, have higher critical currents compared with SIS JJs in transmons ($I_c^{\text{SIS}} \sim 30 \text{ nA}$ [274, 294]), and as a consequence lower inductances. Considering that we expect capacitances comparable with those in SIS JJs, ferro-tunnel JJs are characterized by higher resonance frequencies. This condition holds for arbitrary values of the inductances and the capacitances used in the circuit, and it can be also expressed as

$$L_F C_F < L_I C_b \implies \frac{C_F}{I_{cf}} < \frac{C_b}{I_{cl}}. \quad (5.29)$$

We will use standard critical current I_{cl} and bias capacitance C_b values for the SIS JJ in a transmon circuit ($I_{cl} \sim 30 \text{ nA}$ and $C_b \sim 40 \text{ fF}$) [238],

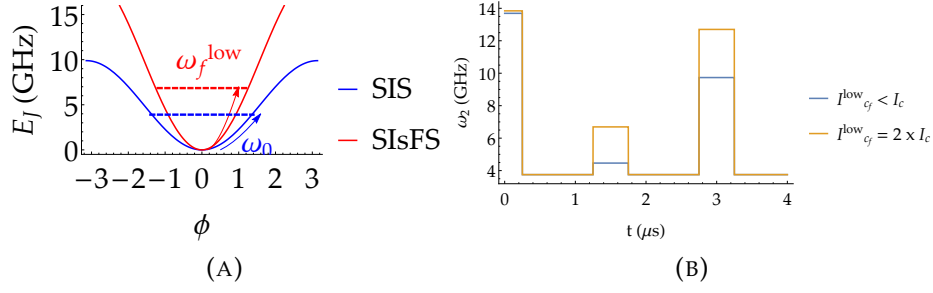


FIGURE 5.16: In (a): comparison between the energy potential landscape of the **SIS JJ** and the **SFS JJ** in the low-level states for $I_{cf} \sim 2I_c$. In (b): comparison between the qubit ω_2 resonance frequency tuning with the magnetic field sequence $H(t)$ for $I_{cf} \sim 2I_c$ and $I_{cf} < I_c$

thanks to which we can have charging energies of about 400 MHz ($C_g \sim 10$ fF). We will require that conditions 5.22, 5.28 and 5.29 hold, and that C_b is of the same order of magnitude of C_F . We will also require that $C_c < C_b$ and C_g . Within these conditions, the resonance frequencies as a function of I_{cf} are reported in Fig. 5.12 for some values of C_f and C_c . As one can observe, the order of magnitude of ω_1 is compatible with typical qubit frequency values, but it can be tuned by I_{cf} only if $I_{cf} < I_{c1}$. This is an unphysical situation, because the critical current in **SIsFS JJs** are more likely to be higher than in **SIS JJs** typically used in qubits, as it occurs for the devices analyzed in this work. The resonance frequency ω_2 , instead, can be tuned by I_{cf} , satisfying the request in Eq. 5.29. Nevertheless, it ranges between values ten times higher compared with common frequency values achieved in standard transmon circuits (4 to 8 GHz), hard testing the typical equipment used to characterize transmon devices (Chap. 2).

The only way to reduce ω_2 by at least one order of magnitude is to increase the bias capacitance C_b towards some pF and using a current for the **SIS JJ** of ~ 10 nA. We first impose that $C_b = C_F$ (Fig. 5.13 (A)). The dashed lines represent the lower limit for I_{cf} , which satisfies the condition in Eq. 5.29. Moreover, the smaller is the coupling capacitance C_c , the steeper is the increase with respect to I_{cf} , i. e. the ω_2 tuning by magnetic field pulses can give a bigger separation between low- and high-levels, allowing for a higher tunability of the device. We thus fixed C_c to the lowest value analyzed ($C_c = 200$ fF) and the bias capacitance $C_b = 2$ pF, and we searched for lower C_F values (Fig. 5.13 (B)) to guarantee that the condition in Eq. 5.28 is also satisfied. It is clear that also decreasing C_F ω_2 becomes steeper.

By choosing the highest separation between the two I_{cf} levels ($I_{cf}^{\text{low}} > I_{cf}^{\text{low}} + \Delta I$, with ΔI an I_{cf} deviation of the order of $\sim 2\%$), a ferro-tunnel **JJ** with $I_{cf}(H = 0) = 100$ nA, and the capacitances values in Fig. 5.13, we obtain the frequency pulsed-tuning in Fig. 5.14. It turns out that

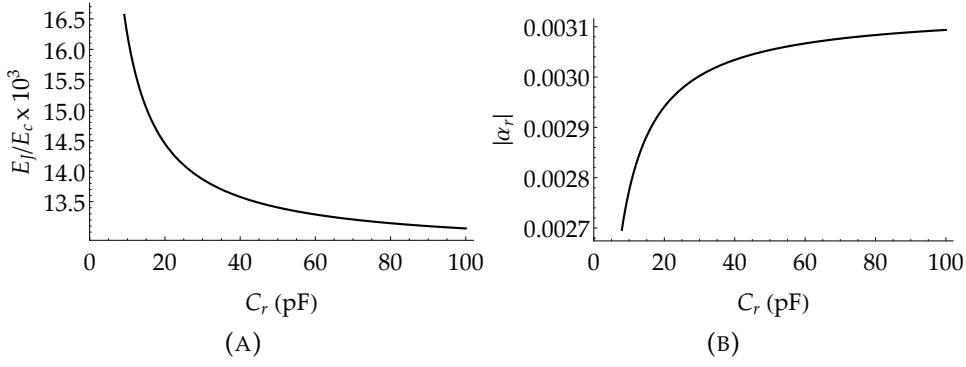


FIGURE 5.17: Ratio E_J/E_c and relative anharmonicity $|\alpha_r|$ for a ferro-transmon in which the SIS JJ is capacitively coupled to a tunnel-SFS JJ as a function of C_r

for $C_c = 200$ fF and C_F slightly smaller than C_b one can obtain a level separations from 60% to 70% and a low- and high-frequency level from 3 GHz to 10 GHz.

Anharmonicity Let us now re-introduce the anharmonic behavior of the JJs. E_J for the two JJs is plotted in Fig. 5.15 as a function of the phase ϕ , and translated by the quantity $E_J(\phi = 0)$ to get a comparison between the two landscapes. As one can observe, the potential energy for the SIS JJ is anharmonic in the plotting range in each analyzed case, while the energy of the SFS JJ is similar to that of a harmonic oscillator when $I_{cf} \gg I_c$, as expected from the analyzed critical currents values. This no more holds in the low-level state, in which the anharmonicity becomes comparable with that of the SIS JJ. Since we want to avoid the formation of an SFS-based two-level system coupled to the SIS one, we will request that the low-level current must be at least $I_{cf}^{\text{low}} \sim 2I_c$. Within this picture, we optimized the parameters of the SFS JJ to guarantee an almost harmonic behavior for the SFS JJ, obtaining however higher operational frequencies (Fig. 5.16).

Estimation of the circuit parameters The last two circuital parameters to be set are the resonator and the gate capacitances, C_r and C_g . While we know that $C_c < C_g < C_b$, C_r must be much larger than the other capacitances of the circuit, there is no known upper limit for C_r . We will set $C_g = 300$ fF, and we will investigate the dependence of the ratio $E_J/E_c = (\hbar\omega_2/E_{C\Sigma})^2/8$ and the relative anharmonicity $\alpha_r = -8\sqrt{8(E_c/\hbar\omega_2)^2}$ at the first order on C_r in the initialization state to understand which is the best C_r . Here E_c corresponds to the total qubit capacitance C_Σ in Eq. 5.10.

As one can observe in Fig. 5.17, E_J/E_c and $|\alpha_r|$ saturate above $C_r \sim 20$ pF, and change with a variation rate of the order of 1% from $C_r = 50$ pF. However, these values are far larger than common resonator capacitances C_r [274, 275], hard testing the scalability of the device.

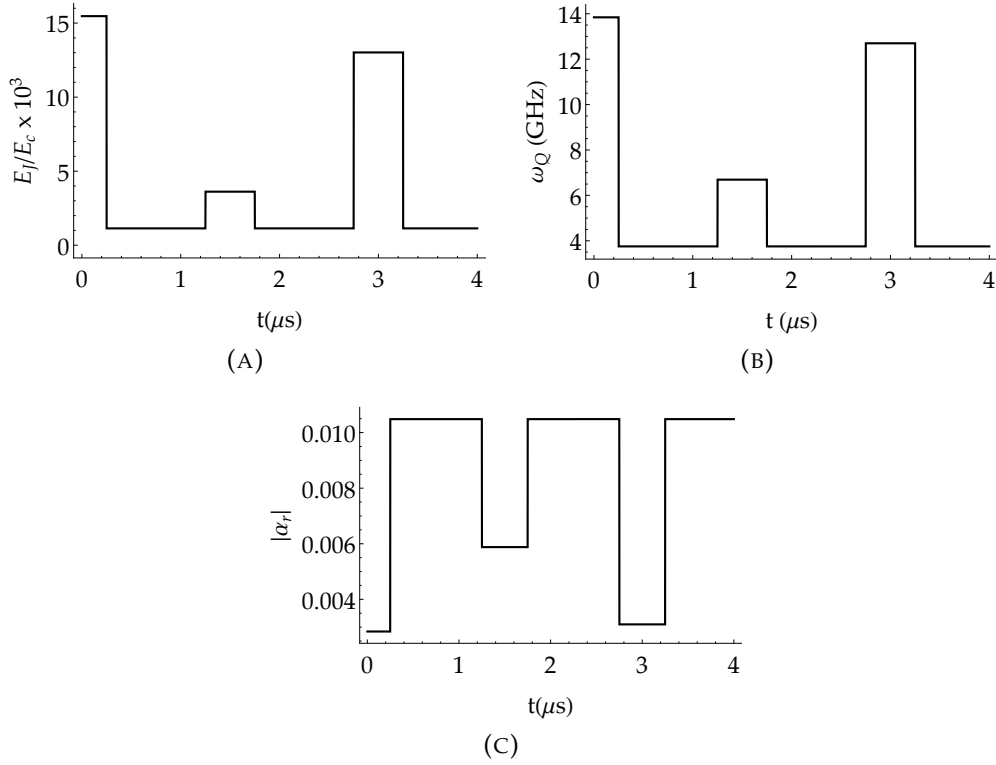


FIGURE 5.18: Ratio E_J/E_c , qubit frequency ω_Q and absolute value of the relative anharmonicity α_r for a ferro-transmon with an SIS JJ capacitively coupled to a Py based SFS JJs as a function of the pulse sequence $H(t)$ from the high to the low-current level state

The enhancement of the capacitances in play occurs because we need to guarantee a suitable capacitive coupling between the SIS and the SFS JJs, without interfering with the RO, thus making this design hard to realize. For instance, the area of the gate capacitance C_g must be increased by a factor ~ 30 compared with the dimensions in conventional transmon devices, and the bias capacitance C_b is expected to be larger than $\sim 50A_b$, with A_b typical areas of bias capacitors in conventional transmons.

Conclusions and perspectives

In this work, I have explored the physics of **SFS JJs**, with a special focus on **SI_fS JJs** with GdN barriers. The coexistence of ferromagnetic ordering in the barrier and tunnel transport between the superconducting electrodes in these devices gives rise to several interesting phenomena, including spin-triplet superconductivity [21, 22]. The microscopic study of the transport mechanisms in NbN-GdN-NbN **JJs** down to very low temperatures was fundamental to better understand the role played by the I_f barrier in these devices [21–23, 223]. I have shown that spin-triplet superconductivity in spin-filter devices is directly correlated to the peculiar incipient 0- π transition observed in the $I_c(T)$ curves measured, which can be tuned employing weak external magnetic fields of the order of a flux quantum [25]. This is an original self-consistent protocol to unambiguously demonstrate triplet-superconductivity in **JJs**. Triplet-superconductivity, combined with the hysteretic memory behavior and the arising of spin-polarization phenomena, makes these devices promising for novel implementations in spintronics and classical superconducting circuits.

I have also carried out a detailed study on the electrodynamic parameters of **SI_fS JJs**[23]. The microscopic approach employed here allows to understand that the quasiparticles dissipation in tunnel **SFS JJs** gives quality factors comparable to those in **SIS JJs**, suitable also for the integration of **SFS JJs** inside superconducting quantum circuit, such as qubits. This approach can be extended also for other kinds of tunnel **SFS JJs**, such as **SI_sFS**, which are currently much more flexible than GdN-based **JJs**. The comparative analysis of **SI_sFS JJs** with different ferromagnetic barriers and different sizes is fundamental in order to propose novel hybrid ferromagnetic quantum devices.

In this work, I have proposed a transmon circuit designs, in which one of the **SIS JJs** of a DC-SQUID is replaced by a tunnel-**SFS JJ**[25]. Circuitual simulations on the two proposals allow to understand that, in order to guarantee suitable E_J/E_c ratios, α_r and ω_Q , the tunnel **SFS JJs** must have critical currents of the order of tens to hundreds of nanoamperes [25], which can be achieved using **JJs** with areas less than some μm^2 . It is therefore required to scale the dimensions of these devices, and Py-based devices may answer this request [42]. An alternative design, in which a non-tunable **SIS JJ** is capacitively coupled to a tunnel-**SFS JJ** was also proposed.

The pulsed tuning of ω_Q exploiting the residual magnetization in the F barrier of the **SFS JJ** may be also assisted, or possibly totally replaced, by the use of RF-pulses [40]. This subject is currently under study, but certainly open the possibility to a full-RF pulsed tuning of transmon circuits.

The ferromagnetic transmon here proposed may be feasible not only for what concerns the improvement of the performance of transmon qubits, in

which the alternative digital tuning of the frequency may help in reducing unavoidable flux-noise decoherence, but it can constitute a novel platform for the study of the basic physics in ferromagnetic JJs[25]. Measurements of relaxation, dephasing and coherence times in such devices could give fundamental information on the magnetization and the local field noise in a MW-environment (Ohmic and $1/f$). We can also exploit the quantum sensitivity of a qubit to study the unconventional phenomena in hybrid SFS JJs. The qubit may be used as a *quantum detector*, able to discriminate the nature of the transport mechanisms in these devices, including spin-triplet superconductivity, and allowing to get information on the magnetization dynamics and phenomena like the spin-polarization.

A

Triton DC and RF system CADs

The parts in the Triton cryostat were designed by using *IronCAD* software and were built at the INFN workshop at the University of Naples "Federico II". In the DC set-up, I designed: the thermal anchoring for the brass-powder filters, the coil-supports and the sample stage. In the RF set-up, I designed the thermal anchoring for the [High-Electron Mobility Transistor \(HEMT\)](#) amplifiers.

A.1 Brass-powder filters

The brass-powder filters were mechanically and thermally anchored to the IAP-plate using two L-structures in [Oxygen Free High Conductivity \(OFHC\)](#). The CADs are reported in Fig. [A.1](#). This solution was the most practical to reduce the clutter of the powder filters, which can not be miniaturized at will.

A.2 DC-sample stage

In Fig. [A.2](#) we show the sample stage parts. This solution was the best compromise to achieve both a good thermal anchoring with the [Mixing Chamber \(MC\)](#) of both the lines and the sample stage, and minimal space to allocate screens for the magnetic field protection, the coil support and the sample holder. This is a feasible plug&play set-up, which can be moved and modified.

Special care was given to the coil-support: the fundamental request is that the center of the coil must coincide with the location of the sample. Given the dimensions of the sample-holder, which anyway gave the possibility to thermalize the DC-lines near the sample stage, it was necessary to use additional

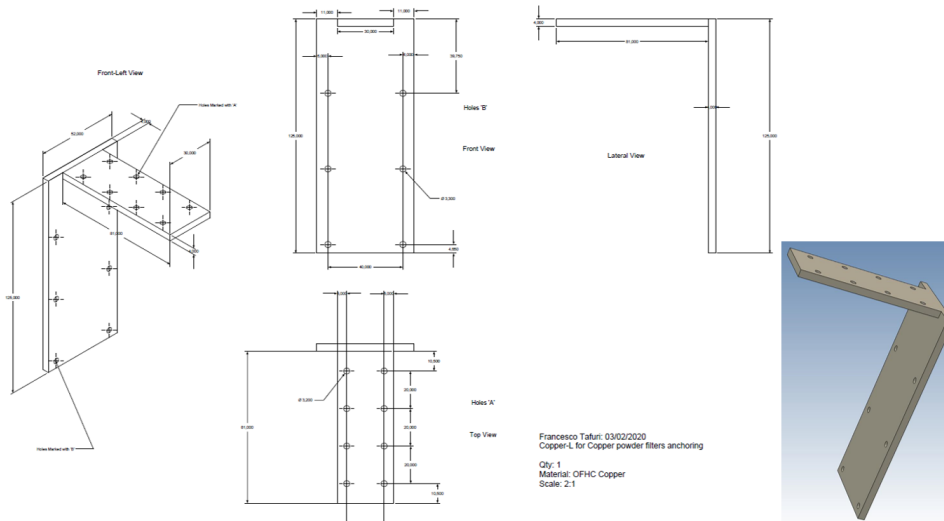


FIGURE A.1: CAD for the L-supports of the powder-filters in the Triton system

stands for the coil support. Nevertheless, the coil must be decoupled from the sample-stage, and non-conducting supports were fundamental.

Insulating stands with dimensions of the order of tens of centimeters and diameters of few millimeters can be subjected to mechanical stress. Moreover, there are few plastic/resins for which the performances at extremely low-temperatures have been already tested. Among these materials, it is well known the Teflon. However, the Teflon is characterized by a tensile breaking load of the order of $\sim 20 \text{ N/mm}^2$, i. e. they can support no more than fractions of grams¹. Instead, the nylon polyamide can sustain loads ten times heavy with a lower thermal conductivity [295–298]. We then decided to use such material for the link with the sample stage, together with the **Stainless-Steel (SS)**, another famous non-conducting alloy already used by Oxford instruments. In Fig. A.3 (A) and (B) we show the coil holder CADs.

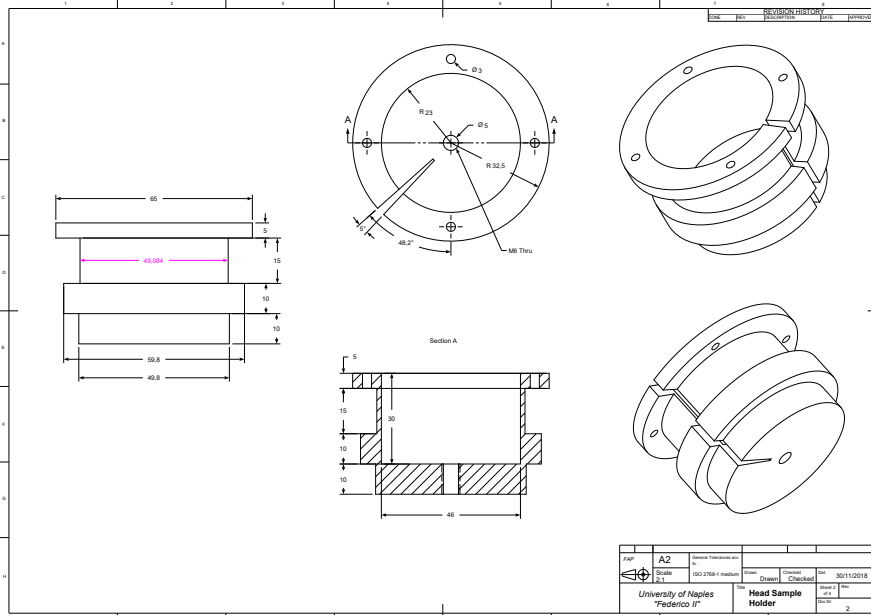
The residual heat Joule on the coil due to the dissipation on the conducting pins (gold) of the coil lines and other dissipative stages in the coil was driven from the sample stage to the cold-plate. We used three home-made insulating twists, with an inner copper-core and a copper washer at one of the ends (Fig. A.3 (C)).

A.3 Amplifiers

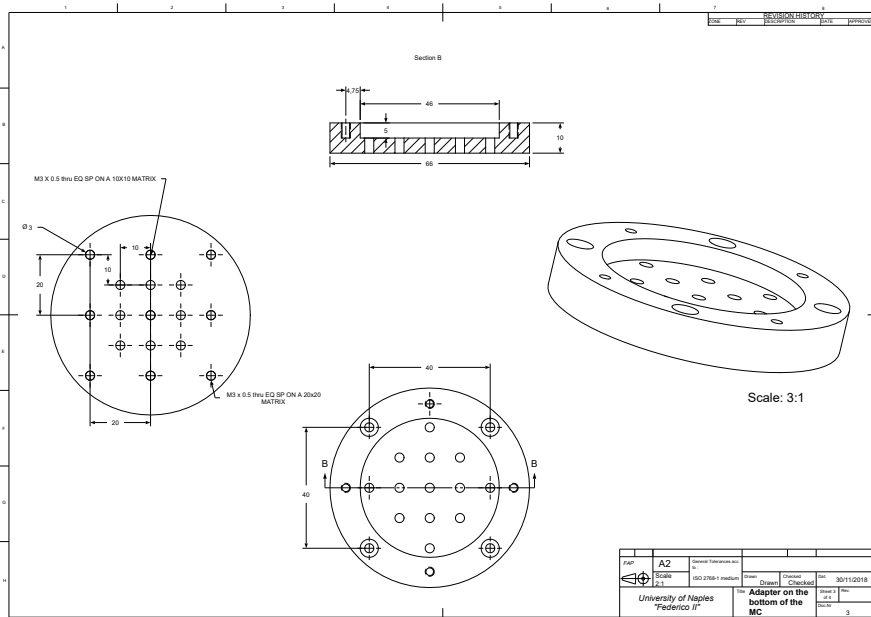
The amplifiers are mechanically and thermally anchored on the 4K-plate with an **OFHC** copper-made U-support.

¹<http://www.engineerplant.it/dtec/proprieta-materiali-plastici.php>

APPENDIX A. TRITON DC AND RF SYSTEM CADs



(A)

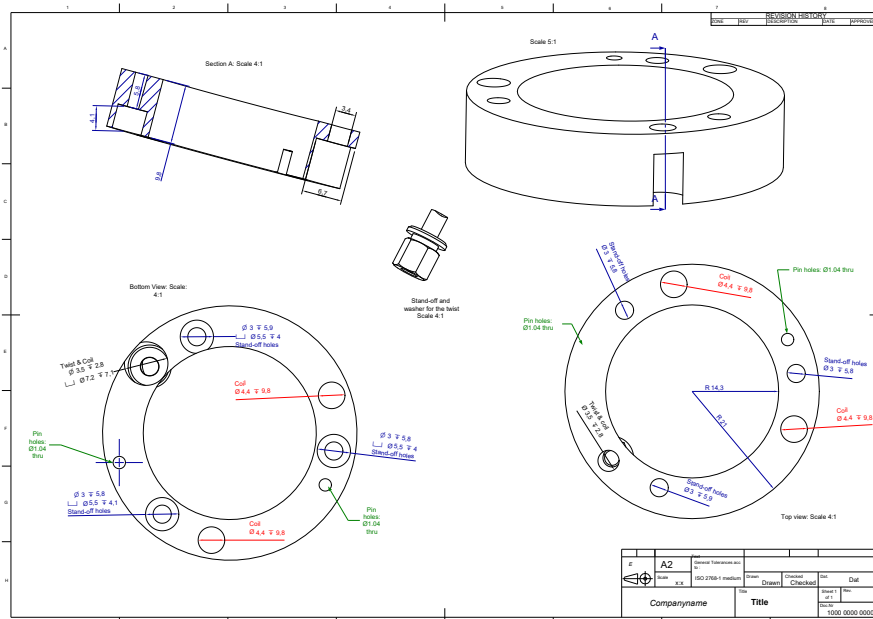


(B)



(C)

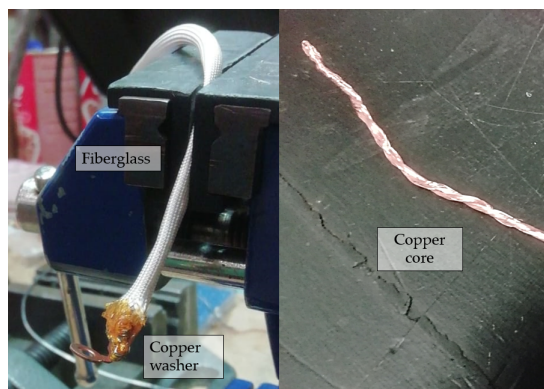
FIGURE A.2: In (a): CAD for the holder of the DC stage; in (b) CAD for the connecting element of the DC stage to the MC; in (c) final view



(A)

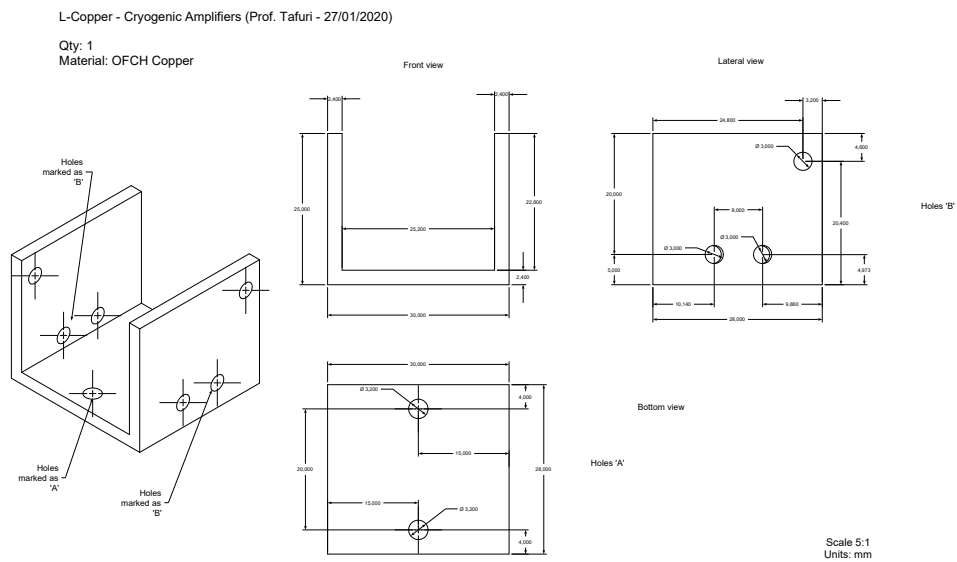


(B)

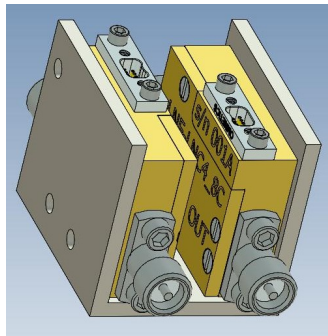


(C)

FIGURE A.3: In (a): CAD for the coil holder of the DC stage; in (b) copper coil ring; in (d) insulating twist



(A)



(B)



(C)

FIGURE A.4: In (a): CAD for the copper U-support of the HEMT amplifiers anchored at the 4K-plate in the Triton; in (b) render of the U-support; in (c) mounted U-support on the 4K-plate

B

Software

B.1 PSCAN2 and MiTMojCo

B.1.1 The codes

PSCAN2¹ is a PYTHON module optimized to simulate [Single Flux Quantum \(SFQ\)](#) logic-based superconducting circuits that typically work at 4.2 K. One of the subroutines of this software allows to simulate the $I(V)$ characteristic of a JJ in electronic circuits with different degrees of complexity.

PSCAN2 (Portable Superconductor Circuit ANalyzer) imports the circuit schematics in a standard SPICE netlist.

LISTING B.1: file `.cir` for the simulations of the $I(V)$ curves in spin-filter JJs

```
v1 n0 0 v1
r1 n1 n0 r1
j1 n1 0 tjm('tjm_1',ic,wbc,wvg,wvrat,wrrat)
.END
```

As an example, we show our circuit schematics used for the $I(V)$ curve simulations in List. B.1, in which the elements are labeled as in the netlist file `.cir` and the nodes are highlighted (second and third column in the file). The ground node is always labeled as 0, while the other nodes are defined as n_i . The first column of the `.cir` file, instead, refers to the elements: v_1 is the voltage source, r_1 is the shunt resistor and j_1 is the JJ. Finally, the last column is the law that governs the element physics.

Among the elements model for a JJ PSCAN2 allows for a modelization in terms of:

- the [Resistively and Capacitively Shunted Junction \(RCSJ\)](#) model (`rsj(ic,Rn,C)`);

¹<http://stacks.iop.org/0953-2048/4/i=11/a=031>

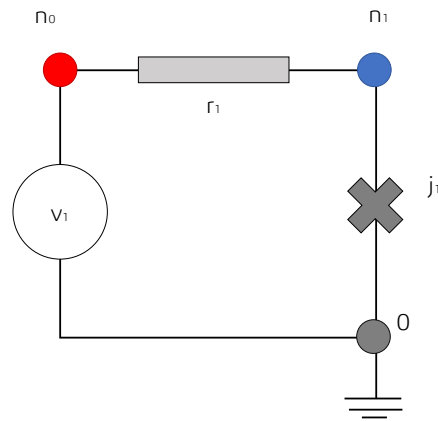


FIGURE B.1: Example of a SPICE netlist in PSCAN2 for the simulations of the $I(V)$ curves in spin-filter JJs

- the non-linear **RCSJ** ($rsj(ic, R_n, V_g, n, C)$);
- the **Tunnel Junction Microscopic (TJM)** model ($tjm(coeff_set_name, ic, wbc, wvg, wvrat, wrrat)$),

where ic is the critical current, R_n the normal resistance, c the JJ capacitance, V_g the gap voltage and n the polynomial order of the non-linear **RCSJ** approximation. The **TJM** modelization requires as parameters: ic , the Stewart-McCumber parameter wbc , the gap voltage wvg , the ratio between $I_c R_N$ and V_g , $wvrat$, and the ratio between R_N and the subgap resistance R_{sg} , $wrrat$. These parameters can be also collected in a `.hdl` file as

LISTING B.2: file `.hdl`: The `.hdl` file is composed of a setting parameters section and the `CIRCUIT JJ()` that identifies the SPICE netlist and the external (variables) or internal (fixed) parameters (`PARAMETER`) of the simulation. x_i , x_j , x_l , x_{j1}/x_j and x_r are the initialization values for the circuit.

```
PARAMETER
xi = 1.0, xj = 1.0, xl = 1.0, xr = 1.0,
wbc=100, wvg=2.8, wvrat=0.07, wrrat=0.0001,
tseq = 100;

CIRCUIT JJ()
{
PARAMETER j =1, i1=0;
external xj1=1.0;
}
```

Finally, the first argument in $tjm()$ is the ensemble of the coefficient resulting from a Dirichlet approximation for the kernels of quasi-particles $\bar{j}_{qp}(\tau)$ and pairs $j_p(\tau)$ in Eqs. 1.48. As a matter of fact, $\bar{j}_{qp}(\tau)$ and $j_p(\tau)$ in Eqs. 1.48 can

be written as

$$j_p(\tau) = \operatorname{Re} \sum_{n=0}^{N-1} A_n e^{p_n \tau}, \quad (\text{B.1})$$

$$\bar{j}_{qp}(\tau) = \operatorname{Re} \sum_{n=0}^{N-1} B_n e^{p_n \tau}, \quad (\text{B.2})$$

where A_n , B_n and p_n are complex Dirichlet coefficients. Such approximation for the total normalized Josephson current $\bar{j}(\tau)$ was first proposed by Odintsov et al. [142] and allows to relate $\bar{j}_{qp}(\tau)$ and $j_p(\tau)$ to a series of integrals of the type:

$$G(t) = -p \int_{-\infty}^t dt' e^{p(t-t')} g(t'), \quad (\text{B.3})$$

where g is a function of time [142]. The value at the time $t + \Delta t$ for each of these integrals can be expressed via its value at the earlier time t ,

$$G(t + \Delta t) = e^{p\Delta t} G(t) - p \int_t^{t+\Delta t} dt' e^{p(t+\Delta t-t')} g(t'). \quad (\text{B.4})$$

allowing for an optimization of the number of integrations and an overall improvement of the simulation speed [142, 153]. `'tjml'` are, as an example, the Dirichlet coefficients provided for the user in the open-source PSCAN2 package. However, we can easily use self-calculated coefficients ensembles using external codes, like MITMOJCO (Microscopic Tunneling Model for Josephson Contacts).

MITMOJCO, available under the GNU General Public License at <https://github.com/drgulevich/mitmojco>, is a C-code designed for microscopic calculation of the superconducting pairs and quasiparticles current in JJs [153, 299]. It creates a TunnelCurrentType pointer

LISTING B.3: MiTMojCo TunnelCurrentType pointer

```
TunnelCurrentType* mitmojco_create(
    char *filename,
    double a_supp,
    double kgap,
    double dt,
    int Ntotal,
    double *phi,
    int Nskip,
    int *skip);
```

where

- `char *filename` is the file in which we collect the tunnel current amplitudes;
- `double a_supp` is the suppression parameter (Chap. 3);
- `double kgap` is the normalized gap frequency $k = \omega_P / \omega_g$, with $\omega_g = 2eV_g / \hbar$;

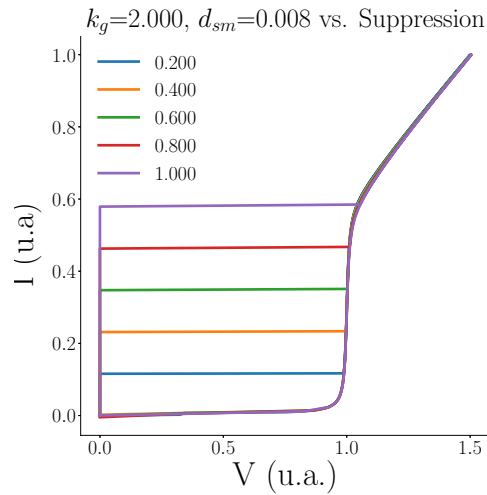


FIGURE B.2: Simulations of $I(V)$ curves in arbitrary units as a function of the suppression parameter α for a fixed k_g and Dirichlet coefficients

- `double dt` is the integration time-step;
- `double *phi` a pointer to the superconducting phase-difference;
- `int Ntotal` the size of the array `phi`;
- `int Nskip` and `int *skipinds` are parameters related to the boundary-conditions in the algorithms [153, 299].

The algorithm MITMOJCO implemented by Gulevich et al. [153, 299] allows also to take into account the smearing of the Riedel singularities at the gap introducing a Lorentzian correction with smearing parameter δ , adjustable by the user.

In the `filename.fit`, the code collects the Dirichlet coefficients that best fit the exact solution for the phase-difference across the junction, given the parameters defined above. The discussion on the quality of the fit and the error on the Dirichlet parameters can be found in Ref. [153, 299].

B.1.2 Discussion on the $I(V)$ curves simulations parameters

The $I(V)$ curves TJM simulations are always calculated using the following procedure:

- we set the parameters of the circuit (I_c, V_g, \dots);
- we set the average time of integration dt (the longer, the better is the estimation of the time-dependent quasiparticles tunnel current amplitude);
- we calculate the mean-time average voltage $\langle V \rangle$ across the JJ solving the equation for the equivalent circuit of the JJ (Fig. 1.14) as a function of the bias current I_b (the voltage bias V_b), with a certain step ΔI (ΔV).

The latter point, in particular, consists in solving the differential equation for the phase φ

$$\frac{d^2\varphi}{d\tau^2} + \alpha_N \frac{d\varphi}{d\tau} + \bar{j}(\tau) = j_b \quad (\text{B.5})$$

as a function of the bias current j_b from a minimum value j_b^{\min} to a maximum j_b^{\max} , with a predetermined step Δj_b . Here, τ is the normalized time defined as

$$\tau = \frac{t}{\omega_P}, \quad (\text{B.6})$$

j_b is the normalized current bias I_b/I_c , and α_N is the damping parameter due to the pure normal state resistance term:

$$\alpha_N = \frac{1}{2k\alpha \text{Re}(j_p(0))}, \quad (\text{B.7})$$

with $\text{Re}(j_p(0))$ real part of the normalized Cooper pair tunneling current at zero frequency. $\bar{j}(\tau)$ is related to the normalized and reduced total tunneling current in the TJM model $\bar{j}(\tau) = I(\tau)/I_c$ (Sec. 1.3.1) as

$$\begin{aligned} \bar{j}(\tau) = & \frac{k}{\text{Re}(j_p(0))} \\ & \int_0^\infty j_p(k\tau') \sin\left(\frac{\varphi(\tau) - \varphi(\tau - \tau')}{2}\right) \\ & + \bar{j}_{\text{qp}}(k\tau') \sin\left(\frac{\varphi(\tau) + \varphi(\tau - \tau')}{2}\right) d\tau'. \end{aligned} \quad (\text{B.8})$$

For numerical purposes, in fact, it is common to extract the normal resistance contribution in the JJ by introducing a reduced quasiparticles kernel $\bar{j}_{\text{qp}}(t) = \bar{I}_{\text{qp}}(t)/I_c$, in place of the complete normalized quasiparticles term $j_{\text{qp}} = I_{\text{qp}}(t)/I_c$ [142, 151, 153] by setting

$$I_{\text{qp}}(t) = -\delta'(t - 0) + \bar{I}_{\text{qp}}(t). \quad (\text{B.9})$$

In this way, the pure normal contribution that gives rise to an instantaneous response (term $\alpha_N \frac{d\varphi}{d\tau}$ in Eq. B.5) is separated from the reduced quasiparticle current (term $\bar{j}_{\text{qp}}(\tau)$ in Eq. B.5), which instead depends on the history of the evolution in time of the superconducting phase difference [300]. For each value of j_b , we let the system evolve for a time τ_{wait} , and then we perform an average of the instantaneous values of $d\varphi/d\tau$, proportional to the voltage by means of the second Josephson equation [26, 27, 142, 299].

In this section, we discuss the effect of the fitting parameters, i. e. the parameters that are not easy to define experimentally from the $I(V)$ curves, as occurs for I_c , V_g and R_N : the suppression factor α , the Stewart Mc-Cumber parameter β and the subgap resistance R_{sg} .

The suppression parameter α weights the ratio between the switching voltage $I_c R_N$ and the gap voltage V_g . It is a value ranging from 0 to 1: standard JJs show suppression factors of the order of 1. In Fig. B.2, we show a collection

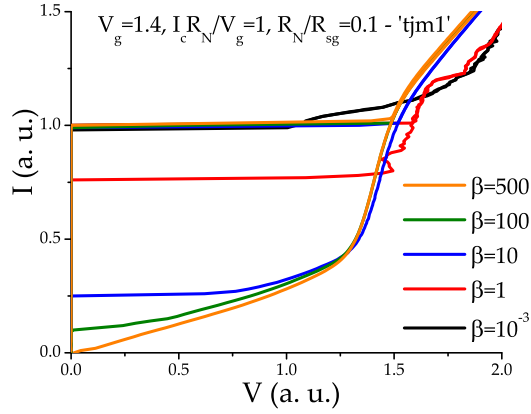


FIGURE B.3: Simulations of $I(V)$ curves in arbitrary units as a function of the Stewart-McCumber parameter β for fixed R_N/R_{sg} , V_g , $I_c R_N/V_g$ and Dirichlet coefficients

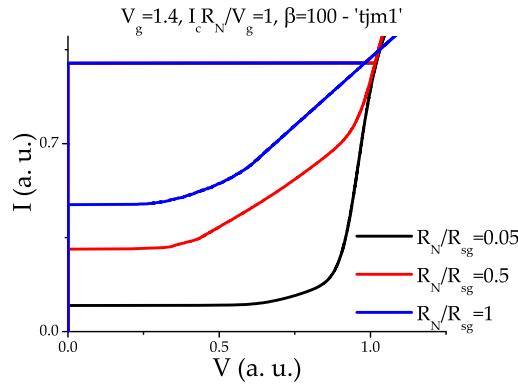


FIGURE B.4: Simulations of $I(V)$ curves in arbitrary units as a function of the Stewart-McCumber parameter β for fixed R_N/R_{sg} , V_g , $I_c R_N/V_g$ and Dirichlet coefficients

of curves as a function of α for a fixed k_g and Dirichlet coefficients (d_{sm}).

k_g , instead, weights the amplitude of the hysteresis, and it is related to the capacitance of the barrier C . By using the MITMOJCO based C-code, this parameter can not be directly related to the quality factor, while PSCAN2 allows for a direct estimation of Q_0 through the Stewart-McCumber parameter β , which affects the hysteresis in the $I(V)$ characteristics. Given its importance we here show a comparison of the $I(V)$ curves in arbitrary units performed with PSCAN2 as a function of β , instead of k_g (Fig. B.3). The more β tends to 0, the more we can recover an overdamped JJ.

In Fig. B.4, we instead discuss the dependence of the $I(V)$ curve subgap shape on R_N/R_{sg} . The smaller is this parameter, the squared is the subgap branch, while it tends to a linear shape when it reaches ~ 1 .

Finally, we show in Fig. B.5 the $I(V)$ curves fit on a standard SIS JJ from Hypres with Nb electrodes and an AlO_x barrier as a function of the temperature T . The more T increases, the more the suppression becomes important. As a consequence, we performed the fitting with MITMOJCO given the easiness with which we can set the temperature in the code, and we obtained the

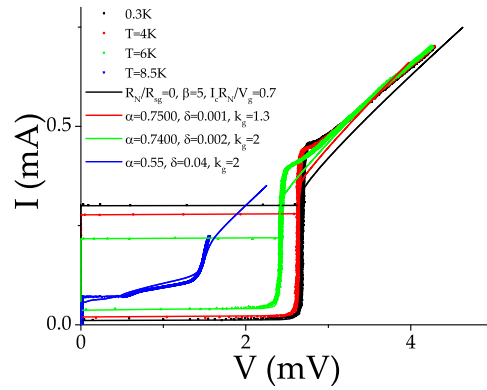


FIGURE B.5: Fitting of the $I(V)$ curves in a high-quality SIS JJ from Hypres

curves for $T > 4$ K. Also the parameter k_g is affected by the temperature: the more V_g decreases, the more it increases. These curves have been compared with the simulation performed with PSCAN2 at 0.3 K: we succeeded to recover the squared shape of the subgap branch in the limit of the smallest R_N/R_{SG} ratio that we can set in PSCAN2. As a consequence, the curve is well-fitted for any $\beta > 5$. This implies that a self-consistent fitting procedure must be performed to get suitable fitting parameters, both by analyzing samples with different areas and barrier thickness, so as we have done on spin-filter JJs.

C

The Transmon: an overview

C.1 Qubit Hamiltonian derivation: a protocol

It is well known that quantum mechanics is the best tool to describe microscopic systems, but it is much less intuitive that the very same physics can also describe macroscopic systems, such as electrical circuits, employing the quantization of the circuit Hamiltonian.

The quantization of electric circuits is performed always with the same protocol [301]:

- write down the Lagrangian \mathcal{L} ;
- identify generalized coordinates and momenta of the circuit;
- write down the classical Hamiltonian \mathcal{H} ;
- promote the generalized coordinates and momenta to operators obeying canonical commutation relations.

An electrical circuit can be described as several elements connected to nodes. Every two-pole element of a circuit form a branch b , and to each element correspond a node charge and a node flux [267]. The flux-node method uses as generalized coordinates the flux, defined as [267]

$$\Phi_n(t) = \int_{-\infty}^t dt' V_n(t'), \quad (\text{C.1})$$

where V_n is the voltage at node n . The corresponding generalized momentum is the charge

$$Q_n(t) = \int_{-\infty}^t dt' I_n(t'), \quad (\text{C.2})$$

with I_n that denotes the current passing through the node. The sign of the charge depends on that of the current, which is arbitrary, while the voltage

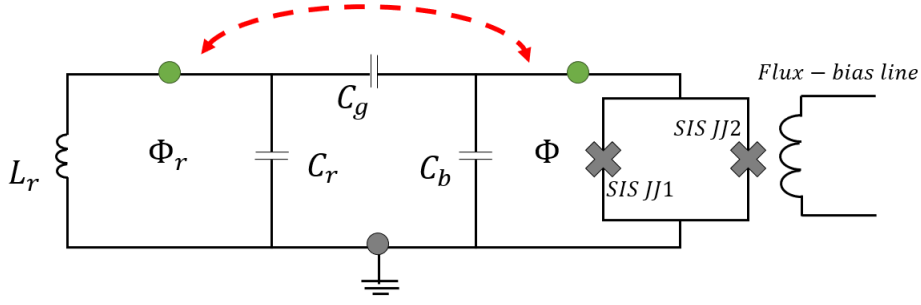


FIGURE C.1: Circuitual schematics of a transmon: in green, the active nodes are highlighted, while the grey circle refers to the ground node. The coupling between the two fluxes is given by the coupling gate capacitance C_g

orientation is, in general, the opposite of the current sign [267]. We will define active nodes as those at which both capacitances and inductances meet, and passive nodes as those where only one of these two elements converges [267]. The nodes connected to the ground are defined as ground nodes. Thus, to each active node we can assign a flux which is the algebraic sum of all the fluxes in the path to the ground node.

Assigned the flux variables, the circuit Lagrangian \mathcal{L} is given by the difference of the electric and the magnetic energies $E_e(\dot{\Phi}_i)$ and $E_m(\Phi)$,

$$\mathcal{L} = E_e(\dot{\Phi}_i) - E_m(\Phi). \quad (\text{C.3})$$

and allows for the determination of the momenta Q_i as

$$Q_i = \partial_{\dot{\Phi}_i} \mathcal{L}(\dot{\Phi}_i, \Phi_i). \quad (\text{C.4})$$

The classical Hamiltonian \mathcal{H} can be found by defining a vector $\dot{\Phi}$ [302],

$$\dot{\Phi} = \begin{Bmatrix} \dot{\Phi}_1 \\ \dot{\Phi}_2 \\ \dots \\ \dot{\Phi}_n \end{Bmatrix} \quad (\text{C.5})$$

related to the momentum vector by the matrix relation

$$\begin{Bmatrix} Q_1 \\ Q_2 \\ \dots \\ Q_n \end{Bmatrix} = \mathcal{M}^{-1} \begin{Bmatrix} \dot{\Phi}_1 \\ \dot{\Phi}_2 \\ \dots \\ \dot{\Phi}_n \end{Bmatrix}. \quad (\text{C.6})$$

The inversion of the matrix allows to write the classical Hamiltonian as

$$\mathcal{H} = \frac{1}{2} \mathbf{Q}^T \mathcal{M} \mathbf{Q} + E_m(\Phi), \quad (\text{C.7})$$

which can be finally quantized using the correspondence principle: the charge and fluxes variables (or the reduced charge and flux $n = Q/(2e)$ and $\varphi = 2\pi\Phi/\phi_0$) transform into operators, so that [302, 303]

$$[\hat{\varphi}, \hat{n}] = i. \quad (\text{C.8})$$

This procedure applies to any electrical quantum circuit, but in the following we will mostly focus on the transmon.

C.2 The transmon Hamiltonian

The transmon circuit schematics here taken as a reference is that of Ref.[145], in which the resonator is schematized with an LC oscillator. It is capacitively coupled to the qubit by the capacitance C_g . We associate to the active flux nodes (green dots) the generalized coordinates Φ_r and Φ . Thus, the electric energy is

$$E_e(\dot{\Phi}_r, \dot{\Phi}) = \frac{C_r \dot{\Phi}_r^2}{2} + \frac{C_b \dot{\Phi}^2}{2} + \frac{C_g (\dot{\Phi}_r - \dot{\Phi})^2}{2}. \quad (\text{C.9})$$

The magnetic energy, instead, is given by the sum of the magnetic energy of the resonator and the JJs in the DC-SQUID,

$$E_m(\Phi_r, \Phi_1, \Phi_2) = \frac{\Phi_r^2}{2L_r} - E_{J1} \cos\left(\frac{2\pi\Phi_1}{\phi_0}\right) - E_{J2} \cos\left(\frac{2\pi\Phi_2}{\phi_0}\right), \quad (\text{C.10})$$

with $\Phi_{1(2)}$ fluxes relative to the JJs in the SQUID. Since the two junctions lay inside a superconducting loop, the flux-quantization equation holds [26]:

$$\Phi_1 - \Phi_2 = n\phi_0 + \Phi_{\text{ext}}, \quad (\text{C.11})$$

where Φ_{ext} is the flux due to an external magnetic field perpendicular to the SQUID plane. Defining for convenience the effective flux $\Phi = (\Phi_1 + \Phi_2)/2$ and the total Josephson energy $E_{J\Sigma} = E_{J1} + E_{J2}$, the magnetic energy of the system reads as

$$E_m(\dot{\Phi}_r, \Phi) = \frac{\Phi_r^2}{2L_r} - E_{J\Sigma} \cos\left(\frac{\pi\Phi_{\text{ext}}}{\phi_0}\right) \sqrt{1 + d^2 \tan^2\left(\frac{\pi\Phi_{\text{ext}}}{\phi_0}\right)} \cos\left(\frac{2\pi\Phi}{\phi_0} - \varphi_0\right), \quad (\text{C.12})$$

with $d = \frac{E_{J2} - E_{J1}}{E_{J2} + E_{J1}}$ junction asymmetry and $\varphi_0 = d \tan(\pi\Phi_{\text{ext}}/\phi_0)$. The phase φ_0 can be set to zero with a shift of variables for constant external magnetic field fluxes (gauge transformation).

The total transmon Lagrangian reads as

$$\mathcal{L} = \frac{C_r \dot{\Phi}_r^2}{2} + \frac{C_b \dot{\Phi}^2}{2} + \frac{C_g (\dot{\Phi}_r - \dot{\Phi})^2}{2} - \frac{\Phi_r^2}{2L_r} + E_J(\Phi_{\text{ext}}) \cos\left(\frac{2\pi\Phi}{\phi_0}\right), \quad (\text{C.13})$$

where

$$E_J(\Phi_{\text{ext}}) = E_{J\Sigma} \cos\left(\frac{\pi\Phi_{\text{ext}}}{\phi_0}\right) \sqrt{1 + d^2 \tan^2\left(\frac{\pi\Phi_{\text{ext}}}{\phi_0}\right)} \quad (\text{C.14})$$

is the *tunable* Josephson energy. The tuning of E_J is generally accomplished through inductively coupled superconducting flux-bias lines.

Finally, once known the momentum vector \mathbf{Q} , given by $\partial_{\dot{\Phi}_i} \mathcal{L}$, and the coordinate vector $\dot{\Phi}$

$$\dot{\Phi} = \begin{pmatrix} \dot{\Phi}_r \\ \dot{\Phi} \end{pmatrix}, \quad (\text{C.15})$$

we can calculate the matrix \mathcal{M}^{-1} , which reads as

$$\mathcal{M}^{-1} = \begin{pmatrix} C_g + C_r & -C_g \\ -C_g & C_g + C_b \end{pmatrix}, \quad (\text{C.16})$$

where the off-diagonal elements represent the coupling between the resonator and the qubit. Inverting the matrix \mathcal{M}^{-1} and using Eq.C.7 we obtain the classical transmon Hamiltonian

$$\mathcal{H} = \frac{Q_r^2}{2C_{\Sigma r}} + \frac{Q^2}{2C_\Sigma} + \frac{QQ_r}{C_{\Sigma \text{coupl}}} + \frac{\Phi_r^2}{2L_r} - E_J(\Phi_{\text{ext}}) \cos\left(\frac{2\pi\Phi}{\phi_0}\right), \quad (\text{C.17})$$

which is given by the sum of the harmonic oscillator Hamiltonian of the resonator,

$$\mathcal{H}_r = \frac{Q_r^2}{2C_{\Sigma r}} + \frac{\Phi_r^2}{2L_r}, \quad (\text{C.18})$$

the qubit Hamiltonian,

$$\mathcal{H}_Q = \frac{Q^2}{2C_\Sigma} - E_J(\Phi_{\text{ext}}) \cos\left(\frac{2\pi\Phi}{\phi_0}\right), \quad (\text{C.19})$$

and the coupling Hamiltonian,

$$\mathcal{H}_{\text{coupl}} = \frac{QQ_r}{C_{\Sigma \text{coupl}}}. \quad (\text{C.20})$$

C.2.1 The charge dispersion vs. the anharmonicity in a transmon

The reliance of the transmon qubit to charge noise can be understood by analyzing the qubit Hamiltonian \mathcal{H}_Q in terms of the normalized charges and fluxes $n - n_g$, with $n = Q/(2e)^1$ and $\varphi = 2\pi\Phi/\phi_0$,

$$\mathcal{H}_Q = 4E_{C_\Sigma}(n - n_g)^2 - E_J(\Phi_{\text{ext}}) \cos(\varphi). \quad (\text{C.21})$$

¹Here we introduce the gate charge in analogy with the CPB [145] to make a comparison between the two systems.

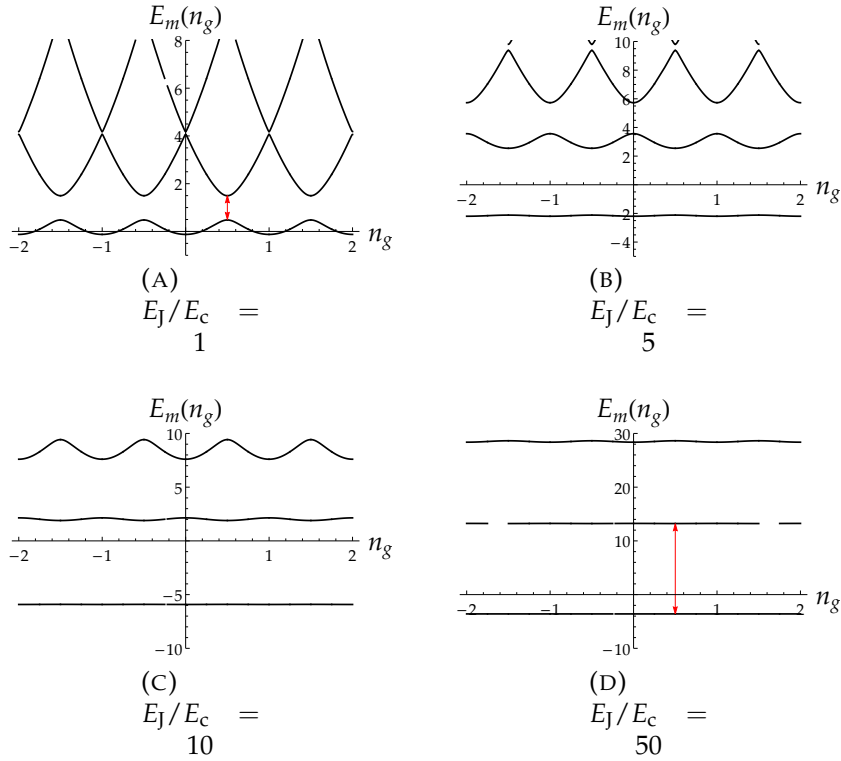


FIGURE C.2: Eigenergies E_0 , E_1 and E_2 of the hamiltonian \mathcal{H}_Q in Eq.C.21 for unitary E_c as a function of the ratio E_J/E_c [145]

The quantization $n \rightarrow \hat{n}$ and $\varphi \rightarrow \hat{\varphi}$ leads to the quantum qubit Hamiltonian, exactly solvable in the phase-basis in terms of Mathieu functions [261, 304, 305]. The eigenergies are plotted in Fig.C.2 as a function of E_J/E_c (for unitary E_c), where $E_c = e^2/(2C_\Sigma)$. The eigenergies lose their dispersion as a function of the charge, becoming almost flat in the limit of high E_J/E_c ratios [145] (Fig.C.2).

The charge dispersion of the level m in the limit of large E_J/E_c decreases exponentially with the E_J/E_c [145]. As a matter of fact, mapping the transmon with a quantum charged rotor, the E_J acts the role of a gravitational field and the kinetic charge term identifies the angular momentum of the rotor for $n_g = 0$ [145]. The dynamics for large E_J/E_c is dominated by E_J , and only small oscillations of the phase are favored. In such perturbative picture, the effect of the charge enters only in *instanton* tunneling events, which in the *Wentzel-Kramers-Brillouin* (WKB) approximation leads to the aforementioned exponential dependence of the charge dispersion as a function of the ratio E_J/E_c .

The drawback is that for higher E_J/E_c also the separation between the energy levels of the qubit compared with that of the first two energy levels, or relative anharmonicity $\alpha_{m_r} = (E_{m+1,m} - E_{m,m-1})/E_{01}$, decreases, i. e. it could be hard to isolate a pure two-level system. Nevertheless, the performances of a transmon qubit are only slightly affected by the decrease in anharmonicity, while the improvement due to the decrease in the charge noise is much more efficient [145, 147, 204]. In fact, in the limit of small phase-oscillations, the

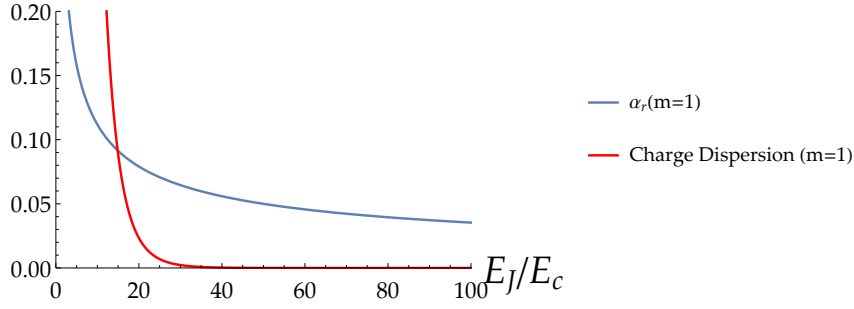


FIGURE C.3: Comparison between the charge dispersion and the relative anharmonicity α_r in a transmon qubit as a function of the ratio E_J/E_C for the level $m = 1$

qubit is a *Duffing oscillator*,

$$\mathcal{H}_Q = -E_J(\Phi_{\text{ext}}) + \hbar\omega_Q \left(b^\dagger b + \frac{1}{2} \right) - \frac{E_{C_\Sigma}}{2} (b + b^\dagger)^4, \quad (\text{C.22})$$

where b^\dagger and b are the creation and annihilation operators

$$\begin{aligned} b^\dagger &= (\phi - iN)/\sqrt{2} \\ b &= (\phi + iN)/\sqrt{2}, \end{aligned} \quad (\text{C.23})$$

and $N^2 = \frac{8E_{C_\Sigma}}{\hbar\omega_Q} n^2$ and $\phi^2 = \frac{E_J(\Phi_{\text{ext}})}{\hbar\omega_Q} \varphi^2$. The eigenenergies of this Hamiltonian within the time-independent perturbation theory give for the first energy level

$$\alpha_{1r} \sim -(8E_J(\Phi_{\text{ext}})/E_{C_\Sigma})^{-1/2}, \quad (\text{C.24})$$

which only scales with a power-law compared with the exponential decrease of the charge noise (see Fig.C.3).

C.2.2 Transmon read-out and circuit QED

In a transmon the qubit is embedded in a superconducting transmission line resonator that opens up the possibility of [Quantum Non-Demolition \(QND\)](#) read-out of the qubit state. The coupling between the qubit and the resonator is effective if the qubit is located in a voltage antinode of the [EM](#)-signal through the transmission line. In the limit $C_r \gg C_b$, C_g ($C_g \sim 40 - 200$ fF[[274](#), [275](#)]), the quantized resonator Hamiltonian in Eq.C.18 in the single-photon limit, i. e. for powers of the [EM](#)-probe signal of the order of < -70 dB), is

$$\mathcal{H}_r = \hbar\omega_r a^\dagger a, \quad (\text{C.25})$$

where $\omega_r = (L_r C_{\Sigma_r})^{-1/2}$ is the resonance frequency of the transmission line and a and a^\dagger accounts for the annihilation and creation of one photon inside the resonator, defined as $a(a^\dagger) = \frac{N_r \mp i\phi_r}{\sqrt{2}}$. The coupling between the qubit and

the resonator in Eq.C.20 depends both on the coupling capacitance C_g and the C_b and the resonator parameters: it can be written, in fact, as

$$\mathcal{H}_{\text{coup}} = 2\beta e V_{\text{rms}}^0 (a + a^\dagger) \hat{n}, \quad (\text{C.26})$$

where $V_{\text{rms}}^0 = \sqrt{\hbar\omega_r/(2C_r)}$ is the root-mean-square voltage local oscillator, and the parameter $\beta = C_g/(C_b + C_g)$ is the coupling strength. As a consequence, in the qubit states basis $|i\rangle$ (with frequencies ω_i), the transmon Hamiltonian reads as

$$\mathcal{H} = \hbar\omega_r a^\dagger a + \sum_j \omega_i |i\rangle \langle i| + \sum_{i,j} \hbar g_{ij} |i\rangle \langle j| (a + a^\dagger), \quad (\text{C.27})$$

where $g_{ij} = 2\beta e V_{\text{rms}}^0 \langle i|n|j\rangle$ is the coupling energy.

Employing the [Rotating Wave Approximation \(RWA\)](#) to eliminate terms describing simultaneous excitation (de-excitation) of the qubit and the resonator, and considering that only nearest-neighbor coupling $g_{i,i+1}$ matters [145], we arrive at the effective generalized [Jayne-Cummings \(JC\)](#) Hamiltonian

$$\mathcal{H} = \hbar\omega_r a^\dagger a + \hbar \sum_j \omega_i |i\rangle \langle i| + \sum_j \hbar g_{JJ} |j\rangle \langle j+1| (a + a^\dagger). \quad (\text{C.28})$$

For a sufficiently large anharmonicity, the transmon can be then mapped to a spin-1/2 system, with ground state $|0\rangle \rightarrow |\downarrow\rangle$ and excited state $|1\rangle \rightarrow |\uparrow\rangle$, and the transmon Hamiltonian is nothing more than a generalized Rabi Hamiltonian,

$$\mathcal{H}_Q = \hbar\omega_r a^\dagger a + \hbar\omega_Q \frac{\sigma_z}{2} + \hbar g (a\sigma_+ + a^\dagger\sigma_-). \quad (\text{C.29})$$

Here the coupling term connects only states $|n-1, \uparrow\rangle$ and $|n, \downarrow\rangle$, known as *bare states*. In this case, the Hamiltonian is 2×2 block-diagonal, with exact analytic solutions. The eigenstates are known as *dressed states*,

$$\begin{cases} |0\rangle = |0, \uparrow\rangle \\ |n, +\rangle = \cos \theta_n |n-1, \uparrow\rangle + \sin \theta_n |n, \downarrow\rangle \\ |n, -\rangle = -\sin \theta_n |n-1, \uparrow\rangle + \cos \theta_n |n, \downarrow\rangle, \end{cases} \quad (\text{C.30})$$

with eigenenergies

$$\begin{cases} E_0 = -\hbar\frac{\delta}{2} \\ E_{n\pm} = n\hbar\omega_r \pm \frac{\hbar}{2} \sqrt{4g^2n + \delta^2}. \end{cases} \quad (\text{C.31})$$

The quantity δ is defined as the difference between the qubit frequency ω_Q and the resonator frequency ω_r , and it is also known as *detuning*².

Depending on the capacitances of the circuit and the detuning, we can have the following situations:

²The angle θ_n satisfies the condition $\tan 2\theta_n = 2g\sqrt{n}/\delta$.

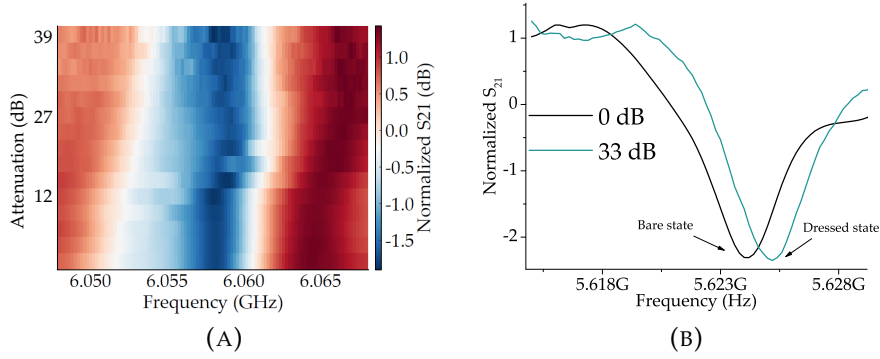


FIGURE C.4: In (a): density plot for the dispersive shift measured on a planar transmon qubit changing the input power; in (b) single acquired traces for two values of the attenuation on the RO input signal. The measurement has been performed using the pulsed-wave spectroscopy, with an IF frequency for the mixer up/down conversion of 33 MHz and a RO pulse duration of 25 μ s. S_{21} refers to the magnitude of the transmission parameter

$g \sim 0$ or $\delta \rightarrow \infty$: the resonator is strongly decoupled from the qubit and the dressed states energies reduce to

$$\begin{cases} E_0^{g=0} = -\hbar\frac{\delta}{2} \\ E_{n\pm}^{g=0} = n\hbar\omega_r \pm \hbar\frac{\delta}{2}. \end{cases} \quad (\text{C.32})$$

The eigenstates coincide with the bare states, i. e. by probing the resonator with an EM field, no evidence of the two-level system will emerge.

$g/\delta \ll 1$: the resonator is or weakly coupled to the qubit or far-detuned from the qubit frequency, and the dressed states energies reduce to

$$\begin{cases} E_0^{\text{disp}} = -\hbar\frac{\delta}{2} \\ E_{n\pm}^{\text{disp}} = n\hbar\omega_r \pm \left(\hbar\frac{\delta}{2} + \hbar\chi n\right). \end{cases} \quad (\text{C.33})$$

This regime is known as *dispersive regime*: decreasing the power of the EM probe-signal, a dynamical Stark shift in the resonator frequency is observed, by an amount $\chi n = \frac{g^2}{\delta}$. Typical detunings are of the order of some gigahertz [274, 275].

$g \rightarrow \infty$ or $\delta \sim 0$: we fall in the *strong-coupling regime*, where photons are emitted and re-adsorbed by the qubit before they are lost.

It is important to stress that in all these regimes the coupling g increases with E_J/E_C . This is because the charge dispersion is a response to the DC-component of the transmon spectrum, while the coupling to the oscillating field in the cavity is an AC-response [145]. Remarkably, the transmon is highly

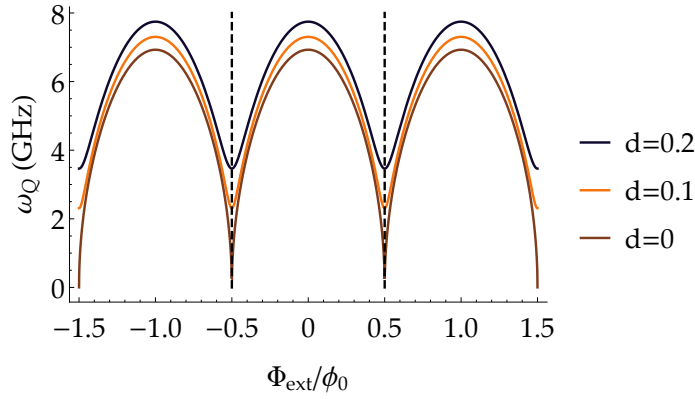


FIGURE C.5: Modulation of a transmon qubit frequency with Josephson energy $E_J = 15$ GHz and charging energy $E_c = 200$ MHz as a function of the normalized flux-field bias to the quantum magnetic flux ϕ_0 and the junctions asymmetry [204]. The dashed lines refer to the sweet spots: the slope of the energy-dispersion relation in the sweet-spots decreases increasing the asymmetry, i. e. the qubit is less sensitive to flux noise

polarizable in the limit of large E_J/E_c and responds strongly to electric fields at all frequencies.

In Fig.C.4, we show as an example the dispersive shift observed on a Al-based planar transmon qubit characterized in collaboration with SeeQC-EU, with methods reported in Chap.2. Decreasing the intensity of the MW probe of the resonator adding a series of attenuator the resonance in the transmission parameter S_{21} found at 6.092 05 GHz is shifted to 6.093 31 GHz. For this device, $\delta = 1.960$ GHz and $g = 46$ MHz.

C.2.3 Flux modulation

The implementation of fast-gate operations with high-fidelity requires that the qubit frequency can be tuned in a certain range of values [204, 212, 306–308]. In a transmon, the key element is the DC-SQUID. Given that the transition frequency ω_Q is related to the DC-SQUID Josephson energy as

$$\omega_Q \sim \sqrt{8E_J/E_c} \quad (\text{C.34})$$

and that E_J depends on the external flux-bias Φ_{ext} as in Eq.C.14, we can tune the qubit frequency applying a current through flux-bias lines inductively coupled to the transmon [204]. This unavoidably induces flux-noise, and a way to improve the coherence is to use asymmetric DC-SQUIDs, i. e. characterized by an asymmetry parameter $d \neq 0$. Asymmetric DC-SQUIDs are less sensitive to random flux-fluctuations far from the sweet spots, i. e. the minima and the maxima of the Josephson dispersion relation [204, 309]. The expected frequency flux-modulation changes as in Fig.C.5 as a function of d .

In Fig.C.6, we show the flux-modulation of an Al-based qubit. Its characteristic frequency is of the order of 3.6 GHz, and it can be tuned in a range of

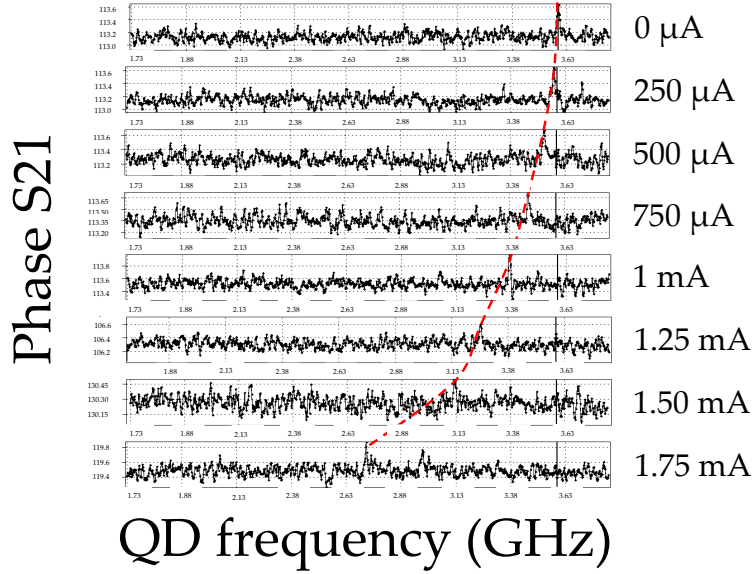


FIGURE C.6: Modulation of a planar transmon qubit QD frequency as a function of the flux-bias

the order of tens of megahertz. The peak corresponding to the qubit resonance measured with methods reported in Chap.2 shifts to smaller values increasing the flux-bias current to ~ 1.75 mA, which corresponds approximately to half-flux quantum. Also the resonator frequency (Read-Out (RO) bare resonance 5.858 GHz) in the dispersive regime modulates with the flux (Fig.C.7).

C.3 Noise and decoherence in a qubit

The decoherence in a superconducting qubit is the most important limitation for its implementation in a full-quantum processor. It is due to random and uncontrollable physical processes due to the measurement equipment and, in general, the environment in which the qubit is embedded, which is the main source of noise [204, 310–313]. In an open system the dynamical evolution of the qubit is no more deterministic: in presence of noise, the qubit state will be lost the more time passes [204, 310–313].

Noise sources can couple to the qubit along the z -axes of the Bloch sphere (along the qubit quantization axis) or in the $x - y$ -plane perpendicular to this direction, i. e. we can define two decay rates [204, 310–313]:

- the longitudinal relaxation rate $\Gamma_1 = \frac{1}{T_1}$;
- the transverse relaxation rate $\Gamma_2 = \frac{1}{T_2}$.

Longitudinally coupled noise sources drive transitions from the ground state $|0\rangle$ to the excited state $|1\rangle$, or *vice-versa*[287]. A qubit in $|1\rangle$ emits energy to the environment and relaxes to zero with a rate $\Gamma_{1\downarrow}$, while a qubit in $|0\rangle$ adsorbs energy and is excited to $|1\rangle$ with a rate $\Gamma_{1\uparrow}$. Normally, excitations at low temperatures ($k_B T \ll \hbar\omega_Q$) are less likely to be observed, which means that $\Gamma_1 \sim \Gamma_{1\downarrow}$. In the picture of the Boltzmann equilibrium statistics, in fact,

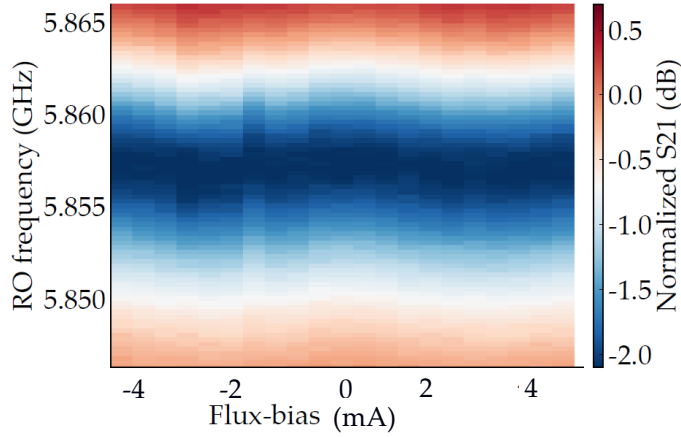


FIGURE C.7: Modulation of a planar transmon qubit RO frequency in the dispersive regime, i. e. in the dressed state as a function of the flux-bias

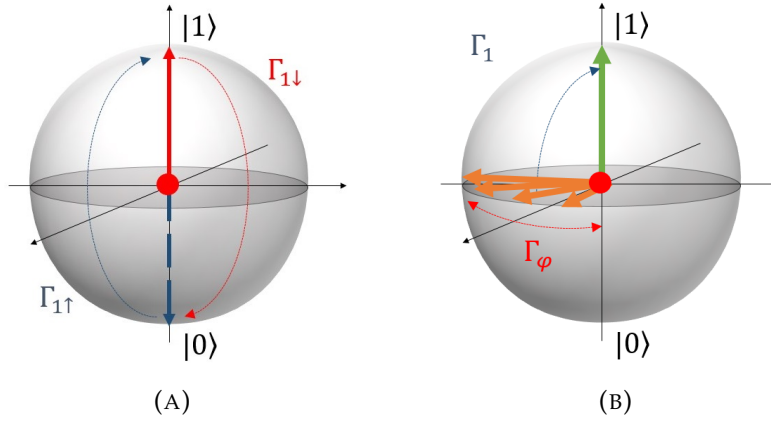


FIGURE C.8: In (A): Longitudinal qubit relaxation represented on the Bloch sphere; in (B): Transverse qubit relaxation represented on the Bloch sphere

$\Gamma_{1\uparrow} \sim e^{-\frac{\hbar\omega_Q}{k_B T}} \Gamma_{1\downarrow}$, i. e. for $k_B T \ll \hbar\omega_Q$ $\Gamma_{1\uparrow}$ is exponentially smaller than $\Gamma_{1\downarrow}$. The transverse energy relaxation, instead, is related to both energy relaxation and pure dephasing [204], resulting in a loss of coherence at a rate

$$\Gamma_2 = \frac{\Gamma_1}{2} + \Gamma_\varphi, \quad (\text{C.35})$$

Low-frequency noise induces random shifts of ω_Q that lead to pure dephasing, while high-frequencies fluctuations induce transitions between different qubit states, i. e. relaxation [204, 310–313].

C.3.1 Decoherence in a transmon qubit

Dephasing in a transmon qubit is due to fluctuations of

- the charge [145, 267, 287, 314–316];

- the flux [145, 317];
- the critical current [145, 318]³,

which induce an overall broadening of the qubit energy levels, while among the noise sources that enter in the longitudinal relaxation decay, we have:

- spontaneous radiation emission, due to the coupling of the qubit with the EM field inside the resonator [145, 314, 319];
- Purcell effect [145, 315, 320];
- quasiparticles tunneling [145, 321, 322];
- flux-coupling [145, 323];
- dielectric losses [145, 324].

Other sources are the coupling to spurious resonator modes, impinging of vortices, and bulk-interface piezoelectric phonon emission, and all the external parameters fluctuations at frequencies comparable to the qubit frequency [145]. The total longitudinal relaxation time T_1 is then given by

$$T_1 = \frac{1}{\sum_i T_{1i}^{-1}}, \quad (\text{C.36})$$

and it will be dominated by the smaller relaxation time measured, and the same occurs for the dephasing total time.

Though a strong effort was given to the understanding of each of these noise sources, we will here focus on the quasiparticles tunneling and the flux-noise, given their influence on the ferro-transmon proposal here discussed.

Quasiparticles tunneling Thermal breaking of Cooper pairs can increase the number of quasiparticles N_{qp} in the system. In the limit $E_J/E_c \gg 1$ and $N_{\text{qp}} \rightarrow 1$ for $T \rightarrow 0$ [145], the quasiparticles tunneling induce decoherence with a rate

$$\Gamma_{\text{qp}} = \frac{N_{\text{qp}}}{\nu V 2e^2 h R}, \quad (\text{C.37})$$

where R is the quasiparticles resistance of the JJ, ν is the density of states and V the volume of the JJ. It is therefore important to have high subgap resistance for the JJ to reduce the quasiparticles decoherence rate, and it motivates the importance of the estimation of the subgap resistance in ferro-tunnel JJs discussed in Sec.4.1.

³Trapping and de-trapping of charges associated with spatial reconfigurations of ions inside the tunneling junction [145, 318]

TABLE C.1: Comparison between the longitudinal relaxation and dephasing time in a transmon circuit, estimated using common device parameters, and reported in Ref.[145]

Noise	T_1	T_φ
Radiation emission	0.3 ms	-
Purcell effect	1.6 μ s	-
Quasiparticles tunneling	1 s	-
Flux-coupling (M)	0.02 s – 1 s	-
Flux-coupling (M')	70 ms	-
Charge noise	-	8 s
Flux noise	-	1 μ s
Current noise	-	35 μ s

Flux-coupling The flux coupling in a transmon allows for an *in situ* tuning of E_J . Nevertheless, it also opens up additional channels for energy relaxation.

Let us first consider the flux-coupling with the superconducting ring inside the qubit. The overall flux applied to the SQUID Φ_{ext} can be decomposed as

$$\Phi_{\text{ext}} = \Phi_{\text{ext}}^0 + \Phi_{\text{ext}}^n \quad (\text{C.38})$$

with $\Phi_{\text{ext}}^n \ll \Phi_{\text{ext}}^0$ small noise [145]. We can perform a Taylor expansion of $E_J(\Phi_{\text{ext}})$,

$$E_J(\Phi_{\text{ext}}) = E_J(\Phi_{\text{ext}}^0) + \mathcal{A}\Phi_{\text{ext}}^n \quad (\text{C.39})$$

with $\mathcal{A} = \partial_{\Phi_{\text{ext}}} E_J(\Phi_{\text{ext}})|_{\Phi_{\text{ext}}^0}$ [145]. The perturbative treatment of the noise allows to relate the relaxation rate to the noise power spectrum $S_{\Phi_n}(\omega) = M^2 S_{I_n}(\omega)$, with M mutual coupling inductance [145]. At low temperatures $S_{I_n}(\omega)$ is

$$S_{I_n}(\omega) = 2\Theta(\omega) \frac{\hbar\omega_Q}{R}, \quad (\text{C.40})$$

with R environment impedance [145]. Within these considerations, the relaxation rate due to the flux coupling with the superconducting ring is

$$\Gamma_1^M = \frac{2\omega_Q}{\hbar R} \Theta(\omega) |\langle \uparrow | \mathcal{A} | \downarrow \rangle|^2 M^2. \quad (\text{C.41})$$

Flux-coupling, however, can also appear between the flux-lines and the overall circuit, through of the mutual coupling M' . If the environment resistance is R , the power dissipated is $P = M'^2 \omega^4 2C\hbar\omega / 2R$ [145], so that

$$T_1^{M'} \sim \frac{R}{M'^2 \omega^4 C}. \quad (\text{C.42})$$

In Tab.C.1, we report the comparison between estimated T_1 and T_φ for a transmon qubit using common device parameters, as reported in Ref.[145]. From the estimations in Ref.[145], it seems clear that the flux-noise strongly contributes to dephasing, while the major source of relaxation is given instead

by the Purcell effect. These rough estimations are consistent with the fact that, in very good devices, coherence times $T_2 = (1/(2T_1) + 1/T_\phi)^{-1}$ from tens to hundreds of microseconds can be achieved. Nevertheless, it is necessary to increase such coherence times to higher levels to successfully implement multi-qubit devices exploitable in quantum processors, searching for new kind of circuit designs, tuning of the qubit frequency and RO of conventional transmons.

Physical Constants

Electric charge	$e = 1.6 \times 10^{-19} \text{ C}$
Dielectric constant in vacuum	$\epsilon_0 = 8.85 \times 10^{-12} \text{ F/m}$
Magnetic flux quantum	$\phi_0 = 2.06 \times 10^{-15} \text{ Wb}$
Planck constant	$h = 6.63 \times 10^{-34} \text{ J s}$
Speed of light	$c = 2.998 \times 10^8 \text{ m/s}$
Dirac constant	$\hbar = 1.05 \times 10^{-34} \text{ J s}$ $\hbar = 6.58 \times 10^{-16} \text{ eV s}$
Speed of light	$c = 2.998 \times 10^8 \text{ m/s}$
Boltzmann constant	$k_B = 1.38 \times 10^{-23} \text{ J/K}$ $k_B = 8.62 \times 10^{-5} \text{ eV/K}$

Acronyms

- AB** Ambegaokar-Baratoff. 12, 24, 29, 70, 71, 73
- AWG** Arbitrary Waveform Generator. 50, 51
- BCS** Bardeen-Cooper-Schrieffer. 12, 24, 67
- CLR** Current Length relation. 10–14
- CMRAM** Cryogenic Magnetic Random Access Memory. 7, 28, 80, 81, 89–93, 98, 101
- CN** Copper Nickel. 43
- CP** Carr-Purcell. 57
- CPB** Cooper pair box. 81, 95–98
- CPMG** Carr-Purcell-Melbourn-Gill. 57
- CPR** Current Phase Relation. 14, 71, 74–76, 82
- CW** Continuous Wave. 54
- DFT** Density Functional Theory. 61
- DU** Dilution Unit. 34
- DUT** Device Under Test. 51
- EBL** Electron-Beam-Litography. 93
- EM** ElectroMagnetic. 44, 49, 136
- ETP** Electrolytic Tough Pitch. 37
- FFLO** Fulde-Ferrel-Larkin-Ovchinnikov. 11–13
- FFT** Fast Fourier Transform. 51
- FIB** Focused Ion Beam. 93
- HEMT** High-Electron Mobility Transistor. 44, 51, 98, 119, 123
- IF** Intermediate-Frequency. 50, 51, 53

- IGH** Intelligent Gas Handling system. 35
- IVC** Inner Vacuum Chamber. 31, 35
- JC** Jayne-Cummings. 137
- JJ** Josephson Junction. 3–10, 14, 18–29, 42–44, 61–63, 65, 67, 69–74, 77, 79–90, 92–94, 96–103, 106–117, 124, 125, 127–130, 137, 142
- JJs** Josephson Junctions. 1–5, 7–18, 21, 22, 24, 26–31, 35, 39, 40, 60–73, 75–77, 79–104, 106, 109, 113–118, 124–126, 128, 130, 133, 142
- JT** Joule-Thomson. 34
- LNPB** Low-Noise Power Block. 44
- LO** Local Oscillator. 50, 51, 53, 54
- LOS** Lines of Sight. 35
- LRTC** Long-Ranged spin-Triplet Correlation. 14–17
- MC** Mixing Chamber. 33–35, 38, 39, 44, 45, 47, 48, 119, 121
- MCM** Multi-Chip Module. 48
- MQT** Macroscopic Quantum Tunneling. 2, 25, 27, 30, 80, 86
- MW** MicroWave. 2, 44
- NLRCSJ** Non-Linear RCSJ. 22
- NVC** Nitrogen-Vacancy Centers. 98
- OFHC** Oxygen Free High Conductivity. 119, 120
- OVC** Outer Vacuum Chamber. 35
- PC** Pre-Cooling. 33, 34
- PD** Phase Diffusion. 27, 82–84, 86, 87
- PTR** Pulse Tube Refrigerator. 33
- QD** Qubit Drive. 50, 51, 53–57
- QND** Quantum Non-Demolition. 48, 97, 136
- QNS** Quantum Noise Spectroscopy. 98
- RCSJ** Resistively and Capacitively Shunted Junction. 19–22, 24, 25, 27, 82–84, 124, 125

- RO** Read-Out. 50, 51, 53–57, 88, 98, 100, 105, 106, 116, 138, 140, 141, 144
- RT** Room-Temperature. 31, 32, 36, 37, 39, 43, 44, 46, 47, 51, 52, 62
- RWA** Rotating Wave Approximation. 52, 137
- SCD** Switching Current Distribution. 27, 41–43, 81, 85–87
- SCN** Silver-plated Copper Nickel. 43
- SFQ** Single Flux Quantum. 28, 89, 90, 124
- SFS** Superconductor/Ferromagnet/Superconductor. 1–4, 7–17, 19, 28, 39, 60, 70, 75, 80, 81, 88–90, 92, 96, 98–101, 103, 104, 106–118
- SI_fS** Superconductor/Insulating Ferromagnet/Superconductor. 2, 17, 28, 60, 70, 117
- SIFS** Superconductor/Insulator/Ferromagnet/Superconductor. 28, 89
- SIS** Superconductor/Insulator/Superconductor. 3, 4, 10–12, 17–19, 21, 28, 67, 81, 88, 94, 99–104, 106–117, 129
- SIsFS** Superconductor/Insulator/small superconducting buffer/ Ferromagnet/Superconductor. 2, 28, 42, 44, 80, 89–94, 100, 102, 103, 113, 114, 117
- SNR** Signal to Noise Ratio. 55, 56
- SNS** Superconductor/Normal metal/Superconductor. 3, 4, 10–12, 88
- SOC** Spin Orbit Coupling. 14, 16, 17, 65, 74, 78
- SRTC** Short-Ranged spin-Triplet Correlation. 15
- SS** Stainless-Steel. 32, 39, 43, 120
- TA** Thermal Activation. 25, 27, 30, 87
- TJM** Tunnel Junction Microscopic. 17, 18, 22, 23, 66–68, 81–86, 88, 93, 94, 125, 127, 128
- VNA** Vector Network Analyzer. 37, 49, 105
- WKB** Wentzel-Kramers-Brillouin. 67, 135

Bibliography

- [1] B. D. (Brian David) Josephson. *Non-linear conduction in superconductors / Brian David Josephson*. eng. 1964.
- [2] John J.L. Morton and Brendon W. Lovett. “Hybrid Solid-State Qubits: The Powerful Role of Electron Spins”. In: *Annual Review of Condensed Matter Physics* 2.1 (2011), pp. 189–212. DOI: [10.1146/annurev-conmatphys-062910-140514](https://doi.org/10.1146/annurev-conmatphys-062910-140514). eprint: <https://doi.org/10.1146/annurev-conmatphys-062910-140514>. URL: <https://doi.org/10.1146/annurev-conmatphys-062910-140514>.
- [3] Y. Kubo et al. “Hybrid Quantum Circuit with a Superconducting Qubit Coupled to a Spin Ensemble”. In: *Phys. Rev. Lett.* 107 (22 Nov. 2011), p. 220501. DOI: [10.1103/PhysRevLett.107.220501](https://doi.org/10.1103/PhysRevLett.107.220501). URL: <https://link.aps.org/doi/10.1103/PhysRevLett.107.220501>.
- [4] Ze-Liang Xiang et al. “Hybrid quantum circuits: Superconducting circuits interacting with other quantum systems”. In: *Rev. Mod. Phys.* 85 (2 Apr. 2013), pp. 623–653. DOI: [10.1103/RevModPhys.85.623](https://doi.org/10.1103/RevModPhys.85.623). URL: <https://link.aps.org/doi/10.1103/RevModPhys.85.623>.
- [5] G. de Lange et al. “Realization of Microwave Quantum Circuits Using Hybrid Superconducting-Semiconducting Nanowire Josephson Elements”. In: *Phys. Rev. Lett.* 115 (12 Sept. 2015), p. 127002. DOI: [10.1103/PhysRevLett.115.127002](https://doi.org/10.1103/PhysRevLett.115.127002). URL: <https://link.aps.org/doi/10.1103/PhysRevLett.115.127002>.
- [6] Lucas Casparis et al. “Superconducting gatemon qubit based on a proximitized two-dimensional electron gas”. In: *Nature Nanotechnology* 13.10 (Oct. 2018), pp. 915–919. ISSN: 1748-3395. DOI: [10.1038/s41565-018-0207-y](https://doi.org/10.1038/s41565-018-0207-y). URL: <https://doi.org/10.1038/s41565-018-0207-y>.
- [7] Webpage Microsoft. <https://cloudblogs.microsoft.com/quantum/2018/09/06/developing-a-topological-qubit/>.
- [8] Joel I-Jan Wang et al. “Coherent control of a hybrid superconducting circuit made with graphene-based van der Waals heterostructures”. In: *Nature Nanotechnology* 14.2 (Feb. 2019), pp. 120–125. ISSN: 1748-3395. DOI: [10.1038/s41565-018-0329-2](https://doi.org/10.1038/s41565-018-0329-2). URL: <https://doi.org/10.1038/s41565-018-0329-2>.

- [9] Morten Kjaergaard et al. “Superconducting Qubits: Current State of Play”. In: *Annual Review of Condensed Matter Physics* 11.1 (2020), pp. 369–395. DOI: [10.1146/annurev-conmatphys-031119-050605](https://doi.org/10.1146/annurev-conmatphys-031119-050605). eprint: <https://doi.org/10.1146/annurev-conmatphys-031119-050605>. URL: <https://doi.org/10.1146/annurev-conmatphys-031119-050605>.
- [10] He-Liang Huang et al. “Superconducting quantum computing: a review”. In: *Science China Information Sciences* 63.8 (July 2020), p. 180501. ISSN: 1869-1919. DOI: [10.1007/s11432-020-2881-9](https://doi.org/10.1007/s11432-020-2881-9). URL: <https://doi.org/10.1007/s11432-020-2881-9>.
- [11] A. I. Buzdin. “Proximity effects in superconductor-ferromagnet heterostructures”. In: *Rev. Mod. Phys.* 77 (3 Sept. 2005), pp. 935–976. DOI: [10.1103/RevModPhys.77.935](https://link.aps.org/doi/10.1103/RevModPhys.77.935). URL: <https://link.aps.org/doi/10.1103/RevModPhys.77.935>.
- [12] F. S. Bergeret, A. F. Volkov, and K. B. Efetov. “Odd triplet superconductivity and related phenomena in superconductor-ferromagnet structures”. In: *Rev. Mod. Phys.* 77 (4 Nov. 2005), pp. 1321–1373. DOI: [10.1103/RevModPhys.77.1321](https://link.aps.org/doi/10.1103/RevModPhys.77.1321). URL: <https://link.aps.org/doi/10.1103/RevModPhys.77.1321>.
- [13] J. W. A. Robinson, J. D. S. Witt, and M. G. Blamire. “Controlled Injection of Spin-Triplet Supercurrents into a Strong Ferromagnet”. In: *Science* 329.5987 (2010), pp. 59–61. ISSN: 0036-8075. DOI: [10.1126/science.1189246](https://doi.org/10.1126/science.1189246). eprint: <http://science.sciencemag.org/content/329/5987/59.full.pdf>. URL: <http://science.sciencemag.org/content/329/5987/59>.
- [14] Trupti S. Khaire et al. “Observation of Spin-Triplet Superconductivity in Co-Based Josephson Junctions”. In: *Phys. Rev. Lett.* 104 (13 Mar. 2010), p. 137002. DOI: [10.1103/PhysRevLett.104.137002](https://link.aps.org/doi/10.1103/PhysRevLett.104.137002). URL: <https://link.aps.org/doi/10.1103/PhysRevLett.104.137002>.
- [15] Matthias Eschrig. “Spin-polarized supercurrents for spintronics”. In: *Physics Today* (1 2011), p. 43. DOI: [10.1063/1.3541944](https://physicstoday.scitation.org/doi/10.1063/1.3541944). URL: <https://physicstoday.scitation.org/doi/10.1063/1.3541944>.
- [16] J. Linder and Jason W. A. Robinson. “Superconducting spintronics”. In: *Nature Physics* 11 (2015), pp. 307–315. DOI: [10.1038/nphys3242](https://doi.org/10.1038/nphys3242). URL: <https://doi.org/10.1038/nphys3242>.
- [17] M G Blamire and J W A Robinson. “The interface between superconductivity and magnetism: understanding and device prospects”. In: *Journal of Physics: Condensed Matter* 26.45 (Oct. 2014), p. 453201. DOI: [10.1088/0953-8984/26/45/453201](https://doi.org/10.1088/0953-8984/26/45/453201). URL: <https://doi.org/10.1088/0953-8984/26/45/453201>.
- [18] D. S. Holmes, A. L. Ripple, and M. A. Manheimer. “Energy-Efficient Superconducting Computing—Power Budgets and Requirements”. In: *IEEE Transactions on Applied Superconductivity* 23.3 (2013), pp. 1701610–1701610. DOI: [10.1109/TASC.2013.2244634](https://doi.org/10.1109/TASC.2013.2244634).

- [19] T. Kato, A. A. Golubov, and Y. Nakamura. “Decoherence in a superconducting flux qubit with a π -junction”. In: *Phys. Rev. B* 76 (17 Nov. 2007), p. 172502. DOI: [10.1103/PhysRevB.76.172502](https://doi.org/10.1103/PhysRevB.76.172502). URL: <https://link.aps.org/doi/10.1103/PhysRevB.76.172502>.
- [20] D. Massarotti et al. “Electrodynamics of Josephson junctions containing strong ferromagnets”. In: *Phys. Rev. B* 98 (14 Oct. 2018), p. 144516. DOI: [10.1103/PhysRevB.98.144516](https://doi.org/10.1103/PhysRevB.98.144516). URL: <https://link.aps.org/doi/10.1103/PhysRevB.98.144516>.
- [21] R. Caruso et al. “Tuning of Magnetic Activity in Spin-Filter Josephson Junctions Towards Spin-Triplet Transport”. In: *Phys. Rev. Lett.* 122 (4 Feb. 2019), p. 047002. DOI: [10.1103/PhysRevLett.122.047002](https://doi.org/10.1103/PhysRevLett.122.047002). URL: <https://link.aps.org/doi/10.1103/PhysRevLett.122.047002>.
- [22] Ahmad H. G. et al. “Manuscript in preparation”. In: (2021).
- [23] H.G. Ahmad et al. “Electrodynamics of Highly Spin-Polarized Tunnel Josephson Junctions”. In: *Phys. Rev. Applied* 13 (1 Jan. 2020), p. 014017. DOI: [10.1103/PhysRevApplied.13.014017](https://doi.org/10.1103/PhysRevApplied.13.014017). URL: <https://link.aps.org/doi/10.1103/PhysRevApplied.13.014017>.
- [24] D. Massarotti et al. “Macroscopic quantum tunnelling in spin filter ferromagnetic Josephson junctions”. In: *Nature Communications* (2015), p. 7376. DOI: [10.1038/ncomms8376](https://doi.org/10.1038/ncomms8376). URL: <https://doi.org/10.1038/ncomms8376>.
- [25] Ahmad H. G. et al. “Manuscript in preparation”. In: (2021).
- [26] A. Barone and G. Paternò. *Physics and Application of the Josephson Effect*. John Wiley and Sons, 1982.
- [27] K. K. Likharev. *Dynamics of Josephson junctions and circuits*. Gordon&Breach, 1986.
- [28] AF Andreev. “The Thermal Conductivity of the Intermediate State in Superconductors”. In: *JETP* 19.5 (1964), p. 1228.
- [29] G. E. Blonder, M. Tinkham, and T. M. Klapwijk. “Transition from metallic to tunneling regimes in superconducting microconstrictions: Excess current, charge imbalance, and supercurrent conversion”. In: *Phys. Rev. B* 25 (7 Apr. 1982), pp. 4515–4532. DOI: [10.1103/PhysRevB.25.4515](https://doi.org/10.1103/PhysRevB.25.4515). URL: <https://link.aps.org/doi/10.1103/PhysRevB.25.4515>.
- [30] C. W. J. Beenakker. “Random-matrix theory of quantum transport”. In: *Rev. Mod. Phys.* 69 (3 July 1997), pp. 731–808. DOI: [10.1103/RevModPhys.69.731](https://doi.org/10.1103/RevModPhys.69.731). URL: <https://link.aps.org/doi/10.1103/RevModPhys.69.731>.
- [31] B. Pannetier and H. Courtois. “Andreev Reflection and Proximity effect”. In: *Journal of Low Temperature Physics* 118.5 (Mar. 2000), pp. 599–615. ISSN: 1573-7357. DOI: [10.1023/A:1004635226825](https://doi.org/10.1023/A:1004635226825). URL: <https://doi.org/10.1023/A:1004635226825>.

- [32] C. W. J. Beenakker. “Universal limit of critical-current fluctuations in mesoscopic Josephson junctions”. In: *Phys. Rev. Lett.* 67 (27 Dec. 1991), pp. 3836–3839. DOI: [10.1103/PhysRevLett.67.3836](https://doi.org/10.1103/PhysRevLett.67.3836). URL: <https://link.aps.org/doi/10.1103/PhysRevLett.67.3836>.
- [33] Michael Tinkham. *Introduction to superconductivity*. Courier Corporation, 2004.
- [34] G. Wild et al. “Josephson coupling and Fiske dynamics in ferromagnetic tunnel junctions”. In: *The European Physical Journal B* 78.4 (Dec. 2010), pp. 509–523. ISSN: 1434-6036. DOI: [10.1140/epjb/e2010-10636-4](https://doi.org/10.1140/epjb/e2010-10636-4). URL: <https://doi.org/10.1140/epjb/e2010-10636-4>.
- [35] M G Blamire et al. “Field modulation of the critical current in magnetic Josephson junctions”. In: *Superconductor Science and Technology* 26.5 (Apr. 2013), p. 055017. DOI: [10.1088/0953-2048/26/5/055017](https://doi.org/10.1088/0953-2048/26/5/055017). URL: <https://doi.org/10.1088/0953-2048/26/5/055017>.
- [36] V. V. Bol’ginov et al. “Magnetic switches based on Nb-PdFe-Nb Josephson junctions with a magnetically soft ferromagnetic interlayer”. In: *JETP Letters* 95.7 (June 2012), pp. 366–371. ISSN: 1090-6487. DOI: [10.1134/S0021364012070028](https://doi.org/10.1134/S0021364012070028).
- [37] Valery V. Ryazanov et al. “Magnetic Josephson Junction Technology for Digital and Memory Applications”. In: *Physics Procedia* 36 (Jan. 2012), pp. 35–41. ISSN: 1875-3892. URL: <https://www.sciencedirect.com/science/article/pii/S1875389212020639>.
- [38] T.I. Larkin et al. “Ferromagnetic Josephson switching device with high characteristic voltage”. In: *Applied Physics Letters* 100.22 (2012), p. 222601. DOI: [10.1063/1.4723576](https://doi.org/10.1063/1.4723576). URL: <https://doi.org/10.1063/1.4723576>.
- [39] I. V. Vernik et al. “Magnetic Josephson Junctions With Superconducting Interlayer for Cryogenic Memory”. In: *IEEE Transactions on Applied Superconductivity* 23.3 (2013), pp. 1701208–1701208. DOI: [10.1109/TASC.2012.2233270](https://doi.org/10.1109/TASC.2012.2233270). URL: <https://ieeexplore.ieee.org/document/6377273>.
- [40] R. Caruso et al. “RF assisted switching in magnetic Josephson junctions”. In: *Journal of Applied Physics* 123 (Apr. 2018), p. 133901. DOI: [10.1063/1.5018854](https://doi.org/10.1063/1.5018854).
- [41] R. Caruso et al. “Properties of ferromagnetic Josephson junctions for memory applications”. In: *IEEE Transactions on Applied Superconductivity* (2018). DOI: [10.1109/TASC.2018.2836979](https://doi.org/10.1109/TASC.2018.2836979).
- [42] Loredana Parlato et al. “Characterization of scalable Josephson memory element containing a strong ferromagnet”. In: *Journal of Applied Physics* 127.19 (2020), p. 193901. DOI: [10.1063/5.0004554](https://doi.org/10.1063/5.0004554). eprint: <https://doi.org/10.1063/5.0004554>. URL: <https://doi.org/10.1063/5.0004554>.
- [43] K. H. J. Buschow. *Concise encyclopedia of magnetic and superconducting materials*. 2nd ed. Elsevier Ltd., 2005.

- [44] Matthias Eschrig and Tomas Löfwander. “Triplet supercurrents in clean and disordered half-metallic ferromagnets”. In: *Nature Physics* 4.2 (Feb. 2008), pp. 138–143. ISSN: 1745-2481. DOI: [10.1038/nphys831](https://doi.org/10.1038/nphys831). URL: <https://doi.org/10.1038/nphys831>.
- [45] M. S. Anwar et al. “Long-range supercurrents through half-metallic ferromagnetic CrO₂”. In: *Phys. Rev. B* 82 (10 Sept. 2010), p. 100501. DOI: [10.1103/PhysRevB.82.100501](https://link.aps.org/doi/10.1103/PhysRevB.82.100501). URL: <https://link.aps.org/doi/10.1103/PhysRevB.82.100501>.
- [46] M.S. Anwar and J.Aarts. “Inducing supercurrents in thin films of ferromagnetic CrO₂”. In: *Superconductor Science and Technology* 24.2 (Jan. 2011), p. 024016. DOI: [10.1088/0953-2048/24/2/024016](https://doi.org/10.1088/0953-2048/24/2/024016). URL: <https://doi.org/10.1088/0953-2048/24/2/024016>.
- [47] M. S. Anwar et al. “Long range supercurrents in ferromagnetic CrO₂ using a multilayer contact structure”. In: *Applied Physics Letters* 100.5 (2012), p. 052602. DOI: [10.1063/1.3681138](https://doi.org/10.1063/1.3681138). eprint: <https://doi.org/10.1063/1.3681138>. URL: <https://doi.org/10.1063/1.3681138>.
- [48] K. K. Likharev. “Superconducting weak links”. In: *Rev. Mod. Phys.* 51 (1 Jan. 1979), pp. 101–159. DOI: [10.1103/RevModPhys.51.101](https://link.aps.org/doi/10.1103/RevModPhys.51.101). URL: <https://link.aps.org/doi/10.1103/RevModPhys.51.101>.
- [49] Vinay Ambegaokar and Alexis Baratoff. “Tunneling Between Superconductors”. In: *Phys. Rev. Lett.* 10 (11 June 1963), pp. 486–489. DOI: [10.1103/PhysRevLett.10.486](https://link.aps.org/doi/10.1103/PhysRevLett.10.486). URL: <https://link.aps.org/doi/10.1103/PhysRevLett.10.486>.
- [50] Peter Fulde and Richard A. Ferrell. “Superconductivity in a Strong Spin-Exchange Field”. In: *Phys. Rev.* 135 (3A Aug. 1964), A550–A563. DOI: [10.1103/PhysRev.135.A550](https://link.aps.org/doi/10.1103/PhysRev.135.A550). URL: <https://link.aps.org/doi/10.1103/PhysRev.135.A550>.
- [51] AI Larkin and Yu N Ovchinnikov. “Density of states in inhomogeneous superconductors”. In: *Sov. Phys. JETP* 34 (1972), pp. 1144–1150.
- [52] Klaus D. Usadel. “Generalized Diffusion Equation for Superconducting Alloys”. In: *Phys. Rev. Lett.* 25 (8 Aug. 1970), pp. 507–509. DOI: [10.1103/PhysRevLett.25.507](https://link.aps.org/doi/10.1103/PhysRevLett.25.507). URL: <https://link.aps.org/doi/10.1103/PhysRevLett.25.507>.
- [53] V. V. Ryazanov et al. “Coupling of Two Superconductors through a Ferromagnet: Evidence for a π Junction”. In: *Phys. Rev. Lett.* 86 (11 Mar. 2001), pp. 2427–2430. DOI: [10.1103/PhysRevLett.86.2427](https://link.aps.org/doi/10.1103/PhysRevLett.86.2427). URL: <https://link.aps.org/doi/10.1103/PhysRevLett.86.2427>.
- [54] V.V. Ryazanov et al. “Coupling of two superconductors through a ferromagnet. SFS π -junctions and intrinsically-frustrated superconducting networks”. In: *Physics-Uspekhi* 44.10S (Oct. 2001), pp. 81–86. DOI: [10.1070/1063-7869/44/10s/s18](https://doi.org/10.1070/1063-7869/44/10s/s18). URL: <https://doi.org/10.1070/1063-7869/44/10s/s18>.

- [55] A. A. Golubov, M. Yu. Kupriyanov, and E. Il'ichev. "The current-phase relation in Josephson junctions". In: *Rev. Mod. Phys.* 76 (2 Apr. 2004), pp. 411–469. DOI: [10.1103/RevModPhys.76.411](https://doi.org/10.1103/RevModPhys.76.411). URL: <https://link.aps.org/doi/10.1103/RevModPhys.76.411>.
- [56] Gert Eilenberger. "Transformation of Gorkov's equation for type II superconductors into transport-like equations". In: *Zeitschrift für Physik A Hadrons and nuclei* 214.2 (Apr. 1968), pp. 195–213. ISSN: 0939-7922. DOI: [10.1007/BF01379803](https://doi.org/10.1007/BF01379803). URL: <https://doi.org/10.1007/BF01379803>.
- [57] Alexandre I Buzdin and M Yu Kupriyanov. "Josephson junction with a ferromagnetic layer". In: *JETP Lett* 53.6 (1991), p. 321.
- [58] Zoran Radović et al. "Transition temperatures of superconductor-ferromagnet superlattices". In: *Physical Review B* 44.2 (1991), p. 759.
- [59] JS Jiang et al. "Oscillatory superconducting transition temperature in Nb/Gd multilayers". In: *Physical review letters* 74.2 (1995), p. 314.
- [60] LV Mercaldo et al. "Superconducting-critical-temperature oscillations in Nb/CuMn multilayers". In: *Physical Review B* 53.21 (1996), p. 14040.
- [61] Y Obi et al. "Oscillation phenomenon of transition temperatures in Nb/Co and V/Co superconductor/ferromagnet multilayers". In: *Physica C: Superconductivity* 317 (1999), pp. 149–153.
- [62] Th Mühge et al. "Possible origin for oscillatory superconducting transition temperature in superconductor/ferromagnet multilayers". In: *Physical review letters* 77.9 (1996), p. 1857.
- [63] M Velez et al. "Enhancement of superconductivity by decreased magnetic spin-flip scattering: Nonmonotonic T_c dependence with enhanced magnetic ordering". In: *Physical Review B* 59.22 (1999), p. 14659.
- [64] L Lazar et al. "Superconductor/ferromagnet proximity effect in Fe/Pb/Fe trilayers". In: *Physical Review B* 61.5 (2000), p. 3711.
- [65] Alexander V. Veretennikov et al. "Supercurrents through the superconductor-ferromagnet-superconductor (SFS) junctions". In: *Physica B: Condensed Matter* 284-288 (2000), pp. 495–496. ISSN: 0921-4526. DOI: [https://doi.org/10.1016/S0921-4526\(99\)02086-4](https://doi.org/10.1016/S0921-4526(99)02086-4). URL: <https://www.sciencedirect.com/science/article/pii/S0921452699020864>.
- [66] IA Garifullin et al. "Re-entrant superconductivity in the superconductor/ferromagnet V/Fe layered system". In: *Physical Review B* 66.2 (2002), p. 020505.
- [67] Anatoli S Sidorenko et al. "Oscillations of the critical temperature in superconducting Nb/Ni bilayers". In: *Annalen der Physik* 12.1-2 (2003), pp. 37–50.
- [68] J. Kehrle et al. "Critical temperature oscillations and reentrant superconductivity due to the FFLO like state in F/S/F trilayers". In: *Annalen der Physik* 524.1 (2012), pp. 37–47. DOI: <https://doi.org/10.1002/andp.201100133>. eprint: <https://onlinelibrary.wiley.com/doi/pdf/10.1002/andp.201100133>. URL: <https://onlinelibrary.wiley.com/doi/abs/10.1002/andp.201100133>.

- [69] V. I. Zdravkov et al. "Reentrant superconductivity and superconducting critical temperature oscillations in F/S/F trilayers of $Cu_{41}Ni_{59}/Nb/Cu_{41}Ni_{59}$ grown on cobalt oxide". In: *Journal of Applied Physics* 114.3 (2013), p. 033903. DOI: [10.1063/1.4813131](https://doi.org/10.1063/1.4813131). eprint: <https://doi.org/10.1063/1.4813131>. URL: <https://doi.org/10.1063/1.4813131>.
- [70] F. Chiodi et al. "Supra-oscillatory critical temperature dependence of Nb-Ho bilayers". In: *EPL (Europhysics Letters)* 101.3 (Feb. 2013), p. 37002. DOI: [10.1209/0295-5075/101/37002](https://doi.org/10.1209/0295-5075/101/37002). URL: <https://doi.org/10.1209/0295-5075/101/37002>.
- [71] V. A. Tumanov, Yu. V. Goryunov, and Yu. N. Proshin. "Oscillations of the Critical Temperature in a (Fe/Cr/Fe)/V/Fe Heterostructure". In: *JETP Letters* 107.7 (Apr. 2018), pp. 426–430. ISSN: 1090-6487. DOI: [10.1134/S002136401807010X](https://doi.org/10.1134/S002136401807010X). URL: <https://doi.org/10.1134/S002136401807010X>.
- [72] V. V. Ryazanov et al. "Intrinsically frustrated superconducting array of superconductor-ferromagnet-superconductor π junctions". In: *Phys. Rev. B* 65 (2 Dec. 2001), p. 020501. DOI: [10.1103/PhysRevB.65.020501](https://doi.org/10.1103/PhysRevB.65.020501). URL: <https://link.aps.org/doi/10.1103/PhysRevB.65.020501>.
- [73] S. M. Frolov et al. "Measurement of the current-phase relation of superconductor/ferromagnet/superconductor π Josephson junctions". In: *Phys. Rev. B* 70 (14 Oct. 2004), p. 144505. DOI: [10.1103/PhysRevB.70.144505](https://doi.org/10.1103/PhysRevB.70.144505). URL: <https://link.aps.org/doi/10.1103/PhysRevB.70.144505>.
- [74] F. Born et al. "Multiple $0 - \pi$ transitions in superconductor/insulator/-ferromagnet/superconductor Josephson tunnel junctions". In: *Phys. Rev. B* 74 (14 Oct. 2006), p. 140501. DOI: [10.1103/PhysRevB.74.140501](https://doi.org/10.1103/PhysRevB.74.140501). URL: <https://link.aps.org/doi/10.1103/PhysRevB.74.140501>.
- [75] S. M. Frolov et al. "Josephson interferometry and Shapiro step measurements of superconductor-ferromagnet-superconductor $0 - \pi$ junctions". In: *Phys. Rev. B* 74 (2 July 2006), p. 020503. DOI: [10.1103/PhysRevB.74.020503](https://doi.org/10.1103/PhysRevB.74.020503). URL: <https://link.aps.org/doi/10.1103/PhysRevB.74.020503>.
- [76] V. A. Oboznov et al. "Thickness Dependence of the Josephson Ground States of Superconductor-Ferromagnet-Superconductor Junctions". In: *Phys. Rev. Lett.* 96 (19 May 2006), p. 197003. DOI: [10.1103/PhysRevLett.96.197003](https://doi.org/10.1103/PhysRevLett.96.197003). URL: <https://link.aps.org/doi/10.1103/PhysRevLett.96.197003>.
- [77] J. W. A. Robinson et al. "Critical Current Oscillations in Strong Ferromagnetic π Junctions". In: *Phys. Rev. Lett.* 97 (17 Oct. 2006), p. 177003. DOI: [10.1103/PhysRevLett.97.177003](https://doi.org/10.1103/PhysRevLett.97.177003). URL: <https://link.aps.org/doi/10.1103/PhysRevLett.97.177003>.
- [78] M. Weides et al. "High quality ferromagnetic 0 and π Josephson tunnel junctions". In: *Applied Physics Letters* 89.12 (2006), p. 122511. DOI: [10.1063/1.2356104](https://doi.org/10.1063/1.2356104). eprint: <https://doi.org/10.1063/1.2356104>. URL: <https://doi.org/10.1063/1.2356104>.

- [79] S. Piano et al. “ $0-\pi$ oscillations in nanostructured Nb/Fe/Nb Josephson junctions”. In: *The European Physical Journal B* 58.2 (July 2007), pp. 123–126. ISSN: 1434-6036. DOI: [10.1140/epjb/e2007-00210-8](https://doi.org/10.1140/epjb/e2007-00210-8). URL: <https://doi.org/10.1140/epjb/e2007-00210-8>.
- [80] J. W. A. Robinson et al. “Zero to π transition in superconductor-ferromagnet-superconductor junctions”. In: *Phys. Rev. B* 76 (9 Sept. 2007), p. 094522. DOI: [10.1103/PhysRevB.76.094522](https://link.aps.org/doi/10.1103/PhysRevB.76.094522). URL: <https://link.aps.org/doi/10.1103/PhysRevB.76.094522>.
- [81] M. Kemmler et al. “Magnetic interference patterns in $0-\pi$ superconductor/insulator/ferromagnet/superconductor Josephson junctions: Effects of asymmetry between 0 and π regions”. In: *Phys. Rev. B* 81 (5 Feb. 2010), p. 054522. DOI: [10.1103/PhysRevB.81.054522](https://link.aps.org/doi/10.1103/PhysRevB.81.054522). URL: <https://link.aps.org/doi/10.1103/PhysRevB.81.054522>.
- [82] R. Loria et al. “Robustness of the $0-\pi$ transition against compositional and structural ageing in superconductor/ferromagnetic/superconductor heterostructures”. In: *Phys. Rev. B* 92 (18 Nov. 2015), p. 184106. DOI: [10.1103/PhysRevB.92.184106](https://link.aps.org/doi/10.1103/PhysRevB.92.184106). URL: <https://link.aps.org/doi/10.1103/PhysRevB.92.184106>.
- [83] Feng Li, Wei Peng, and Zhen Wang. “The $0-\pi$ Phase Transition in Epitaxial NbN/Ni₆₀Cu₄₀/NbN Josephson Junctions”. In: *Chinese Physics Letters* 36.4 (Apr. 2019), p. 047401. DOI: [10.1088/0256-307x/36/4/047401](https://doi.org/10.1088/0256-307x/36/4/047401). URL: <https://doi.org/10.1088/0256-307x/36/4/047401>.
- [84] H v. Löhneysen et al. “Proximity effect between superconductors and ferromagnets: from thin films to nanostructures”. In: *Annalen der Physik* 14.9-10 (2005), pp. 591–601.
- [85] I. A. Garifullin. “Recent experimental results on the superconductor/ferromagnet proximity effect”. In: *JETP Letters* 93.10 (July 2011), p. 612. ISSN: 1090-6487. DOI: [10.1134/S0021364011100079](https://doi.org/10.1134/S0021364011100079). URL: <https://doi.org/10.1134/S0021364011100079>.
- [86] L.N. Bulaevskii, V.V. Kuzii, and A.A. Sobyenin. “Superconducting system with weak coupling to the current in the ground state”. In: *JETP Lett. (USSR) (Engl. Transl.); (United States)* 25:7 (1977).
- [87] T. Kontos et al. “Inhomogeneous Superconductivity Induced in a Ferromagnet by Proximity Effect”. In: *Phys. Rev. Lett.* 86 (2 Jan. 2001), pp. 304–307. DOI: [10.1103/PhysRevLett.86.304](https://link.aps.org/doi/10.1103/PhysRevLett.86.304). URL: <https://link.aps.org/doi/10.1103/PhysRevLett.86.304>.
- [88] Y. Blum et al. “Oscillations of the Superconducting Critical Current in Nb-Cu-Ni-Cu-Nb Junctions”. In: *Phys. Rev. Lett.* 89 (18 Oct. 2002), p. 187004. DOI: [10.1103/PhysRevLett.89.187004](https://link.aps.org/doi/10.1103/PhysRevLett.89.187004). URL: <https://link.aps.org/doi/10.1103/PhysRevLett.89.187004>.
- [89] T. Kontos et al. “Josephson Junction through a Thin Ferromagnetic Layer: Negative Coupling”. In: *Phys. Rev. Lett.* 89 (13 Sept. 2002), p. 137007. DOI: [10.1103/PhysRevLett.89.137007](https://link.aps.org/doi/10.1103/PhysRevLett.89.137007). URL: <https://link.aps.org/doi/10.1103/PhysRevLett.89.137007>.

- [90] A. I. Buzdin, L. N. Bulaevskii, and S. V. Panyukov. "Critical-current oscillations as a function of the exchange field and thickness of the ferromagnetic metal (F) in an S-F-S Josephson junction". In: *JETP Letters* 35.4 (Feb 1982), pp. 178–180. ISSN: 0021-3640. URL: http://inis.iaea.org/search/search.aspx?orig_q=RN:14748338.
- [91] A Buzdin and AE Koshelev. "Periodic alternating 0-and π -junction structures as realization of φ -Josephson junctions". In: *Physical Review B* 67.22 (2003), p. 220504.
- [92] S. V. Bakurskiy et al. "Compact Josephson ϕ -Junctions". In: *Functional Nanostructures and Metamaterials for Superconducting Spintronics: From Superconducting Qubits to Self-Organized Nanostructures*. Ed. by Anatolie Sidorenko. Cham: Springer International Publishing, 2018, pp. 49–71. ISBN: 978-3-319-90481-8. DOI: [10.1007/978-3-319-90481-8_3](https://doi.org/10.1007/978-3-319-90481-8_3). URL: https://doi.org/10.1007/978-3-319-90481-8_3.
- [93] H. Sickinger et al. "Experimental Evidence of a φ Josephson Junction". In: *Phys. Rev. Lett.* 109 (10 Sept. 2012), p. 107002. DOI: [10.1103/PhysRevLett.109.107002](https://doi.org/10.1103/PhysRevLett.109.107002). URL: <https://link.aps.org/doi/10.1103/PhysRevLett.109.107002>.
- [94] Yasuhiro Asano et al. "Odd-frequency pairs and Josephson current through a strong ferromagnet". In: *Phys. Rev. B* 76 (22 Dec. 2007), p. 224525. DOI: [10.1103/PhysRevB.76.224525](https://doi.org/10.1103/PhysRevB.76.224525). URL: <https://link.aps.org/doi/10.1103/PhysRevB.76.224525>.
- [95] A. Buzdin. "Direct Coupling Between Magnetism and Superconducting Current in the Josephson φ_0 Junction". In: *Phys. Rev. Lett.* 101 (10 Sept. 2008), p. 107005. DOI: [10.1103/PhysRevLett.101.107005](https://doi.org/10.1103/PhysRevLett.101.107005). URL: <https://link.aps.org/doi/10.1103/PhysRevLett.101.107005>.
- [96] I Margaris, V Paltoglou, and N Flytzanis. "Zero phase difference supercurrent in ferromagnetic Josephson junctions". In: *Journal of Physics: Condensed Matter* 22.44 (Oct. 2010), p. 445701. DOI: [10.1088/0953-8984/22/44/445701](https://doi.org/10.1088/0953-8984/22/44/445701). URL: <https://doi.org/10.1088/0953-8984/22/44/445701>.
- [97] S V Bakurskiy et al. "Josephson φ -junctions based on structures with complex normal/ferromagnet bilayer". In: *Superconductor Science and Technology* 26.1 (Nov. 2012), p. 015005. DOI: [10.1088/0953-2048/26/1/015005](https://doi.org/10.1088/0953-2048/26/1/015005). URL: <https://doi.org/10.1088/0953-2048/26/1/015005>.
- [98] D M Heim et al. "Ferromagnetic planar Josephson junction with transparent interfaces: a φ junction proposal". In: *Journal of Physics: Condensed Matter* 25.21 (May 2013), p. 215701. DOI: [10.1088/0953-8984/25/21/215701](https://doi.org/10.1088/0953-8984/25/21/215701). URL: <https://doi.org/10.1088/0953-8984/25/21/215701>.
- [99] S. V. Bakurskiy et al. "Protected 0 – π states in SIsFS junctions for Josephson memory and logic". In: *Applied Physics Letters* 113.8 (2018), p. 082602. DOI: [10.1063/1.5045490](https://doi.org/10.1063/1.5045490). eprint: <https://doi.org/10.1063/1.5045490>. URL: <https://doi.org/10.1063/1.5045490>.

- [100] Yu. M. Shukrinov, I. R. Rahmonov, and A. E. Botha. “Peculiarities of IV-characteristics and magnetization dynamics in the φ_0 Josephson junction”. In: *Low Temperature Physics* 46.9 (2020), pp. 932–938. DOI: [10.1063/10.0001716](https://doi.org/10.1063/10.0001716). eprint: <https://doi.org/10.1063/10.0001716>. URL: <https://doi.org/10.1063/10.0001716>.
- [101] Z. Radović, L. Dobrosavljević-Grujić, and B. Vujičić. “Coexistence of stable and metastable 0 and π states in Josephson junctions”. In: *Phys. Rev. B* 63 (21 May 2001), p. 214512. DOI: [10.1103/PhysRevB.63.214512](https://doi.org/10.1103/PhysRevB.63.214512). URL: <https://link.aps.org/doi/10.1103/PhysRevB.63.214512>.
- [102] Z. Radović, N. Lazarides, and N. Flytzanis. “Josephson effect in double-barrier superconductor-ferromagnet junctions”. In: *Phys. Rev. B* 68 (1 July 2003), p. 014501. DOI: [10.1103/PhysRevB.68.014501](https://doi.org/10.1103/PhysRevB.68.014501). URL: <https://link.aps.org/doi/10.1103/PhysRevB.68.014501>.
- [103] N. M. Chtchelkatchev et al. “ π -0 transition in superconductor-ferromagnet-superconductor junctions”. In: *Journal of Experimental and Theoretical Physics Letters* 74.6 (Sept. 2001), pp. 323–327. ISSN: 1090-6487. DOI: [10.1134/1.1421408](https://doi.org/10.1134/1.1421408). URL: <https://doi.org/10.1134/1.1421408>.
- [104] E. Goldobin et al. “Josephson junctions with second harmonic in the current-phase relation: Properties of φ junctions”. In: *Phys. Rev. B* 76 (22 Dec. 2007), p. 224523. DOI: [10.1103/PhysRevB.76.224523](https://doi.org/10.1103/PhysRevB.76.224523). URL: <https://link.aps.org/doi/10.1103/PhysRevB.76.224523>.
- [105] M. Nashaat et al. “Microwave induced tunable subharmonic steps in superconductor-ferromagnet-superconductor Josephson junction”. In: *Low Temperature Physics* 45.12 (2019), pp. 1246–1251. DOI: [10.1063/10.0000203](https://doi.org/10.1063/10.0000203). eprint: <https://doi.org/10.1063/10.0000203>. URL: <https://doi.org/10.1063/10.0000203>.
- [106] W. Guichard et al. “Phase Sensitive Experiments in Ferromagnetic-Based Josephson Junctions”. In: *Phys. Rev. Lett.* 90 (16 Apr. 2003), p. 167001. DOI: [10.1103/PhysRevLett.90.167001](https://doi.org/10.1103/PhysRevLett.90.167001). URL: <https://link.aps.org/doi/10.1103/PhysRevLett.90.167001>.
- [107] A. V. Ustinov and V. K. Kaplunenko. “Rapid single-flux quantum logic using π -shifters”. In: *Journal of Applied Physics* 94.8 (2003), pp. 5405–5407. DOI: [10.1063/1.1604964](https://doi.org/10.1063/1.1604964). URL: <https://aip.scitation.org/doi/abs/10.1063/1.1604964>.
- [108] A. Bauer et al. “Spontaneous Supercurrent Induced by Ferromagnetic π Junctions”. In: *Phys. Rev. Lett.* 92 (21 May 2004), p. 217001. DOI: [10.1103/PhysRevLett.92.217001](https://doi.org/10.1103/PhysRevLett.92.217001). URL: <https://link.aps.org/doi/10.1103/PhysRevLett.92.217001>.
- [109] S. Kawabata et al. “Macroscopic quantum dynamics of π junctions with ferromagnetic insulators”. In: *Phys. Rev. B* 74 (18 Nov. 2006), p. 180502. DOI: [10.1103/PhysRevB.74.180502](https://doi.org/10.1103/PhysRevB.74.180502). URL: <https://link.aps.org/doi/10.1103/PhysRevB.74.180502>.

- [110] A. K. Feofanov et al. "Implementation of superconductor/ferromagnet/ superconductor π -shifters in superconducting digital and quantum circuits". In: *Nature Physics* 6 (2010), p. 593. DOI: [10.1038/nphys1700](https://doi.org/10.1038/nphys1700).
- [111] Igor Žutić, Jaroslav Fabian, and S. Das Sarma. "Spintronics: Fundamentals and applications". In: *Rev. Mod. Phys.* 76 (2 Apr. 2004), pp. 323–410. DOI: [10.1103/RevModPhys.76.323](https://doi.org/10.1103/RevModPhys.76.323). URL: <https://link.aps.org/doi/10.1103/RevModPhys.76.323>.
- [112] Kaveh Lahabi et al. "Controlling supercurrents and their spatial distribution in ferromagnets". In: *Nature Communications* 8.1 (Dec. 2017), p. 2056. ISSN: 2041-1723. DOI: [10.1038/s41467-017-02236-2](https://doi.org/10.1038/s41467-017-02236-2). URL: <https://doi.org/10.1038/s41467-017-02236-2>.
- [113] S. Kawabata et al. "Efficient electron refrigeration using superconductor/spin-filter devices". In: *Applied Physics Letters* 103.3 (2013), p. 032602. DOI: [10.1063/1.4813599](https://doi.org/10.1063/1.4813599). URL: <https://doi.org/10.1063/1.4813599>.
- [114] Norman O. Birge. "Spin-triplet supercurrents in Josephson junctions containing strong ferromagnetic materials". In: *Philosophical Transactions of the Royal Society A: Mathematical, Physical and Engineering Sciences* 376.2125 (2018), p. 20150150. DOI: [10.1098/rsta.2015.0150](https://doi.org/10.1098/rsta.2015.0150). eprint: <https://royalsocietypublishing.org/doi/pdf/10.1098/rsta.2015.0150>. URL: <https://royalsocietypublishing.org/doi/abs/10.1098/rsta.2015.0150>.
- [115] F. S. Bergeret, A. F. Volkov, and K. B. Efetov. "Long-Range Proximity Effects in Superconductor-Ferromagnet Structures". In: *Phys. Rev. Lett.* 86 (18 Apr. 2001), pp. 4096–4099. DOI: [10.1103/PhysRevLett.86.4096](https://doi.org/10.1103/PhysRevLett.86.4096). URL: <https://link.aps.org/doi/10.1103/PhysRevLett.86.4096>.
- [116] Kadigrobov, A., Shekhter, R. I., and Jonson, M. "Quantum spin fluctuations as a source of long-range proximity effects in diffusive ferromagnet-superconductor structures". In: *Europhys. Lett.* 54.3 (2001), pp. 394–400. DOI: [10.1209/epl/i2001-00107-2](https://doi.org/10.1209/epl/i2001-00107-2). URL: <https://doi.org/10.1209/epl/i2001-00107-2>.
- [117] P. Coleman, E. Miranda, and A. Tsvelik. "Odd-frequency pairing in the Kondo lattice". In: *Phys. Rev. B* 49 (13 Apr. 1994), pp. 8955–8982. DOI: [10.1103/PhysRevB.49.8955](https://doi.org/10.1103/PhysRevB.49.8955). URL: <https://link.aps.org/doi/10.1103/PhysRevB.49.8955>.
- [118] Elihu Abrahams et al. "Properties of odd-gap superconductors". In: *Phys. Rev. B* 52 (2 July 1995), pp. 1271–1278. DOI: [10.1103/PhysRevB.52.1271](https://doi.org/10.1103/PhysRevB.52.1271). URL: <https://link.aps.org/doi/10.1103/PhysRevB.52.1271>.
- [119] M. Houzet and A. I. Buzdin. "Long range triplet Josephson effect through a ferromagnetic trilayer". In: *Phys. Rev. B* 76 (6 Aug. 2007), p. 060504. DOI: [10.1103/PhysRevB.76.060504](https://doi.org/10.1103/PhysRevB.76.060504). URL: <https://link.aps.org/doi/10.1103/PhysRevB.76.060504>.

- [120] E. C. Gingrich et al. "Spin-triplet supercurrent in Co/Ni multilayer Josephson junctions with perpendicular anisotropy". In: *Phys. Rev. B* 86 (22 Dec. 2012), p. 224506. DOI: [10.1103/PhysRevB.86.224506](https://doi.org/10.1103/PhysRevB.86.224506). URL: <https://link.aps.org/doi/10.1103/PhysRevB.86.224506>.
- [121] J W A Robinson et al. "Supercurrent enhancement in Bloch domain walls". In: *Scientific reports* 2 (2012), p. 699. ISSN: 2045-2322. DOI: [10.1038/srep00699](https://doi.org/10.1038/srep00699). URL: <https://europepmc.org/articles/PMC3458244>.
- [122] P. V. Leksin et al. "Evidence for Triplet Superconductivity in a Superconductor-Ferromagnet Spin Valve". In: *Phys. Rev. Lett.* 109 (5 Aug. 2012), p. 057005. DOI: [10.1103/PhysRevLett.109.057005](https://doi.org/10.1103/PhysRevLett.109.057005). URL: <https://link.aps.org/doi/10.1103/PhysRevLett.109.057005>.
- [123] P. V. Leksin et al. "Superconducting spin-valve effect and triplet superconductivity in CoO_x/Fe1/Cu/Fe2/Cu/Pb multilayer". In: *Phys. Rev. B* 91 (21 June 2015), p. 214508. DOI: [10.1103/PhysRevB.91.214508](https://doi.org/10.1103/PhysRevB.91.214508). URL: <https://link.aps.org/doi/10.1103/PhysRevB.91.214508>.
- [124] William M. Martinez, W. P. Pratt, and Norman O. Birge. "Amplitude Control of the Spin-Triplet Supercurrent in S/F/S Josephson Junctions". In: *Phys. Rev. Lett.* 116 (7 Feb. 2016), p. 077001. DOI: [10.1103/PhysRevLett.116.077001](https://doi.org/10.1103/PhysRevLett.116.077001). URL: <https://link.aps.org/doi/10.1103/PhysRevLett.116.077001>.
- [125] Victor M. Edelstein. "Triplet superconductivity and magnetoelectric effect near the s-wave-superconductor-normal-metal interface caused by local breaking of mirror symmetry". In: *Phys. Rev. B* 67 (2 Jan. 2003), p. 020505. DOI: [10.1103/PhysRevB.67.020505](https://doi.org/10.1103/PhysRevB.67.020505). URL: <https://link.aps.org/doi/10.1103/PhysRevB.67.020505>.
- [126] M Smidman et al. "Superconductivity and spin-orbit coupling in non-centrosymmetric materials: a review". In: *Reports on Progress in Physics* 80.3 (Jan. 2017), p. 036501. DOI: [10.1088/1361-6633/80/3/036501](https://doi.org/10.1088/1361-6633/80/3/036501). URL: <https://doi.org/10.1088/1361-6633/80/3/036501>.
- [127] V. M. Edel'shtein. "Characteristics of the Cooper pairing in two-dimensional noncentrosymmetric electron systems". In: *Soviet Physics - JETP (English Translation)* 68.6 (1989), pp. 1244–1249. ISSN: 0038-5646. URL: http://inis.iaea.org/search/search.aspx?orig_q=RN:22082571.
- [128] F. S. Bergeret and I. V. Tokatly. "Spin-orbit coupling as a source of long-range triplet proximity effect in superconductor-ferromagnet hybrid structures". In: *Phys. Rev. B* 89 (13 Apr. 2014), p. 134517. DOI: [10.1103/PhysRevB.89.134517](https://doi.org/10.1103/PhysRevB.89.134517). URL: <https://link.aps.org/doi/10.1103/PhysRevB.89.134517>.
- [129] M. M. Desjardins et al. "Synthetic spin-orbit interaction for Majorana devices". In: *Nature Materials* 18.10 (Oct. 2019), pp. 1060–1064. ISSN: 1476-4660. DOI: [10.1038/s41563-019-0457-6](https://doi.org/10.1038/s41563-019-0457-6). URL: <https://doi.org/10.1038/s41563-019-0457-6>.

- [130] Tong Zhou et al. “Tunable magnetic textures in spin valves: From spintronics to Majorana bound states”. In: *Phys. Rev. B* 99 (13 Apr. 2019), p. 134505. DOI: [10.1103/PhysRevB.99.134505](https://doi.org/10.1103/PhysRevB.99.134505). URL: <https://link.aps.org/doi/10.1103/PhysRevB.99.134505>.
- [131] Narayan Mohanta et al. “Electrical Control of Majorana Bound States Using Magnetic Stripes”. In: *Phys. Rev. Applied* 12 (3 Sept. 2019), p. 034048. DOI: [10.1103/PhysRevApplied.12.034048](https://doi.org/10.1103/PhysRevApplied.12.034048). URL: <https://link.aps.org/doi/10.1103/PhysRevApplied.12.034048>.
- [132] Johannes R. Eskilt et al. “Long-ranged triplet supercurrent in a single in-plane ferromagnet with spin-orbit coupled contacts to superconductors”. In: *Phys. Rev. B* 100 (22 Dec. 2019), p. 224519. DOI: [10.1103/PhysRevB.100.224519](https://doi.org/10.1103/PhysRevB.100.224519). URL: <https://link.aps.org/doi/10.1103/PhysRevB.100.224519>.
- [133] Kun-Rok Jeon et al. “Tunable Pure Spin Supercurrents and the Demonstration of Their Gateability in a Spin-Wave Device”. In: *Phys. Rev. X* 10 (3 July 2020), p. 031020. DOI: [10.1103/PhysRevX.10.031020](https://doi.org/10.1103/PhysRevX.10.031020). URL: <https://link.aps.org/doi/10.1103/PhysRevX.10.031020>.
- [134] César González-Ruano et al. “Superconductivity-induced change in magnetic anisotropy in epitaxial ferromagnet-superconductor hybrids with spin-orbit interaction”. In: *Phys. Rev. B* 102 (2 July 2020), p. 020405. DOI: [10.1103/PhysRevB.102.020405](https://doi.org/10.1103/PhysRevB.102.020405). URL: <https://link.aps.org/doi/10.1103/PhysRevB.102.020405>.
- [135] Jan Aarts and Alexander Yu. Rusanov. “The effects of magnetization switching on the superconducting properties of S/F bilayers and F/S/F trilayers”. In: *Comptes Rendus Physique* 7.1 (2006). Superconductivity and magnetism, pp. 99–106. ISSN: 1631-0705. DOI: <https://doi.org/10.1016/j.crhy.2005.12.005>. URL: <https://www.sciencedirect.com/science/article/pii/S1631070505001891>.
- [136] M. Flokstra and J. Aarts. “Domain-wall enhancement of superconductivity in superconductor/ferromagnet hybrids: Case of weak ferromagnets”. In: *Phys. Rev. B* 80 (14 Oct. 2009), p. 144513. DOI: [10.1103/PhysRevB.80.144513](https://doi.org/10.1103/PhysRevB.80.144513). URL: <https://link.aps.org/doi/10.1103/PhysRevB.80.144513>.
- [137] A. S. Mel’nikov et al. “Interference Phenomena and Long-Range Proximity Effect in Clean Superconductor-Ferromagnet Systems”. In: *Phys. Rev. Lett.* 109 (23 Dec. 2012), p. 237006. DOI: [10.1103/PhysRevLett.109.237006](https://doi.org/10.1103/PhysRevLett.109.237006). URL: <https://link.aps.org/doi/10.1103/PhysRevLett.109.237006>.
- [138] Adrian Iovan, Taras Golod, and Vladimir M. Krasnov. “Controllable generation of a spin-triplet supercurrent in a Josephson spin valve”. In: *Phys. Rev. B* 90 (13 Oct. 2014), p. 134514. DOI: [10.1103/PhysRevB.90.134514](https://doi.org/10.1103/PhysRevB.90.134514). URL: <https://link.aps.org/doi/10.1103/PhysRevB.90.134514>.

- [139] W. C. Stewart. "CURRENT-VOLTAGE CHARACTERISTICS OF JOSEPHSON JUNCTIONS". In: *Applied Physics Letters* 12.8 (1968), pp. 277–280. DOI: [10.1063/1.1651991](https://doi.org/10.1063/1.1651991). eprint: <https://doi.org/10.1063/1.1651991>. URL: <https://doi.org/10.1063/1.1651991>.
- [140] N. R. Werthamer. "Nonlinear Self-Coupling of Josephson Radiation in Superconducting Tunnel Junctions". In: *Phys. Rev.* 147 (1 July 1966), pp. 255–263. DOI: [10.1103/PhysRev.147.255](https://link.aps.org/doi/10.1103/PhysRev.147.255). URL: <https://link.aps.org/doi/10.1103/PhysRev.147.255>.
- [141] Ovchinnikov Y. N. Larkin A. I. In: *J.Exptl.Theoret.Phys.(U.S.S.R.)* 51 (1966), p. 1535.
- [142] A. Odintsov, V. Semenov, and A. Zorin. "Specific problems of numerical analysis of the Josephson junction circuits". In: *IEEE Transactions on Magnetics* 23.2 (Mar. 1987), pp. 763–766. ISSN: 0018-9464. DOI: [10.1109/TMAG.1987.1064907](https://doi.org/10.1109/TMAG.1987.1064907).
- [143] J. R. Kirtley et al. "Measurement of the Intrinsic Subgap Dissipation in Josephson Junctions". In: *Phys. Rev. Lett.* 61 (20 Nov. 1988), pp. 2372–2375. DOI: [10.1103/PhysRevLett.61.2372](https://link.aps.org/doi/10.1103/PhysRevLett.61.2372). URL: <https://link.aps.org/doi/10.1103/PhysRevLett.61.2372>.
- [144] R. Cristiano et al. "The effective dissipation in Nb/AlO_x/Nb Josephson tunnel junctions by return current measurements". In: *Journal of Applied Physics* 81.11 (1997), pp. 7418–7426. DOI: [10.1063/1.365282](https://doi.org/10.1063/1.365282). URL: <https://doi.org/10.1063/1.365282>.
- [145] J. Koch et al. "Charge-insensitive qubit design derived from the Cooper pair box". In: *Phys. Rev. A* 76 (4 Oct. 2007), p. 042319. DOI: [10.1103/PhysRevA.76.042319](https://link.aps.org/doi/10.1103/PhysRevA.76.042319). URL: <https://link.aps.org/doi/10.1103/PhysRevA.76.042319>.
- [146] J. Clarke and F. K. Wilhelm. "Superconducting quantum bits". In: *Nature* 453 (2008), pp. 1031–1042. DOI: [10.1038/nature07128](https://doi.org/10.1038/nature07128).
- [147] M. H. Devoret and R. J. Schoelkopf. "Superconducting circuits for quantum information: an outlook". In: *Science* 339 (2013), p. 1169. DOI: [10.1126/science.1231930](https://doi.org/10.1126/science.1231930).
- [148] K. Serniak et al. "Hot Nonequilibrium Quasiparticles in Transmon Qubits". In: *Phys. Rev. Lett.* 121 (15 Oct. 2018), p. 157701. DOI: [10.1103/PhysRevLett.121.157701](https://link.aps.org/doi/10.1103/PhysRevLett.121.157701). URL: <https://link.aps.org/doi/10.1103/PhysRevLett.121.157701>.
- [149] A.S. Vasenko et al. "Dissipative current in SIFS Josephson junctions". In: *Physica C: Superconductivity* 470.19 (2010). Vortex Matter in Nanostructured Superconductors, pp. 863–866. ISSN: 0921-4534. DOI: <https://doi.org/10.1016/j.physc.2010.02.081>. URL: <https://www.sciencedirect.com/science/article/pii/S0921453410001887>.
- [150] I.O. Kulik. "Magnitude of the Critical Josephson Tunnel Current". In: *JETP* 22 (4 Apr. 1966), p. 841. URL: http://www.jetp.ac.ru/cgi-bin/dn/e_022_04_0841.pdf.

- [151] A. Zorin, K. Likharev, and S. Turovets. “Dynamics of Josephson tunnel junctions with a finite-width Riedel peak”. In: *IEEE Transactions on Magnetics* 19.3 (May 1983), pp. 629–632. ISSN: 0018-9464. DOI: [10.1109/TMAG.1983.1062475](https://doi.org/10.1109/TMAG.1983.1062475).
- [152] C. A. Hamilton and Sidney Shapiro. “Experimental Demonstration of the Riedel Peak”. In: *Phys. Rev. Lett.* 26 (8 Feb. 1971), pp. 426–428. DOI: [10.1103/PhysRevLett.26.426](https://link.aps.org/doi/10.1103/PhysRevLett.26.426). URL: <https://link.aps.org/doi/10.1103/PhysRevLett.26.426>.
- [153] D. R. Gulevich, V. P. Koshelets, and F. V. Kusmartsev. “Josephson flux-flow oscillator: The microscopic tunneling approach”. In: *Phys. Rev. B* 96 (2 July 2017), p. 024515. DOI: [10.1103/PhysRevB.96.024515](https://doi.org/10.1103/PhysRevB.96.024515). URL: <https://link.aps.org/doi/10.1103/PhysRevB.96.024515>.
- [154] M. Iansiti et al. “Charging energy and phase delocalization in single very small Josephson tunnel junctions”. In: *Phys. Rev. Lett.* 59 (4 July 1987), pp. 489–492. DOI: [10.1103/PhysRevLett.59.489](https://doi.org/10.1103/PhysRevLett.59.489). URL: <https://link.aps.org/doi/10.1103/PhysRevLett.59.489>.
- [155] J. M. Martinis and R. L. Kautz. “Classical phase diffusion in small hysteretic Josephson junctions”. In: *Phys. Rev. Lett.* 63 (14 Oct. 1989), pp. 1507–1510. DOI: [10.1103/PhysRevLett.63.1507](https://doi.org/10.1103/PhysRevLett.63.1507). URL: <https://link.aps.org/doi/10.1103/PhysRevLett.63.1507>.
- [156] R. L. Kautz and J. M. Martinis. “Noise-affected IV curves in small hysteretic Josephson junctions”. In: *Phys. Rev. B* 42 (16 Dec. 1990), pp. 9903–9937. DOI: [10.1103/PhysRevB.42.9903](https://doi.org/10.1103/PhysRevB.42.9903). URL: <https://link.aps.org/doi/10.1103/PhysRevB.42.9903>.
- [157] H.A. Kramers. “Brownian motion in a field of force and the diffusion model of chemical reactions”. In: *Physica* 7.4 (1940), pp. 284–304. ISSN: 0031-8914. DOI: [https://doi.org/10.1016/S0031-8914\(40\)90098-2](https://doi.org/10.1016/S0031-8914(40)90098-2). URL: <http://www.sciencedirect.com/science/article/pii/S0031891440900982>.
- [158] T. A. Fulton and L. N. Dunkleberger. “Lifetime of the zero-voltage state in Josephson tunnel junctions”. In: *Phys. Rev. B* 9 (11 June 1974), pp. 4760–4768. DOI: [10.1103/PhysRevB.9.4760](https://doi.org/10.1103/PhysRevB.9.4760). URL: <https://link.aps.org/doi/10.1103/PhysRevB.9.4760>.
- [159] A. O. Caldeira and A. J. Leggett. “Influence of Dissipation on Quantum Tunneling in Macroscopic Systems”. In: *Phys. Rev. Lett.* 46 (4 Jan. 1981), pp. 211–214. DOI: [10.1103/PhysRevLett.46.211](https://doi.org/10.1103/PhysRevLett.46.211). URL: <https://link.aps.org/doi/10.1103/PhysRevLett.46.211>.
- [160] Michel H. Devoret, John M. Martinis, and John Clarke. “Measurements of Macroscopic Quantum Tunneling out of the Zero-Voltage State of a Current-Biased Josephson Junction”. In: *Phys. Rev. Lett.* 55 (18 Oct. 1985), pp. 1908–1911. DOI: [10.1103/PhysRevLett.55.1908](https://doi.org/10.1103/PhysRevLett.55.1908). URL: <https://link.aps.org/doi/10.1103/PhysRevLett.55.1908>.

- [161] J. M. Martinis, M. H. Devoret, and J. Clarke. “Experimental tests for the quantum behavior of a macroscopic degree of freedom: the phase difference across a Josephson junction”. In: *Phys. Rev. B* 35 (10 Apr. 1987), pp. 4682–4698. DOI: [10.1103/PhysRevB.35.4682](https://doi.org/10.1103/PhysRevB.35.4682). URL: <https://link.aps.org/doi/10.1103/PhysRevB.35.4682>.
- [162] Hermann Grabert, Peter Olschowski, and Ulrich Weiss. “Quantum decay rates for dissipative systems at finite temperatures”. In: *Phys. Rev. B* 36 (4 Aug. 1987), pp. 1931–1951. DOI: [10.1103/PhysRevB.36.1931](https://doi.org/10.1103/PhysRevB.36.1931). URL: <https://link.aps.org/doi/10.1103/PhysRevB.36.1931>.
- [163] Ulrich Weiss. *Quantum Dissipative Systems*. 3rd. WORLD SCIENTIFIC, 2008. DOI: [10.1142/6738](https://doi.org/10.1142/6738). eprint: <https://www.worldscientific.com/doi/pdf/10.1142/6738>. URL: <https://www.worldscientific.com/doi/abs/10.1142/6738>.
- [164] L. Longobardi et al. “Quantum crossover in moderately damped epitaxial NbN/MgO/NbN junctions with low critical current density”. In: *Applied Physics Letters* 99.6 (2011), p. 062510. DOI: [10.1063/1.3624471](https://doi.org/10.1063/1.3624471). URL: <https://doi.org/10.1063/1.3624471>.
- [165] D. Massarotti et al. “Escape dynamics in moderately damped Josephson junctions (Review Article)”. In: *Low Temperature Physics* 38.4 (2012), pp. 263–272. DOI: [10.1063/1.3699625](https://doi.org/10.1063/1.3699625). eprint: <https://doi.org/10.1063/1.3699625>. URL: <https://doi.org/10.1063/1.3699625>.
- [166] M. Lisitskiy et al. “Bias current ramp rate dependence of the crossover temperature from Kramers to phase diffusion switching in moderately damped NbN/AlN/NbN Josephson junctions”. In: *Journal of Applied Physics* 116.4 (2014), p. 043905. DOI: [10.1063/1.4890317](https://doi.org/10.1063/1.4890317). eprint: <https://doi.org/10.1063/1.4890317>. URL: <https://doi.org/10.1063/1.4890317>.
- [167] L. Longobardi et al. “Effects of Capacitance on Phase Dynamics of YBa₂Cu₃O_{7-x} Josephson Junctions”. In: *IEEE Transactions on Applied Superconductivity* 25.3 (2015), pp. 1–5. DOI: [10.1109/TASC.2014.2375854](https://doi.org/10.1109/TASC.2014.2375854).
- [168] G. Rotoli et al. “Classical resonant activation of a Josephson junction embedded in an LC circuit”. In: *Phys. Rev. B* 75 (14 Apr. 2007), p. 144501. DOI: [10.1103/PhysRevB.75.144501](https://doi.org/10.1103/PhysRevB.75.144501). URL: <https://link.aps.org/doi/10.1103/PhysRevB.75.144501>.
- [169] E. Ben-Jacob et al. “Lifetime of oscillatory steady states”. In: *Phys. Rev. A* 26 (5 Nov. 1982), pp. 2805–2816. DOI: [10.1103/PhysRevA.26.2805](https://doi.org/10.1103/PhysRevA.26.2805). URL: <https://link.aps.org/doi/10.1103/PhysRevA.26.2805>.
- [170] D. Stornaiuolo et al. “Resolving the effects of frequency-dependent damping and quantum phase diffusion in YBCO Josephson junctions”. In: *Phys. Rev. B* 87 (13 Apr. 2013), p. 134517. DOI: [10.1103/PhysRevB.87.134517](https://doi.org/10.1103/PhysRevB.87.134517). URL: <https://link.aps.org/doi/10.1103/PhysRevB.87.134517>.

- [171] M. Weides et al. “ $0-\pi$ Josephson Tunnel Junctions with Ferromagnetic Barrier”. In: *Phys. Rev. Lett.* 97 (24 Dec. 2006), p. 247001. DOI: [10.1103/PhysRevLett.97.247001](https://doi.org/10.1103/PhysRevLett.97.247001). URL: <https://link.aps.org/doi/10.1103/PhysRevLett.97.247001>.
- [172] M. Weides, K. Tillmann, and H. Kohlstedt. “Fabrication of high quality ferromagnetic Josephson junctions”. In: *Physica C: Superconductivity and its Applications* 437-438 (2006). Proceedings of the Fourth International Conference on Vortex Matter in Nanostructured Superconductors VORTEX IV, pp. 349–352. ISSN: 0921-4534. DOI: <https://doi.org/10.1016/j.physc.2005.12.046>. URL: <https://www.sciencedirect.com/science/article/pii/S0921453405008749>.
- [173] J. Pfeiffer et al. “Static and dynamic properties of 0 , π , and $0-\pi$ ferromagnetic Josephson tunnel junctions”. In: *Phys. Rev. B* 77 (21 June 2008), p. 214506. DOI: [10.1103/PhysRevB.77.214506](https://doi.org/10.1103/PhysRevB.77.214506). URL: <https://link.aps.org/doi/10.1103/PhysRevB.77.214506>.
- [174] A. A. Bannykh et al. “Josephson tunnel junctions with a strong ferromagnetic interlayer”. In: *Phys. Rev. B* 79 (5 Feb. 2009), p. 054501. DOI: [10.1103/PhysRevB.79.054501](https://doi.org/10.1103/PhysRevB.79.054501). URL: <https://link.aps.org/doi/10.1103/PhysRevB.79.054501>.
- [175] D Sprungmann et al. “Josephson tunnel junctions with ferromagnetic Fe_{0.75}Co_{0.25}barriers”. In: *Journal of Physics D: Applied Physics* 42.7 (Mar. 2009), p. 075005. DOI: [10.1088/0022-3727/42/7/075005](https://doi.org/10.1088/0022-3727/42/7/075005). URL: <https://doi.org/10.1088/0022-3727/42/7/075005>.
- [176] M Weides et al. “Critical current diffraction pattern of SIFS Josephson junctions with a step-like F-layer”. In: *Superconductor Science and Technology* 23.9 (Aug. 2010), p. 095007. DOI: [10.1088/0953-2048/23/9/095007](https://doi.org/10.1088/0953-2048/23/9/095007). URL: <https://doi.org/10.1088/0953-2048/23/9/095007>.
- [177] Hiroshi Ito et al. “Fabrication of superconductor-ferromagnet-insulator-superconductor Josephson junctions with critical current uniformity applicable to integrated circuits”. In: *Applied Physics Express* 10.3 (Feb. 2017), p. 033101. DOI: [10.7567/apex.10.033101](https://doi.org/10.7567/apex.10.033101). URL: <https://doi.org/10.7567/apex.10.033101>.
- [178] J. Pfeiffer et al. “Escape Rate Measurements and Microwave Spectroscopy of 0 , π , and $0-\pi$ ferromagnetic Josephson Tunnel Junctions”. In: *arXiv: Superconductivity* (2009).
- [179] N. Ruppelt et al. “Observation of $0-\pi$ transition in SIFS Josephson junctions”. In: *Applied Physics Letters* 106.2 (2015), p. 022602. DOI: [10.1063/1.4905672](https://doi.org/10.1063/1.4905672). eprint: <https://doi.org/10.1063/1.4905672>. URL: <https://doi.org/10.1063/1.4905672>.
- [180] D M Heim et al. “The effect of normal and insulating layers on $0-\pi$ transitions in Josephson junctions with a ferromagnetic barrier”. In: *New Journal of Physics* 17.11 (Nov. 2015), p. 113022. DOI: [10.1088/1367-2630/17/11/113022](https://doi.org/10.1088/1367-2630/17/11/113022). URL: <https://doi.org/10.1088/1367-2630/17/11/113022>.

- [181] Shiro Kawabata et al. “Cooper pair transport and macroscopic quantum dynamics in Josephson junctions through ferromagnetic insulators”. In: *Physica C: Superconductivity and its Applications* 468.7 (2008). Proceedings of the Fifth International Conference on Vortex Matter in Nanostructured Superconductors, pp. 701–704. ISSN: 0921-4534. DOI: <https://doi.org/10.1016/j.physc.2007.11.069>. URL: <https://www.sciencedirect.com/science/article/pii/S0921453408000865>.
- [182] S. Kawabata et al. “Josephson π State in a Ferromagnetic Insulator”. In: *Phys. Rev. Lett.* 104 (11 Mar. 2010), p. 117002. DOI: [10.1103/PhysRevLett.104.117002](https://doi.org/10.1103/PhysRevLett.104.117002). URL: <https://link.aps.org/doi/10.1103/PhysRevLett.104.117002>.
- [183] K. Senapati, M. G. Blamire, and Z. H. Barber. “Spin-filter Josephson junctions”. In: *Nature Materials* (2011), p. 849. DOI: [10.1038/nmat3116](https://doi.org/10.1038/nmat3116). URL: <https://doi.org/10.1038/nmat3116>.
- [184] M. G. Blamire et al. *Spin filter superconducting tunnel junctions*. 2012. DOI: [10.1117/12.928403](https://doi.org/10.1117/12.928403). URL: <https://doi.org/10.1117/12.928403>.
- [185] A. Pal et al. “Electric-Field-Dependent Spin Polarization in GdN Spin Filter Tunnel Junctions”. In: *Advanced Materials* 25.39 (2013), pp. 5581–5585. DOI: [10.1002/adma.201300636](https://doi.org/10.1002/adma.201300636). eprint: <https://onlinelibrary.wiley.com/doi/pdf/10.1002/adma.201300636>. URL: <https://onlinelibrary.wiley.com/doi/abs/10.1002/adma.201300636>.
- [186] S. Kawabata et al. “Efficient electron refrigeration using superconductor/spin-filter devices”. In: *Applied Physics Letters* 103.3 (2013), p. 032602. DOI: [10.1063/1.4813599](https://doi.org/10.1063/1.4813599). URL: <https://doi.org/10.1063/1.4813599>.
- [187] Avradeep Pal and M. G. Blamire. “Large interfacial exchange fields in a thick superconducting film coupled to a spin-filter tunnel barrier”. In: *Phys. Rev. B* 92 (18 Nov. 2015), p. 180510. DOI: [10.1103/PhysRevB.92.180510](https://doi.org/10.1103/PhysRevB.92.180510). URL: <https://link.aps.org/doi/10.1103/PhysRevB.92.180510>.
- [188] F. S. Bergeret, A. Verso, and A. F. Volkov. “Spin-polarized Josephson and quasiparticle currents in superconducting spin-filter tunnel junctions”. In: *Phys. Rev. B* 86 (6 Aug. 2012), p. 060506. DOI: [10.1103/PhysRevB.86.060506](https://doi.org/10.1103/PhysRevB.86.060506). URL: <https://link.aps.org/doi/10.1103/PhysRevB.86.060506>.
- [189] Avradeep P. et al. “Pure second harmonic current-phase relation in spin-filter Josephson junctions”. In: *Nature Communications* (2014), p. 3340. URL: <https://doi.org/10.1002/adma.201300636>.
- [190] Y. Zhu et al. “Superconducting exchange coupling between ferromagnets”. In: *Nature Materials* 16 (2016), p. 195. DOI: [10.1038/nmat4753](https://doi.org/10.1038/nmat4753). URL: <https://doi.org/10.1038/nmat4753>.
- [191] URL: <https://pdf.medicalexpo.com/pdf/oxford-instruments/triton/100694-213183.html>.
- [192] URL: https://nanoscience.oxinst.com/assets/uploads/Kelvinox_brochure_3299_July2017.pdf.

- [193] P. Das, R. Bruyn de Ouboter, and K. W. Taconis. “A Realization of a London-Clarke-Mendoza Type Refrigerator”. In: *Low Temperature Physics LT9*. Ed. by J. G. Daunt et al. Boston, MA: Springer US, 1965, pp. 1253–1255. ISBN: 978-1-4899-6443-4.
- [194] James C. Ho, H. R. O’Neal, and Norman E. Phillips. “Low Temperature Heat Capacities of Constantan and Manganin”. In: *Review of Scientific Instruments* 34.7 (1963), pp. 782–783. DOI: [10.1063/1.1718572](https://doi.org/10.1063/1.1718572). eprint: <https://doi.org/10.1063/1.1718572>. URL: <https://doi.org/10.1063/1.1718572>.
- [195] F. P. Milliken et al. “50 Ω characteristic impedance low-pass metal powder filters”. In: *Review of Scientific Instruments* 78.2 (2007), p. 024701. DOI: [10.1063/1.2431770](https://doi.org/10.1063/1.2431770). eprint: <https://doi.org/10.1063/1.2431770>. URL: <https://doi.org/10.1063/1.2431770>.
- [196] A. Fukushima et al. “Attenuation of microwave filters for single-electron tunneling experiments”. In: *IEEE Transactions on Instrumentation and Measurement* 46.2 (1997), pp. 289–293.
- [197] A. Lukashenko and A. V. Ustinov. “Improved powder filters for qubit measurements”. In: *Review of Scientific Instruments* 79.1 (2008), p. 014701. DOI: [10.1063/1.2827515](https://doi.org/10.1063/1.2827515). eprint: <https://doi.org/10.1063/1.2827515>. URL: <https://doi.org/10.1063/1.2827515>.
- [198] John H. Scofield. “Frequency-domain description of a lock-in amplifier”. In: *American Journal of Physics* 62.2 (1994), pp. 129–133. DOI: [10.1119/1.17629](https://doi.org/10.1119/1.17629). eprint: <https://doi.org/10.1119/1.17629>. URL: <https://doi.org/10.1119/1.17629>.
- [199] D. Massarotti et al. “Breakdown of the escape dynamics in Josephson junctions”. In: *Phys. Rev. B* 92 (5 Aug. 2015), p. 054501. DOI: [10.1103/PhysRevB.92.054501](https://doi.org/10.1103/PhysRevB.92.054501). URL: <https://link.aps.org/doi/10.1103/PhysRevB.92.054501>.
- [200] David M Pozar. *Microwave engineering*. John wiley & sons, 2011.
- [201] T. Mimura. “The early history of the high electron mobility transistor (HEMT)”. In: *IEEE Transactions on Microwave Theory and Techniques* 50.3 (2002), pp. 780–782. DOI: [10.1109/22.989961](https://doi.org/10.1109/22.989961).
- [202] *In quantum bit al tempo del CoVid19*. it. 2020. URL: https://napoli.repubblica.it/cronaca/2020/04/07/news/il_quantum_bit_al_tempo_del_covid-19-253407349/.
- [203] *Seeqc’s Naples Team Achieves Quantum Computing Milestone*. 2021. URL: <https://www.businesswire.com/news/home/20210405005484/en/Seeqc%E2%80%99s-Naples-Team-Achieves-Quantum-Computing-Milestone>.
- [204] P. Krantz et al. “A quantum engineer’s guide to superconducting qubits”. In: *Applied Physics Reviews* 6.2 (2019), p. 021318. DOI: [10.1063/1.5089550](https://doi.org/10.1063/1.5089550). eprint: <https://doi.org/10.1063/1.5089550>. URL: <https://doi.org/10.1063/1.5089550>.

- [205] Mahdi Naghiloo. “Introduction to experimental quantum measurement with superconducting qubits”. In: *arXiv preprint arXiv:1904.09291* (2019).
- [206] A. Wallraff et al. “Strong coupling of a single photon to a superconducting qubit using circuit quantum electrodynamics”. In: *Nature* 431 (7005 Sept. 2004), pp. 162–167. DOI: [10.1038/nature02851](https://doi.org/10.1038/nature02851). URL: <https://doi.org/10.1038/nature02851>.
- [207] Doron Meshulach and Yaron Silberberg. “Coherent quantum control of two-photon transitions by a femtosecond laser pulse”. In: *Nature* 396.6708 (Nov. 1998), pp. 239–242. ISSN: 1476-4687. DOI: [10.1038/24329](https://doi.org/10.1038/24329). URL: <https://doi.org/10.1038/24329>.
- [208] Seth Lloyd and Lorenza Viola. “Engineering quantum dynamics”. In: *Phys. Rev. A* 65 (1 Dec. 2001), p. 010101. DOI: [10.1103/PhysRevA.65.010101](https://link.aps.org/doi/10.1103/PhysRevA.65.010101). URL: <https://link.aps.org/doi/10.1103/PhysRevA.65.010101>.
- [209] Sébastien Gleyzes et al. “Quantum jumps of light recording the birth and death of a photon in a cavity”. In: *Nature* 446.7133 (Mar. 2007), pp. 297–300. ISSN: 1476-4687. DOI: [10.1038/nature05589](https://doi.org/10.1038/nature05589). URL: <https://doi.org/10.1038/nature05589>.
- [210] R. J. Thompson, G. Rempe, and H. J. Kimble. “Observation of normal-mode splitting for an atom in an optical cavity”. In: *Phys. Rev. Lett.* 68 (8 Feb. 1992), pp. 1132–1135. DOI: [10.1103/PhysRevLett.68.1132](https://link.aps.org/doi/10.1103/PhysRevLett.68.1132). URL: <https://link.aps.org/doi/10.1103/PhysRevLett.68.1132>.
- [211] Michel Le Bellac. *A Short Introduction to Quantum Information and Quantum Computation*. Cambridge University Press, 2006. DOI: [10.1017/CB09780511755361](https://doi.org/10.1017/CB09780511755361).
- [212] R. Barends et al. “Coherent Josephson Qubit Suitable for Scalable Quantum Integrated Circuits”. In: *Phys. Rev. Lett.* 111 (8 Aug. 2013), p. 080502. DOI: [10.1103/PhysRevLett.111.080502](https://link.aps.org/doi/10.1103/PhysRevLett.111.080502). URL: <https://link.aps.org/doi/10.1103/PhysRevLett.111.080502>.
- [213] H. Y. Carr and E. M. Purcell. “Effects of Diffusion on Free Precession in Nuclear Magnetic Resonance Experiments”. In: *Phys. Rev.* 94 (3 May 1954), pp. 630–638. DOI: [10.1103/PhysRev.94.630](https://link.aps.org/doi/10.1103/PhysRev.94.630). URL: <https://link.aps.org/doi/10.1103/PhysRev.94.630>.
- [214] J. E. Tanner and E. O. Stejskal. “Restricted Self-Diffusion of Protons in Colloidal Systems by the Pulsed-Gradient, Spin-Echo Method”. In: *The Journal of Chemical Physics* 49.4 (1968), pp. 1768–1777. DOI: [10.1063/1.1670306](https://doi.org/10.1063/1.1670306). eprint: <https://doi.org/10.1063/1.1670306>. URL: <https://doi.org/10.1063/1.1670306>.
- [215] Jonas Bylander et al. “Noise spectroscopy through dynamical decoupling with a superconducting flux qubit”. English. In: *Nature Physics* 7.7 (July 2011), pp. 565–570. ISSN: 1745-2473. DOI: [10.1038/nphys1994](https://doi.org/10.1038/nphys1994).

- [216] N. Banerjee et al. "Evidence for spin selectivity of triplet pairs in superconducting spin valves". In: *Nature Communications* 5.1 (Jan. 2014), p. 3048. ISSN: 2041-1723. DOI: [10.1038/ncomms4048](https://doi.org/10.1038/ncomms4048). URL: <https://doi.org/10.1038/ncomms4048>.
- [217] A. Di Bernardo et al. "Signature of magnetic-dependent gapless odd frequency states at superconductor/ferromagnet interfaces". In: *Nature Communications* 6.1 (Sept. 2015), p. 8053. ISSN: 2041-1723. DOI: [10.1038/ncomms9053](https://doi.org/10.1038/ncomms9053). URL: <https://doi.org/10.1038/ncomms9053>.
- [218] Kun-Rok Jeon et al. "Enhanced spin pumping into superconductors provides evidence for superconducting pure spin currents". In: *Nature Materials* 17.6 (June 2018), pp. 499–503. ISSN: 1476-4660. DOI: [10.1038/s41563-018-0058-9](https://doi.org/10.1038/s41563-018-0058-9). URL: <https://doi.org/10.1038/s41563-018-0058-9>.
- [219] R. J. Gambino et al. "Magnetic Properties and Structure of GdN and GdN_{1-x}O_x". In: *Journal of Applied Physics* 41.3 (1970), pp. 933–934. DOI: [10.1063/1.1659030](https://doi.org/10.1063/1.1659030). eprint: <https://doi.org/10.1063/1.1659030>. URL: <https://doi.org/10.1063/1.1659030>.
- [220] F. Leuenberger et al. "X-ray magnetic circular dichroism at the Gd $L_{2,3}$ absorption edges in GdN layers: The influence of lattice expansion". In: *Phys. Rev. B* 73 (21 June 2006), p. 214430. DOI: [10.1103/PhysRevB.73.214430](https://link.aps.org/doi/10.1103/PhysRevB.73.214430). URL: <https://link.aps.org/doi/10.1103/PhysRevB.73.214430>.
- [221] J.-H. Park et al. "Direct evidence for a half-metallic ferromagnet". In: *Nature* 392.6678 (Apr. 1998), pp. 794–796. ISSN: 1476-4687. DOI: [10.1038/33883](https://doi.org/10.1038/33883). URL: <https://doi.org/10.1038/33883>.
- [222] F. Leuenberger et al. "GdN thin films: Bulk and local electronic and magnetic properties". In: *Phys. Rev. B* 72 (1 July 2005), p. 014427. DOI: [10.1103/PhysRevB.72.014427](https://link.aps.org/doi/10.1103/PhysRevB.72.014427). URL: <https://link.aps.org/doi/10.1103/PhysRevB.72.014427>.
- [223] Halima Giovanna Ahmad et al. "Critical Current Suppression in Spin-Filter Josephson Junctions". In: *Journal of Superconductivity and Novel Magnetism* 33.10 (Oct. 2020), pp. 3043–3049. ISSN: 1557-1947. DOI: [10.1007/s10948-020-05577-0](https://doi.org/10.1007/s10948-020-05577-0). URL: <https://doi.org/10.1007/s10948-020-05577-0>.
- [224] Davide Massarotti and Francesco Tafuri. "Current-Voltage Characteristics". In: *Fundamentals and Frontiers of the Josephson Effect*. Ed. by Francesco Tafuri. Cham: Springer International Publishing, 2019, pp. 253–274. ISBN: 978-3-030-20726-7. DOI: [10.1007/978-3-030-20726-7_11](https://doi.org/10.1007/978-3-030-20726-7_11). URL: https://doi.org/10.1007/978-3-030-20726-7_11.
- [225] J. G. Simmons. "Electric Tunnel Effect between Dissimilar Electrodes Separated by a Thin Insulating Film". In: *Journal of Applied Physics* 34.9 (1963), pp. 2581–2590. DOI: [10.1063/1.1729774](https://doi.org/10.1063/1.1729774). URL: <https://doi.org/10.1063/1.1729774>.

- [226] Roberta Caruso et al. “Low temperature characterization of high efficiency spin-filter Josephson junctions”. In: *EPJ Web Conf.* 233 (2020), p. 05007. DOI: [10.1051/epjconf/202023305007](https://doi.org/10.1051/epjconf/202023305007). URL: <https://doi.org/10.1051/epjconf/202023305007>.
- [227] T. Tokuyasu, J. A. Sauls, and D. Rainer. “Proximity effect of a ferromagnetic insulator in contact with a superconductor”. In: *Phys. Rev. B* 38 (13 Nov. 1988), pp. 8823–8833. DOI: [10.1103/PhysRevB.38.8823](https://link.aps.org/doi/10.1103/PhysRevB.38.8823). URL: <https://link.aps.org/doi/10.1103/PhysRevB.38.8823>.
- [228] M. Minutillo et al. “Anomalous Josephson effect in S/SO/F/S heterostructures”. In: *Phys. Rev. B* 98 (14 Oct. 2018), p. 144510. DOI: [10.1103/PhysRevB.98.144510](https://link.aps.org/doi/10.1103/PhysRevB.98.144510). URL: <https://link.aps.org/doi/10.1103/PhysRevB.98.144510>.
- [229] D. Belitz and T. R. Kirkpatrick. “Even-parity spin-triplet superconductivity in disordered electronic systems”. In: *Phys. Rev. B* 46 (13 Oct. 1992), pp. 8393–8408. DOI: [10.1103/PhysRevB.46.8393](https://link.aps.org/doi/10.1103/PhysRevB.46.8393). URL: <https://link.aps.org/doi/10.1103/PhysRevB.46.8393>.
- [230] A. F. Volkov, F. S. Bergeret, and K. B. Efetov. “Odd Triplet Superconductivity in Superconductor-Ferromagnet Multilayered Structures”. In: *Phys. Rev. Lett.* 90 (11 Mar. 2003), p. 117006. DOI: [10.1103/PhysRevLett.90.117006](https://link.aps.org/doi/10.1103/PhysRevLett.90.117006). URL: <https://link.aps.org/doi/10.1103/PhysRevLett.90.117006>.
- [231] Y. Tanaka and A. A. Golubov. “Theory of the Proximity Effect in Junctions with Unconventional Superconductors”. In: *Phys. Rev. Lett.* 98 (3 Jan. 2007), p. 037003. DOI: [10.1103/PhysRevLett.98.037003](https://link.aps.org/doi/10.1103/PhysRevLett.98.037003). URL: <https://link.aps.org/doi/10.1103/PhysRevLett.98.037003>.
- [232] Mehran Kardar. “Domain walls subject to quenched impurities (invited)”. In: *Journal of Applied Physics* 61.8 (1987), pp. 3601–3604. DOI: [10.1063/1.338687](https://doi.org/10.1063/1.338687). eprint: <https://doi.org/10.1063/1.338687>. URL: <https://doi.org/10.1063/1.338687>.
- [233] Bernard Dennis Cullity and Chad D Graham. *Introduction to magnetic materials*. John Wiley & Sons, 2011.
- [234] E. Goldobin et al. “Memory cell based on a φ Josephson junction”. In: *Applied Physics Letters* 102.24 (2013), p. 242602. DOI: [10.1063/1.4811752](https://doi.org/10.1063/1.4811752). eprint: <https://doi.org/10.1063/1.4811752>. URL: <https://doi.org/10.1063/1.4811752>.
- [235] Bethany M. Niedzielski et al. “Spin-valve Josephson junctions for cryogenic memory”. In: *Phys. Rev. B* 97 (2 Jan. 2018), p. 024517. DOI: [10.1103/PhysRevB.97.024517](https://link.aps.org/doi/10.1103/PhysRevB.97.024517). URL: <https://link.aps.org/doi/10.1103/PhysRevB.97.024517>.
- [236] L. B. Ioffe et al. “Environmentally decoupled sds-wave Josephson junctions for quantum computing”. In: *Nature* 398 (6729 1999), pp. 679–681. ISSN: 1476-4687. URL: <https://doi.org/10.1038/19464>.

- [237] E. Terzioglu and M. R. Beasley. “Complementary Josephson junction devices and circuits: a possible new approach to superconducting electronics”. In: *IEEE Transactions on Applied Superconductivity* 8.2 (June 1998), pp. 48–53. ISSN: 1051-8223. DOI: [10.1109/77.678441](https://doi.org/10.1109/77.678441).
- [238] J. Majer et al. “Coupling superconducting qubits via a cavity bus”. In: *Nature* 449 (7161 Sept. 2007), pp. 443–447. DOI: [10.1038/nature06184](https://doi.org/10.1038/nature06184). URL: <https://doi.org/10.1038/nature06184>.
- [239] Y. C. Chen, M. P. A. Fisher, and A. J. Leggett. “The return of a hysteretic Josephson junction to the zero-voltage state: IV characteristic and quantum retrapping”. In: *Journal of Applied Physics* 64.6 (1988), pp. 3119–3142. DOI: [10.1063/1.341527](https://doi.org/10.1063/1.341527). URL: <https://doi.org/10.1063/1.341527>.
- [240] J. M. Kivioja et al. “Observation of Transition from Escape Dynamics to Underdamped Phase Diffusion in a Josephson Junction”. In: *Phys. Rev. Lett.* 94 (24 June 2005), p. 247002. DOI: [10.1103/PhysRevLett.94.247002](https://doi.org/10.1103/PhysRevLett.94.247002). URL: <https://link.aps.org/doi/10.1103/PhysRevLett.94.247002>.
- [241] J. Männik et al. “Crossover from Kramers to phase-diffusion switching in moderately damped Josephson junctions”. In: *Phys. Rev. B* 71 (22 June 2005), p. 220509. DOI: [10.1103/PhysRevB.71.220509](https://doi.org/10.1103/PhysRevB.71.220509). URL: <https://link.aps.org/doi/10.1103/PhysRevB.71.220509>.
- [242] Myung-Ho Bae et al. “Multiple-retrapping processes in the phase-diffusion regime of high- T_c intrinsic Josephson junctions”. In: *Phys. Rev. B* 79 (10 Mar. 2009), p. 104509. DOI: [10.1103/PhysRevB.79.104509](https://doi.org/10.1103/PhysRevB.79.104509). URL: <https://link.aps.org/doi/10.1103/PhysRevB.79.104509>.
- [243] H. F. Yu et al. “Quantum Phase Diffusion in a Small Underdamped Josephson Junction”. In: *Phys. Rev. Lett.* 107 (6 Aug. 2011), p. 067004. DOI: [10.1103/PhysRevLett.107.067004](https://doi.org/10.1103/PhysRevLett.107.067004). URL: <https://link.aps.org/doi/10.1103/PhysRevLett.107.067004>.
- [244] Luigi Longobardi et al. “Thermal hopping and retrapping of a Brownian particle in the tilted periodic potential of a NbN/MgO/NbN Josephson junction”. In: *Phys. Rev. B* 84 (18 Nov. 2011), p. 184504. DOI: [10.1103/PhysRevB.84.184504](https://doi.org/10.1103/PhysRevB.84.184504). URL: <https://link.aps.org/doi/10.1103/PhysRevB.84.184504>.
- [245] Luigi Longobardi et al. “Direct Transition from Quantum Escape to a Phase Diffusion Regime in YBaCuO Biepitaxial Josephson Junctions”. In: *Phys. Rev. Lett.* 109 (5 Aug. 2012), p. 050601. DOI: [10.1103/PhysRevLett.109.050601](https://doi.org/10.1103/PhysRevLett.109.050601). URL: <https://link.aps.org/doi/10.1103/PhysRevLett.109.050601>.
- [246] M. Iansiti et al. “Charging effects and quantum properties of small superconducting tunnel junctions”. In: *Phys. Rev. B* 39 (10 Apr. 1989), pp. 6465–6484. DOI: [10.1103/PhysRevB.39.6465](https://doi.org/10.1103/PhysRevB.39.6465). URL: <https://link.aps.org/doi/10.1103/PhysRevB.39.6465>.

- [247] C. Bonnelle and N. Spectorv. *Rare-Earths and Actinides in High Energy Spectroscopy*. Springer International Publishing AG. Part of Springer Nature, 2015, p. 109.
- [248] A. Kawakami, Y. Uzawa, and Z. Wang. “Development of epitaxial NbN/MgO/NbN–superconductor-insulator-superconductor mixers for operations over the Nb gap frequency”. In: *Applied Physics Letters* 83.19 (2003), pp. 3954–3956. DOI: [10.1063/1.1625431](https://doi.org/10.1063/1.1625431). eprint: <https://doi.org/10.1063/1.1625431>. URL: <https://doi.org/10.1063/1.1625431>.
- [249] Di Palma Luigi. “Phase dynamics in spin-filter Josephson junctions”. In: *Master Thesis* (2019). URL: http://www.fisica.unina.it/documents/12375590/13725484/2899_DiPalmaL_16-10-2019.pdf/125e8b15-19f3-4e20-bb44-12367a38ded1.
- [250] Massarotti D. *Macroscopic quantum phenomena in superconductors: study of phase dynamics and dissipation in moderately damped Josephson junctions*. 2013. URL: <http://www.fedoa.unina.it/id/eprint/9207>.
- [251] Castellano M.G. et al. “Characterization of a fabrication process for the integration of superconducting qubits and rapid-single-flux-quantum circuits”. In: *Superconductor Science and Technology* 19.8 (July 2006), pp. 860–864. DOI: [10.1088/0953-2048/19/8/030](https://doi.org/10.1088/0953-2048/19/8/030). URL: <https://doi.org/10.1088/0953-2048/19/8/030>.
- [252] A. V. Shcherbakova et al. “Fabrication and measurements of hybrid Nb/Al Josephson junctions and flux qubits with π -shifters”. In: *Superconductor Science and Technology* 28.2 (Jan. 2015), p. 025009. DOI: [10.1088/0953-2048/28/2/025009](https://doi.org/10.1088/0953-2048/28/2/025009). URL: <https://doi.org/10.1088/0953-2048/28/2/025009>.
- [253] I. A. Golovchanskiy et al. “Magnetization dynamics in dilute Pd_{1-x}Fe_x thin films and patterned microstructures considered for superconducting electronics”. In: *Journal of Applied Physics* 120.16 (2016), p. 163902. DOI: [10.1063/1.4965991](https://doi.org/10.1063/1.4965991). eprint: <https://doi.org/10.1063/1.4965991>. URL: <https://doi.org/10.1063/1.4965991>.
- [254] I.A. Golovchanskiy et al. “Interplay of Magnetization Dynamics with a Microwave Waveguide at Cryogenic Temperatures”. In: *Phys. Rev. Applied* 11 (4 Apr. 2019), p. 044076. DOI: [10.1103/PhysRevApplied.11.044076](https://doi.org/10.1103/PhysRevApplied.11.044076). URL: <https://link.aps.org/doi/10.1103/PhysRevApplied.11.044076>.
- [255] V. V. Bol’ginov, O. A. Tikhomirov, and L. S. Uspenskaya. “Two-component magnetization in Pd₉₉Fe₀₁ thin films”. In: *JETP Letters* 105.3 (Feb. 2017), pp. 169–173. ISSN: 1090-6487. DOI: [10.1134/S0021364017030055](https://doi.org/10.1134/S0021364017030055). URL: <https://doi.org/10.1134/S0021364017030055>.
- [256] C. Bell et al. “Spin dynamics in a superconductor-ferromagnet proximity system”. In: *Physical review letters* 100.4 (2008), p. 047002.

- [257] Samme M. Dahir, Anatoly F. Volkov, and Ilya M. Eremin. “Phase-dependent spin polarization of Cooper pairs in magnetic Josephson junctions”. In: *Phys. Rev. B* 100 (13 Oct. 2019), p. 134513. DOI: [10.1103/PhysRevB.100.134513](https://doi.org/10.1103/PhysRevB.100.134513). URL: <https://link.aps.org/doi/10.1103/PhysRevB.100.134513>.
- [258] Roberta Satariano et al. “Inverse magnetic hysteresis of the Josephson supercurrent: study of the magnetic properties of thin Nb/Py interface”. In: *Submitted to Phys. Rev. B* ().
- [259] Satariano Roberta et al. “In preparation”. In: (2021).
- [260] Di Palma Luigi et al. “In preparation”. In: (2021).
- [261] Denis Vion. “Course 14 - Josephson Quantum Bits Based on a Cooper Pair Box”. In: *Quantum Entanglement and Information Processing*. Ed. by Daniel Estève, Jean-Michel Raimond, and Jean Dalibard. Vol. 79. Les Houches. Elsevier, 2004, pp. 521–559. DOI: [https://doi.org/10.1016/S0924-8099\(03\)80038-0](https://doi.org/10.1016/S0924-8099(03)80038-0). URL: <http://www.sciencedirect.com/science/article/pii/S0924809903800380>.
- [262] Webpage Intel. <https://newsroom.intel.com/news-releases/intel-invests-us50-million-to-advance-quantum-computing/>.
- [263] Webpage IBM. <https://www-03.ibm.com/press/us/en/pressrelease/49661.wss>.
- [264] Davide Castelecchi. “Quantum computers ready to leap out of the lab in 2017”. In: *Nature* 541 (Jan. 2017), pp. 9–10. DOI: [10.1038/541009a](https://doi.org/10.1038/541009a). URL: <https://www.nature.com/news/quantum-computers-ready-to-leap-out-of-the-lab-in-2017-1.21239>.
- [265] Webpage Rigetti. <https://www.hpcwire.com/2018/09/07/rigetti-launches-quantum-cloud-services-announces-1million-challenge/>.
- [266] Paul Benioff. “The computer as a physical system: A microscopic quantum mechanical Hamiltonian model of computers as represented by Turing machines”. In: *Journal of Statistical Physics* (May 1980), pp. 563–591. DOI: [10.1007/BF01011339](https://doi.org/10.1007/BF01011339). URL: <https://doi.org/10.1007/BF01011339>.
- [267] D. Vion et al. “Manipulating the Quantum State of an Electrical Circuit”. In: *Science* 296.5569 (2002), pp. 886–889. ISSN: 0036-8075. DOI: [10.1126/science.1069372](https://doi.org/10.1126/science.1069372). eprint: <https://science.sciencemag.org/content/296/5569/886.full.pdf>. URL: <https://science.sciencemag.org/content/296/5569/886>.
- [268] F. G. Paauw et al. “Tuning the Gap of a Superconducting Flux Qubit”. In: *Phys. Rev. Lett.* 102 (9 Mar. 2009), p. 090501. DOI: [10.1103/PhysRevLett.102.090501](https://doi.org/10.1103/PhysRevLett.102.090501). URL: <https://link.aps.org/doi/10.1103/PhysRevLett.102.090501>.

- [269] Vladimir E. Manucharyan et al. “Fluxonium: Single Cooper-Pair Circuit Free of Charge Offsets”. In: *Science* 326.5949 (2009), pp. 113–116. ISSN: 0036-8075. DOI: [10.1126/science.1175552](https://doi.org/10.1126/science.1175552). eprint: <https://science.sciencemag.org/content/326/5949/113.full.pdf>. URL: <https://science.sciencemag.org/content/326/5949/113>.
- [270] Yu Chen et al. “Qubit Architecture with High Coherence and Fast Tunable Coupling”. In: *Phys. Rev. Lett.* 113 (22 Nov. 2014), p. 220502. DOI: [10.1103/PhysRevLett.113.220502](https://doi.org/10.1103/PhysRevLett.113.220502). URL: <https://link.aps.org/doi/10.1103/PhysRevLett.113.220502>.
- [271] Ioan M. Pop et al. “Coherent suppression of electromagnetic dissipation due to superconducting quasiparticles”. In: *Nature* 508 (7496 Apr. 2014), pp. 369–372. DOI: [10.1038/nature13017](https://doi.org/10.1038/nature13017). URL: <https://doi.org/10.1038/nature13017>.
- [272] Y. Nakamura, Yu. A. Pashkin, and J. S. Tsai. “Coherent control of macroscopic quantum states in a single-Cooper-pair box”. In: *Nature* 398 (6730 Apr. 1999), pp. 786–788. DOI: [10.1038/19718](https://doi.org/10.1038/19718). URL: <https://doi.org/10.1038/19718>.
- [273] K. W. Lehnert et al. “Measurement of the Excited-State Lifetime of a Microelectronic Circuit”. In: *Phys. Rev. Lett.* 90 (2 Jan. 2003), p. 027002. DOI: [10.1103/PhysRevLett.90.027002](https://doi.org/10.1103/PhysRevLett.90.027002). URL: <https://link.aps.org/doi/10.1103/PhysRevLett.90.027002>.
- [274] J. A. Schreier et al. “Suppressing charge noise decoherence in superconducting charge qubits”. In: *Phys. Rev. B* 77 (18 May 2008), p. 180502. DOI: [10.1103/PhysRevB.77.180502](https://doi.org/10.1103/PhysRevB.77.180502). URL: <https://link.aps.org/doi/10.1103/PhysRevB.77.180502>.
- [275] Chad Rigetti et al. “Superconducting qubit in a waveguide cavity with a coherence time approaching 0.1 ms”. In: *Phys. Rev. B* 86 (10 Sept. 2012), p. 100506. DOI: [10.1103/PhysRevB.86.100506](https://doi.org/10.1103/PhysRevB.86.100506). URL: <https://link.aps.org/doi/10.1103/PhysRevB.86.100506>.
- [276] O. A. Mukhanov. “Energy-Efficient Single Flux Quantum Technology”. In: *IEEE Transactions on Applied Superconductivity* 21.3 (2011), pp. 760–769. DOI: [10.1109/TASC.2010.2096792](https://doi.org/10.1109/TASC.2010.2096792).
- [277] G Wendin. “Quantum information processing with superconducting circuits: a review”. In: *Reports on Progress in Physics* 80.10 (Sept. 2017), p. 106001. DOI: [10.1088/1361-6633/aa7e1a](https://doi.org/10.1088/1361-6633/aa7e1a). URL: <https://doi.org/10.1088/1361-6633/aa7e1a>.
- [278] Youngkyu Sung et al. “Multi-level quantum noise spectroscopy”. In: *Nature Communications* 12.1 (Feb. 2021), p. 967. ISSN: 2041-1723. DOI: [10.1038/s41467-021-21098-3](https://doi.org/10.1038/s41467-021-21098-3). URL: <https://doi.org/10.1038/s41467-021-21098-3>.
- [279] E. Paladino et al. “ $1/f$ noise: Implications for solid-state quantum information”. In: *Rev. Mod. Phys.* 86 (2 Apr. 2014), pp. 361–418. DOI: [10.1103/RevModPhys.86.361](https://doi.org/10.1103/RevModPhys.86.361). URL: <https://link.aps.org/doi/10.1103/RevModPhys.86.361>.

- [280] C. L. Degen, F. Reinhard, and P. Cappellaro. “Quantum sensing”. In: *Rev. Mod. Phys.* 89 (3 July 2017), p. 035002. DOI: [10.1103/RevModPhys.89.035002](https://doi.org/10.1103/RevModPhys.89.035002). URL: <https://link.aps.org/doi/10.1103/RevModPhys.89.035002>.
- [281] John Preskill. “Quantum Computing in the NISQ era and beyond”. In: *Quantum* 2 (Aug. 2018), p. 79. ISSN: 2521-327X. DOI: [10.22331/q-2018-08-06-79](https://doi.org/10.22331/q-2018-08-06-79). URL: <https://doi.org/10.22331/q-2018-08-06-79>.
- [282] Carlos A. Meriles et al. “Imaging mesoscopic nuclear spin noise with a diamond magnetometer”. In: *The Journal of Chemical Physics* 133.12 (2010), p. 124105. DOI: [10.1063/1.3483676](https://doi.org/10.1063/1.3483676). eprint: <https://doi.org/10.1063/1.3483676>. URL: <https://doi.org/10.1063/1.3483676>.
- [283] Y. Romach et al. “Spectroscopy of Surface-Induced Noise Using Shallow Spins in Diamond”. In: *Phys. Rev. Lett.* 114 (1 Jan. 2015), p. 017601. DOI: [10.1103/PhysRevLett.114.017601](https://doi.org/10.1103/PhysRevLett.114.017601). URL: <https://link.aps.org/doi/10.1103/PhysRevLett.114.017601>.
- [284] Gonzalo A. Álvarez and Dieter Suter. “Measuring the Spectrum of Colored Noise by Dynamical Decoupling”. In: *Phys. Rev. Lett.* 107 (23 Nov. 2011), p. 230501. DOI: [10.1103/PhysRevLett.107.230501](https://doi.org/10.1103/PhysRevLett.107.230501). URL: <https://link.aps.org/doi/10.1103/PhysRevLett.107.230501>.
- [285] L. M. K. Vandersypen and I. L. Chuang. “NMR techniques for quantum control and computation”. In: *Rev. Mod. Phys.* 76 (4 Jan. 2005), pp. 1037–1069. DOI: [10.1103/RevModPhys.76.1037](https://doi.org/10.1103/RevModPhys.76.1037). URL: <https://link.aps.org/doi/10.1103/RevModPhys.76.1037>.
- [286] J. D. Carter and J. D. D. Martin. “Coherent manipulation of cold Rydberg atoms near the surface of an atom chip”. In: *Phys. Rev. A* 88 (4 Oct. 2013), p. 043429. DOI: [10.1103/PhysRevA.88.043429](https://doi.org/10.1103/PhysRevA.88.043429). URL: <https://link.aps.org/doi/10.1103/PhysRevA.88.043429>.
- [287] G. Ithier et al. “Decoherence in a superconducting quantum bit circuit”. In: *Phys. Rev. B* 72 (13 Oct. 2005), p. 134519. DOI: [10.1103/PhysRevB.72.134519](https://doi.org/10.1103/PhysRevB.72.134519). URL: <https://link.aps.org/doi/10.1103/PhysRevB.72.134519>.
- [288] Tatsuro Yuge, Susumu Sasaki, and Yoshiro Hirayama. “Measurement of the Noise Spectrum Using a Multiple-Pulse Sequence”. In: *Phys. Rev. Lett.* 107 (17 Oct. 2011), p. 170504. DOI: [10.1103/PhysRevLett.107.170504](https://doi.org/10.1103/PhysRevLett.107.170504). URL: <https://link.aps.org/doi/10.1103/PhysRevLett.107.170504>.
- [289] Kevin C. Young and K. Birgitta Whaley. “Qubits as spectrometers of dephasing noise”. In: *Phys. Rev. A* 86 (1 July 2012), p. 012314. DOI: [10.1103/PhysRevA.86.012314](https://doi.org/10.1103/PhysRevA.86.012314). URL: <https://link.aps.org/doi/10.1103/PhysRevA.86.012314>.

- [290] Gerardo A. Paz-Silva and Lorenza Viola. “General Transfer-Function Approach to Noise Filtering in Open-Loop Quantum Control”. In: *Phys. Rev. Lett.* 113 (25 Dec. 2014), p. 250501. DOI: [10.1103/PhysRevLett.113.250501](https://doi.org/10.1103/PhysRevLett.113.250501). URL: <https://link.aps.org/doi/10.1103/PhysRevLett.113.250501>.
- [291] Burm Baek et al. “Hybrid superconducting-magnetic memory device using competing order parameters”. In: *Nature Communications* 5.1 (May 2014), p. 3888. ISSN: 2041-1723. DOI: [10.1038/ncomms4888](https://doi.org/10.1038/ncomms4888). URL: <https://doi.org/10.1038/ncomms4888>.
- [292] Bethany M Niedzielski et al. “S/F/S Josephson junctions with single-domain ferromagnets for memory applications”. In: *Superconductor Science and Technology* 28.8 (July 2015), p. 085012. DOI: [10.1088/0953-2048/28/8/085012](https://doi.org/10.1088/0953-2048/28/8/085012). URL: <https://doi.org/10.1088/0953-2048/28/8/085012>.
- [293] E. C. Gingrich et al. “Controllable $0-\pi$ Josephson junctions containing a ferromagnetic spin valve”. In: *Nature Physics* 12.6 (June 2016), pp. 564–567. ISSN: 1745-2481. DOI: [10.1038/nphys3681](https://doi.org/10.1038/nphys3681). URL: <https://doi.org/10.1038/nphys3681>.
- [294] Jay M. Gambetta, Jerry M. Chow, and Matthias Steffen. “Building logical qubits in a superconducting quantum computing system”. In: *npj Quantum Information* 3.1 (Jan. 2017), p. 2. ISSN: 2056-6387. DOI: [10.1038/s41534-016-0004-0](https://doi.org/10.1038/s41534-016-0004-0). URL: <https://doi.org/10.1038/s41534-016-0004-0>.
- [295] JE Campbell, EA Eldridge, and JK Thompson. *Handbook on Materials for Superconducting Machinery*. Tech. rep. BATTELLE COLUMBUS LABS OHIO METALS and CERAMICS INFORMATION CENTER, 1974.
- [296] JG Weisend II. “„Introduction To Cryostat Design””. In: *Short Courses ICEC* (2010).
- [297] JG Weisend. “Principles of Cryostat Design”. In: *Cryostat Design*. Springer, 2016, pp. 1–45.
- [298] Thomas J Peterson and JG Weisend II. “Properties of Fluids and Materials at Cryogenic Temperatures”. In: *Cryogenic Safety*. Springer, 2019, pp. 1–13.
- [299] D.R. Gulevich. “MiTMojCo: Microscopic Tunneling Model for Josephson Contacts”. In: *Computer Physics Communications* 251 (2020), p. 107091. ISSN: 0010-4655. DOI: <https://doi.org/10.1016/j.cpc.2019.107091>. URL: <http://www.sciencedirect.com/science/article/pii/S0010465519304011>.
- [300] Richard E. Harris. “Intrinsic response time of a Josephson tunnel junction”. In: *Phys. Rev. B* 13 (9 May 1976), pp. 3818–3821. DOI: [10.1103/PhysRevB.13.3818](https://doi.org/10.1103/PhysRevB.13.3818). URL: <https://link.aps.org/doi/10.1103/PhysRevB.13.3818>.

- [301] Bernard Yurke and John S. Denker. “Quantum network theory”. In: *Phys. Rev. A* 29 (3 Mar. 1984), pp. 1419–1437. DOI: [10.1103/PhysRevA.29.1419](https://doi.org/10.1103/PhysRevA.29.1419). URL: <https://link.aps.org/doi/10.1103/PhysRevA.29.1419>.
- [302] Claude Cohen-Tannoudji, Bernard Diu, and Franck Laloë. *Quantum mechanics*. Trans. of : Mécanique quantique. Paris : Hermann, 1973. New York, NY: Wiley, 1977. URL: <https://cds.cern.ch/record/101367>.
- [303] C.C. Gerry and P.L. Knight. *Introductory Quantum Optics*. Cambridge University Press, 2005.
- [304] John M. Martinis. “Course 13 - Superconducting Qubits and the Physics of Josephson Junctions”. In: *Quantum Entanglement and Information Processing*. Ed. by Daniel Estève, Jean-Michel Raimond, and Jean Dalibard. Vol. 79. Les Houches. Elsevier, 2004, pp. 487–520. DOI: [https://doi.org/10.1016/S0924-8099\(03\)80037-9](https://doi.org/10.1016/S0924-8099(03)80037-9). URL: <http://www.sciencedirect.com/science/article/pii/S0924809903800379>.
- [305] Michel H Devoret and John M Martinis. “Course 12 - Superconducting Qubits”. In: *Quantum Entanglement and Information Processing*. Ed. by Daniel Estève, Jean-Michel Raimond, and Jean Dalibard. Vol. 79. Les Houches. Elsevier, 2004, pp. 443–485. DOI: [https://doi.org/10.1016/S0924-8099\(03\)80036-7](https://doi.org/10.1016/S0924-8099(03)80036-7). URL: <http://www.sciencedirect.com/science/article/pii/S0924809903800367>.
- [306] L. DiCarlo et al. “Demonstration of two-qubit algorithms with a superconducting quantum processor”. In: *Nature* 460.7252 (July 2009), pp. 240–244. ISSN: 1476-4687. DOI: [10.1038/nature08121](https://doi.org/10.1038/nature08121). URL: <https://doi.org/10.1038/nature08121>.
- [307] J. Kelly et al. “State preservation by repetitive error detection in a superconducting quantum circuit”. In: *Nature* 519.7541 (Mar. 2015), pp. 66–69. ISSN: 1476-4687. DOI: [10.1038/nature14270](https://doi.org/10.1038/nature14270). URL: <https://doi.org/10.1038/nature14270>.
- [308] Matthew Reagor et al. “Demonstration of universal parametric entangling gates on a multi-qubit lattice”. In: *Science Advances* 4.2 (2018). DOI: [10.1126/sciadv.aao3603](https://doi.org/10.1126/sciadv.aao3603). eprint: <https://advances.sciencemag.org/content/4/2/eaao3603.full.pdf>. URL: <https://advances.sciencemag.org/content/4/2/eaao3603>.
- [309] M. D. Hutchings et al. “Tunable Superconducting Qubits with Flux-Independent Coherence”. In: *Phys. Rev. Applied* 8 (4 Oct. 2017), p. 044003. DOI: [10.1103/PhysRevApplied.8.044003](https://doi.org/10.1103/PhysRevApplied.8.044003). URL: <https://link.aps.org/doi/10.1103/PhysRevApplied.8.044003>.
- [310] Alexander Shnirman et al. “Noise and Decoherence in Quantum Two-Level Systems”. In: *Physica Scripta* T102.1 (2002), p. 147. DOI: [10.1238/physica.topical.102a00147](https://doi.org/10.1238/physica.topical.102a00147). URL: <https://doi.org/10.1238/physica.topical.102a00147>.

- [311] F. K. Wilhelm et al. “Superconducting Qubits II: Decoherence”. In: *Manipulating Quantum Coherence in Solid State Systems*. Ed. by Michael E. Flatté and I. Tifrea. Dordrecht: Springer Netherlands, 2007, pp. 195–232. ISBN: 978-1-4020-6137-0.
- [312] Luca Chirolli and Guido Burkard. “Decoherence in solid-state qubits”. In: *Advances in Physics* 57.3 (2008), pp. 225–285. DOI: [10.1080/00018730802218067](https://doi.org/10.1080/00018730802218067). eprint: <https://doi.org/10.1080/00018730802218067>. URL: <https://doi.org/10.1080/00018730802218067>.
- [313] Anatoly Yu Smirnov and Mohammad H Amin. “Theory of open quantum dynamics with hybrid noise”. In: *New Journal of Physics* 20.10 (Oct. 2018), p. 103037. DOI: [10.1088/1367-2630/aae79c](https://doi.org/10.1088/1367-2630/aae79c). URL: <https://doi.org/10.1088/1367-2630/aae79c>.
- [314] D. I. Schuster et al. “Resolving photon number states in a superconducting circuit”. In: *Nature* 445.7127 (Feb. 2007), pp. 515–518. ISSN: 1476-4687. DOI: [10.1038/nature05461](https://doi.org/10.1038/nature05461). URL: <https://doi.org/10.1038/nature05461>.
- [315] A. A. Houck et al. “Generating single microwave photons in a circuit”. In: *Nature* 449.7160 (Sept. 2007), pp. 328–331. ISSN: 1476-4687. DOI: [10.1038/nature06126](https://doi.org/10.1038/nature06126). URL: <https://doi.org/10.1038/nature06126>.
- [316] A. B. Zorin et al. “Background charge noise in metallic single-electron tunneling devices”. In: *Phys. Rev. B* 53 (20 May 1996), pp. 13682–13687. DOI: [10.1103/PhysRevB.53.13682](https://doi.org/10.1103/PhysRevB.53.13682). URL: <https://link.aps.org/doi/10.1103/PhysRevB.53.13682>.
- [317] Frederick C. Wellstood, Cristian Urbina, and John Clarke. “Low-frequency noise in dc superconducting quantum interference devices below 1 K”. In: *Applied Physics Letters* 50.12 (1987), pp. 772–774. DOI: [10.1063/1.98041](https://doi.org/10.1063/1.98041). eprint: <https://doi.org/10.1063/1.98041>. URL: <https://doi.org/10.1063/1.98041>.
- [318] D. J. Van Harlingen et al. “Decoherence in Josephson-junction qubits due to critical-current fluctuations”. In: *Phys. Rev. B* 70 (6 Aug. 2004), p. 064517. DOI: [10.1103/PhysRevB.70.064517](https://doi.org/10.1103/PhysRevB.70.064517). URL: <https://link.aps.org/doi/10.1103/PhysRevB.70.064517>.
- [319] J. D. Jackson. “Classical Electrodynamics, 3rd ed.” In: *American Journal of Physics* 67.9 (1999), pp. 841–842. DOI: [10.1119/1.19136](https://doi.org/10.1119/1.19136). eprint: <https://doi.org/10.1119/1.19136>. URL: <https://doi.org/10.1119/1.19136>.
- [320] E. M. Purcell, H. C. Torrey, and R. V. Pound. “Resonance Absorption by Nuclear Magnetic Moments in a Solid”. In: *Phys. Rev.* 69 (1-2 Jan. 1946), pp. 37–38. DOI: [10.1103/PhysRev.69.37](https://doi.org/10.1103/PhysRev.69.37). URL: <https://link.aps.org/doi/10.1103/PhysRev.69.37>.
- [321] Roman Lutchyn, Leonid Glazman, and Anatoly Larkin. “Quasiparticle decay rate of Josephson charge qubit oscillations”. In: *Phys. Rev. B* 72 (1 July 2005), p. 014517. DOI: [10.1103/PhysRevB.72.014517](https://doi.org/10.1103/PhysRevB.72.014517). URL: <https://link.aps.org/doi/10.1103/PhysRevB.72.014517>.

- [322] R. M. Lutchyn, L. I. Glazman, and A. I. Larkin. “Kinetics of the superconducting charge qubit in the presence of a quasiparticle”. In: *Phys. Rev. B* 74 (6 Aug. 2006), p. 064515. DOI: [10.1103/PhysRevB.74.064515](https://doi.org/10.1103/PhysRevB.74.064515). URL: <https://link.aps.org/doi/10.1103/PhysRevB.74.064515>.
- [323] Robert J Schoelkopf et al. “Noise and measurement backaction in superconducting circuits: qubits as spectrometers of quantum noise”. In: *Noise and Information in Nanoelectronics, Sensors, and Standards*. Vol. 5115. International Society for Optics and Photonics. 2003, pp. 356–376.
- [324] John M. Martinis et al. “Decoherence in Josephson Qubits from Dielectric Loss”. In: *Phys. Rev. Lett.* 95 (21 Nov. 2005), p. 210503. DOI: [10.1103/PhysRevLett.95.210503](https://doi.org/10.1103/PhysRevLett.95.210503). URL: <https://link.aps.org/doi/10.1103/PhysRevLett.95.210503>.